# HYBRID PHASE-CHANGING NANOSTRUCTURES: FROM RECONFIGURABLE PLASMONIC DEVICES TO ULTRAFAST DYNAMICS

By

Kannatassen Appavoo

Dissertation
Submitted to the Faculty of the
Graduate School of Vanderbilt University
in partial fulfillment of the requirements
for the degree of

DOCTOR OF PHILOSOPHY
in
Interdisciplinary Materials Science
December, 2012
Nashville, Tennessee

Approved:
Professor Richard F. Haglund Jr.
Professor Sokrates T. Pantelides
Professor Sandra J. Rosenthal
Professor Jason G. Valentine
Professor Sharon M. Weiss

To mum and dad,

For the strength and unquestioning support to let their one and only son be at the antipode of their world to pursue his dreams.

To Professor Haglund,

For giving me a shot.

# ACKNOWLEDGMENTS

स यो हैतानन्तवत उपास्तेऽन्तवन्तꣳस लोकं जयत्यथ
या हैताननन्तानुपास्तेऽनन्तꣳ स लोकं जयति ॥ १३ ॥

And he who worships them as finite, obtains a finite world,
But he worships them as infinite, obtains an infinite world.
~ *The Upanishads*

I still have recollections of being 12 years old and telling friends and family, or whoever would actually listen, that my plan was to move to the United States to pursue my very own geeky American dream: studying science in a high-tech laboratory. To the people and institutions that made this a reality – my parents, Professor Haglund, Khalef, Royal College of Port-Louis, Berea College and Vanderbilt University – thank you.

Above all, my deep sense of gratitude goes to Professor Haglund who is the singular reason for my doctoral work to have seen daylight. I consider myself privileged to have worked with him on a daily basis as his own example of extraordinary hard work is a true inspiration to me and many others. Besides giving me a chance to work in his laboratory, teaching me how to become an independent researcher and showing me the esoteric art of getting a paper published, his trust in me was unparalleled, providing me many a times "carte blanche" on my scientific hunches. To Professor Haglund: I remain indebted to you for the many years or lives to come.

To my committee members – Professors Sokrates T. Pantelides, Sandra J. Rosenthal, Jason G. Valentine and Sharon M. Weiss – I thank you for your time and scientific guidance,

and most importantly for sharing your love of science with me. Thank you for believing in me and encouraging me on a regular basis to collaborate with your respective research groups. I hope that my dissertation truly reflects the extent of my collaboration with each and every one of you. A special “thank you” goes to Professor Valentine for providing me a glimpse of the joys and difficulties in starting a laboratory and for introducing me to metamaterials.

For their support and friendship, I thank the past and present members of the Applied Optical Physics group. I thank Andej Halabica and Ben Lawrie for sharing their love of ultrafast with me and Davon Ferrara and Jed Ziegler for teaching me the art of electron-beam lithography. Without them, many of my projects would not have gotten off the ground. Special thanks go to Joyeeta Nag for her encouraging words and never-ending willingness to collaborate with me, to Dr. Ferrara for providing me with my first scientific obsession: interferometric autocorrelation measurements and Robert Marvel for teaching me that the next generation can be as good, if not better than the previous one. Last but not least, it is said by Isaac Newton that “if I have seen further it is by standing on the shoulders of giants.” Although we have never met, I thank René Lopez for introducing vanadium dioxide to the group, the gift that keeps on giving.

Significant portions of my research were conducted at the Vanderbilt Institute for Nanoscale Science and Engineering facilities and consequently I owe my gratitude to all the VINSE staff. Particularly, I thank Professor Hmelo, Bo Choi, Ben Schmidt and Bob Geil for their extensive training sessions. Their expertise and technical advice proved invaluable throughout my time at Vanderbilt University.

My doctoral work was the result of several multi-national collaborations. First, I thank Professor Stefan Maier, Dang-Yuan Lei and Yannick Sonnefraud at Imperial College London for their invaluable expertise and advice regarding both single-particle spectroscopy and simulations of complex nanostructures. I thank Ying Xu, Drew Steigerwald, John Kozub and Sergey Avanesyan for help with my first pump-probe experiments at Vanderbilt University. I thank Simon Wall, together with Professor Martin Wolf and Julia Stähler at the Fritz-Haber-Institut der Max-Planck-Gesellschaft for their collaboration and tremendous insights on ultrafast studies of vanadium dioxide. I thank Professor David Hilton and Nathaniel Brady at The University of Alabama at Birmingham and Rohit Pransankumar and Minah Seo at Los Alamos National Laboratory for their direct contribution to the ultrafast studies of hybrid nanomaterial. I thank Professor Philip Willmott and Stephan Pauli of the Synchrotron facility at the Swiss Light Source. I thank the DTRA group members for providing me with a glimpse of a highly complex collaborative research incorporating biology, chemistry and physics. Finally, my heartfelt gratitude goes to Bin Wang, Dang Yuan Lei and Yannick Sonnefraud who have contributed directly in many ways to adding tremendous scientific depth to my doctoral work.

My interest in phase-changing material and pump-probe spectroscopy was spurred by the infectious enthusiasm of the Phase-Change Non-Volatile Memory group at IBM – Almaden Research Division. So, to Delia Milliron, Simone Raoux, Robert Shelby and Bulent Kurdi: thank you as working with you made it clear that experimental physics is what I should be doing.

I also take this opportunity to thank few teachers and Professors that have directly contributed to shape my views about science: Mr. Thodda, Mr. Chong, Mr. Sungeelee, Prof. Majumdar, Prof. Powell and Prof Amer. You have not only instilled the love of physics in me but have directly helped get me there. Furthermore, I thank the undergraduates and incoming graduate students who have worked closely with me for their summer research or research rotations: Luke Andrea, Ethan Shapera, Yuanmu Yang and Christina McGahan. In many ways, my professional development and future career decisions have been influenced by you. On a more personal note, I thank Sarah Satterwhite, Carol Soren, Sandy Childress, René Colehour for getting the not-so-little things done and making my graduate life run as smoothly as it possibly could, till the last minute.

It is amazing to realize the number of people that it takes to get research done, but even more astounding to me is the ability for science to bring people all over the world together. To all the people with whom I have shared a "wall" or an office, thank you for sharing your traditions and beliefs with me. It is remarkable how many countries (USA, India, China, Russia, Nepal, Iran, Venezuela, Spain, England, Slovakia, France and of course Mauritius) can fit in room 6423 of the Stevenson Center…

Last but not least, I thank my family back home for their love and support. Few special thanks are also required. To BoJana and Rob, thank you for keeping me sane and healthy on a regular basis, but above all for being my friend through thick and thin; you are the two people that I could not afford to lose during my graduate career. To Bolotbek, Remi, Dikshya, Dhiraj, Rod, Christina, Suraj, Subhav, Praneeta, Alina, Peter, Kenny, Vusal, Yordan, Saylee, Seema, Jordan, Terri, Jack, Tamara, Anurag, Shefali, Joy, Sandy, Steve, Robin, Jim and

Buchi: thank you for sharing your lives with me and for providing me with new addictions on a regular basis, rock climbing and eating momos being the latest ones.

To Shiblee, Enrique, Michaela, Andreea and Pritha., I will not thank you for the lovely distractions from my studies; not even for showing me what living means in its various ways, shapes and forms outside of the scientific world, but I will thank you for this: being who you are and staying true to your beliefs, whether or not they made sense to others…

Whether one believes there is a God or not who assigns one to a family, I am blessed to have landed into two sets of amazing homes; to Joanne and Pradeep in little town Berea, thank you for providing a home away from home when I needed it the most; to my parents in tiny island Mauritius, thank you for all your support, trust and love. Although these eight years of being away flew by for me, I know it seemed an eternity for you. So to mum and dad, there can only be one thing to say: I love you.

Kannatassen Appavoo

December 2012

*My dissertation is a result of the work funded partly by National Science Foundation (ECE-0801980), the Office of Science, US Department of Energy (DE-FG02-01ER45916) and the Defense Threat Reduction Agency (HDTRA1-10-1-0047). Portions of this doctoral work were performed at the Vanderbilt Institute of Nanoscale Science and Engineering, using facilities renovated under NSF ARI-R2 DMR-0963361.*

# PREFACE

"What I cannot create, I do not understand"

~ *Richard Feynman, 1965 Nobel Laureate*

The quest for understanding light-matter phenomena has accompanied the evolution of mankind from almost its origins. As a science, it can be traced as far as the Ancient Greek civilization, when during his studies on visual perception, Aristotle realized the importance of the medium in-between the eye and an object. At the core of our abilities for visual perception is the power of optics which is based on one simple fact – *light exhibits the right amount of interaction with matter*. Put more scientifically, light quanta lies in the energy range of electronic and vibrational transitions in matter[1]. For this reason, experiments with light are intuitive and help us to consciously and rationally connect abstract ideas. Nowadays, the detailed study of light-matter interaction has, as its ultimate goal, the spatial and temporal control of selected modes of electromagnetic radiation to particular material excitations.

Over the last century, the ability to understand complex photon-atom interaction has been greatly challenged. However, thanks to the progress in nanotechnology, scientists are now able to routinely tailor, measure and manipulate the properties of nanostructures at the individual level, thus providing a deeper understanding of the coupling mechanism at play. More importantly, such studies have revealed that as we examine even smaller-sized structures, new physical effects become prominent, implying their potential prospect in technological applications. Some of the recent achievements in the field of nano-optics

are highlighted in figure P.1, where nanostructures were tailored to provide unique optical phenomena such as lasing in a single living cell and cloaking, to name a few.

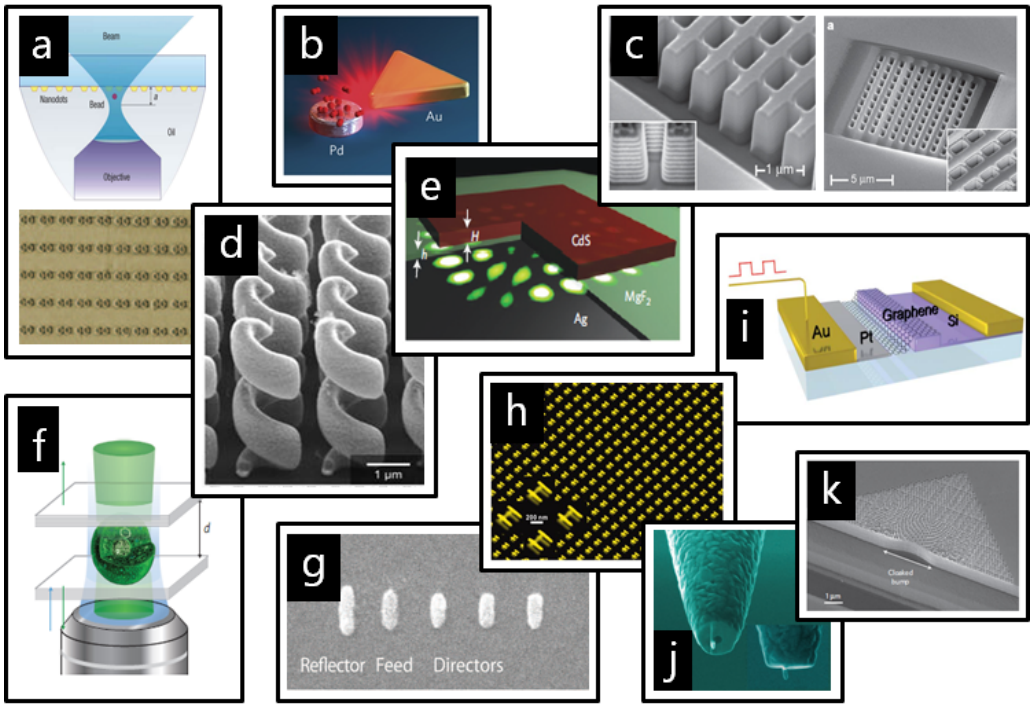


**Figure P.1. Potpourri of Tailored Light-Matter Interaction at the Nanoscale. (a)** Quenching Brownian motion using plasmonic nanometric optical tweezing;[2] **(b)** Single tailored nanofocus for enhanced gas sensing;[3] **(c)** 3D optical metamaterial for negative refractive index;[4] **(d)** Gold helix for broadband circular polarizer;[5] **(e)** Room-temperature sub-diffraction plasmonic laser;[6] **(f)** Single-cell biological laser;[7] **(g)** Nanoantenna coupled to a quantum dot for directional emission;[8] **(h)** 3D plasmonic rulers to determine distances within chemical or biological species;[9] **(i)** Atomic graphene layer for optical broadband modulation;[10] **(j)** Optical monopole antenna for directing single-molecule emission;[11] **(k)** Carpet cloak made of dielectrics.[12]

The *main motivation* of this dissertation is to develop an understanding of reconfigurability in hybrid nanostructures whose optical properties can be uniquely

manipulated on an ultrafast timescale. Controlling the flow of light and charge carriers in plasmonics systems – based on quanta of plasmon oscillations derived from coupled electron-photon modes – is achieved by using the kinetics and dynamics of a phase-transforming material. This work demonstrates precisely how functionality hinges on the expertise in tuning the spatial and temporal features of a quantum material vanadium dioxide ($VO_2$). Since these quantum materials offer many "knobs" to control macroscopic phenomena such as high-temperature superconductivity[13], colossal magnetoresistance[14], multiferroicity[15] or metal-insulator transition[16], this thesis could potentially be generalized to the study of other classes of hybrid nanomaterials. For example, one of such studies could be the coupling of magnetic responses of split-ring resonator metamaterial[17] with manganites to enhance or control magnetic dipole transitions[18]. We devote this thesis to studying the insulator-to-metal transition in $VO_2$ and its role in optimizing modulation of plasmonic functionality in confined nanoscale volumes and on an ultrafast timescales. Fundamental intrinsic properties such as electron-electron interaction, electron-phonon coupling and electron-grain-boundary scattering, intimately connected to phenomena such as defect-mediated nucleation, interfacial effects, electron injection or chemical interface damping will be discussed.

***Chapter 1*** serves as an introduction to both the field of plasmonics and phase-changing vanadium dioxide with a focus on the ultrafast manipulation of such systems. Since the ultimate goal is device-integration, we introduce in this chapter a novel and reliable deposition method for producing thin films and nanostructures of $VO_2$ using *electron-beam evaporation*. Combined with the versatile hole-colloidal mask lithography

technique[19] (Appendix A), cost-effective and large surface areas ($cm^2$ compared to $\mu m^2$) of active substrates could thereafter be implemented in on-chip sensors, catalytic nanodevices or for fundamental ultrafast studies of size-dependent switching in phase-changing material. Since the primary goal of this thesis however is to understand the fundamental properties of such hybrid nanostructures, most structures presented in the subsequent chapters were fabricated by electron-beam lithography for precision.

In ***Chapter 2***, we demonstrate the proof-of-principle that modulation and consequently interrogation can be achieved even at the *level of the single plasmonic nanoantenna.* Incidentally, the sensitivity of our detection system hints towards potentially probing electron scattering mechanisms at grain boundaries of the $VO_2$ domains and at the onset of the phase-transition, that is in the region of strong electron correlation. More importantly, this suggests that near-IR scattering spectroscopy of individuals vanadium dioxide domains could provide tremendous amount of information on the switching properties of other quantum materials. ***Chapter 3*** illustrates this concept by demonstrating that plasmon resonance spectroscopy when combined with electron-beam lithography can be an exquisite method for probing the *intrinsic* properties of *single pristine $VO_2$ nanostructures* as a function of their shape, morphology or interfaces. This chapter is devoted to understanding the properties of the nanostructured $VO_2$ only and at the single domain level. Effect of homointerfaces and defects will be discussed in relation to the novel size-dependent optical switching. Most importantly, domain-boundary engineering to tailor state-of-the-art phase-changing devices is highlighted.

Having gained insights into $VO_2$ properties from previous chapters, ***Chapter 4*** provides a detailed description of various hybrid plasmonic/phase-change architectures that can provide greater modularity while displaying relatively high Q-factors. First, plasmonic nanodisks on active $VO_2$ film exhibiting a single resonance are investigated, followed by stacked plasmonic/PCM nanodisks. Since $VO_2$ films are highly absorptive, fabricating sandwiched nanoparticles is an ideal solution in achieving large modulation contrast – as large as 230 nm between the two states – while reducing absorption drawbacks. This is made possible due to the high change in dielectric contrast of $VO_2$, even when used in rather small quantities. Thereafter, more complex geometries exhibiting anisotropic electron oscillations such as in a split-ring resonator (SRR) structure are studied. The SRR proves not only to be polarization selective but also whose spectral responses can be individually modulated thanks to the size-dependent switching of $VO_2$. In order to emphasize the point that only a small amount of PCM is needed, we explore the effect of *modulation at a distance* by placing a phase-changing nanostructure *near* – but not touching – a plasmonic one. Using a three-stage lithographic procedure, we show exquisite control by placing this phase-changing nanostructure in each unit cell of a two-dimensional gold nanoparticle lattice. This can be extended to the study of *plasmonic assisted switching of phase-changing material* whereby the nanoparticle electromagnetic focus is tailored such that the high electromagnetic energy enhancement in the reactive near-field of the nanoantenna assists or interrogates the switching mechanism. Recently, an enhanced gas nanosensor based on similar principles has been demonstrated[3].

***Chapter 5*** marks a change from studying the optical properties of hybrid nanostructures in equilibrium limit to develop an understanding of the physics at play when these hybrid nanostructures are driven *out of equilibrium*. Although ultrafast materials' properties have been investigated for many bulk single crystals and thin films, this is the first experiment to the best of the author's knowledge that describe the interactions between a plasmonic material and a PCM simultaneously at nanometer length scales and on a femtosecond timescale. In so doing, a novel mechanism involving plasmon-induced hot-electron injection from the metallic nanostructure triggering the $VO_2$ phase transition is reported. This *all-optical ultrafast* demonstration of switching in PCM via electron injection paves the way to *optically induced electronics* (OIE)[20], with the potential of tailoring nanostructures exhibiting strong plasmonic or Fano resonance for wavelength-dependent and efficient dynamic charge doping. Although much of this study deals with the fundamental aspects of the switching mechanism, such an experiment has a broader impact with the potential technological demonstration of an ultrafast broadband switch operating at THz speeds.

The ***Conclusion and Future Directions*** chapter discusses experiments targeted toward a deeper understanding of the fundamental mechanism at play between electrons in plasmonic elements and those in quantum materials. Probing those dynamics in time domain could be performed by implementing a novel technique: ***nano-interferometric frequency resolved optical gating*** (nano-iFROG) which analyses the spectrally resolved second harmonic from non-centrosymmetric nanoparticle as a function time delay. From those "weak-probe" measurements, coherence lifetime, $T_2$, can be

extracted. Such experiments would be conducted near the threshold for switching in order to resolve the dynamics of enhanced scattering – either in pristine $VO_2$ nanoparticle arrays or a single Au nanoparticle "sitting" on a $VO_2$ substrate – during the onsets of the transition. Furthermore, studies to elucidate the defect-mediated nucleation process and the intrinsic size limit for switching $VO_2$ are natural follow-on of chapter 3. For example, high-resolution transmission electron microscopy of quantum-sized stoichiometric nanocrystals of $VO_2$ trapped between graphene layers while undergoing phase transformation could be performed, similar to experiments by Yuk *et al.* and Scholl *et al.* [21,22]. Finally, plasmonically enhanced nanoscale energy transfer mechanisms as shown in chapter 5 provides food for thoughts about tailoring other hybrid nanomaterials that could lead to all-optical switching and control at optimal switching thresholds. Understanding each component, both separately and when strongly coupled is a crucial step toward achieving transistor-type optical nanodevices for manipulating the propagation, absorption and emission of light.

# TABLE OF CONTENTS

# LIST OF FIGURES

## PREFACE



## CHAPTER 1

**CHAPTER 2**



**CHAPTER 3**

**CHAPTER 4**

**CHAPTER 5**



**CHAPTER 6**

**APPENDIX A**



**APPENDIX B**

# LIST OF ABBREVIATIONS

AFM ……Atomic Force Microscopy

ARPES ……Angle-Resolved Photo-Emission Spectroscopy

BBO ……Barium Beta Borate ($BaB_2O_4$)

DOS ……Density of States

DFT ……Density Functional Theory

EBL ……Electron-Beam Lithography

$E_F$ ……Fermi Level

EIT ……Extraordinary Induced Transparency

FDTD ……Finite-Difference Time-Domain

FIB ……Focused Ion Beam

FROG ……Frequency-Resolved Optical-Gating

GGA ……Generalized-Gradient Approximation

HMCL ……Hole-Mask Colloidal Lithography

*i*FROG ……Interferometric Frequency-Resolved Optical-Gating

IMT ……Insulator-to-Metal Transition

NIR ……Near-Infra Red

NS ……Nanostructure

LDA ……Local-Density Approximation

LSPR ……Localized Surface Plasmon Resonance

OIE ……Optically Induced Electronics

PCM ……Phase-Changing Material

PDDA ……Poly-Diallyl-Dimethyl-Ammonium

PEEM ……Photoemission Electron Microscopy

PML ……Perfectly Matching Layer

PSS ……Poly-Styrene Spheres

PT ……Phase Transition

SECM ……Strongly-Correlated Electron Material

SEM ……Scanning Electron Microscopy

SHG ……Second Harmonic Generation

SRR ……Split-Ring Resonator

SPP ……Surface-Plasmon Polariton

TFSF ……Total-Field Scattered-Field

QCM ……Quartz Crystal Microbalance

TEM ……Transmission Electron Microscopy

$VO_2$ ……Vanadium Dioxide

# LIST OF PUBLICATIONS

**Portions of this dissertation have been drawn from the following publications and manuscripts:**

P1. Lei DY, **Appavoo K**, Sonnefraud Y, Haglund RF Jr. and Maier SA, "*Single-Particle Plasmon Resonance Spectroscopy of Phase Transition in Vanadium Dioxide"* **Optics Letters 2010**, Vol. 35, Issue 23, pp. 3988-3990. *link*

P2. **Appavoo K** and Haglund RF Jr., "*Detecting Nanoscale Size Dependence in $VO_2$ Phase Transition Using a Split-Ring Resonator Metamaterial*" **Nano Letters 2011**, 11 (3), pp. 1025–1031. *link*

P3. **Appavoo K***, Lei DY*, Sonnefraud Y, Wang B, Pantelides ST, Maier SA and Haglund RF Jr., *"Role of Defects in Phase Transition of $VO_2$ Nanoparticles Probed by Plasmon Resonance Spectroscopy"* **Nano Letters 2012**, 12 (2), pp. 780-786. *link*

P4. Wall S, Wegkamp D, Foglia F, **Appavoo K**, Nag J, Haglund RF Jr., Stahler J and Wolf M, "*Ultrafast Changes in Lattice Symmetry Probed by Coherent Phonons*" **Nature Communications 2012**, 3, 721. *link*

P5. Marvel RE*, **Appavoo K***, Choi BK, Nag J and Haglund RF Jr., "*Electron-beam deposition of $VO_2$ thin films for optical applications*" **Applied Physics A: Materials Science and Processing 2012**. Springer-Verlag, doi:10.1007/s00339-012-7324-5 *link*

P6. **Appavoo K**, Brady N, Wang B, Seo M, Nag J, Pantelides ST, Prasankumar R, Hilton D, Haglund RF Jr., "*Plasmonic Hot-Electron-Injection Drives Ultrafast Phase Transition*," manuscript submitted to **Nature 2012**.

P7. **Appavoo K** and Haglund RF Jr., "*Polarization-Dependent Hybrid Nanomodulator*" manuscript in preparation for **Nature Communications 2012**.

C1. **Appavoo K**, Lei DY, Sonnefraud Y, Ferrara DW, Nag J, Maier SA and Haglund RF Jr., "*Spectral Modulation of Single Plasmonic Nanostructures*" in *Synthesis and Photonics of Nanoscale Materials VII,* **Proceedings of SPIE 2010** Vol. 758606. *link*

C2. **Appavoo K** and Haglund RF Jr. "*Effect of Phase-Transforming Medium on Coherent Electron Dynamics in Gold Nanoantennas*" in **CLEO:QELS 2011**, Optical Society of America Technical Digest, paper QWD2. *link*

C3. **Appavoo K**, Brady N, Seo M, Nag J, Prasankumar R, Hilton D, Haglund RF Jr., "*Ultrafast Metal-Insulator Transition in $VO_2$ Driven by Electron Injection*" in **Post-deadline CLEO:QELS 2012**, Optical Society of America Technical Digest QTh5B.5. *link*

**The following publications and manuscripts have been/will be published during the course of my PhD but were not included in this dissertation:**

P1. Lei DY*, Fernandez-Dominguez AI*, Sonnefraud Y, **Appavoo K**, Haglund RF Jr., Pendry JB, Maier S, *"Revealing Plasmonic Gap Modes in Particle-on-Film Systems Using Dark-Field Spectroscopy"* **ACS Nano 2012**, 6 (2), pp. 1380-1386. *link*

P2. **Appavoo K**, Casey MC, Gulka CP, Raubach AJ, Warnick KH, Wang B, Ziegler JI, Cliffel DE, Pantelides ST, Wright DW, Haglund RF Jr., "*Self-Decontaminating, Autocatalytic Nanostructured Surfaces for Enhanced Surface-Plasmon Resonance Sensing*" manuscript under review at **Nature Scientific Reports 2012**.

P3. Nag J*, **Appavoo K***, Duscher G, Luo W, Pantelides ST and Haglund RF Jr., "*Control of Ultrafast Switching Dynamics in Epitaxial $VO_2$ Films by W-Doping*" manuscript under review at **Physical Review Letters 2012**.

C1. Ferrara DW, Nag J, MacQuarrie E, **Appavoo K**, Haglund RF Jr., "*Far-field Coupling in Arrays of Gold and Gold/Vanadium Dioxide Nanodimers*" in *Plasmonics: Metallic Nanostructures and Their Optical Properties VII*, **Proceedings of SPIE 2009** Vol. 7394Q. *link*

# CHAPTER 1

# INTRODUCTION

"The most exciting phrase to hear in science, the one that heralds new discoveries, is not "Eureka" but "That's funny..."""

~ *Isaac Asimov*

## 1.1 ABSTRACT

The miniaturization of photonic circuits lies at the foundation of today's most important data processing and telecommunication technologies. Plasmonics, the study of the optical properties of metallic nanostructures is an exciting new device technology and holds the promise of the next generation of circuits, which interfaces both electronic and photonic components in a single chip[23]. As shown in Figure 1.1, plasmonics naturally interfaces with similar size electronic components while enabling such devices to work at the operating speed of photonic networks. However, for plasmonics to be a viable technology, two major hurdles need to be overcome – the ability to guide light in sharply curved waveguides and the need to modulate these signals in such spatially confined spaces. Although such signals can be successfully guided by using surface plasmons as information carriers, modulating these signals in highly confined nanoscale volumes remains a major barrier.

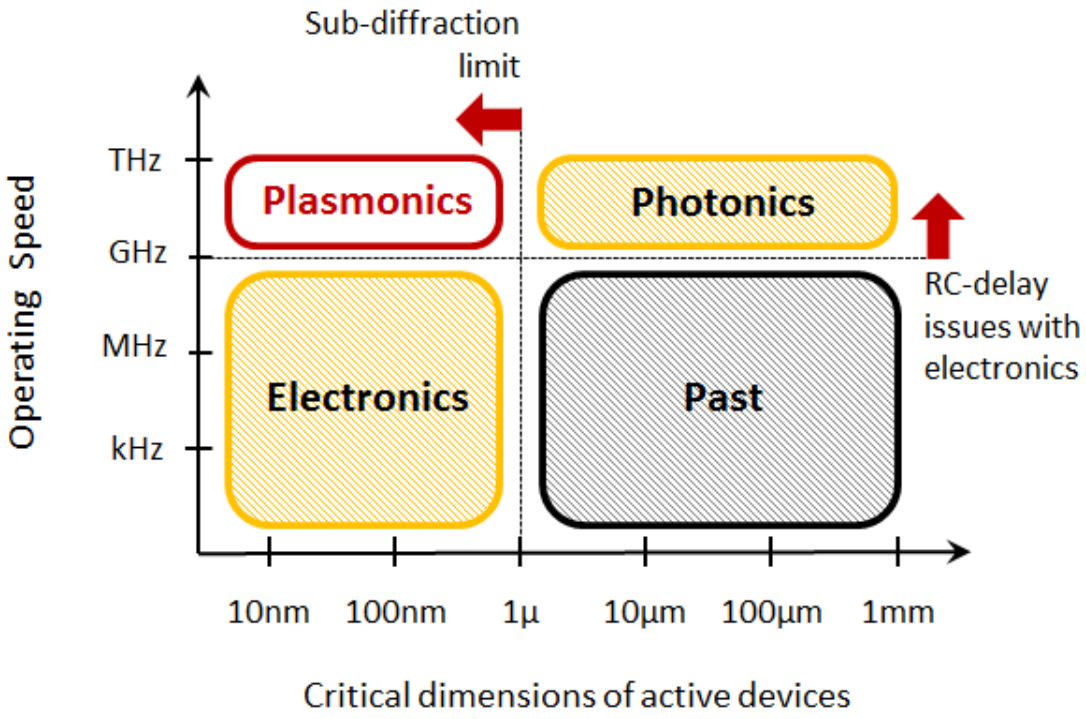


**Figure 1.1: Role of Plasmonics in Today's Device Technology.** Plasmonics naturally interfaces both electronic and photonic components in a single chip, thus enabling such novel devices to work at the operating speed of photonic networks[24].

This chapter serves two purposes: it highlights the fundamental concepts in plasmonics and more importantly, introduces quantum materials[25] as the most promising medium for creating functionality in nanodevices. Here the focus is on prototypical, indeed canonical, vanadium dioxide ($VO_2$) whose properties both in the equilibrium and non-equilibrium limits can be tailored as a function of size, shape and morphology. Thus, $VO_2$ provides many "knobs" for reconfigurability. More broadly, this dissertation shows that a deeper understanding of the symbiosis of plasmonics and quantum materials – both at the nanoscale and at ultrafast timescale – is necessary for the integration of reconfigurable hybrid nanomaterial in modern data-storage and photonics technologies. With the advent

of the necessary fabrication and characterization tools, novel properties in both fields were discovered, giving birth to new fields such as metamaterials. This fact is illustrated in Figure 1.2 that shows exponential growth in the fields of plasmonics, metamaterials and PCM-$VO_2$. The physics of such materials was discovered and described during the late 1960s but their properties were harnessed only in the early 2000s, coinciding with maturing nanofabrication and analysis technologies such as atomic force microscopy (AFM), scanning or transmission electron microscopy (SEM or TEM), focused ion beam (FIB) milling and electron-beam lithography (EBL).

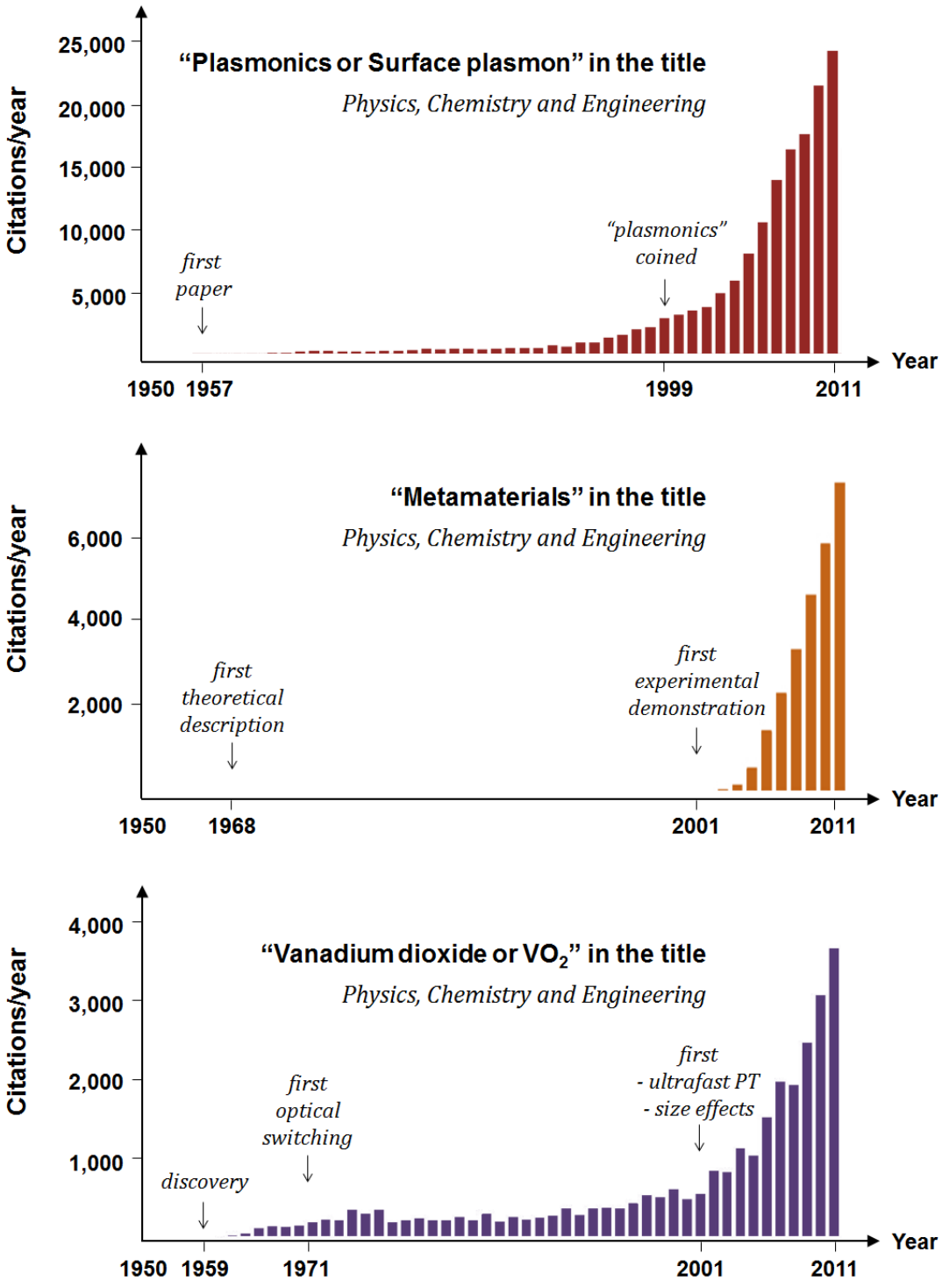


**Figure 1.2: Citations per Year in Plasmonics, Metamaterials and Vanadium Dioxide.** **(a)** Surface plasmon first theoretically investigated in 1957[26] and first calculations of its

dispersion relation in 1966 by Ritchie *et al.*[27] and, the term "plasmonics" coined in 1999 by Brongersma *et al.*[28] **(b)** Metamaterials first described theoretically by Veselago in 1968[29] and experimentally shown in 2001 by Shelby *et al.*[30-33] **(c)** Vanadium dioxide first discovered in 1959 by F. J. Morin[34] and Goodenough *et al.* describing its optical properties in 1972. In 2001, while Cavalleri *et al.* discovered that this solid-solid phase transition could take place in 70 fs [35], Lopez *et al.* demonstrated that $VO_2$ exhibited size-dependent switching properties as well[36,37]. Very recently, Eyert showed how to theoretically obtain the correct band structure for $VO_2$[38]. The data was extracted from Web of Knowledge.

## 1.2 PLASMONICS

### 1.2.1 An Overview

From early artisan studies during pre-modern era symbolized by the 4$^{th}$ Century A.D. Roman Lycurgus Cup in Figure 1.3, plasmonics has evolved to become a respected branch of condensed matter physics, devoted to the study of photon-matter interaction in nanostructured systems. Although the description of the exact coupling mechanism can be traced back to Ritchie *et al.* in 1957[26], it is arguably Heinz Raether who fueled interest of the field when he published his book "Surface Plasmons on Smooth and Rough Surfaces and on Gratings" in 1987[39], describing in great details the concept of surface plasmons and how to excite them. Ten years later with the first experimental observation of extraordinary transmission through metallic subwavelength hole arrays[40] and Pendry' s first theoretical description of a superlens[41], the scientific community showed renewed interest in plasmonics.


**Figure 1.3: 4th Century A.D. Roman Lycurgus Cup.** The Lycurgus Cup (with modern metal mounts) in **(a)** reflected and **(b)** transmitted light. **(c)** TEM image of a silver-gold alloy nanoparticle within the glass of the Lycurgus Cup[42]. © The Trustees of the British Museum, Department of Prehistory and Europe, The British Museum.

The coupling of the energy and propagating properties of photons with the high degree of localization of a free-electron gas in a nanostructure creates a hybrid oscillating electron-photon mode known as a plasmon. In this hybrid excitation, light is effectively squeezed in nanoscale subwavelength spaces that is beyond the diffraction limit (about half a wavelength), reaching recently record confinements of $\sim \lambda/165$ and $\sim \lambda/200$ for quantum metallic nanoparticle[22] and defect in graphene[43], respectively. Due to this extreme confinement and the efficient EM energy transfer between the near- and far-field regions, plasmonics has been proposed for use in diverse fields such as surface-enhanced microscopy[44], photothermal tumor ablation[45,46] and high-resolution lithography[47,48], to name a few. Although such coupling phenomena can occur via bulk plasmon excitation,

surface plasmon polaritons and localized surface plasmon, only the last two are relevant for technological applications, as will be explained later.

### 1.2.2 Theoretical Background and Fundamental Studies of Plasmonics

#### 1.2.2a Propagating Surface Plasmons/Surface Plasmon Polaritons

Surface plasmons are quantized EM surface waves that are localized at the interface between a plasma (typically a metal) and a dielectric material (typically air or silica). While the waves propagate along the metal/air interface, the electron charge density fluctuations in the metal generate electric fields that decay exponentially on either side of the interface. Bulk plasmons are purely longitudinal in character because $\nabla \cdot E \neq 0$ when solving the charge continuity equation, $\nabla \cdot j = -(\partial \rho_e)/\partial t$; a consequence of the fact that at the plasma frequency $\omega_p$, the relative dielectric constant $\varepsilon_r = 0$. On the other hand, surface plasmons can interact directly with photons because they have both transverse and longitudinal components. Since this interaction is strong enough, the photon-plasmon is considered to be a coupled system and is referred to as a polariton. As it is localized at the surface as well, it is also known as a *surface plasmon polariton* (SPP). By solving Maxwell's equations and remembering that at the boundary conditions, the tangential components of $E$ and $H$, together with the normal component of the electric displacement $D$ must be continuous at the interface, the dispersion relation for the SPP propagating along the x-direction is:

$$k_x = \frac{\omega}{c}\sqrt{\frac{\varepsilon_{metal} \cdot \varepsilon_{dielectric}}{\varepsilon_{metal} + \varepsilon_{dielectric}}} \qquad \text{eqn 1.1}$$

For a metal described by a real Drude dielectric function with negligible damping (negligible collision frequency), $\varepsilon_{metal} = 1 - {\omega_p}^2/\omega^2$, figure 1.4(c) shows the SPP dispersion with varying dielectrics. Such SPPs are evanescent, decaying exponentially in the direction normal to the interface and having a decay length ranging from about 10 to a few hundred nanometers. For in-plane propagation, the propagation length is the inverse of the imaginary part of the $k$ vector and is given by:

$$\delta_{SP} = \frac{1}{2{k_x}''} = \frac{c}{\omega} \cdot \sqrt[3]{\frac{\varepsilon_{metal} + \varepsilon_{dielectric}}{\varepsilon_{metal} \cdot \varepsilon_{dielectric}}} \cdot \frac{({\varepsilon_{metal}}')^2}{{\varepsilon_{metal}}''} \qquad \text{eqn 1.2}$$

In the case of silver film for example, it extends to hundreds of micrometers depending on exact metal/dielectric configuration, as shown experimentally by Lamprecht *et al.*[49,50]. Thus, this is considered far enough to transfer optical signals at nanometer length scales, although confinement in the dielectric medium is hindered. This trade-off between localization and loss is common in analyzing plasmonic devices.

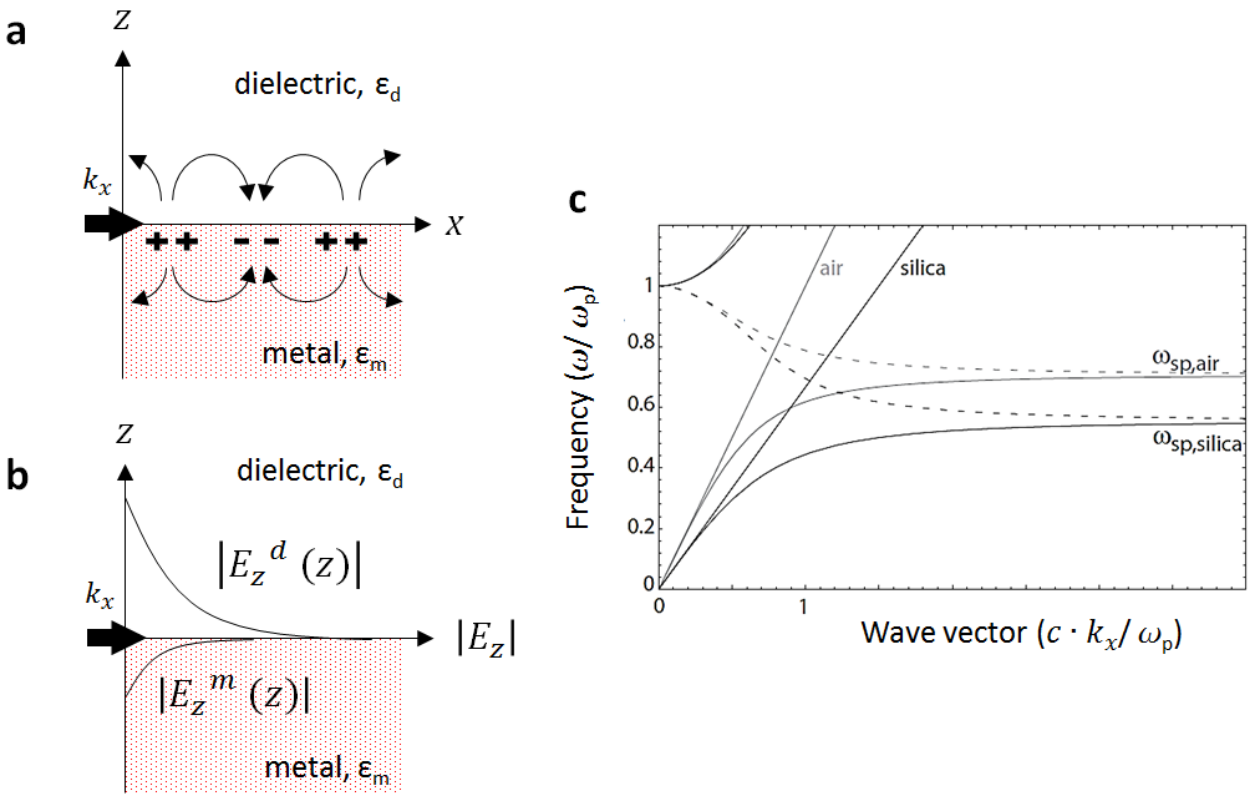


**Figure 1.4: Dispersion Relation for Surface Plasmon Polariton. (a)** Definition of the axes for the interface between a dielectric and a metal. **(b)** Exponential decay of the field amplitudes as a function from interface. **(c)** Dispersion relation for the SPP between a Drude metal and air ($\varepsilon_{diel.}$ = 1) or fused silica ($\varepsilon_{diel.}$ = 2.25) as the dielectric medium. Adapted derivations and figures from references [51,39] and [52].

From Figure 1.4, we see that since the wave vector of the SPP exceeds the wave vector of the photon for the same frequency, it is not possible to excite the SPP directly by shining light on a smooth surface. Therefore, special techniques to compensate for the momentum mismatch (or meet the phase-difference between the SPP modes and the light in the dielectric) are required. A few examples are prism coupling with attenuated total reflection

effect (Kretchmann or Otto configuration[39]), near-field excitation or periodic grating such as grooves or holes. Moreover, since SPP coupling is exquisitely sensitive to variation in the near-field environment, modulation of its intensity or propagation can be easily achieved by controlling the surrounding dielectric, as was demonstrated by Suh *et al.*[53,54].

### 1.2.2b Localized Surface Plasmons

In contrast to SPPs that propagate along the dielectric/metal interface, localized surface plasmons are coupled oscillations of the conduction electrons with EM field that are bound within a finite volume, restricted by the geometrical shape of the nanostructure and, for small nanoparticles, typically resemble dipoles with clouds of charge localized at the poles (Figure 1.5(a)). Moreover, as oppose to SPPs that cannot be excited directly due to phase-matching issues, LSPs can be directly excited thanks primarily to the curved nanoparticle surfaces that act as optical cavities and exert an effective restoring force on the EM-field driven electrons, resulting in a resonance response to the incident field. At the localized surface plasmon resonance (LSPR) frequency – occurring typically in the visible-NIR region – the nanostructures are characterized by large, size-dependent scattering and extinction cross-sections. Similar for the case of SPPs, materials that are considered good plasmonic materials are silver and gold, an sometimes copper. Aluminum, with its resonance in the near-UV, is also of great interest to the plasmonic community[55,56].

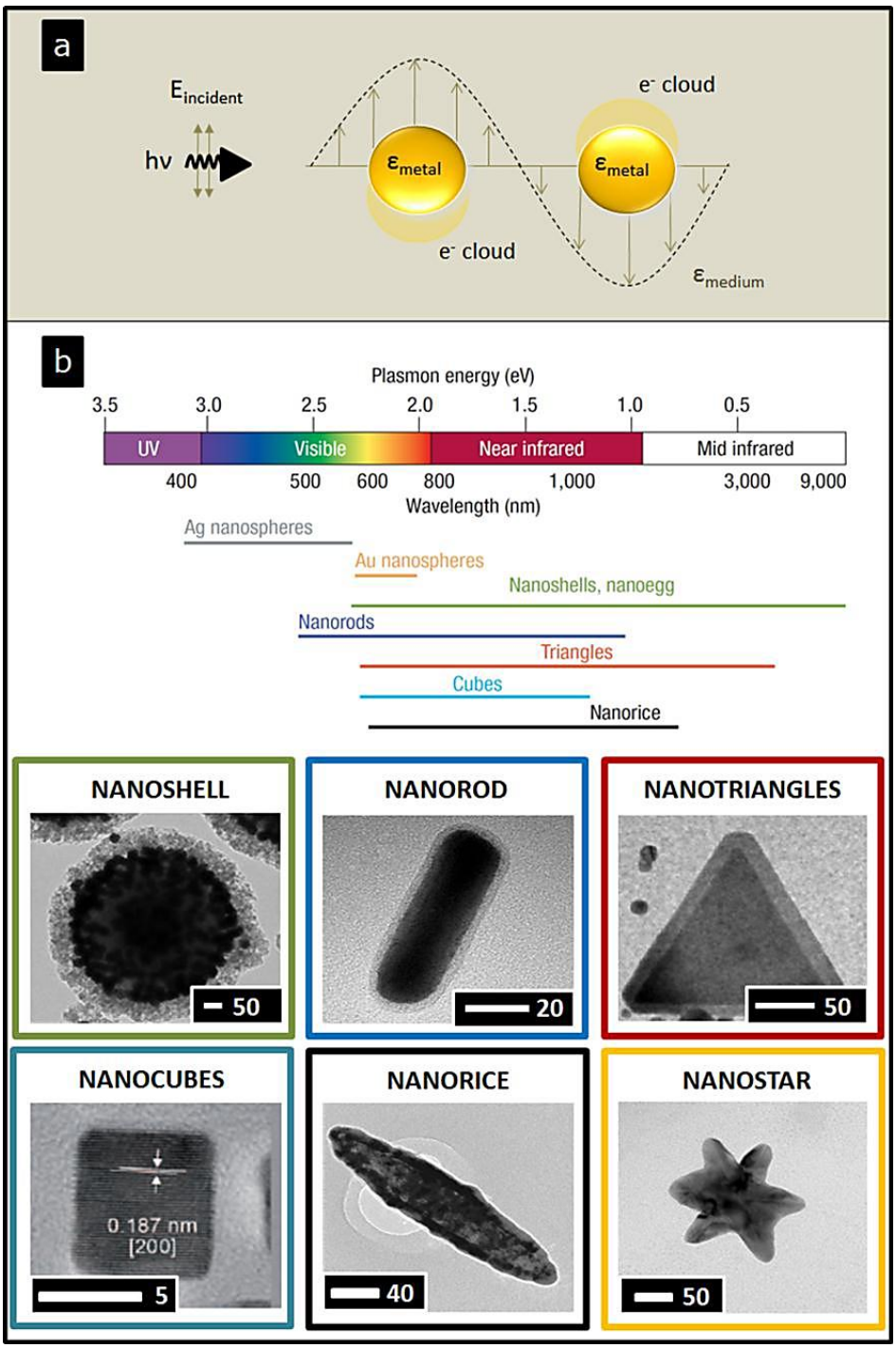


**Figure 1.5: LSPR Overview in Various Metallic Nanoparticles. (a)** Schematic of LSPR resembling a dipole with clouds of charge localized at the poles. **(b)** Variety of nanoparticles fabricated with varying optical responses, ranging from visible to the mid-IR part of the electromagnetic spectrum[57]. **(c)** Collection of individuals nanoparticles

including nanoshells[58,59], nanorods[60], nanotriangles[61]/nanoprisms[62], nanocubes[63], nanorices[64] and nanostars[65].

At the root of plasmonic phenomena is the ability for certain material to be polarized. Polarization, describing the materials interaction with EM waves, can either be electrical or magnetic in nature, although the magnetic polarizability of natural materials is negligible – by a factor of $\sqrt{\varepsilon_o/\mu_o}$ – for frequencies in the hundreds of THz[1]. Therefore, the electrical polarization can be described solely by the complex-valued dielectric function $\varepsilon(\omega)$. While the real part of the dielectric function describes the strength of polarization induced by an external electric field, the imaginary part describes losses that are incurred when polarizing the material. The electromagnetic response of the material is described by the real and imaginary parts of the dielectric, $\varepsilon(\omega) = \varepsilon'(\omega) + i\varepsilon''(\omega)$ or the complex refractive index $\tilde{n} = n + i\kappa$, where $n$ is the refractive index and $\kappa$ is the extinction coefficient (related directly to the absorption coefficient $\alpha(\omega)$).

While the LSP resonance of an arbitrary nanostructure cannot be described analytically, it is useful to describe a simple system to gain physical insights on how various factors conspire to change the spectral features of the resonance. Thus, for a small spherical NS ($a \ll \lambda$) in the quasi-static limit – that is assuming that a plane wave excites all free electrons simultaneously, or that spatial retardation effects over the particle volume are negligible – an induced time-varying oscillating dipole of the form $p(t) = \varepsilon_o \varepsilon_{diel.} \alpha E_o e^{-iwt}$ is created. This dipole radiation mediated by the spherical NS creates scattering of the exciting plane wave. Also, $\alpha$ is the complex polarizability of a material and is equal to the dipole moment per unit volume and is defined as:

$$\alpha(\omega) = 4\pi a^3 \frac{\varepsilon_{metal}(\omega) - \varepsilon_{dielectric}(\omega)}{\varepsilon_{metal}(\omega) + 2\,\varepsilon_{dielectric}(\omega)} \qquad \text{eqn 1.3}$$

A resonant effect can be obtained when $|\varepsilon_{metal}(\omega) + 2\,\varepsilon_{dielectric}(\omega)|$ is a minimum and therefore the Fröhlich condition of $Re\,[\varepsilon_{metal}(\omega)] = -2\,\varepsilon_{dielectric}(\omega)$ is obtained, corresponding to a dipole surface plasmon mode[51]. This resonantly enhanced polarizability therefore enhances the efficiency with which the NS absorbs and scatters the light. These cross-sections can be calculated by solving the Poynting-vector of the **H** and **E** fields in the near field region ($kr \ll 1$):

$$\mathrm{C}_{\text{ scattering}} = \frac{k^4}{6\pi}|\alpha|^2 = \frac{8\pi}{3}k^4a^6\left|\frac{\varepsilon_{met.}(\omega) - \varepsilon_{diel.}(\omega)}{\varepsilon_{met.}(\omega) + 2\,\varepsilon_{diel.}(\omega)}\right|^2 \qquad \text{eqn 1.4}$$

$$\mathrm{C}_{\text{ absorption}} = kIm|\alpha| = 4\pi k a^3 Im\left[\frac{\varepsilon_{met.}(\omega) - \varepsilon_{diel.}(\omega)}{\varepsilon_{met.}(\omega) + 2\,\varepsilon_{diel.}(\omega)}\right] \qquad \text{eqn 1.5}$$

For a spherical NS with volume V and a complex-valued dielectric in the quasi-static limit, the extinction cross-section, that is the sum between $\mathrm{C}_{\text{ scattering}}$ and $\mathrm{C}_{\text{ absorption}}$ is:

$$\mathrm{C}_{\text{ extinction}} = 9\,\frac{w}{c}\,\sqrt[3]{\varepsilon_{diel.}}\,V\,\frac{\varepsilon_{met.}{}'(\omega)}{[\varepsilon_{met.}{}'(\omega) + 2\,\varepsilon_{diel.}(\omega)]^2 + \varepsilon_{met.}{}''(\omega)} \qquad \text{eqn 1.6}$$

Although the discussion has assumed that we operate in the quasi-static limit and that the NSs are vanishingly small, the calculations can actually be applied to NSs with dimensions as large as ~ 100 nm and even when illuminated by light in the visible-NIR region. In the case of larger NSs, this quasi-static limit breaks down due to phase changes of the driving field over the particle volume. In this case, more rigorous electrodynamics calculations are required. The Mie theory developed by Gustav Mie in his seminal 1908 paper[66] consists of expanding both the internal and scattered fields into a set of normal modes described by vector spherical harmonics. Thus, for larger particles, the first mode of the spherical NS polarizability is[51,67]:

$$\alpha_{\text{sphere}} = \left( \frac{1-\left(\frac{1}{10}\right)\left(\varepsilon_{met.}(\omega)+\varepsilon_{diel.}(\omega)\right)x^2+O(x^4)}{\left(\frac{1}{3}+\frac{\varepsilon_{diel.}(\omega)}{\varepsilon_{met.}(\omega)-\varepsilon_{diel.}(\omega)}\right)-\frac{1}{30}\left(\varepsilon_{met.}(\omega)+10\varepsilon_{diel.}(\omega)\right)x^2-i\cdot\frac{4\pi^2\sqrt[3]{\varepsilon_{diel.}(\omega)}}{3}\cdot\frac{V}{{\lambda_o}^3}+O(x^4)} \right)\cdot V \quad \text{eqn 1.7}$$

where $(i)$ $\left(\frac{1}{10}\right)\left(\varepsilon_{met.}(\omega)+\varepsilon_{diel.}(\omega)\right)x^2$ is the retardation of the driving field over the NS volume (shifting the plasmon resonance) (ii) $\frac{1}{30}\left(\varepsilon_{met.}(\omega)+10\varepsilon_{diel.}(\omega)\right)x^2$ is the retardation effect of the depolarization field inside the nanoparticle. For noble metals, this corresponds to a red-shift in the dipole resonance when the NS size increases. This can be easily understood as the distance between the charges at opposite interfaces of the particle increases with size, leading to a smaller restoring force and thus lowering of the frequency. The imaginary term $\frac{4\pi^2\sqrt[3]{\varepsilon_{diel.}(\omega)}}{3}\cdot\frac{V}{{\lambda_o}^3}$ (iii) represents radiation damping caused by direct radiative decay of the coherent electron oscillations into photons. Thus, although the non-

radiative decay routes – absorption due to e-h pairs via intra or interband transitions – are less probable due to a redshift of the plasmon resonance away from the interband transitions, the radiative decay weakens the dipole plasmon strength resulting in linewidth broadening.

The studies of such competing processes have now not only led into studying plasmon resonance response at the single nanoparticle level to minimize inhomogeneous linewidth – but also to performing ultrafast "weak measurements" to probe the coherent loss of electron memory, thus measuring the intrinsic dephasing lifetime of metallic NSs in real time (figure 1.6). This dephasing lifetime, $T_2$, is defined by:

$$\text{Homogeneous linewidth} = \Gamma = \frac{2\hbar}{T_2} \qquad \text{eqn 1.8}$$

The dephasing of coherent electron oscillations can either be caused by energy decay mechanisms or scattering phenomena that changes the momentum of the electrons during elastic collisions. By examining the details of plasmon decay using ultrafast pump-probe techniques, Link and El-Sayed showed that for small gold and silver, $5\ fs < T_2 < 10\ fs$, depending on the NP size and embedding host material[68,69].

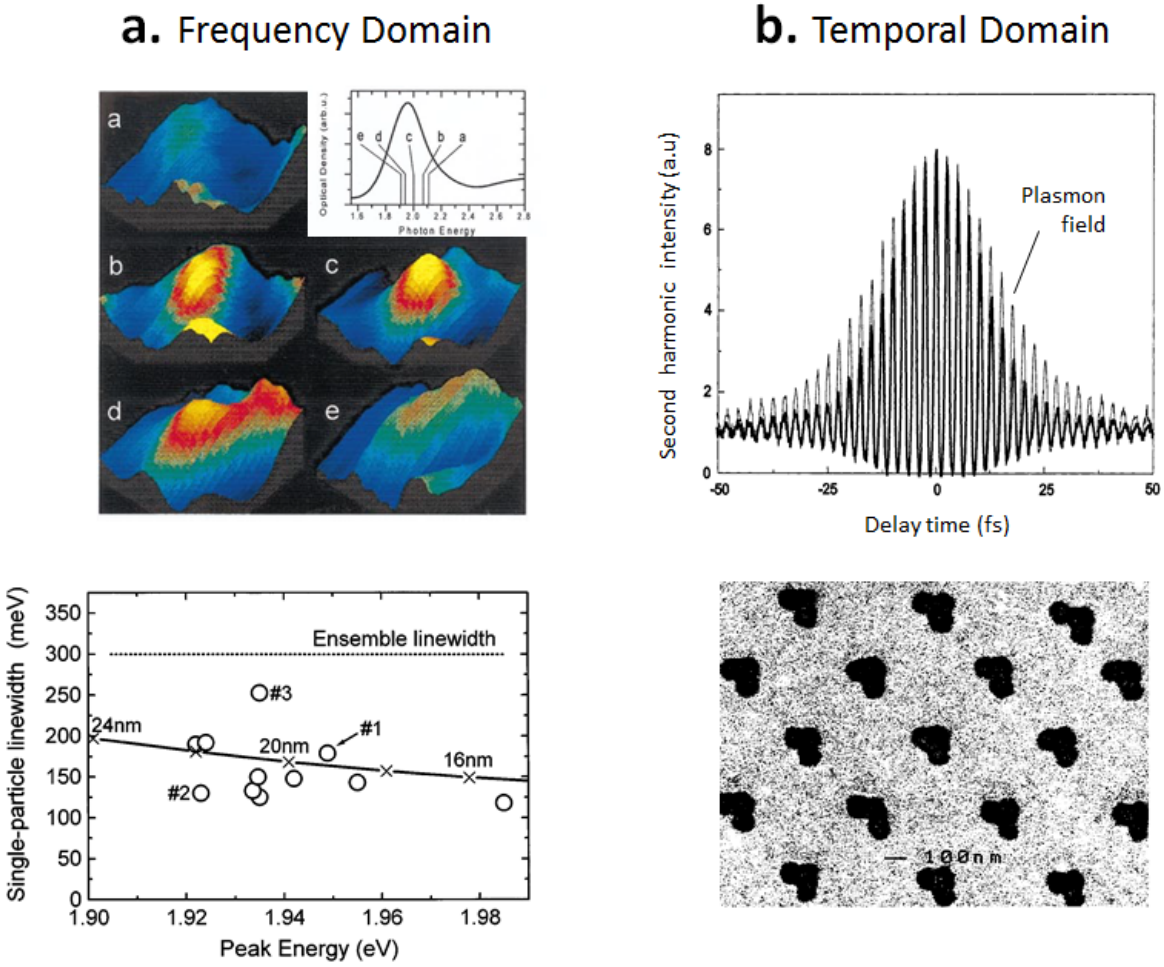


**Figure 1.6: Measurements of Dephasing Time ($T_2$) in Metallic Nanoparticles. (a)** NSOM spectroscopy of single gold nanoparticles measured at (a) 2.11 eV, (b) 2.07 eV, (c) 2.00 eV, (d) 1.94 eV and (e) 1.91 eV. The results compare linewidth vs. peak energy determined from the NPs near-field spectra. The solid line is theoretical results for gold spheres of different radii while the dashed line is the ensemble linewidth (300 meV) as determined from the far-field extinction spectrum[70]. **(b)** SEM of the arrangement of non-centrosymmetric gold nanoparticles for generating second harmonic. The results show second-order interferometric autocorrelation measurement of the (i) laser field obtained by using a BBO crystal (dark line) and (ii) plasmon field when substituting the BBO for the metallic nanoparticles with its characteristic longer lifetime[71,72].

It is possible to selectively tune the radiative and non-radiative decay mechanisms and consequently plasmonic lifetimes in various ways. Sönnichsen *et al.* who showed in 2002 that by fabricating nanorods with a 3:1 aspect ratio whose plasmon resonance was far from interband transitions, this minimized the non-radiative damping and demonstrated a $T_2 = 18$ fs[73]. More recently, it was demonstrated by Aeschilmann *et al.* that $T_2$ could even reach values as high as ~ 100 fs. By introducing a 2D-nanoscopy technique having a 50 nm spatial resolution while probing the electron final state using photoemission electron microscopy (PEEM) after ultrafast excitation, they showed that certain hot spots had unusually long plasmonic phase coherence lifetimes[74]. These observations were best explained by a coupled mode arising from the hybridization of the *dark* surface plasmon polaritons (long coherence lifetime due to poor radiative coupling efficiencies) and the *bright* localized surface plasmon. Therefore, this implies that longer coherence lifetime could be achieved if Fano-like resonances are employed.

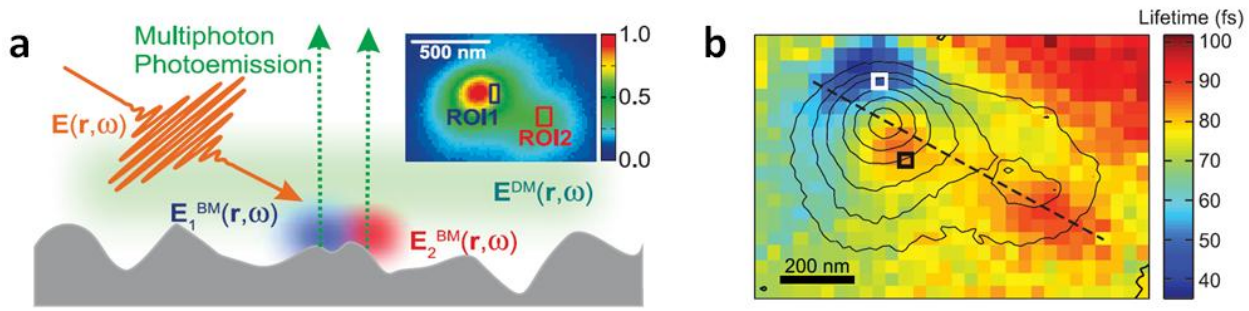


**Figure 1.7: Enhanced Dephasing Time ($T_2$) When LSPs are Coupled to SPPs. (a)** Schematics of the experiments: An incident wave **E** (orange) excites the LSP modes $\mathbf{E_1}^{\textbf{\textit{BrightMode}}}$ (BM) (blue) and $\mathbf{E_2}^{\textbf{\textit{Bright Mode}}}$ (BM) (red) that are coupled to a weakly damped delocalized dark mode $\mathbf{E}^{\textbf{Dark Mode}}$ (DM) (green). The inset shows a photoemission pattern with two marked regions that are analyzed. **(b)** A 2D-nanospectra map showing the

coherence lifetimes for the complete hot spot with the white and black squares marking two locations of interest. Adapted from reference [74].

Furthermore, with the birth of metamaterials, this has also spun intensive research into looking at other (less lossy) materials that could replace metals (Figure 1.6), especially potential plasmonic materials that can produce resonances in the near-IR (telecommunication) region[75,76]. From the generalized Drude-Lorentz model, the dielectric function can be written as:

$$\varepsilon_{mat.}{}'(\omega) + i\,\varepsilon_{mat.}{}''(\omega) = \varepsilon_{interband}(\omega) - \frac{{\omega_p}^2}{\omega\,(\omega + i\Gamma)} \qquad \text{eqn 1.9}$$

where,

$${\omega_p}^2 = \frac{n\,e^2}{\varepsilon_0\,m^*} \qquad \text{eqn 1.10}$$

and,

$$\Gamma = \frac{1}{\tau}$$

with $n$ the number of conduction electron density and $m^*$ is the effective mass of the conduction electrons; $\tau$ is the mean relaxation time of the conduction electrons that arises due to scattering from charge carriers, phonons, lattice defects or grain boundaries scattering. This relative boundary scattering rate depends on the size of the plasmonic particle, so that the relaxation rate for a spherical particle of size $R$ is given by $\Gamma = \Gamma_\infty + A\,\frac{v_F}{R}$. This implies that there is an enhanced decoherence time that arises due scattering at the boundaries and is commonly referred to as chemical interface damping [77]. The details

of the scattering are entailed in the coefficient $A$ and are typically in the order of unity. Moreover, in eqn 1.9, $\varepsilon_{interband}$ is caused by the interband transitions and is 1 when dealing with a free-electron gas[78]. If details of the wavelength-dependent interband transitions have to be included, this is typically done by including the Lorentz oscillator terms[52].

In general, plasmonic response is largest for noble metals as they provide sufficient free electrons to produce large negative real permittivity. But noble metals also suffer from large losses due to the interband electronic transitions originating in the d bands that compete with the LSPR. These losses are detrimental to plasmonic devices and since they are inherent in metallic component, a material with optical gain has to be introduced to compensate for the intrinsic losses – thus introducing an additional degree of structural complexity. For this reason, there has been recent interest in materials that are intrinsically less lossy than the noble metals by virtue of possessing finite band gaps.

Although there are many semiconductors that have wide band gaps ( $> 1.5\ eV$), the degree of doping that is required to reach a negative real permittivity is too high to reach the crossover frequency near the optical range (doping level of at least 3 x $10^{20}$ $cm^{-3}$). Therefore, semiconductor plasmonics is currently out of reach. However, heavily doped oxides or transparent-conducting oxides (TCOs), intermetallics (alloys), ceramics and transition metal nitrides are currently being investigated to substitute metals. It has been found that the optical losses of TCOs can be a factor of four less than silver. Also, unlike metals, these novel materials allow control of their optical properties by doping and more importantly perhaps, they are compatible with standard CMOS nanofabrication process.

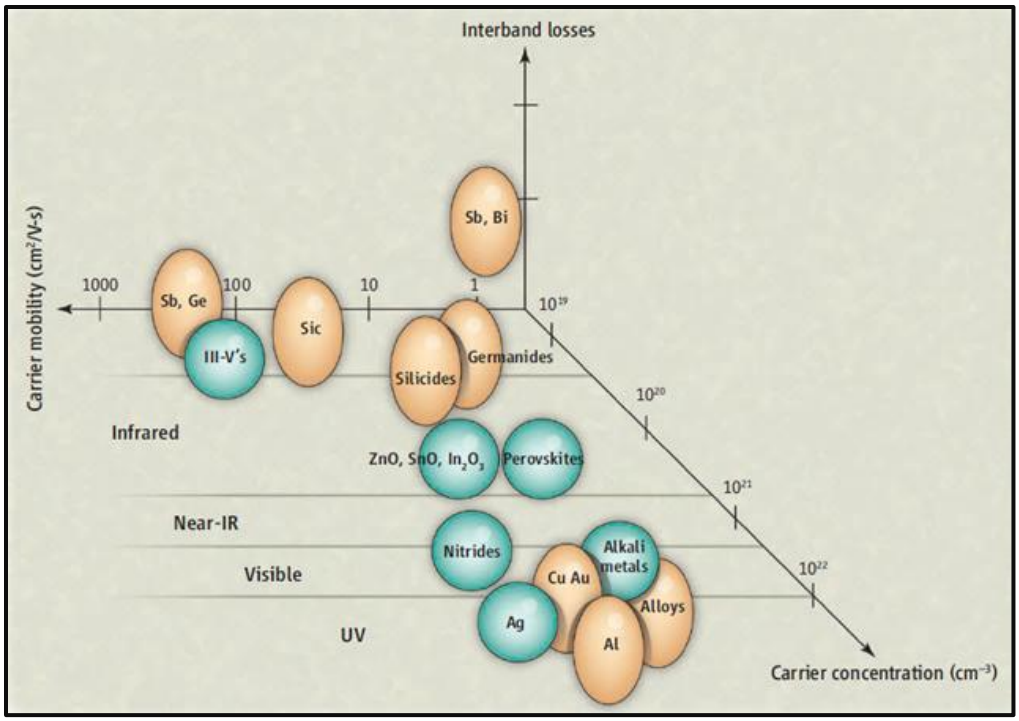


**Figure 1.8: Metamaterials/Plasmonics Map.** The important material parameters such as carrier concentration (maximum doping concentration for semiconductors), carrier mobility, and interband losses can be optimized for various applications. Spherical bubbles represent materials with low interband losses, and elliptical bubbles represent those with larger interband losses in the corresponding part of the electromagnetic spectrum. The figure has been extracted from reference [75].

### 1.2.2c Finite-Difference Time-Domain Simulations for Studying Optical Properties of Complex Plasmonic Geometries

In order to understand the optical properties arising from complex nanostructures in contact with an equally intricate near-field nanoenvironment, it is in general impossible to employ analytical methods, and one must resort instead to computational schemes. Several different 3D full-field EM simulation techniques are presently being used, including finite-element method (e.g. COMSOL), finite-integration technique (e.g. CST STUDIO) and finite-difference time-domain method (e.g. LUMERICAL SOLUTIONS). These simulation tools have been developed to compute detailed field maps and provide physical insights into the optical behavior of nanostructures. Here we focus on the latter technique, although comparisons between all three have been previously made to understand each technique's strengths and weaknesses. This was done in collaboration with Professor Maier's group at Imperial College London, UK.

Finite-difference time-domain (FDTD) simulations first attracted attention in the 1970's when it was realized that the limitations of frequency-domain integral solutions of Maxwell's equations precluded effective modeling of devices and materials that exhibited nonlinear effects. The novel FDTD technique provided a more robust time-domain approach to solving Maxwell's differential (*curl*) equations on spatial grids or lattices. Being a time-domain technique, FDTD could directly compute the impulse response function of the nanostructure and thus naturally treat the potential nonlinear effects as well. At the heart of FDTD technique is its approximation scheme – the central-difference approximation – that discretized the temporal and spatial partial derivatives of Maxwell's

equations. Kane S. Yee's seminal 1966 paper[79] describes the space grid and time-stepping algorithm required (Figure 1.7) while during 1975-1980, Taflove obtained the first stable FDTD model[80] and thereafter found the first steady-state solutions of the 2D and 3D EM wave interactions with material structures[81].

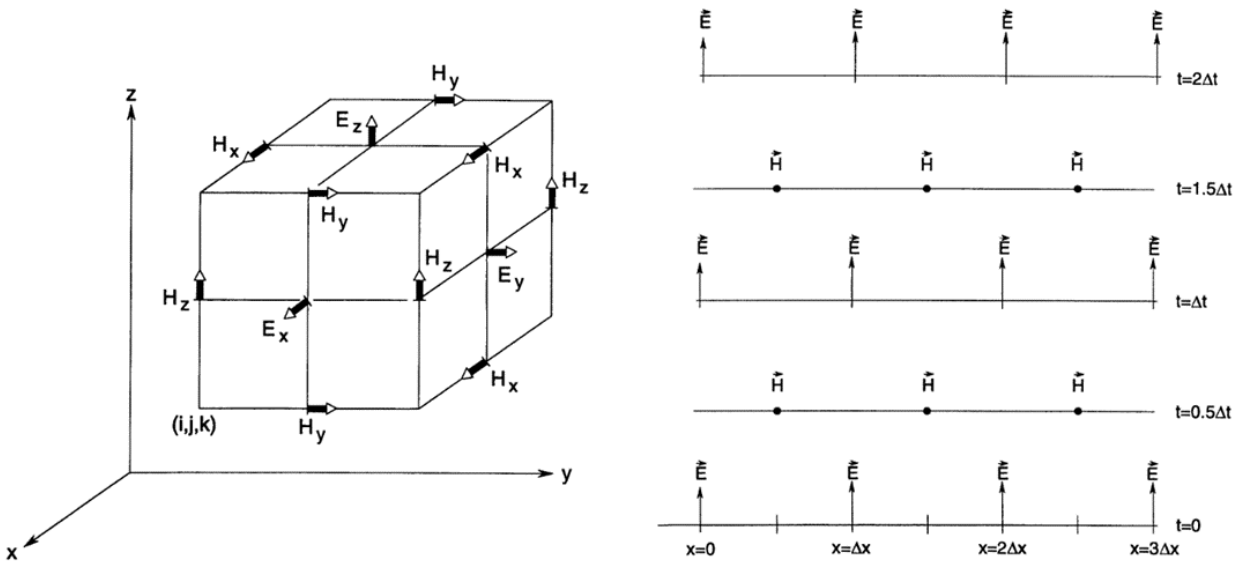


**Figure 1.9: The Original 1966 Yee Cell and its Space-Time Chart.** Illustration of the hexahedral mesh used for FDTD to reduce numerical phase-velocity anisotropy, with its corresponding electric and magnetic field vector components. For 3D simulations, the Yee unit cells are stacked along the x, y and z-axes while the EM interactions are mapped onto these space lattices by assigning the appropriate permittivity values for each electric field component and permeability to each magnetic field component, fulfilling the necessary boundary conditions at the interfaces. The space-time chart depicts the leapfrog time derivatives technique. At initial conditions of $t = 0$, all electric and magnetic fields are zero everywhere in the grid. Adapted from reference [81].

Briefly from Figure 1.6, we see that at the finite-sized grid points the electric and magnetic fields ($E_x, H_x, E_y, H_y, E_z, H_z$) are solved as a function of discrete points in time. An example is:

$$\frac{\mathbf{E}_x^n\left(i+\frac{1}{2},j,k\right) - \mathbf{E}_x^{n-1}\left(i+\frac{1}{2},j,k\right)}{\Delta t}$$

$$= \frac{1}{\varepsilon_r \varepsilon_o}\frac{\mathbf{H}_z^{n-\frac{1}{2}}\left(i+\frac{1}{2},j+\frac{1}{2},k\right) - \mathbf{H}_z^{n-\frac{1}{2}}\left(i+\frac{1}{2},j-\frac{1}{2},k\right)}{\Delta y}$$

$$- \frac{1}{\varepsilon_r \varepsilon_o}\frac{\mathbf{H}_y^{n-\frac{1}{2}}\left(i+\frac{1}{2},j,k+\frac{1}{2}\right) - \mathbf{H}_y^{\boldsymbol{n-\frac{1}{2}}}\left(i+\frac{1}{2},j,k-\frac{1}{2}\right)}{\Delta z} \qquad \text{eqn 1.11}$$

and,

$$\frac{\mathbf{H}_x^{n+\frac{1}{2}}\left(i,j+\frac{1}{2},k+\frac{1}{2}\right) - \mathbf{H}_x^{n-\frac{1}{2}}\left(i,j+\frac{1}{2},k+\frac{1}{2}\right)}{\Delta t}$$

$$= \frac{1}{\mu_r \mu_o}\frac{\mathbf{E}_z^n\left(i,j+\frac{1}{2},k+1\right) - \mathbf{E}_y^n\left(i,j+\frac{1}{2},k\right)}{\Delta z}$$

$$- \frac{1}{\mu_r \mu_o}\frac{\mathbf{E}_z^n\left(i,j+1,k+\frac{1}{2}\right) - \mathbf{E}_{\boldsymbol{z}}^{\boldsymbol{n}}\left(i,j,k+\frac{1}{2}\right)}{\Delta y} \qquad \text{eqn 1.12}$$

where $n$ denotes the time step. These constructed finite difference equations – all 6 of them – are solved iteratively until a steady-state solution is achieved and the algorithm can thereafter proceed to the next lattice point. The accuracy of the code in reproducing the correct optical properties depends on the meshing dimensions chosen for the grid, the boundary conditions (using either periodic or perfectly matching layers) and the correct

dielectric functions; the need for accuracy must be balanced against reasonable limits on computational time and memory requirements..

Additionally, for the FDTD numerical calculations to be stable and converge, the time-step ($\Delta t$) needs to be discretized such that the phase-velocity ($v_p$) in the simulation region satisfies $v_p \cdot \Delta t \leq 0.99 \times \left(\frac{1}{\Delta x^2} + \frac{1}{\Delta y^2} + \frac{1}{\Delta z^2}\right)^{-1/2}$ [82]. This is due to the fact that convergence is dictated by the Courant-Friedrichs-Lewy condition that requires (for a wave propagating across a discrete spatial grid) the grid interval length must be less than the time for the wave to travel adjacent grid points[82]. The 0.99 here represents the Courant stability limit, a default preset in Lumerical FDTD Solutions[83].

Frequency-domain information can thereafter be retrieved by a Fourier analysis of the solution, meaning that the full spectral response for the nanostructure can be obtained in a single simulation run, in contrast to frequency-dependent techniques that give only the response at a single wavelength. This is typically done by sending a white-light broadband plane wave or Gaussian pulse of a few femtoseconds in duration through the nanostructure, as depicted in figure 1.10.

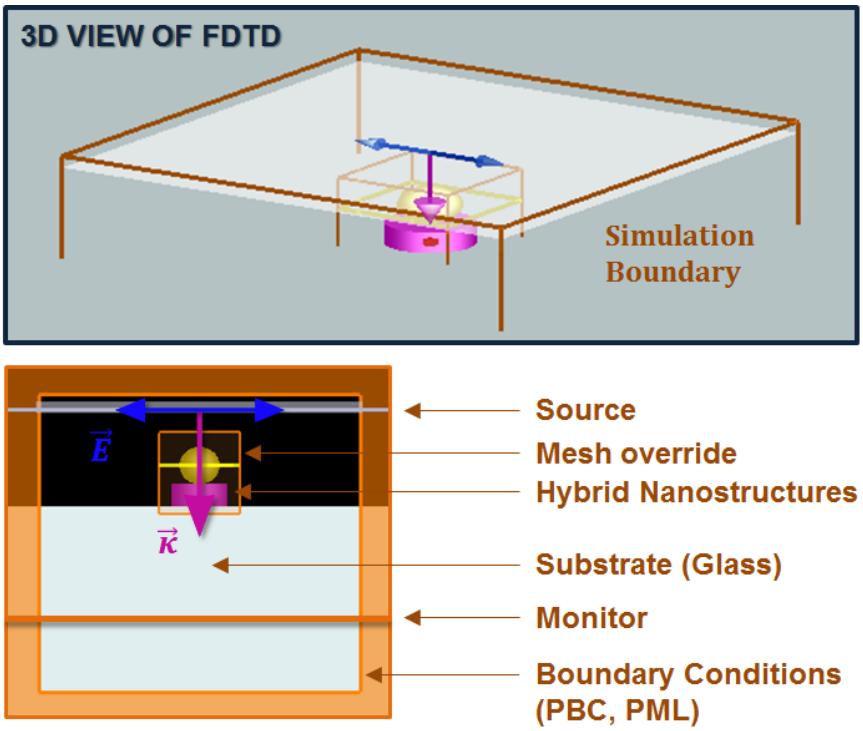


**Figure 1.10: Schematics of Lumerical Solutions FDTD Solver.** 3D view (top) and side view of the computer-aided design (CAD) software Lumerical used to simulate the optical properties of complex nanostructures.

### 1.2.3 Recent Developments in Active Plasmonics

As discussed in the introductory section, although the ability to guide light around sharply-curved structures can now routinely be achieved in plasmonics circuits, modulating these signals at nanometer length scales remains a challenge. The term "active plasmonics" was introduced by the Zheludev group (University of Southampton, UK) when they first reported the concept of using optically activated phase-change (structural change in Ga) waveguide to transiently control propagation of SPPs[84], as shown in Figure 1.11. Although "active plasmonics" referred strictly to the ability in modulating plasmonic signals (SPPs and LSPRs), we use the term in this dissertation to define more broadly the mutual

dynamic interaction between a plasmonic object and its environment. Here, both scenarios will be reviewed.

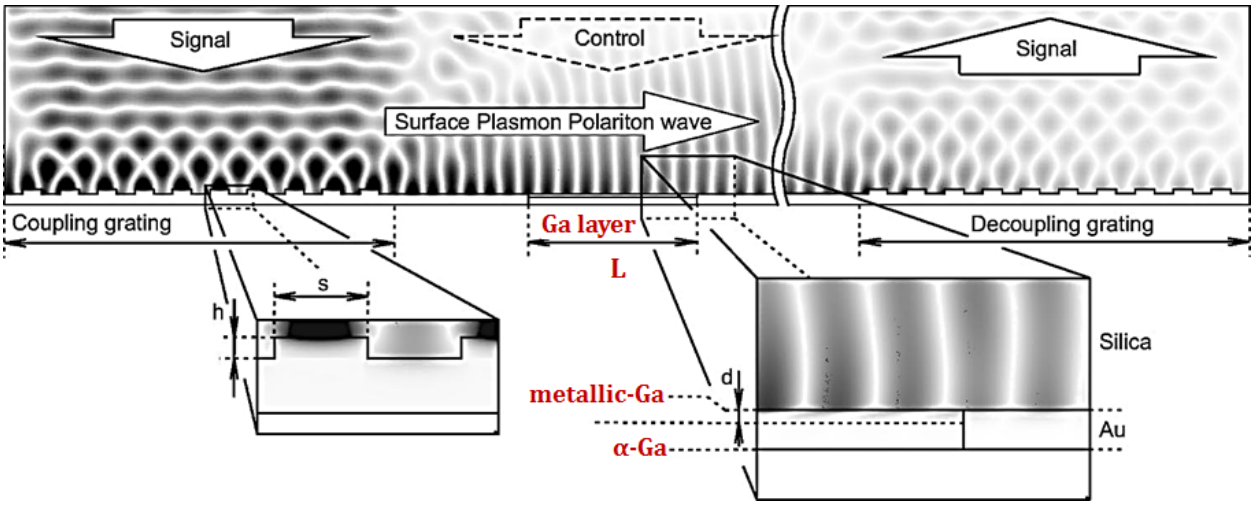


**Figure 1.11: First Device Concept of Active Plasmonics.** A SPP gold-on-silica waveguide containing a gallium switching section. The metallic film is at the bottom of the silica substrate. Field mapping shows the magnitude of the z component of the magnetic field.

Since the demonstration of using of gallium to control the propagation of SPPs, many other material systems and configurations – including thermo-[85,86] and electro-optic[87] media, liquid crystals[88], quantum dots[89], photochromic molecules[90], field-effect plasmonic modulators[91], graphene-based modulators[10], transparent oxides[92] and chalcogenides[93] have been studied, with their characteristic features highlighted in Figure 1.12.

**2004:** KRASAVIN, APL

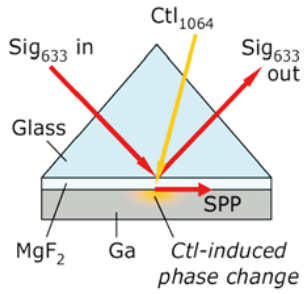


→ Ext. ratio: 9.7 dB
→ Laser fluence: 15 mJ/cm$^2$
→ Oper. wavelength: 633 nm
→ Relax. Time: 20 ns

**2004:** NIKOLAJSEN, APL

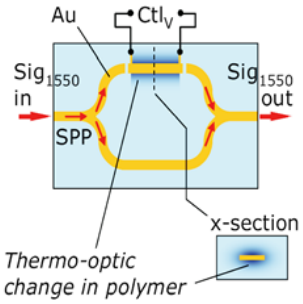


→ Ext. ratio > 35 dB (5.7mm)
→ Electrical power: 8 mW
→ Oper. wavelength:1.55 um
→ Response time: 0.7 ms

**2007:** PACIFICI, NAT. PHOTON

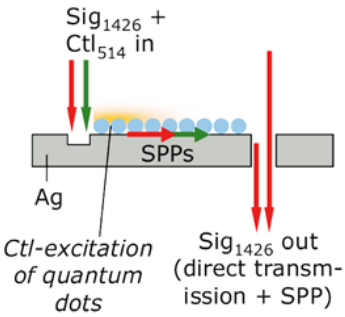


→ Ext. ratio: 0.55 dB (3.6 um)
→ Laser power: 600 W/cm$^2$
→ Oper. wavelength: 1426 nm
→ Response time < 40 ns

**2008:** PALA, NL

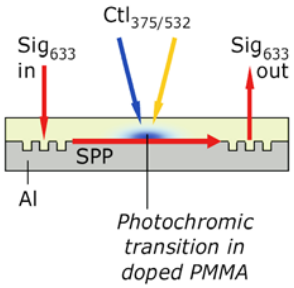


→ Ext. ratio: 6 dB
→ Laser fluence: 6 mW/cm$^2$
→ Oper. wavelength: 633 nm
→ Relax. time: 10 s

**2008:** DICKEN, NL

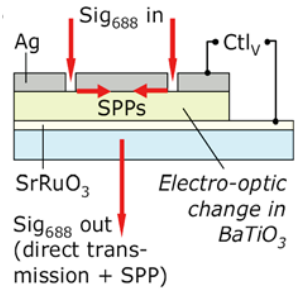


→ Ext. ratio: 0.7 dB
→ Bias: max. 45 V
→ Oper. wavelength: 688 nm
→ Relax. time: NA

**2008:** MacDONALD, NAT. PHOTON

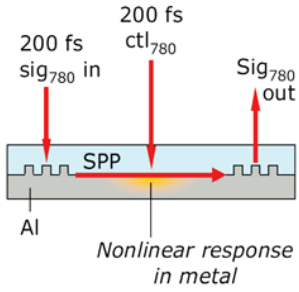


→ Ext. ratio: 1.3 dB
→ Laser fluence: 13 mJ/cm$^2$
→ Oper. wavelength: 780 nm
→ Relax. time < 200 fs or 60 ps

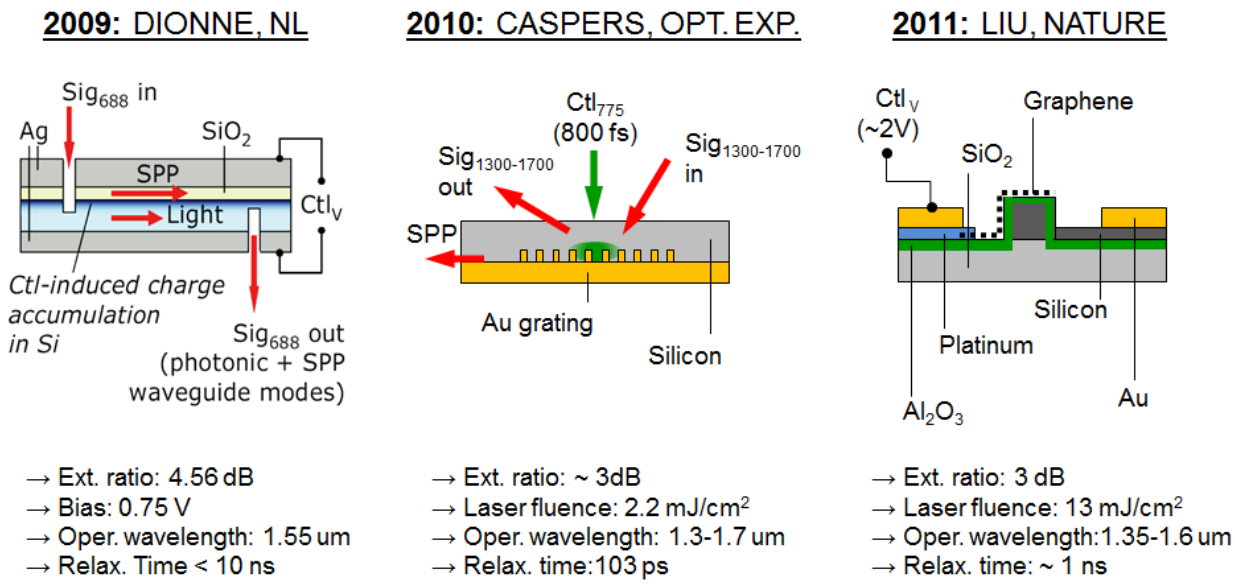


**Figure 1.12: Overview of Nanoscale Modulators.** Schematic of experimental active modulators based on various physical processes. 'Sig' and 'Ctl' indicate signal and control inputs respectively with subscripts denoting light wavelength or electrical bias (subscript 'V'). Adapted from references [94], [95] and [10].

Recently, other classes of materials or switching strategies using specific materials properties have been investigated so as to modulate plasmonic response or be intrinsically used as the plasmonic nanostructure themselves. An example of such novel work are plasmon resonances in high-temperature superconducting YBCO ($YBa_2Cu_3O_{7-\sigma,\ \sigma=0.005}$) split-ring resonator metamaterials[96]. Other such interesting materials systems are electro-optic modulation of ferroelectric oxide thin films (e.g. lead lanthanum zirconate titanate (PLZT)[97], $Bi_4Ti_3O_{12}$, lead zirconate titanate (PZT) and strontium barium niobate (SBN))[98] and effect of strain on the dielectric properties of barium strontium titanate[99,100]. The large electro-optic coefficient (electroabsorption or Kerr effect) in perovskite barium strontium titanate ($Ba_xSr_{1-x}TiO_3$/BSTO) could also provide great functionality in plasmonic devices[101].

## 1.3 VANADIUM DIOXIDE – THE CANONICAL QUANTUM MATERIAL

### 1.3.1 Overview

Solid-state materials with electrons that interact only weakly with each other can be described by the nearly-free electron model[102-104]. Such materials are metals and insulators. In such non-interacting electron system, the band structure is derived from the periodicity of the lattice potential, dictated by the equally spaced ionic cores. Each band can accommodate a finite number of electrons and the bands are separated by an energy gap. The properties of a material are thus dictated by how many electrons contribute to the band and the energy gap separating them. The Fermi level – at zero temperature and in $k$-space – is defined by the separation between the electron-filled states and empty states. Depending on where the Femi level ($E_F$) lies, a material is characterized as a metal ($E_F$ lies within the conduction band) or an insulator ($E_F$ lies at the valence band edge). Moreover, when the energy difference between the highest filled band and the lowest empty band is small, materials are labeled as semiconductors. While metals have low resistivity (e.g. gold is $2 \times 10^{-8}\ \Omega\, m$) and insulators exhibit much higher values (e.g. quartz is $5 \times 10^{24}\ \Omega\, m$), resistivity values for semiconductors can vary greatly, depending upon temperature and defect/impurity concentration. The lack of electron-electron interaction (electron correlations) in these materials ensures that the properties of the band and the energy gap do not vary, independent of the band filling.

Although band-structure calculations can describe the properties of such materials very well, they fail to describe materials whose electrons interact strongly with each other. Such materials have historically been labeled as *strongly electron correlated systems*. An

example is the notorious NiO that, although expected to be a metal from a theoretical perspective, turns out experimentally to be an insulator[105,106]. The term "Mott insulator" was coined to identify materials like NiO that violated the fundamental expectations of band theory. Nowadays, other correlated materials have been discovered, including a variety of d- and f-electron intermetallic compounds, high-temperature superconductors and π-electron organic conductors[107], and are now under intense investigation as understanding the complexity of their physical properties and phase transformation provides a critical test of condensed-matter theory and opens the door to novel applications. For example, understanding the metal-to-insulator in oxides could provide the key to advances in information processing and storage beyond conventional CMOS scaling, as shown in figure 1.13.

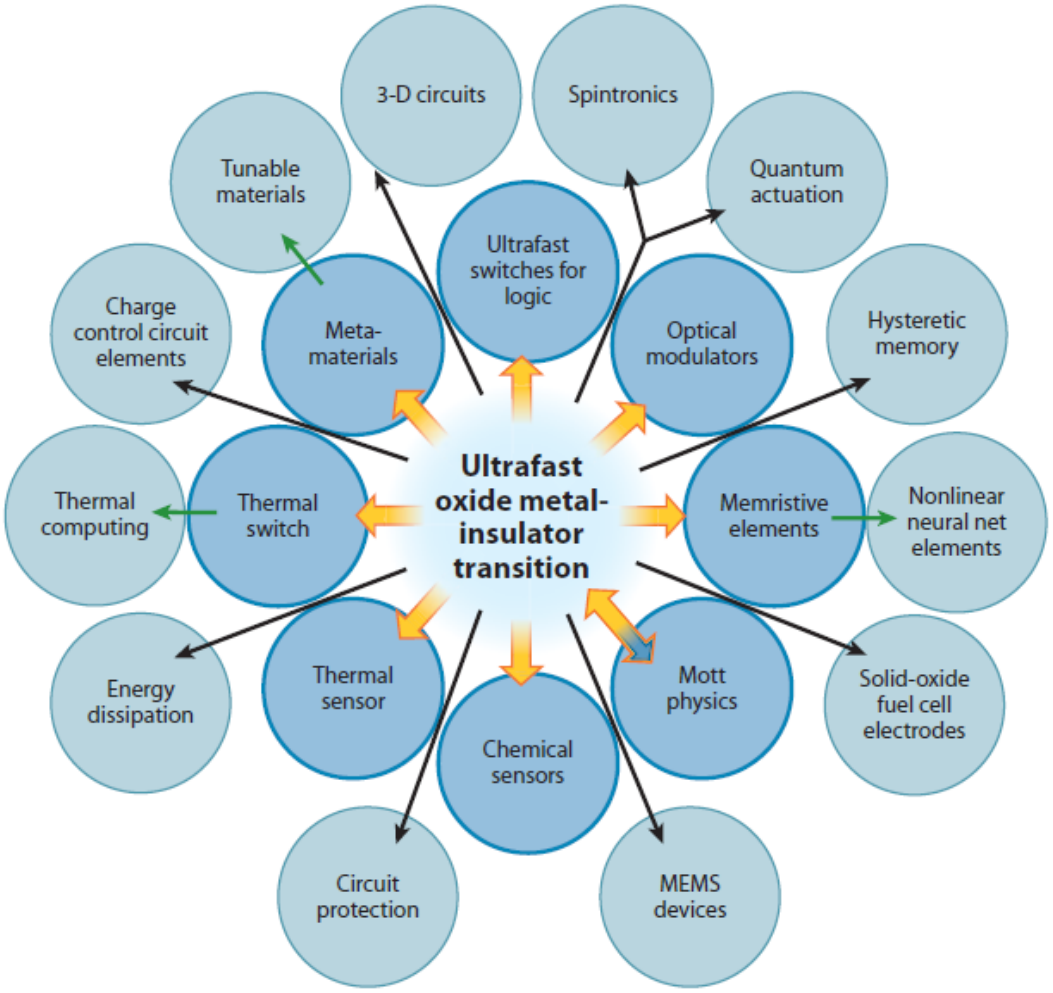


**Figure 1.13: Technologies Utilizing IMT in Strongly Correlated Oxides.** Device technologies benefitting from the metal-to-insulator transition of strongly correlated oxide. From reference [108].

In this section, we focus on the metal-to-insulator transition of vanadium dioxide ($VO_2$). Since the discovery in 1959 by F. J. Morin that bulk $VO_2$ crystals exhibited a first-order phase transition at the near-room temperature of 68$^{O}$C, $VO_2$ has been considered as a canonical phase-change material. Accompanying this phase transition is a change in the resistivity of the material by more than four orders of magnitude, along with a drastic

change in its optical properties, especially in the IR region, as shown in figure 1.14. Despite the simple stoichiometry and structure of $VO_2$, there are still many unresolved puzzles about its MIT, such as the mechanism of its ultrafast switching;[109] the potential for stabilizing the intermediate states (e.g. M2 phase);[110] the origins of its size-dependent switching in $VO_2$ nanoparticles (NPs);[111,112] and nanoscale electronic and structural phase coexistence/non-congruence in thermally modulated $VO_2$[113]. What follows is a discussion of these points of contention, together with highlights of the recent work that are pertinent to the dissertation.

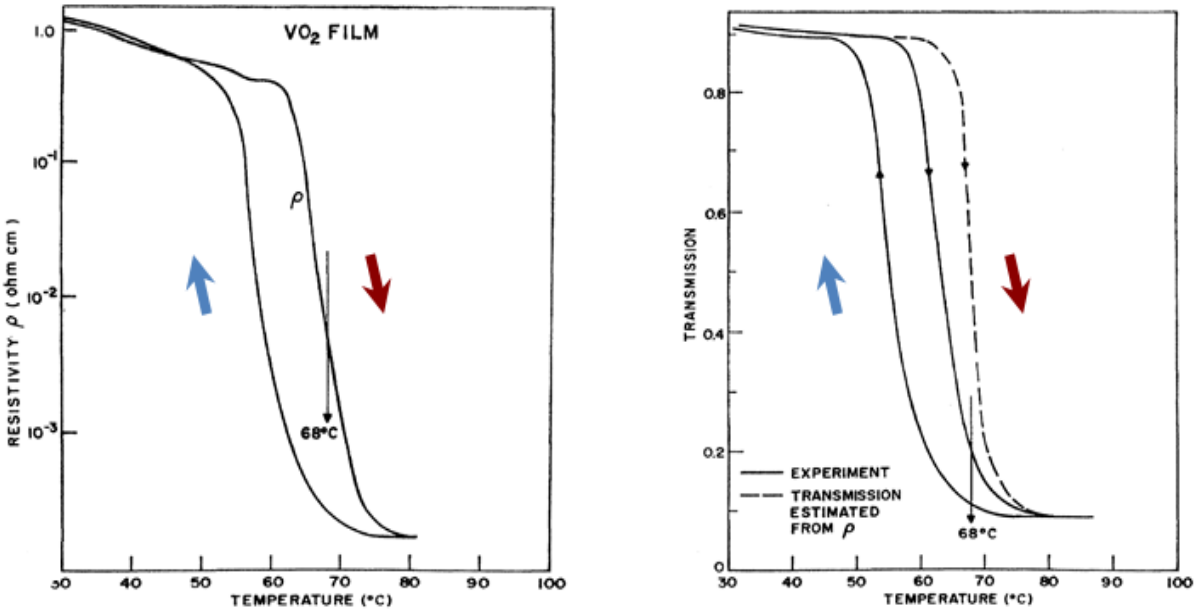


**Figure 1.14: Electrical and optical properties of $VO_2$.** Resistivity and transmission (0.31 eV) data for a 100 nm $VO_2$ thin film[114].

### 1.3.2 Insulator-to-Metal Transition of Vanadium Dioxide in the Equilibrium Limit

#### 1.3.2a Atomic and electronic structure of $VO_2$

Vanadium dioxide belongs to the general class of transition-metal dioxides that are characterized structurally by two distinct modes: a pairing of the metal atoms along the characteristic chains parallel to the tetragonal c-axis and a lateral zigzag displacement[115]. As opposed to the other oxides, only the $d^1$ compounds ($VO_2$ and $NbO_2$) undergo a MIT. In the insulating state, $VO_2$ has a monoclinic structure and belongs to the $P2_1/C$ space group. Its atomic structure is shown in figure 1.15. A distinctive feature of the phase transition is that the V cations are displaced out of the surrounding oxygen octahedral and pairing of the V-V bond occurs in the insulating state that doubles the unit cell ($\mathbf{a}_{ins.} = 2\mathbf{c}_{met.}$; $\mathbf{b}_{ins.} = \mathbf{a}_{met.}$ ; $\mathbf{c}_{ins.} = \mathbf{a}_{met.} - \mathbf{c}_{met.}$), with alternate separations of 2.56 Å and 3.12 Å, in place of the 2.87 Å for the metallic case. Associated with this pairing is also a tilting ("zigzag") dimer arrangement that results in two set of V-O bond lengths in that form the octahedron and surround the V cation (apical V-O bond lengths are 1.77 and 2.01 Å; V-O forming the basal plane are 1.86, 1.89 and 2.03, 2.06 Å). Each V ion shares its five outer electrons (three $3d$ + two $4s$), four of which bonds to the $p$ shells of the two $O^{2-}$ anions, while the rest go into the $3d_\pi$ band (the conduction band in the metallic state).

Above the transition temperature of ~68°C, $VO_2$ transforms to a rutile (tetragonal) configuration, belonging to the $P4_2/mnm$ space group. The V-cations are then located at the center of the octahedral cage formed by the O anions, where they undergo the crystal field splitting depicted in figure 1.16. The overlapping $d_{x^2-y^2}$ and $d_{yz}$ orbitals form the points of connection from one unit cell to the other, represented by lattice vectors of the

tetragonal lattice. Additionally, the V metals ions at the corner and the center are coupled by the $d_{xz}$ orbitals, pointing to the voids between the V atoms of the neighboring octahedral chains where they overlap with the $d_{x^2-y^2}$ orbitals of these chains.

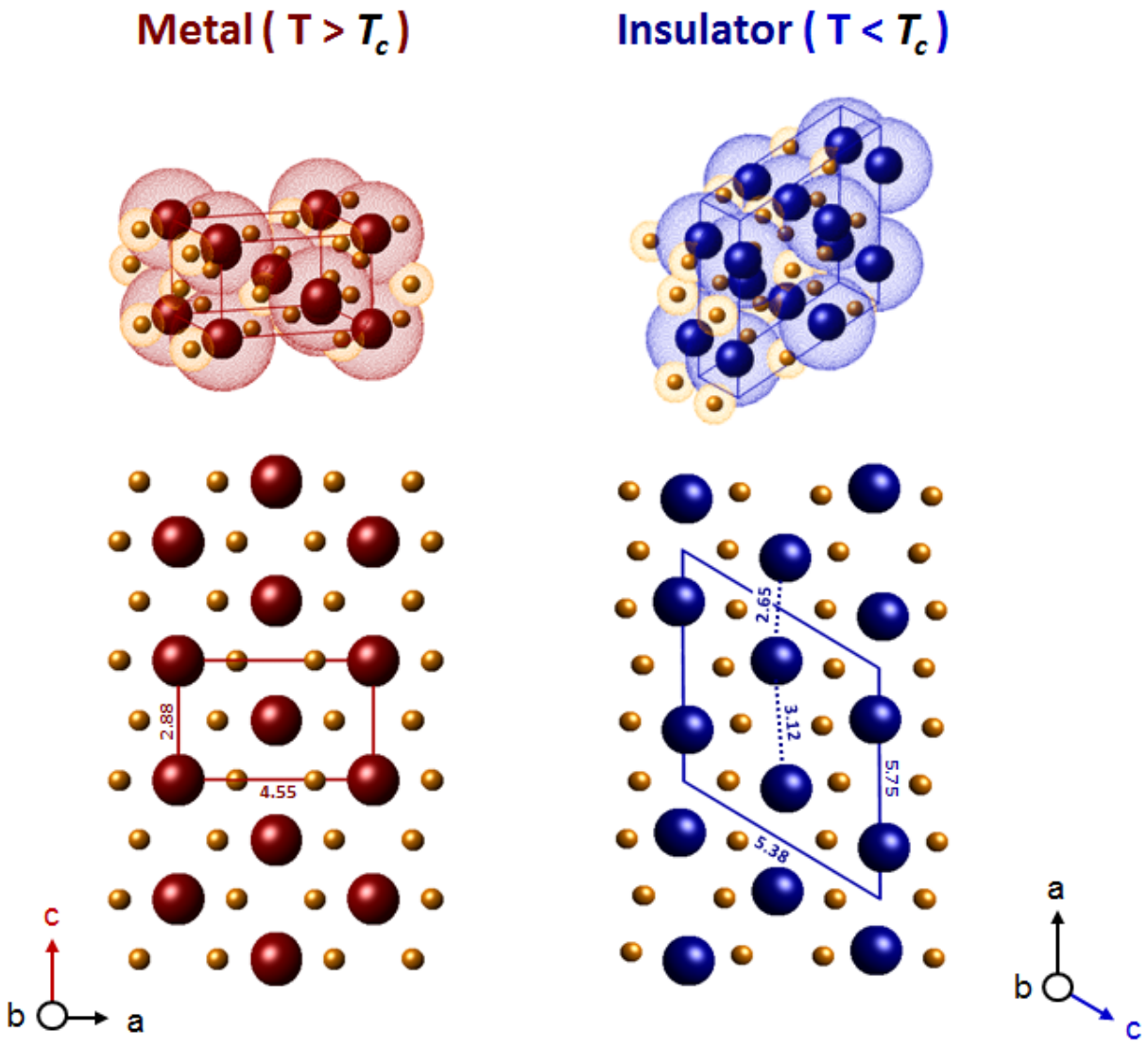


**Figure 1.15: Atomic Structure of $VO_2$.** Atomic configurations of $VO_2$ in its metallic (red) and insulating (blue) states respectively. A 3D unit cell for each state is also shown. In the insulating monoclinic state, that is the angle between the a- and c-axis is β = 122.6°,. Adapted from references [115,116] .

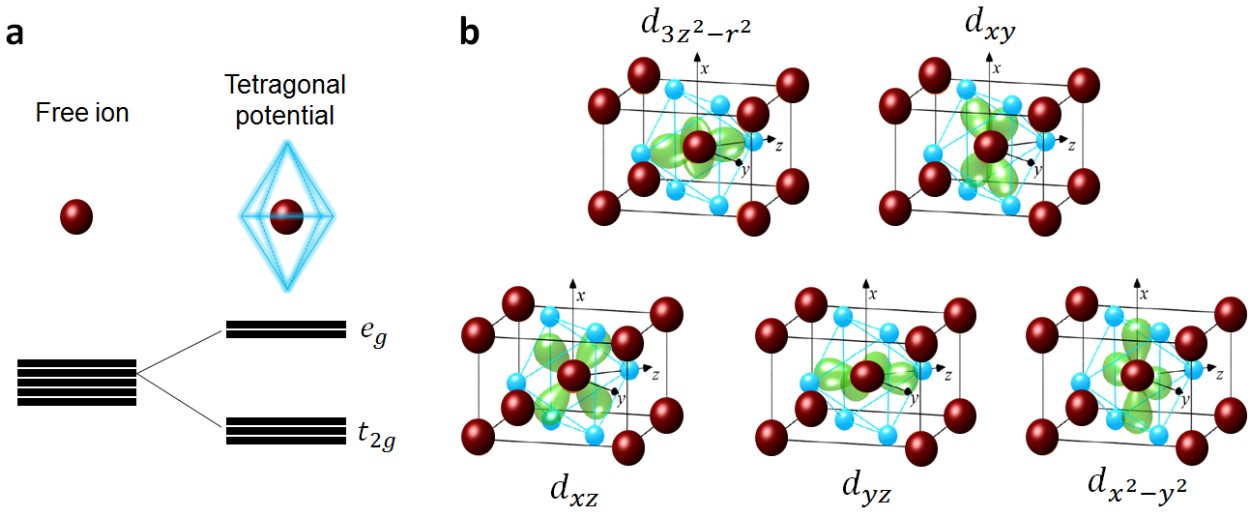


**Figure 1.16: Crystal Field Splitting of the d-Band in $VO_2$. (a)** Typical crystal field splitting in a tetragonal potential. **(b)** Angular distribution of the *d*-orbitals as $VO_2$ undergoes crystal-field splitting in the oxygen tetragonal potential (octahedral cage). The orbitals have been drawn with respect to the *local* octahedral coordinate. Here, the $d_{x^2-y^2}$ orbitals point along the crystallographic rutile c-axis while the local y axes point towards the edges of the basal plane of the octahedron and the $d_{xz}$ and $d_{yz}$ orbitals align towards the faces. Adapted from references [115] and [109].

This hybridization between the O2*p* and the V3*d* orbitals forms the typical σ and π bonds. Since the p-d overlap is stronger for the σ (and σ*) bonds, these states experience greater bonding and anti-bonding splitting. In such an almost perfect octahedral environment, the σ* ($e^{\sigma}_g$ symmetry) and π* ($t_{2g}$ symmetry) states represent orbitals of $d_{3z^2-r^2}/d_{xy}$ and $d_{x^2-y^2}/d_{xz}/d_{yz}$, respectively. Here the *strongest overlap*, as pointed out by Goodenough[117], lies along the rutile c-axis and is due to the metal-metal interactions. The consequences of the crystal-field splitting are depicted in the schematic of the electronic band energies of $VO_2$ in figure 1.17.

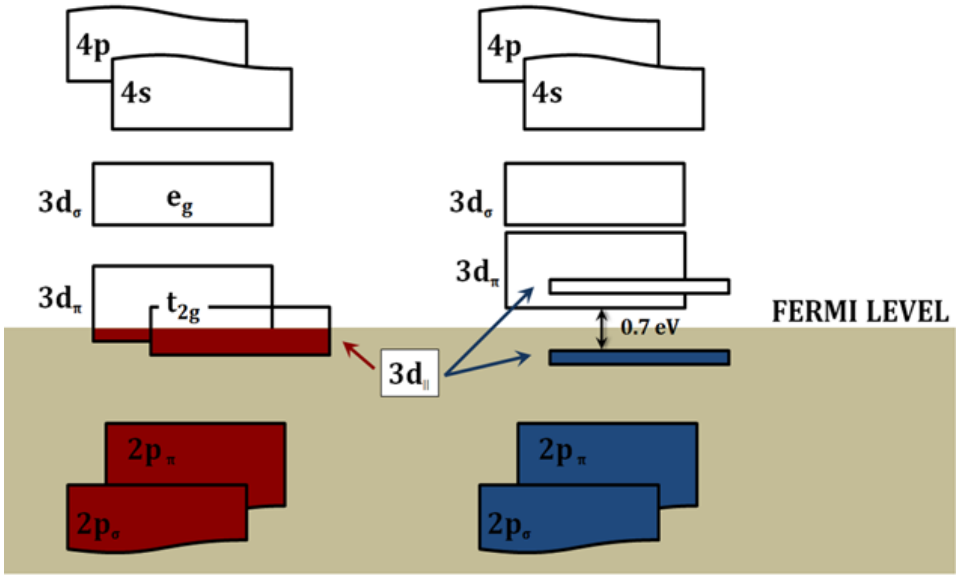


**Figure 1.17: Electronic Energy Bands of $VO_2$.** Electronic band energies of metallic (red) and insulating (blue) $VO_2$. The brown shaded region represents the filled electronic states, with the tightly bound, completely filled O2$p$ orbitals. Note the opening of the ~ 0.7 eV band gap in the insulating state.

### 1.3.2b Elementary switching mechanism: Peierls vs. Mott-Hubbard transition

As discussed in the previous section, the periodic lattice distortion of V-cation chain opens up a band gap between the upward shifted $3d_\pi$ and the lower $3d_{||}$ bands of ~ 0.7 eV. The mechanism that opens the band gap has been the subject of intense debate for more than half a century with two main mechanisms at play.

One possible mechanism is the Peierls effect, which can be simply understood by considering a one dimensional Peierls distortion. As shown from figure 1.18, a half-filled 1D metal is unstable to a structural distortion transforming the metal to an insulator. This can be understood by examining the electronic dispersion relation: when dimerization occurs, the period of the lattice doubles to contain the previous two lattice points and this

corresponds to halving the Brillouin zone. As a result, a gap opens at the Fermi-surface (Brillouin zone edge), causing the material to become an insulator. The width of the gap is dictated by the hopping integrals, $t_1$ and $t_2$, which are functions of two resulting interatomic distances resulting from the PT. This phenomenon arises purely from a structural reconfiguration and is called a *Peierls transition*[105]. Although the long-range Peierls distortion may not accurately describe materials with higher dimensionality, the lattice can still couple to the electrons by polaron formation and affect the electron properties as they move through the crystal. Polaron formation reduces the electron bandwidth, and in turn is responsible for modifying conductivity of the material. In the theory of phase transitions, polaron formation is related to the length scale over which the local fluctuations in electron density or orbital orientation on site affect those same properties on neighboring sites, corresponding to the correlation length (but not to be confused with electron-electron correlation lengths!). More importantly, it is known that the correlation length diverges as $T \rightarrow T_c$, thus implying a temperature-dependent correlation length[118].

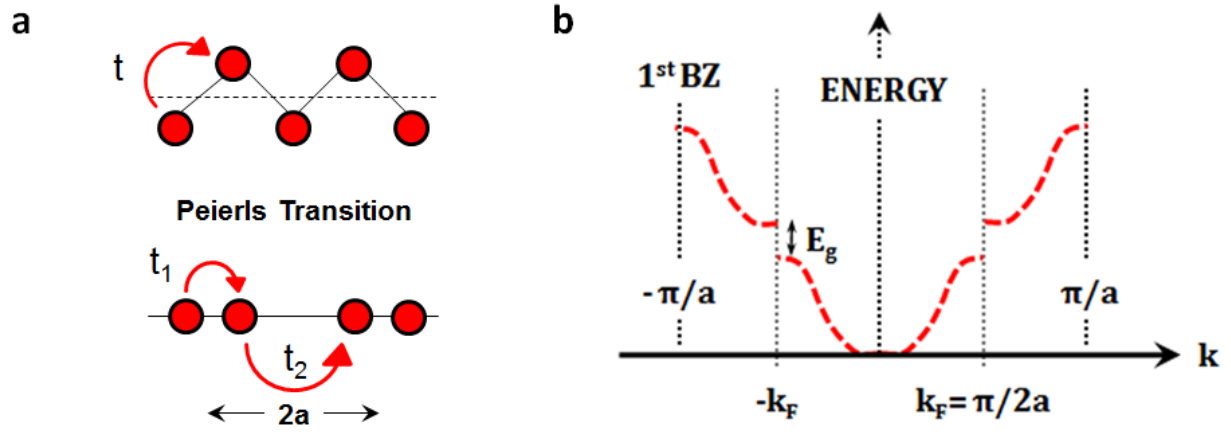


**Figure 1.18: 1D Peierls Transition. (a)** Schematics of a 1D chain of atoms. **(b)** Electronic dispersion relation for the dimerized atomic chain.

Although the Peierls description helps to reproduce some of the striking features of the $VO_2$ phase transition, the effect of electron correlation in $VO_2$ cannot be neglected. Thus, the effect of Coulomb interaction that underlies *Mott-Hubbard theory* of the MIT has to be considered as well. As briefly mentioned earlier, Mott and Peierls realized the importance of including these Coulombic interactions between the electrons, as stated in their seminal 1937 paper: "a rather drastic modification of the present electron theory of metals would be necessary in order to take these facts into account[105]." More specifically, these strong electron correlations arise when the Coulomb interaction between electrons is comparable to, or stronger than, the energy bandwidth of the individual electrons. This is the case for the spatially confined *d* and *f* orbitals. For these electrons, the strong Coulomb interaction between electrons restricts their wave functions to dispersionless bands that do fit the conventional-band theory picture. Such an electron correlation effect was first discussed by Hubbard who introduced the following Hamiltonian as the simplest model for interacting electrons on a lattice (contains only a single atomic orbital, is isotropic and interactions occur only between the nearest neighbor):

$$\mathcal{H} = \sum_{ij,\sigma} (t_{ij} {c_{i\sigma}}^{\dagger} c_{j\sigma} + H.c) + U \sum_{i} n_{i\uparrow} n_{i\downarrow} \qquad \text{eqn 1.13}$$

Here, the first term comes from the tight binding model and corresponds to the kinetic energy of the electrons. The $t_{ij}$ term is the matrix element that describes the hopping of electrons with spin $\sigma$ between orbitals at sites $i$ and $j$ (*hopping rate*). Note that these hopping integrals are not the same as those that determine the band gaps in the Peierls

model. The values of $t_{ij}$ determine the overlap of on-site electronic wavefunctions in the potential generated by the lattice and are thus intrinsically dependent on inter-atomic distances. Larger values of $t_{ij}$ correspond to easier inter-site transitions. $U$ is the local Coulomb interaction between two electrons occupying the same site $i$; thus $n_{i\sigma} = {c_{i\sigma}}^{\dagger} c_{i\sigma}$ is the electron number operator whose expectation value gives the density of electrons at site $i$ with spin $\sigma$ (*interaction rate*)[119]. As schematically drawn by Kotliar and Vollhart[120], figure 1.19 shows the transition of the density of states from a metal to a Mott insulator as the ratio between the interaction energy U becomes greater than the energy bandwidth of the non-interacting electrons, W. When $t >> U$, the tight-binding model is retrieved and the electrons are delocalized throughout the crystal. In the case where $U >> t$, repulsive Coulombic forces dominate and prevent electrons from hopping to other occupied lattice positions. This leads to an insulating behavior because of charge (electron) localization.

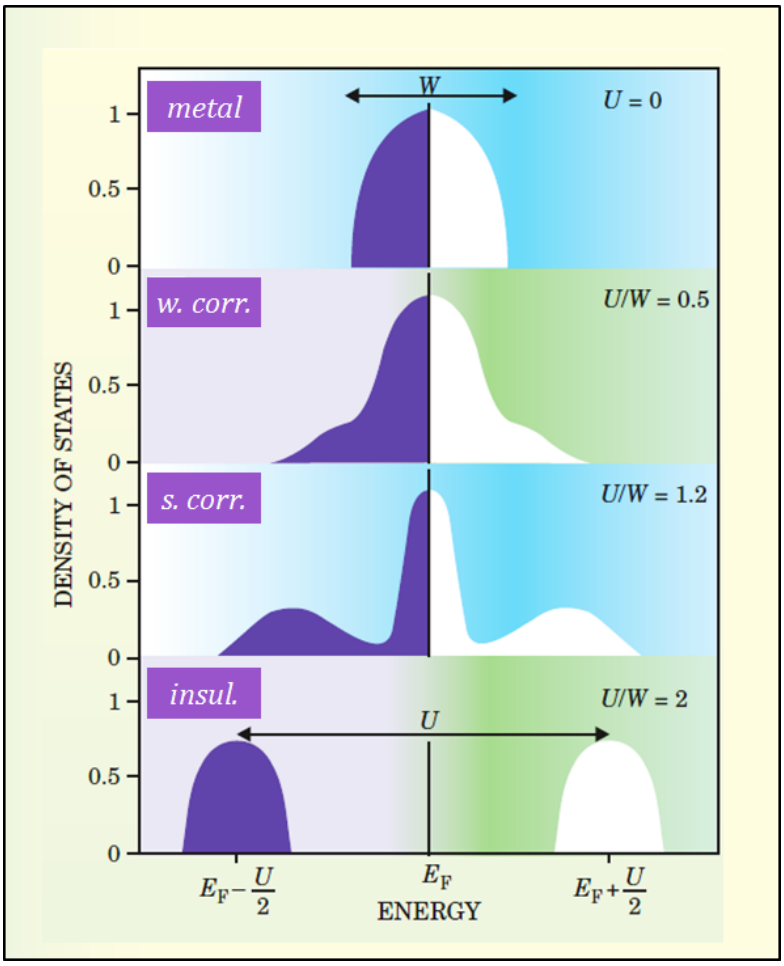


**Figure 1.19: Change in Density of States from a Metal to a Mott-Insulator.** A metal where the interaction energy is zero ($U = 0$), i.e. a free electron system. In the weakly correlated regime ($U/W = 0.5$), the electrons are still considered to be quasiparticles with a DOS that resembles the free electron system. In the strongly correlated regime, the DOS spectrum shows the *characteristic three peaks:* the Hubbard bands that come from the local atomic excitations (broadened by the hopping of electrons away from the atom) and the quasiparticles peak centered at the Fermi level. The Mott-insulator where the electrons interactions are so strong as to cause the quasiparticle peak to vanish. Adapted from reference [120].

Returning specifically to $VO_2$, the question of whether its phase transition (band gap opening) can be described from an electronic model alone (*Mott-Hubbard MIT*) or can the structural reconstruction dictates solely its properties via electron-phonon coupling (*Peierls MIT*) is still controversial. With the advent of nanoscale probes and ultrafast laser techniques, the implications of these two models for the dynamical and spatial characteristics of the MIT have been under increasingly intense scrutiny.

The original suggestion of a Peierls transition in $VO_2$ was made by Goodenough in the early 1970s who postulated that the structural distortion that splits the $3d_{||}$ band was enough to create a band gap[117]. However, Zylbersztejn and Mott soon after argued that the distortion alone was not enough as the upward shifted $3d_{\pi*}$ would actually reduce screening effect between the electrons found in the $3d_{||}$ band[121]. This notion was reinforced in many instances by the fact that density functional theory (DFT) within the local density approximation framework was unable to reproduce the band gap in the insulating (M1) state[115]. However, DFT-LDA provided support for a molecular orbital picture that described correctly M1-$VO_2$ as the stable lowest total energy and yielded structural parameters agreeing with experiments[122]. Very recently, Eyert[38] and Iori *et al.*[123] in 2011 and 2012 respectively have shown how non-local exchange interactions can reproduce the correct band gap in $VO_2$ and thus without additional electron correlations (figure 1.20), closely agreeing with photoemission experiments[124,125]. At the heart of these results is the use of a newly-developed hybrid functionals in the work of Heyd, Scuseria, and Ernzerhof (HSE), that combine the short-range part of the exchange functional using a fixed combination of generalized-gradient approximation (GGA) and Hartree-Fock contributions while the long-

range component and the correlation functional are solely encompassed by GGA[126]. Lastly, a more complex mechanism termed as *Peierls-assisted orbital selective Mott transition*[127] was identified by performing state-of-the-art linear scaling DFT calculations, refined by incorporating non-local dynamical mean-field theory that calculated a 768 atoms supercell. The M1 phase was found to be stable against a certain degree of disorder (e. g. oxygen vacancies) and more importantly, the theory reconciled polarization-dependent X-ray absorption measurements on $VO_2$ in which dramatic switching of orbital occupation from isotropic (in R-phase) to an almost completely polarized $3d_{||}$ orbital in the insulating M1 phase was observed. This highlights the crucial role of the orbital and lattice degrees of freedom in the correlated motion of the electrons and reinforces the idea of an orbital-assisted *collaborative* Mott-Peierls transition[128].

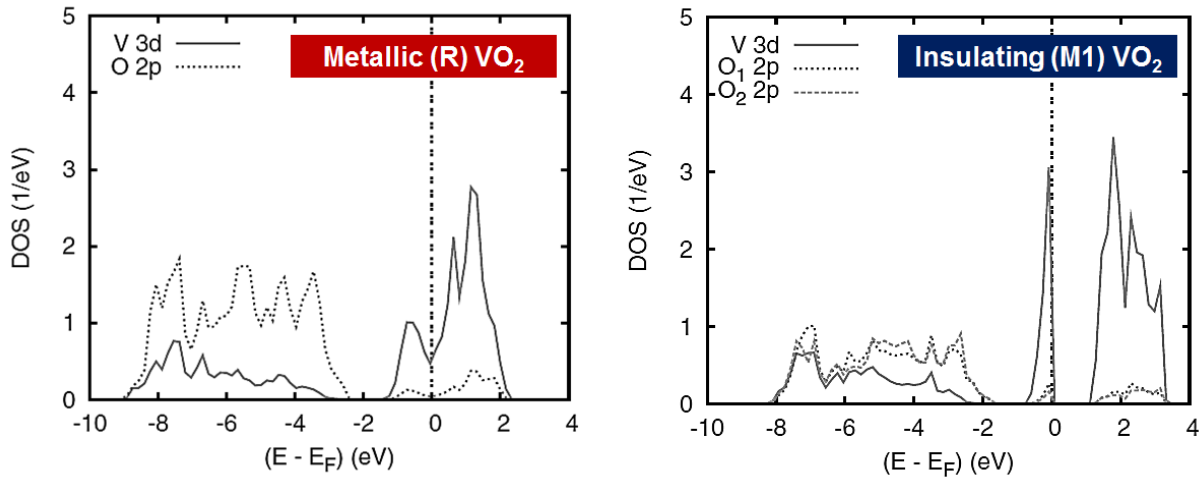


**Figure 1.20: DOS for Metallic and Insulating $VO_2$ Using Hybrid Functional.** Partial DOS of R-$VO_2$ (left) and M1-$VO_2$ (right) using the HSE hybrid functional. Adapted from reference [38]. Note the band gap in the insulating state.

The complexity of the switching mechanism in $VO_2$ has also been highlighted at the nanoscale, where Qazilbash *et al.*[129] demonstrated that the metallic nanopuddles formed during thermal triggering of the phase transition had different optical characteristics from the rutile (R) metallic phase of $VO_2$. The metallic nanopuddles exhibited (i) an optical pseudogap in the electronic density of states, underlying the complex interplay between electronic correlations and charge-ordering due to dimerization; and (ii) diverging effective optical mass in the vicinity of the MIT arising from many-body Coulomb correlations. From these observations, they classified $VO_2$ as a *Mott insulator with charge ordering* reflected in the formation of a strongly correlated metal – metallic nanopuddles – during the phase transformation[129].

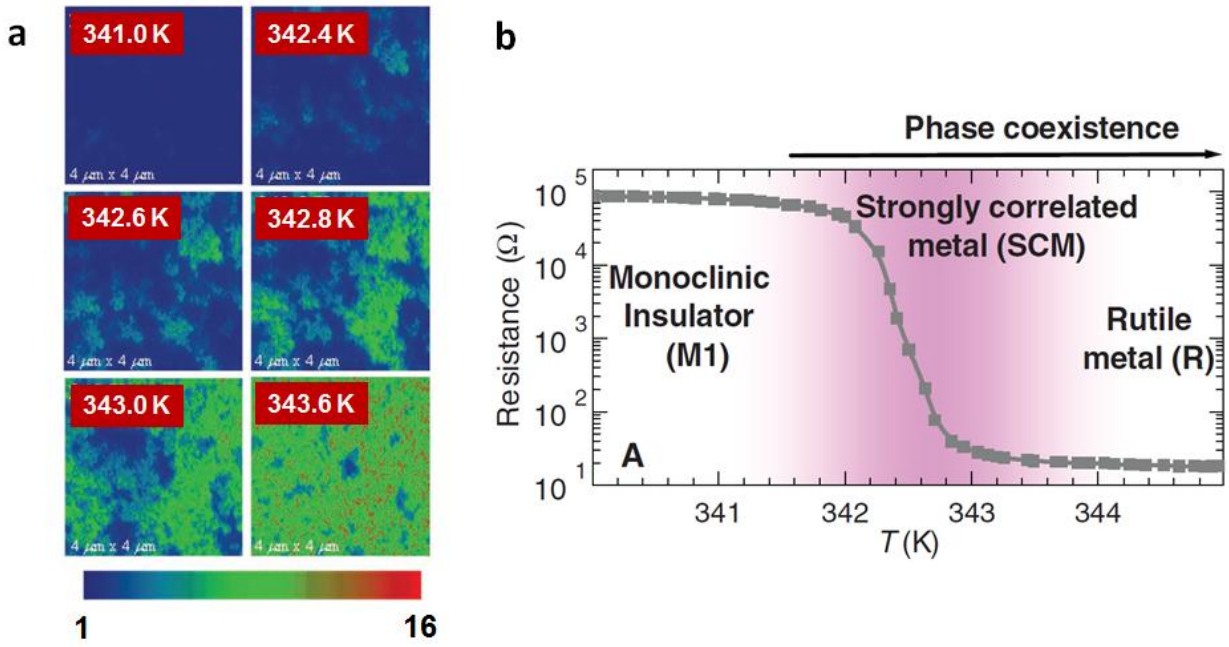


**Figure 1.21: Strongly Correlated Metallic $VO_2$ Nanopuddles. (a)** 4 μ$m$ $x$ 4 μ$m$ near-field scattering images of $VO_2$ nanopuddles as they undergo phase transition. The images were acquired by scattering scanning near-field infrared microscopy (s-SNIM) with a spatial

resolution of 20 nm with the metallic regions being light blue, green and red in color while the insulating regions being dark blue. **(b)** Temperature-dependent resistivity measurement depicting the PT and highlighting the region of strongly correlated metal having divergent quasi-particle mass and an optical pseudogap. Adapted from reference [129].

Further examination of such $VO_2$ films (s-SNIM and micro-XRD) by the same authors[113] revealed that the nanoscale local structural and electronic components of the thermally triggered phase transition do not occur simultaneously in time or congruently in temperature (figure 1.22). While the structural component of the MIT - as measured by X-ray diffraction – showed a non-monotonic transition from the M1 to R phase, the electronic component – measured by the reflectivity in s-SNIM – increased linearly during the phase transition. At microscopic length scales, the atomic and electronic components of the PT could potentially be decoupled. On a similar footing, Nag *et al.* also demonstrated this principle in epitaxially grown films of $VO_2$, arguing that such effect is an intrinsic property of the $VO_2$ phase transition, and not solely due local effects[130]. From effective-medium calculations of the dielectric functions of the two states, they argued that an intermediate metallic state can be formed in which the electron-electron correlations disappear before growth of the metallic rutile state can proceed (figure 1.23). In ***Chapter 3***, we reconcile both results by demonstrating that although this non-congruence is intrinsic to $VO_2$, the effects of grain boundaries and interfaces in thin films tend to blur the differences between the strongly correlated monoclinic metal and the rutile metallic phase that are more easily observed in nanoscale structures[131].

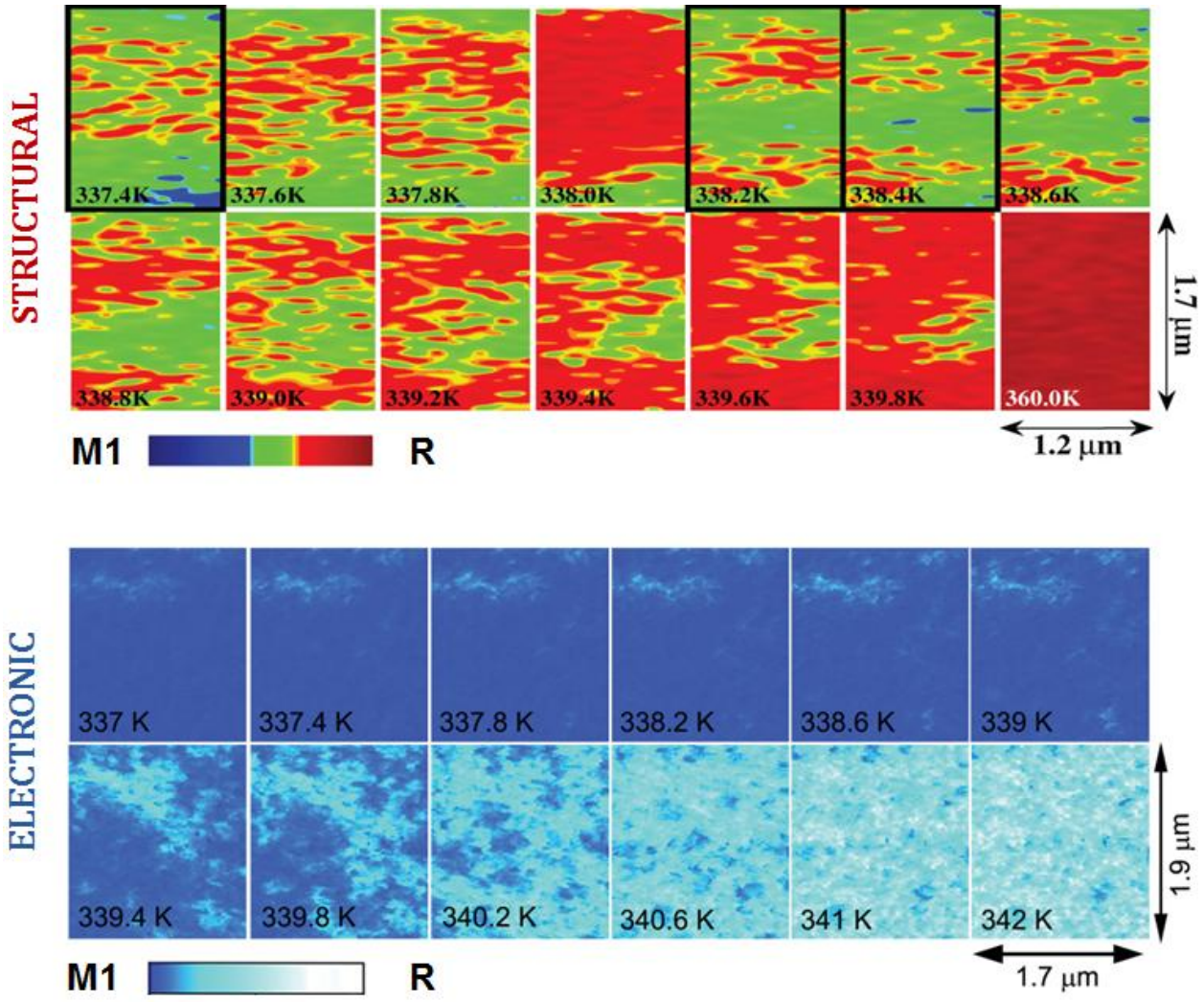


**Figure 1.22: Contrasting Local Nanoscale Electronic and Structural Response of the $VO_2$ Phase Transition. (a)** Spatial maps of the same area depicting structural PT recorded by nanoscale x-ray imaging with variation in intensity of the Bragg Peak from the M1 phase (dark blue) to R phase (red) when thermally triggered. The intermediate intensities (green) shows coexistence of both phases within the x-ray beam spot. **(b)** Spatial maps of the electronic PT probed by the similar s-SNIM technique as shown in figure 1.21. Note the non-monotonic progression of the structural PT, suggesting a sharp transition between the M1 and R phase.

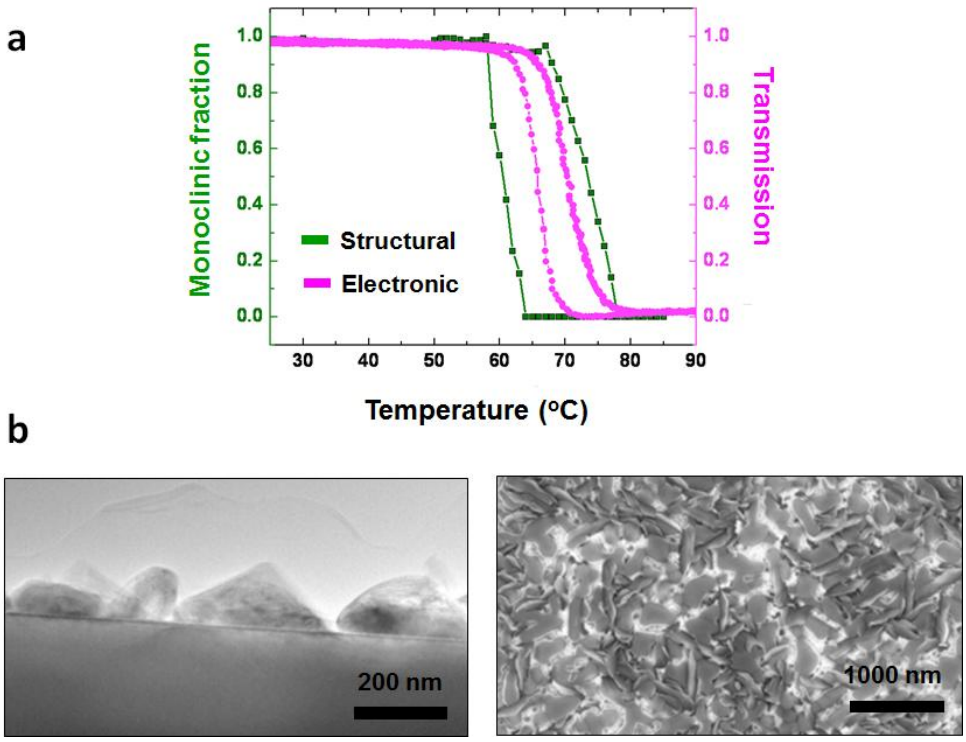


**Figure 1.23: Non-Congruence in the Electronic and Structural Signatures of the $VO_2$ Phase Transition. (a)** Normalized XRD and white-light optical transmission hystereses recording the evolution of the structural and electronic component of the PT of the same epitaxial sample as a function of temperature. **(b)** Side-view TEM and top-view SEM of the sample used.

### 1.3.2c Thermodynamic considerations: the case for heterogeneous nucleation and size-dependent switching

In the equilibrium limit, a solid-solid phase transformation can be defined as a particular phase of a solid characterized by a homogeneous uniform structure and composition and separated from other phases by sharp boundaries, which becomes unstable under a given set of thermodynamic conditions and gives birth to new phase with a different characteristic assembly of same constituent atoms or molecules[132]. Depending on the

relation between the specific property undergoing a discontinuity and the Gibbs free energy, the order of the phase transition can be classified as the same order as the derivative of the Gibbs free energy[133]. Thus,

$$G = H - TS = E + PV - TS \qquad \text{eqn 1.14}$$

and its derivative, $$dG = dE + PdV + VdP - TdS - SdT \qquad \text{eqn 1.15}$$

where G is the Gibbs free energy, E is the internal energy, P is the pressure, V is the volume, T is the temperature and S is the entropy. From the derivative of the Gibbs free energy (with $T$ or $P$ kept constant), we see that:

$$V = \left(\frac{\partial G}{\partial P}\right)_T \quad and \quad S = -\left(\frac{\partial G}{\partial T}\right)_P \qquad \text{eqn 1.16}$$

Therefore, a transition that undergoes a discontinuous change in volume and entropy (i.e. latent heat of transformation) belong to the first-order PT, represented graphically in figure 1.23. At the point where the free-energy curves intersect ($Tc$) the transition II→I occurs. At Tc, the two phases coexist and can be distinguished by their different enthalpies – different structural configurations in our case. To some extent, the Gibbs free energy curves can be extended on both sides of $Tc$ to describe superheating and supercooling effect. Based on this definition of phase transition, vanadium dioxide is typically classified

as a *first-order* transition since its volume ($V$) and entropy ($S$) abruptly change at the thermal equilibrium transition temperature ($T_c$).

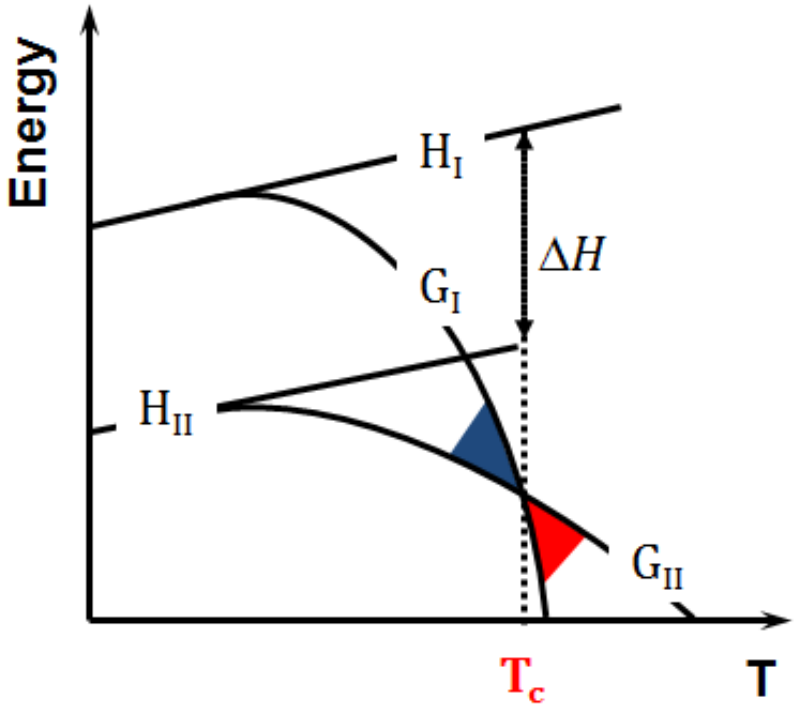


**Figure 1.24: Characteristic of a First-Order Phase Transition.** A first-order phase transition at constant pressure displaying variations in free energies ($G_I$ and $G_{II}$) and enthalpies ($H_I$ and $H_{II}$) for phases I and II respectively. The shaded regions represent the superheated (red) and supercooled (blue) states, while $T_c$ depicts the temperature at which the two phases intersect thermodynamically.

Experimentally, superheating and supercooling effects manifest themselves as a hysteresis due to a temperature difference between heating and cooling transitions as one drives the material across the energy barrier defined thermally by $T_c$. In polycrystalline $VO_2$ films, for example, the hysteresis width is typically between 10-15$^0$C; in bulk single

crystals, on the other hand, the hysteresis width is closer to $2^{0}$C. Accompanied by this lag in the material response to external driving force is a dependence on its previous forward or reverse transformation history, marked by the characteristic signature of a hysteresis. The underlying microscopic description is based on the existence of multiple metastable configurations that are dynamically linked along the transformation path[134]. Such a property, present in $VO_2$ as well, can be harnessed in memristive-type applications[135,136].

A peculiar property of $VO_2$ is a variable hysteresis width manifested in intrinsic size-dependent switching, due to heterogeneous nucleation of the phase transition. This was discovered by Lopez *et al.* in stoichiometric and crystalline $VO_2$ nanoparticles embedded in $SiO_2$ fabricated by ion beam implantation (figure 1.25)[37].

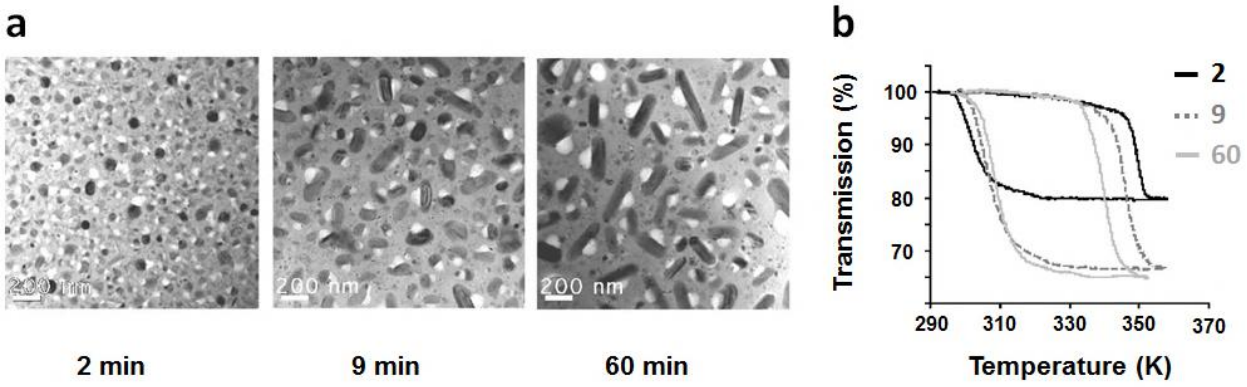


**Figure 1.25: First Observation of Size-Dependent Switching in $VO_2$ Nanoparticles. (a)** SEMs of the various samples studied. **(b)** Transmission hysteresis measurements of said samples, annealed for time durations of 2, 4 and 60 minutes.

In order to understand this property, we first rule out the possibility of homogeneous nucleation. Homogeneous nucleation is an inherently random process because the new phase is driven by thermal fluctuations that bring the atoms to new

positions, corresponding to the product phase. For simplicity, let us assume (i) that there is no significant change in volume between the parent and product phase so as to neglect complex strain fields that might developed at the interface and (ii) that the interfacial energy (γ) between two phases is independent of crystallographic orientation. Consequently, the rate of nucleation is directly related to the change in free energy ($\Delta G$), according to classical nucleation theory. The formation of a product phase having a spherical nuclei is a competition between the decrease in bulk free energy (per unit volume) ($\Delta G_{bulk}$) and an increase in the surface free energy (per unit area of the surface), γ. Consequently, if the spherical embryo has a radius r, then:

$$\Delta G = -\frac{4\pi}{3} r^3 \, \Delta G_{bulk} + 4\pi r^2 \gamma \qquad \text{eqn 1.17}$$

From the equation, if the second term dominates, then the embryo will dissolve back into the parent phase. However, at an instant when the embryo becomes thermodynamically stable, that is when the radius reaches a critical size ($r_{critical}$) such that the first term (negative) dominates the surface energy term, further growth of the new phase will be favored. In the specific case of $VO_2$, this nucleation barrier, $\Delta G$, can be calculated as shown by Lopez *et al.*[37]. Here, the bulk free energy is assumed to be proportional to $|T - T_c|$ with a proportionality constant dictated by the entropy difference between the parent and daughter phase (~ 6.57 x $10^5$ J/m$^3$K)[137] and the surface energy, though not reported in the literature, was approximated to be about 10-20 x $10^{-3}$ J/m$^2$. This is due to the fact that most inorganic materials have surface energies of 1000 ± 100 x $10^{-3}$ J/m$^2$ and thus the difference

between the two $VO_2$ phases can only lie in an even smaller range. From figure 1.25, we see that for a temperature slightly above the transition temperature (341 K), an energy barrier of ~ 250 eV is still required to effect the PT and is thus not consistent with energies found experimentally to switch the $VO_2$ ($k_B \cdot T_c = 8.61 \times 10^{-5} eV/K \cdot 340\ K \approx 30\ meV$). Consequently, the phase transition must be initiated at "potent sites," where the local energy barrier is reduced and where the daughter phase is stable enough inside the parent that transformation can proceed, even under modest driving forces. This process is defined asheterogeneous nucleation.

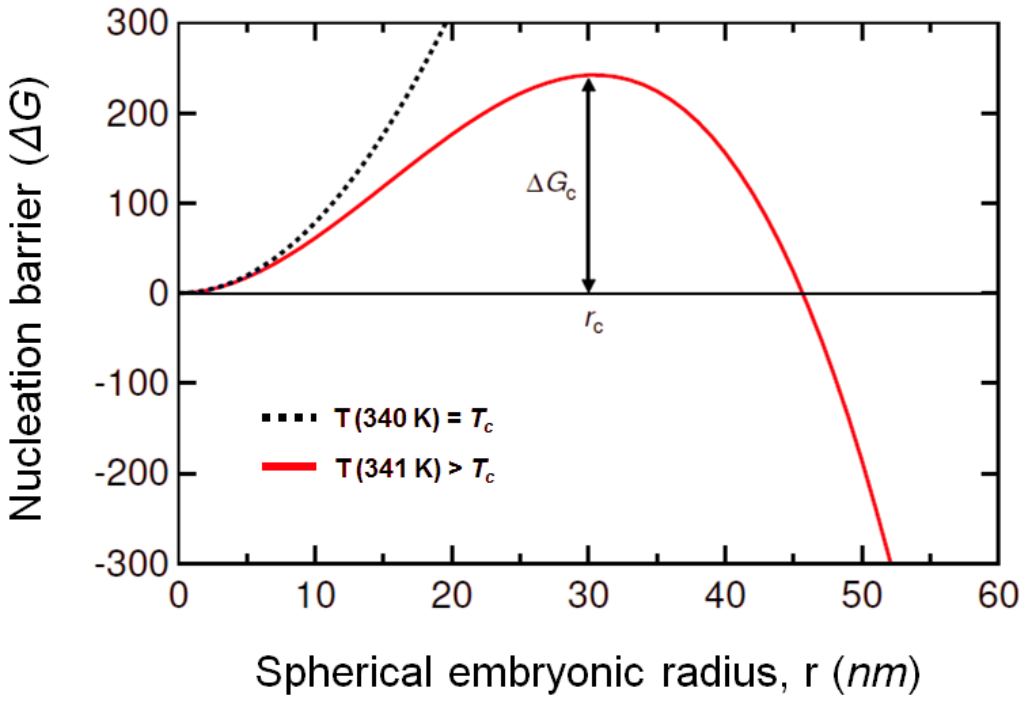


**Figure 1.26: Homogeneous Nucleation Calculations for $VO_2$.** Nucleation barrier energy plotted as a function of embryonic product phase radius for two temperatures (at $T_c$ and $T_c$ +1 K). Adapted from references [37] and [138].

Moreover, in order to understand the size-dependence switching of $VO_2$ and how it relates to the hysteresis width (figure 1.24), a detailed model based on the statistics of heterogeneous nucleation was described by Lopez *et al.*[37]. Here, a transition of the martensitic type – characterized by a high-speed, diffusionless shear transformations – was used as it typically provides a basis for understanding structural transformations[139]. A martensic transition mechanism for $VO_2$ has been described in other studies as well, most notably the work by Klimov *et al.*[140-142].

Although the exact nature of these potent sites was not clearly postulated when it was first described, it was believed to be some type of extrinsic defects since the densities estimated for intrinsic defects ($\sim 10^{11}$) would be too low[36]. Thus, the nature of these nucleation sites could potentially range from vacancies or, wall dislocations to untransformed embryonic regions as well[143]. Recently, Fan *et al.*[144] highlighted the role of the two basic types of crystal defects – point defects and twin walls – by analyzing the degree of supercooling and superheating in single-crystals microbeams of $VO_2$ and thereafter controlling their thermodynamic properties by creating defects in these almost defect-free microbeams. They showed that nanometer-thick twin walls are constantly created and destroyed during the symmetry-raising process of metallization, eliminating the need for superheating by providing seeds for heterogeneous nucleation dynamically rather than statistically. But on the other hand, twining is forbidden when transitioning to the insulating state and the nucleation process relies solely on point defects, resulting in a larger supercooling effect. This is highlighted in figure 1.27. By externally controlling the number of bulk defects via α–particle irradiation, the supercooling could be quenched, thus

also paving the way for unique memory and logic devices. In ***Chapter 3***, we make a strong case that the structural defects initiating the phase transitions are oxygen vacancies that arise due to interfacial strain.

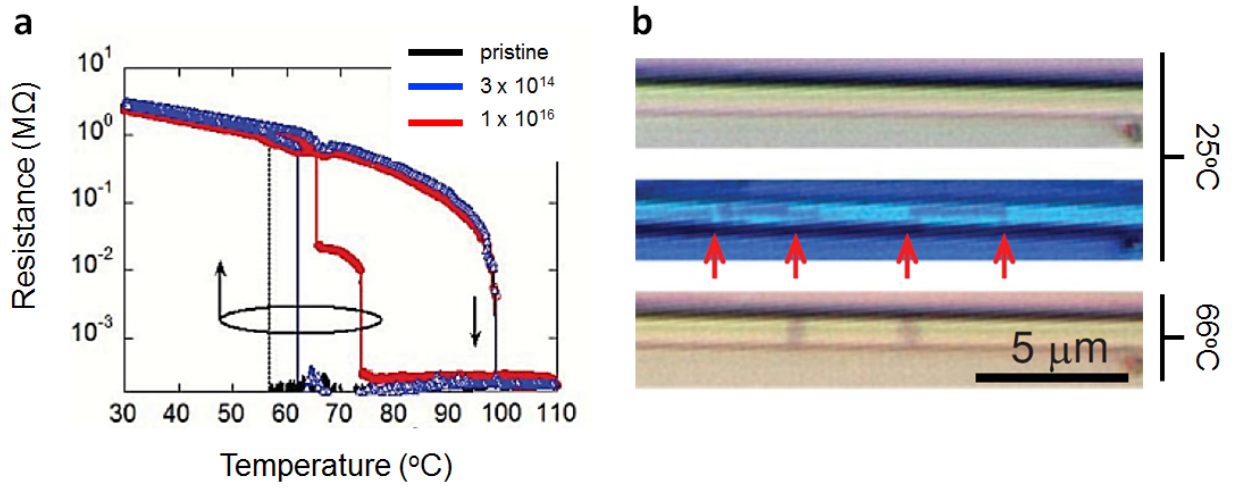


**Figure 1.27: Effect of Irradiation on Superheating and Supercooling Effect. (a)** Temperature-dependent four-probe resistance of a clamped device before and after two doses of α-particle irradiation. The superheating is not affected, yet the supercooling is clearly reduced by the irradiation. **(b)** An optical image (top) and polarized image (middle) of a clamped $VO_2$ microbeam showing twinned M1 domains with twin walls (indicated by arrows) perpendicular to the beam axis, and the nucleation of R domains at some of the twin walls upon heating to 66°C (bottom).

### 1.3.2d Recent Developments in $VO_2$: Fabrication and Switching

Over the last few years, the ability to fabricate high-quality $VO_2$ so as to control its optical and electronic properties has increased significantly. This is being driven by the increasing consideration of $VO_2$ for a wide range of applications, such as in ultrafast switches[145], modulating barriers in multilayered spin switches[146], Mott field-effect transistors[147] and

novel solid-state memory devices[148]. Moreover, given the fact that transition-metal oxides form in an ionic lattice with the charged regions created by defects potentials, non-stoichoimetry in $VO_2$ and oxides in general, can have a huge impact on device performance due to leakage currents or decreased switching effectiveness. Thus, addressing concerns of vanadium dioxide growth in thin-film form (epitaxial or polycrystalline) on various substrates and its fabrication in large quantities or over large areas is of utmost importance. In $VO_2$, these issues are compounded by the fact that stoichiometric, crystalline and switching $VO_2$ occupies a very narrow phase space among the oxides of vanadium that can be formed, as shown in figure 1.28.

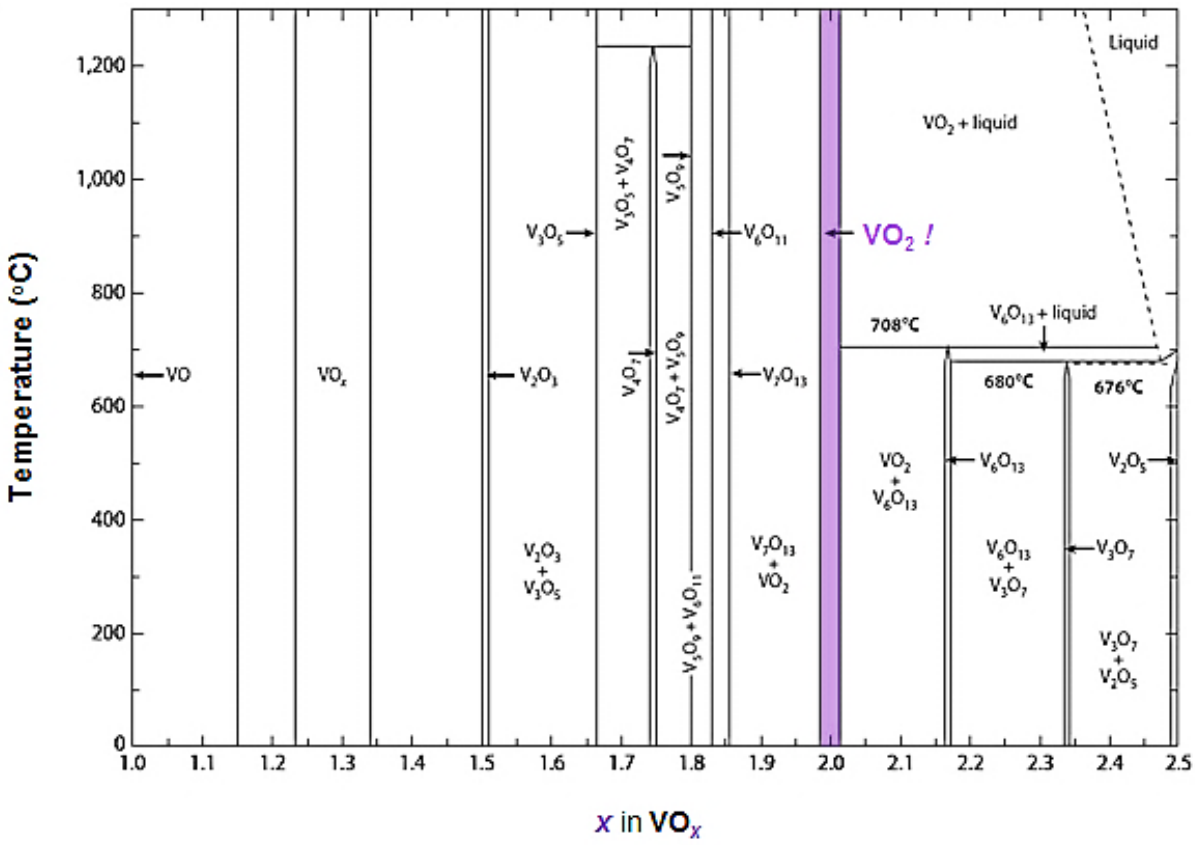


**Figure 1.28: Oxides of Vanadium.** Experimental phase diagram of the $VO_x$ system with corresponding temperatures. Adapted from [149], [150] and [151].

Depending on the details of the experiment or the application, $VO_2$ has been synthesized in various forms, such as bulk single crystal[152], thin polycrystalline[153,154] and epitaxial films[155,156], nanoparticles[36,37], nanobeams[157] and nanowires[158-160]. The fabrication methods that have been employed include sputtering[161], ion-beam implantation[36], pulsed-laser deposition[153,162], sol-gel process[163,164] and chemical vapor deposition[165,166]. $VO_2$ morphology can also be varied depending on the deposition method, deposition temperature, substrate temperature, lattice-matched substrates deposition or ways to

optimize its stoichiometry via precursor deposition rates, annealing times and background pressure have been devised[167].

Among the most noteworthy in these fabrication protocols is the ability to synthesize single-crystalline nanobeams and nanowires that are free of defects[157,168-170]. This has provided a new level of control for studying fundamental properties of the MIT, such as (i) the competition process between the various phases (M1, M2, T, R) to enable better mapping of the $VO_2$ equilibrium phase diagram[110,168,171,172], (ii) the effect of raising (via twin boundary formation) and lowering symmetry[144] on the hysteretic response of $VO_2$ while varying the degree of strain[173] and defect-density to great precision.

Recently, we have developed a reliable and cost-effective method to fabricate crystalline, stoichiometric and switching $VO_2$ on various substrates (glass, silicon and sapphire)[174]. This method consists of electron-beam evaporation of a precursor that is very close to the perfect $VO_2$ stoichiometry so that a fast anneal can already render the film switching. Because of short annealing time, these thin films remain smooth (few nanometers in roughness) even when grown on Si. This is in contrast to previous studies where the long annealing times – following pulsed laser deposition or sputtering – would form $VO_2$ nanoparticulates due to surface dewetting[153]. Moreover, increasing the annealing times does not result in a significant change of optical performance, but only a slight variation in morphology as shown in figure 1.30. This method, although not demonstrated here, could in principle be extended to fabrication of phase-change $VO_2$ thin films at wafer scale. Further details of the experiment and characterization are found in *Appendix A*.

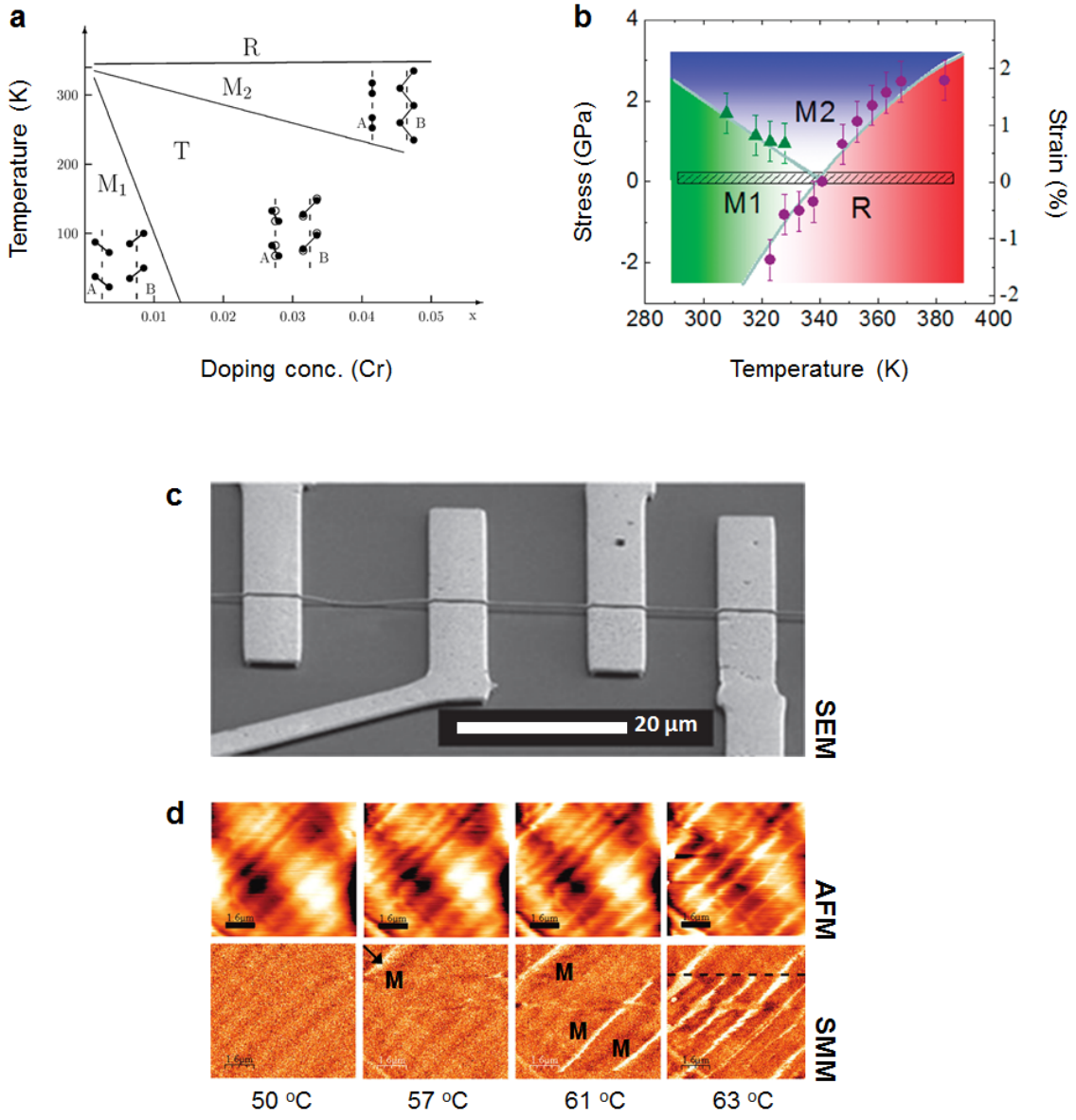


**Figure 1.29: Modification of $VO_2$ Phase Diagram by Doping or Uniaxial Strain. (a)** Structural evolution of $VO_2$ as a function of doping concentration (Cr) and temperature[175]. Similar phase diagrams have been obtained when doped with Al[176]. **(b)** Phase diagram with uniaxial stress (along $c_{rutile}$) obtained by in situ optical and SEM imaging of $VO_2$ beam bending. The eyes are a guide to the eyes while the hatched rectangular area near zero strain is the narrow phase space previously explore in bulk $VO_2$[173]. **(c)** SEM of a suspended nanobeam device displaying buckling at room temperature. **(d)** AFM topography images

(upper row) and corresponding amplitude signal of scanning microwave microscopy (SMM) images (lower row) of $VO_2$ single-crystal nanoplatelets as a function of increasing temperature. The darker color corresponds to lower height in AFM and lower conductance in SMM images. M denotes the metallic domains formation. Scale bars in all AFM and SMM figures were 1.6μm.

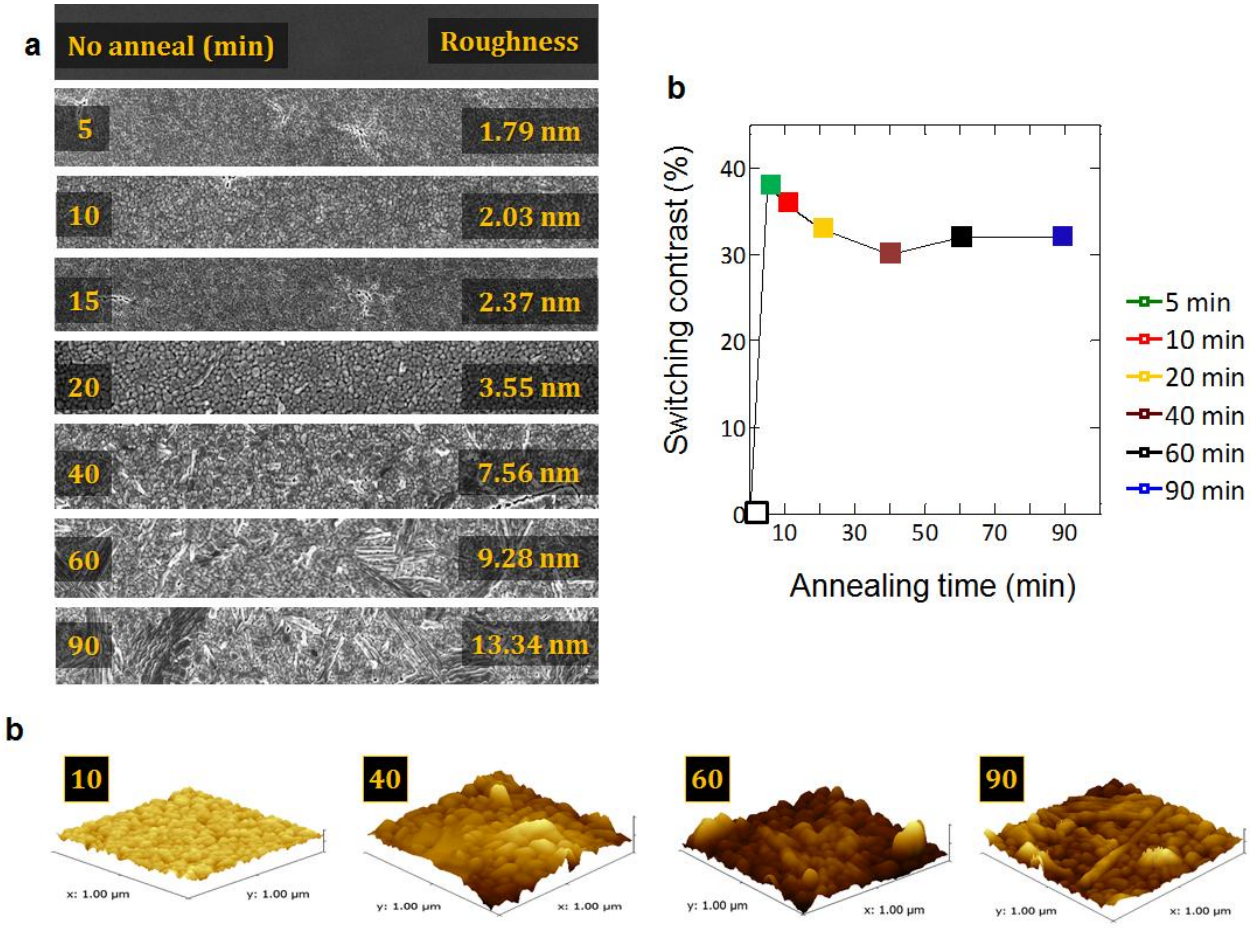


**Figure 1.30: Characterization of Samples Fabricated by Electron-Beam Evaporation.** **(a)** AFM of $VO_2$ samples with varying annealing times. Average surface roughness is quoted on the right. **(b)** Switching contrast obtained from white-light transmission measurement as a function of annealing time. **(c)** AFM for various films ($1\,\mu m \times 1\,\mu m$) depicting the

topography of the samples. Increasing duration of the annealing process induces an Oswald-type ripening effect as shown by the formation of rod-like features.

Along with various techniques to fabricate switchable $VO_2$ have come novel techniques to trigger the phase transformation, beyond the standard thermal and optical techniques. Recently, it has been shown that hydrogenation[177] and terahertz-field in split-ring metamaterials[178] could be potential avenues to modulate $VO_2$ properties as well. More technologically relevant is the ability to use current or electric field to induce switching in $VO_2$, emphasizing the Mott character of the phase transition in this case[179-181]. Although there has been much controversy over the cause of the switching because application of a voltage can lead to Joule heating as well as carrier transport, few recent experiments[182] have now settled this issue by showing that with no current flowing through the device, the phase transition is still induced by a gated electric field. Therefore, a field-effect transistor incorporating $VO_2$ (Mott transistors) could not only have lower operating thresholds, but could provide greater flexibility as well by circumventing RC-transit time limitations[182,183]. Recently, this has been extended to metal-insulator-semiconductor field effect transistors (MISFETs) based on strongly correlated properties of $VO_2$[184,185]. By electrostatically doping only a small number of charges at the surface, pre-existing localized electrons were driven into a mobile state, thus switching the device at very low thresholds ($\sim$ 1 V). Therefore, the potential for using $VO_2$ in field effect transistors is still a subject of active research[186-190], as shown by the examples in figure 1.31.

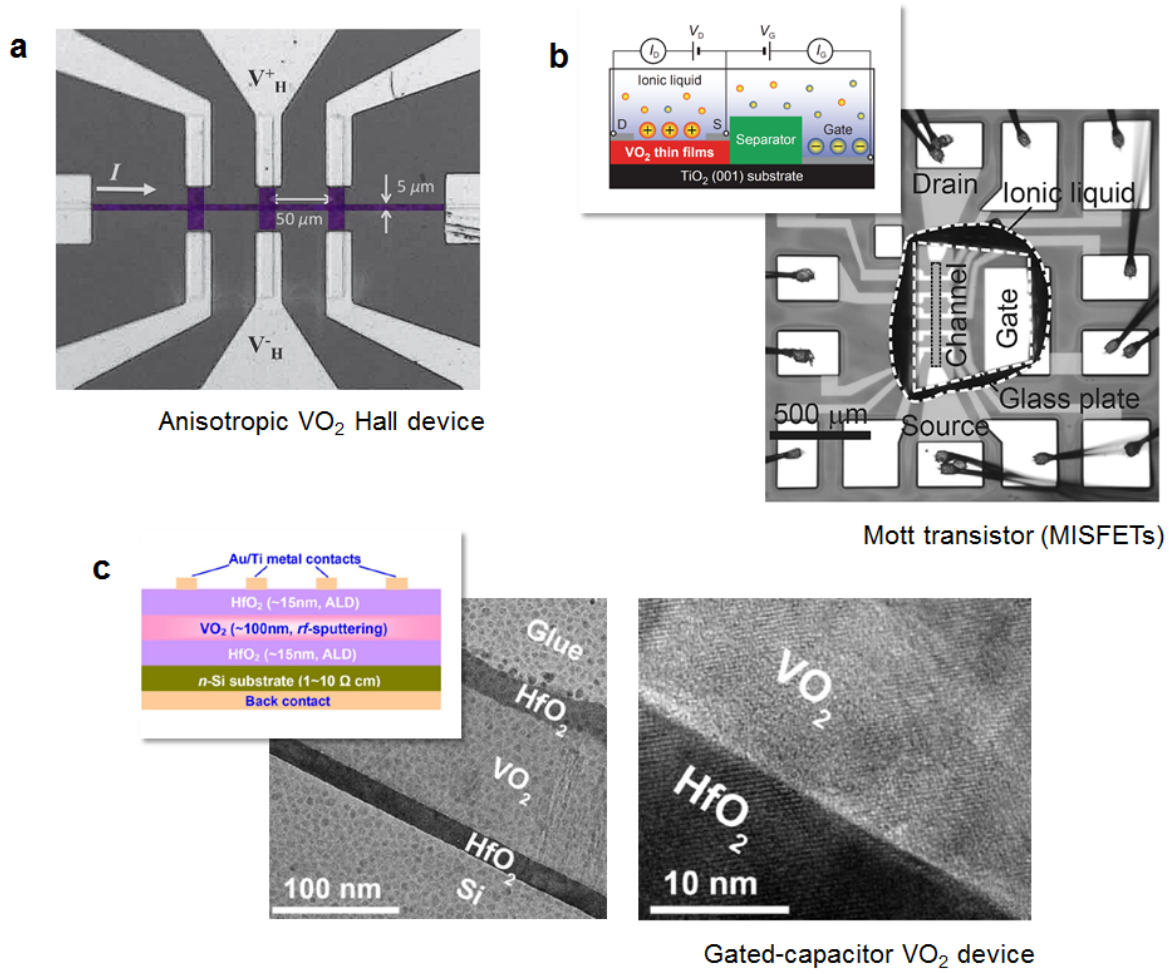


**Figure 1.31: Electrical Devices Incorporating $VO_2$. (a)** Anisotropic transport properties of epitaxial $VO_2$ Hall device. Optical image of a $VO_2$ Hall bar with Au top contacts. The Hall bar was patterned by photolithography and the film outside the pattern was etched via RIE. The width is 5 μm and the spacing between contacts along the bar is 50 μm[191]. **(b)** $VO_2$-based electric-double-layer transistor (VO2-EDLT). A small droplet of an ionic liquid, DEME-TFSI, covers both a channel and a gate electrode so that ions can freely move between these areas back and forth depending on a gate voltage, enabling electrical switching[184]. **(c)** Schematic of $HfO_2/VO_2/HfO_2/Si$ stack structure capacitor device. Cross-sectional TEM image of the capacitor device along with cross-sectional HRTEM image of $VO_2$-$HfO_2$ interface region[187].

### 1.3.3 Non-Equilibrium Limit: A Perspective from Ultrafast Timescales

Since one of the main goals of this dissertation is to provide the first description of the ultrafast properties of hybrid plasmonic/phase-change materials, a brief description of the non-equilibrium mechanism at play in $VO_2$ is necessary. Therefore, understanding the coupling mechanism of $VO_2$ provides a window on a broader class of ultrafast photo-control properties in quantum materials found in inorganic and organic[192] correlated-electron systems. In $VO_2$, interest in its non-equilibrium dynamics from both a fundamental perspective and for technological applications were spurred when Roach and Balberg first proposed that the phase transformation could occur in less than 10 picoseconds, *provided* that enough energy was deposited during this time period[193]. Figure 1.27 depicts this work, where the optical response of a 160 nm of $VO_2$ film was recorded following excitation by a ruby laser.

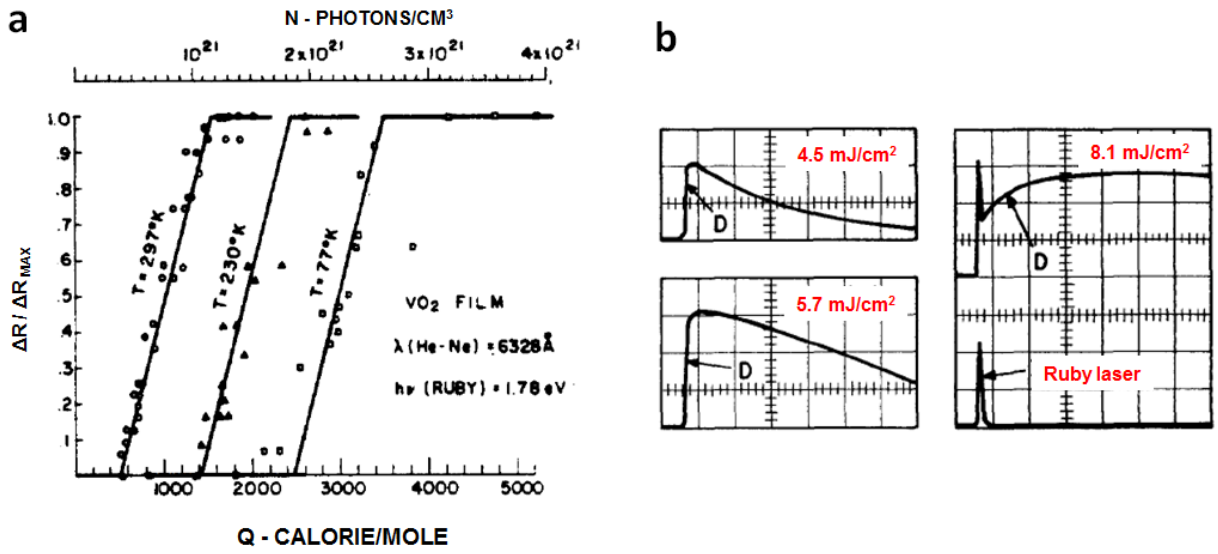


**Figure 1.32: First Optical Excitation of the MIT in $VO_2$. (a)** The measured fractional change of the reflected signal as a function of the number of photons or energy absorbed in

the film during ruby pulse absorption. **(b)** Oscilloscope tracing of the first-order diffraction signal D vs. time for various values of the ruby-laser excitation intensity energy. Vertical scale for D is 0.017% $I_o$ div, where $I_o$ is the incident-probe-beam intensity. The time scale is 200 nsec/div. Adapted from references [193] and [194].

### 1.3.3a General theory background in ultrafast spectroscopy

The ability to measure the fundamental temporal dynamics in a material requires capturing a series of snapshots while the system is evolving in time. The duration of these snapshots, i.e. exposure time, dictates the resolution at which the dynamics of the system can be resolved. If the dynamics are much faster than the duration of the snapshot, information about the system is thus lost. Consequently, one needs snapshots or pulses that are shorter than the event one would like to interrogate. The first example of such time-resolved studies was the study of whether all four hooves of a horse would be simultaneously off the ground while it is galloping. In this experiment entitled "*Sallie Gardner at a Gallop*", Muybridge used twelve cameras to sequentially take photographs as the horse was travelling across this field of view. By developing a high shutter speed to record photographs with a time resolution of one millisecond, the corresponding images were acquired (Figure 1.28), clearly demonstrating that at a given point in time all four hooves were off the ground. This settled the debated[195].

Nowadays, this concept has been extended to understanding physical, chemical and biological processes in a time-resolved fashion, permitting insights into mechanisms such as molecular binding[196], chemical reactions[197,198], phase transitions[35,199] and dephasing processes[200,201] that occur on the picosecond ($1 \times 10^{-12}\ sec$) or even femtosecond

($1 \times 10^{-15}\ sec$) timescales. In condensed matter systems, the short and long range order that exist in a lattice can provide other interesting effects that are metastable and therefore short-lived. Consequently, ultrafast techniques are required not only to trigger these mechanisms, but probe these hidden states as well[13,202,203].

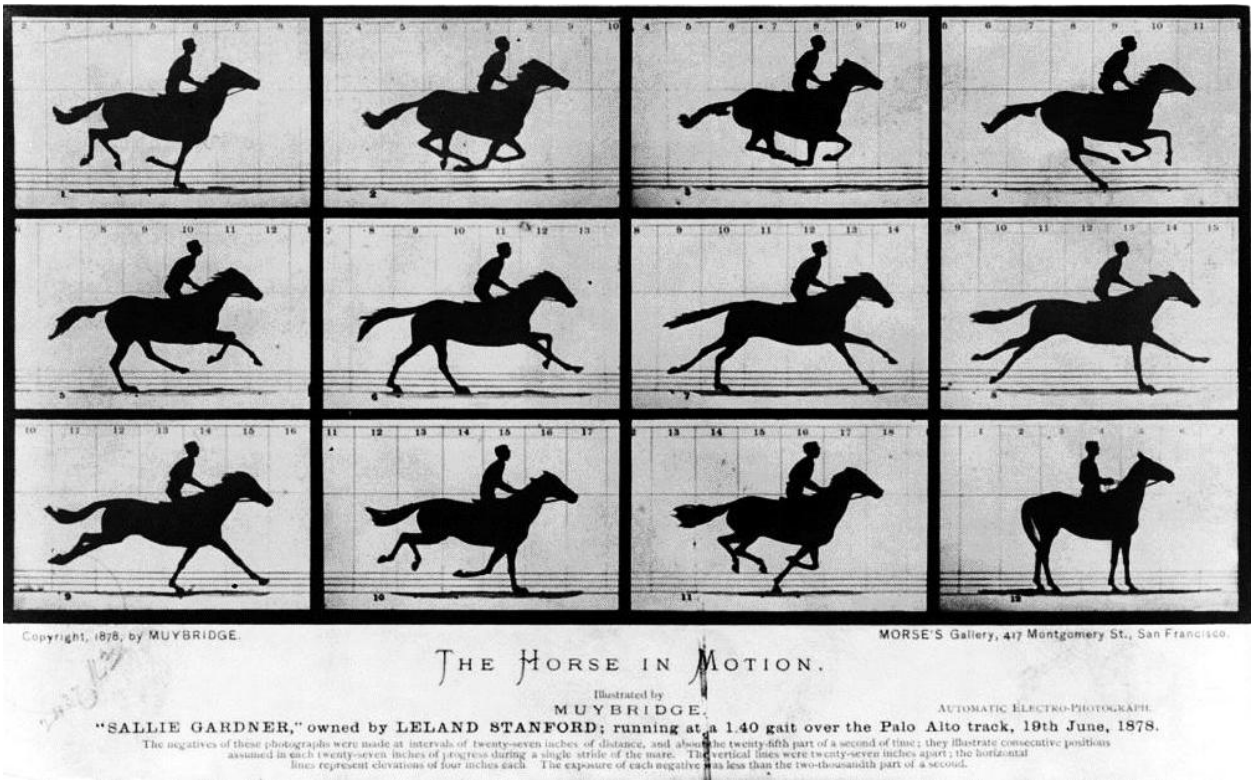


**Figure 1.33: The First Report of Time-Resolved Measurement: "*Sallie Gardner at a Gallop*."** The measurement was used to settle the debate that all four of a horse's hooves are off the ground at a given point in time during the gallop. From reference [195].

At the basis of such experiment is the ability to trigger a material response with an ultrashort pulse such that either carriers can be excited across energy bands or atomic vibrations can be set into motion (phonons). The use of femtosecond pulses to study the ultrafast dynamics of semiconductors was first demonstrated by Shank *et al.* [204].

Thereafter, studies of ultrafast solid-liquid[205] and solid-solid[35] phase transformation were also demonstrated. Since such excitation schemes in materials can lead to formation of metallic states with drastic optical changes analogous to chemical doping, the term photodoping was coined, highlighting the ability to control materials properties with light.

Currently, advances in the field of ultrafast science have two directions: the gradual development of faster probes by pushing the temporal resolution into the attosecond regime ($1 \times 10^{-18}\, sec$) that will lead to an understanding of even faster electronic processes. The other direction is to extend established static techniques such as x-ray diffraction[206], electron diffraction[199], photoemission[207-210] and potentially transmission electron microscopy to the femtosecond timescale, enabling the study of atomic motions and Fermi surfaces in a time-resolved fashion. Recently, Perfetti *et al.* demonstrated the ability to measure the time evolution of the electronic structure during a MIT by angle-resolved photoemission electron spectroscopy[211], highlighting the collapse of the band gap within 100 fs. Perhaps even more fundamentally important is the novel ability to excite vibrational modes of a material to control its electronic phase. This work was demonstrated by Rini *et al.* by using intense pulses in the mid-IR, corresponding to a perturbation of the phonon mode in a perovskite-structure beyond its tolerance factor, to excite a manganite[212], changing it from a paramagnetic insulator to a ferromagnetic metal phase. This concept has been extended to rectified phonon fields that can exert a directional force onto the crystal (thanks to lattice anharmonicities), inducing abrupt displacement of the atoms from their equilibrium positions and therefore opening a new direction for the optical control of solids in their electronic ground state that is different

from carrier excitation[213]. As will be discussed in the next section, a few of these ultrafast techniques have been employed to aid in the understanding of the phase transition in $VO_2$.

### 1.3.3b Recent developments in ultrafast dynamics of $VO_2$

Ultrafast studies of $VO_2$ can be classified into three main categories, namely (i) metallic domain formation along with its associated relaxation mechanisms (ii) elementary mechanistic studies of the optically-driven phase transition and (iii) technological applications.

Briefly, for the first case, it was found by Lysenko *et al.* that the temperature distribution in the $VO_2$ film following pulse excitation becomes uniform in $\sim 10^{-12}$ to $10^{-9}$ second range, depending on the details of the film (thickness and morphology) and excitation pulse (light absorption and pump fluence)[214]. More importantly, it was discovered that relaxation of $VO_2$ on single crystal substrates was $\sim$ 50 times faster[215] than on amorphous ones, as summarized in figure 1.29. This suggests than phonon transport could potentially be tailored in epitaxial $VO_2$, where reduced phonon scattering at the $VO_2$/substrate would result.

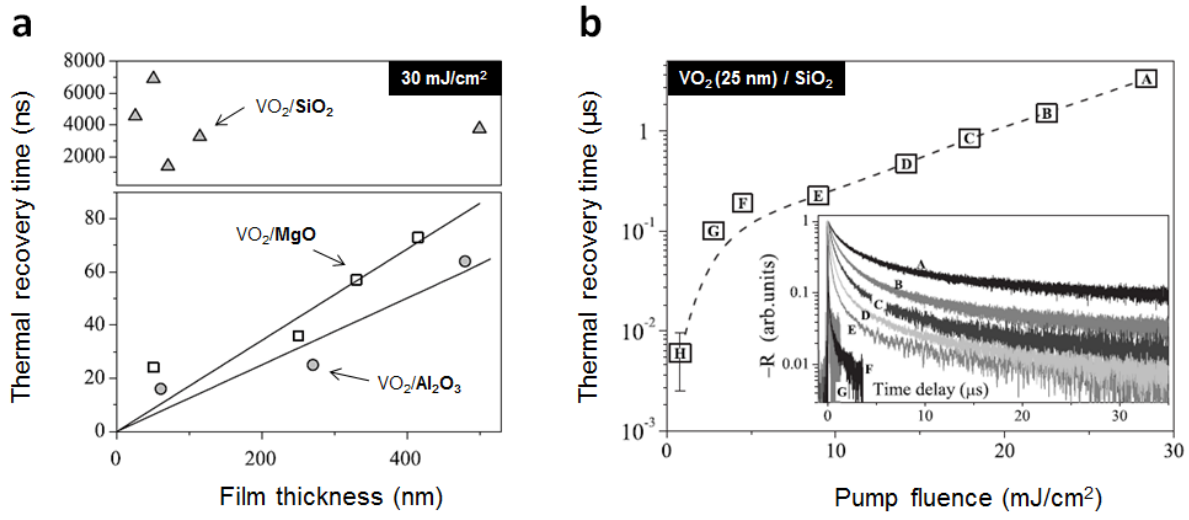


**Figure 1.34: Recovery Dynamics of $VO_2$.** (a) Substrates effect on the thermal recovery time as a function of film thickness. (b) Metal to insulator recovery time as a function of pump fluence for a specific film thickness of $VO_2$ (25 nm). From reference [215] and [216].

Hilton *et al.* later discussed the ultrafast complexity of such systems at near-threshold switching behavior where a percolation model could still be applied (i.e. as opposed to high pump fluences where $VO_2$ PT is prompt and non-thermal). By using optical-pump terahertz-probe spectroscopy, transport measurements were conducted that would have otherwise been impossible due to absence of a macroscopic pathway because of phase separation and domain formation. Interestingly, they found that there was a ~ 100 ps rise time for the film to reach a metallic phase, independent of the exciting pump fluence. Since this is much longer than the time it takes for photoconductivity to develop due to carrier excitation to the conduction band (as in typical semiconductor) and also longer than lattice heating via carrier thermalization (~ 10 ps), they hypothesized that these conductivity dynamics are more complex than a simple heating beyond $T_c$. Moreover, by increasing the temperature of the $VO_2$ film, they showed that the conductivity

discrepancy (between the maximum obtainable conductivity by heating and the actual conductivity obtained with pulses that could heat the sample beyond $T_c$) would decrease, as shown in figure 1.30. Therefore, this demonstrated that there is a "stiffness" with respect to driving the insulator-to-metal transition and that this "stiffness" decreases as the temperature of the $VO_2$ material is raised. This can be interpreted as a softening of the phonon modes of the insulating system.

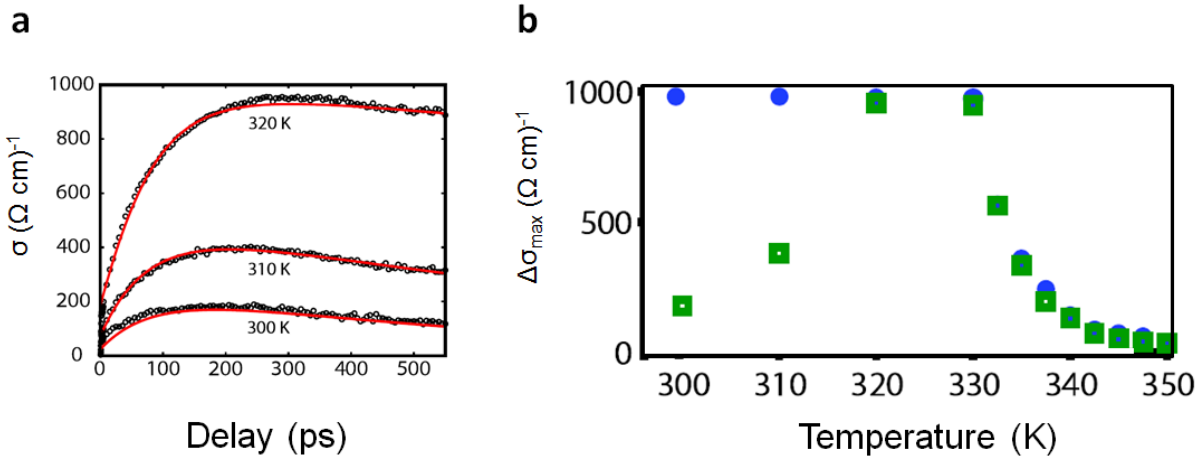


**Figure 1.35: Near-Threshold Behavior Probed by Ultrafast THz Spectroscopy. (a)** Time-resolved conductivity for various sample temperatures. (b) Maximum conductivity change. From reference [217].

More than half a century after its discovery, the mechanism underlying the MIT is still under intense debate. Ever since it became clear that a subtle balance between cell-doubling and carrier localization was responsible for the PT and that structural remodeling was possible on a sub-picosecond timescale, this has generated many ultrafast studies to refine understanding in $VO_2$ and correlated oxides in general[35]. Before discussing the details of some of these important results, we point out that the observed ultrafast

response cannot be explained by mere excitation of carriers across a semiconductor band gap for many reasons, namely **(i)** *e-h* pairs creations at these densities would result in a decrease (increase) of reflectivity (transmission); **(ii)** the response would not have any fluence threshold dependence and would not saturate with fluence as well; **(iii)** the long lifetime of the relaxation cannot be attributed to hot carriers (~ 10s of picoseconds). Consequently, it is important to note that there are three regimes for the ultrafast PT, namely **(i)** below the fluence threshold where no PT occurs, **(ii)** slightly above the threshold where there is a small amount of the $VO_2$ that metallizes due to thermal diffusion of heat and **(iii)** the saturation region where the structural phase transition can occur on a sub-picosecond timescale[218]. In the work of Cavalleri *et al.* (2001), this was the first time that ultrafast optical and x-ray measurements were performed in conjunction and most importantly, the first experiment of non-thermal order-disorder PT where the product state was *directly* identified. Thereafter, using the same technique, Cavalleri et al. proposed that such time-resolved measurements could distinguish whether the dynamics was due to a Peierls or Mott mechanism. They argued that by varying the pulse duration and tracking the $VO_2$ response, this could result in two scenarios, namely: if the response is prompt and follows the laser pulse, this would demonstrate the electronic character while if the response was limited to a certain timescale, this would mean that the structural phase transition alone dictates the insulating ground state and that the ultrafast PT was set by atomic motion. Figure 1.30 demonstrates that the latter scenario was favored and a structural bottleneck of ~ 75 fs was found, corresponding to half cycle of a V-V oscillation.

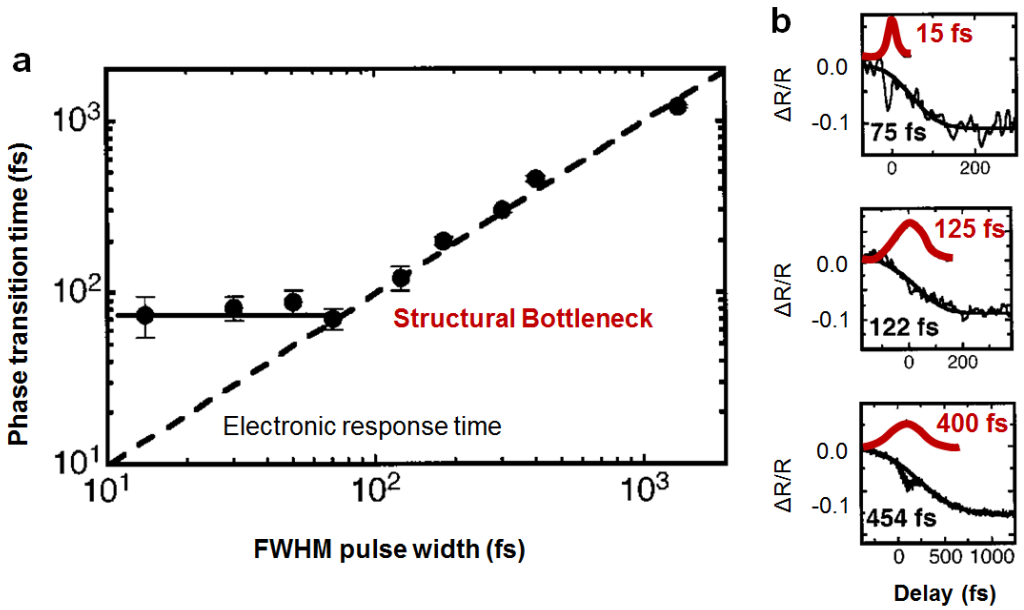


**Figure 1.36: Evidence for $VO_2$ Ultrafast PT Dictated by Structural Transformation.** **(a)** Phase transition rise time as a function of the duration of the exciting pulse. **(b)** Few examples of pump-probe reflectivity experiments of the photoinduced PT. From reference [219].

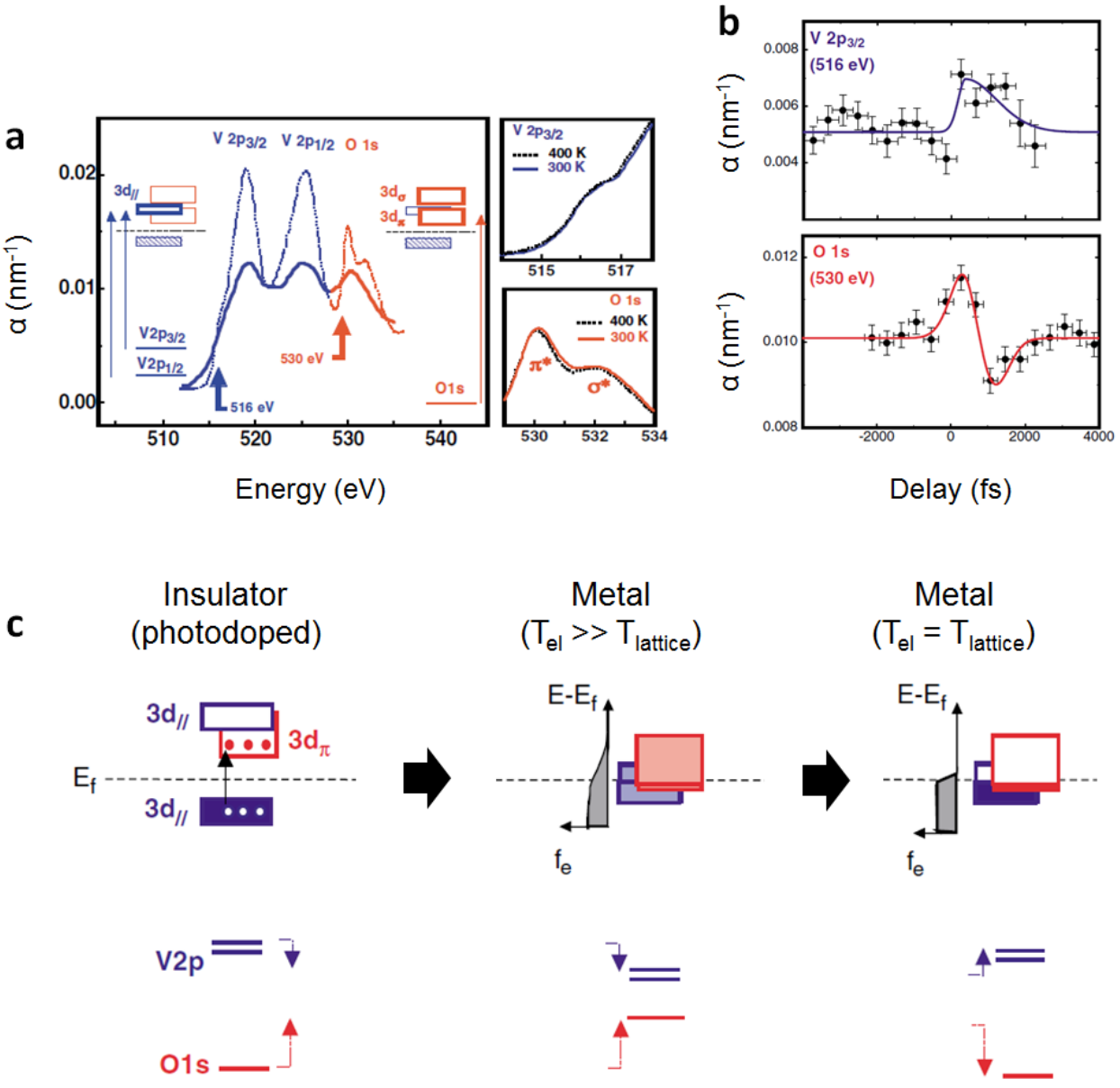


**Figure 1.37: Ultrafast Selective X-Ray Absorption Measurements. (a)** Static soft x-ray transmission absorption measurement of free-standing $VO_2$ film at the V*2p* and O*1s* absorption resonances. **(b)** Femtosecond x-ray absorption measurements at the 516 eV and 530 eV resonances. Vertical error bars represent one standard deviation of the photon counting distribution. Horizontal error bars reflect the long-term drift in the delay between laser pump and x-ray probe pulses measured via cross correlation with visible femtosecond synchrotron pulses. Solid lines are guides to the eye. **(c)** Schematics of the

photoinduced rearrangement of the electronic population between the $3d_{//}$ valence band and the mixed $3d_{\pi}$ orbitals. This results in band gap collapse and the creation of a non-equilibrium electron distribution, increasing (decreasing) the V*2p* (O*1s*) binding energies due to transient charge transfer from the $V^{4+}$ anions to $O^{2-}$ anions. These transient core-level shifts reestablish the valency of the equilibrium metal as the hot electron distribution thermalizes.

With the discovery of this structural bottleneck in $VO_2$ ultrafast PT, understanding the details of the electronic dynamics (electron-orbital modifications) and consequent coupling to the lattice was the next logical step. As pointed out by Cavalleri, beyond identifying the resultant metallic phase, the dynamics of complex electronic structure cannot be fully understood by visible-IR spectroscopy alone. This is due to the fact that at these wavelengths, the response is extremely sensitive to the joint density of band gap states and the collective response of the electronic plasma (at nearly 1 eV). Thus, a novel time-resolved technique to probe the variously hybridized valence states of $VO_2$ had to be developed. Ultrafast x-ray absorption spectroscopy, developed by the Schoenlein group at the Lawrence Berkeley National Laboratory, provided the selective method to probe such local electronic, magnetic and short range atomic structures with elemental specificity. Thus, by tuning the x-ray to specific resonances of the $VO_2$ system (via dipole selection rules: V$3d_{//}$ from the V*2p* (= 516 eV) and the V$3d_{\pi}$ (mixing of the V*3d* and O*2p* orbitals) from the O*1s* (= 530 eV))[220], as shown in figure 1.31, they provided an explanation for the transient shifts in core-level orbitals, along with the importance of hole doping as a key ingredient to modifying orbital coupling[221]. The sensitivity of the phase transition to hole doping has been demonstrated both experimentally in device type geometries[179,222] and

theoretically by extending the Brinkman-Rice picture, but taking into account inhomogeneity of the system[223,224]. Furthermore, the idea of hole photodoping driving the IMT is reinforced by the fact that as opposed to the bulk crystal that can only undergo phase transition with optical pulses at or above the band gap energy (0.67 eV), thin films can be switched by photon energies below the band gap, extending to 0.18 eV. This is made possible due to the presence of defect states in the middle of the gap that mediate the formation of holes[225].

Since the bottleneck (corresponding to half the V-V oscillation period) is too fast to be attributed to lattice heating effects as electronic excitation is largely decoupled from the lattice during these sub-100 fs, the most likely explanation for the collapse of the band gap is that the atomic structure vibrates coherently and is brought about by optical phonons. Such explanation is supported by the fact that Raman responses of $VO_2$ show that direct optical excitation couples with the Raman-active Ag modes (*totally symmetric*) that map the insulating state onto the metallic one[218]. More precisely, the M1 phase can be mapped onto the R phase by two normal vibrational modes of the V atoms located at the Γ–point as a result of the Brillouin zone folding in the monoclinic phase[226,227], corresponding to a tilting and a stretching mode. It was subsequently demonstrated by Kübler *et al.*[228] and Kim *et al.*[229] separately that the coherent phonon modes can be an excellent marker of the phase transition, revealing dynamics of the V-V dimer oscillations and the possible presence of a transient *monoclinic correlated metal* (MCM) respectively. Further analysis of Kübler's work resulted in the observation of a non-linear coherently driven atomic oscillations twice that of the originally found 6.1 THz phonon frequency[109]. The proposed scheme -

developed using the Biermann cluster dynamical mean-field theory framework for $VO_2$[230] (molecular solid of V dimers embedded in an O-octahedra matrix) – suggests that the removal of an electron from the V-V dimer lead to a destabilization of the dimer and a local oscillation. Using pump pulses of 12 fs and a full 2D ultrabroadband THz probe (both phase and amplitude resolved) with a time resolution of 40 fs[231,232], the multiple participating degrees of freedom in the form of these coherent phonon oscillations were directly observed and were found to last for a few picoseconds only, as shown in figure 1.32 and 1.33. We note however that such oscillations could potentially last for longer times, as revealed by direct time-resolved measurement of the structural phase transition (unit cell vibration monitored by x-ray)[233,234], suggesting that the optical probe monitored loss of phononic coherence rather than the disappearance of these modes due to thermalization. As Cavalleri *et al.* pointed out, such a system may exhibit residual vibrational coherence even in the product phase, but can become invisible to optical probing due to a change of symmetry that renormalizes the relevant vibration to the edge of the Brillouin zone[218].

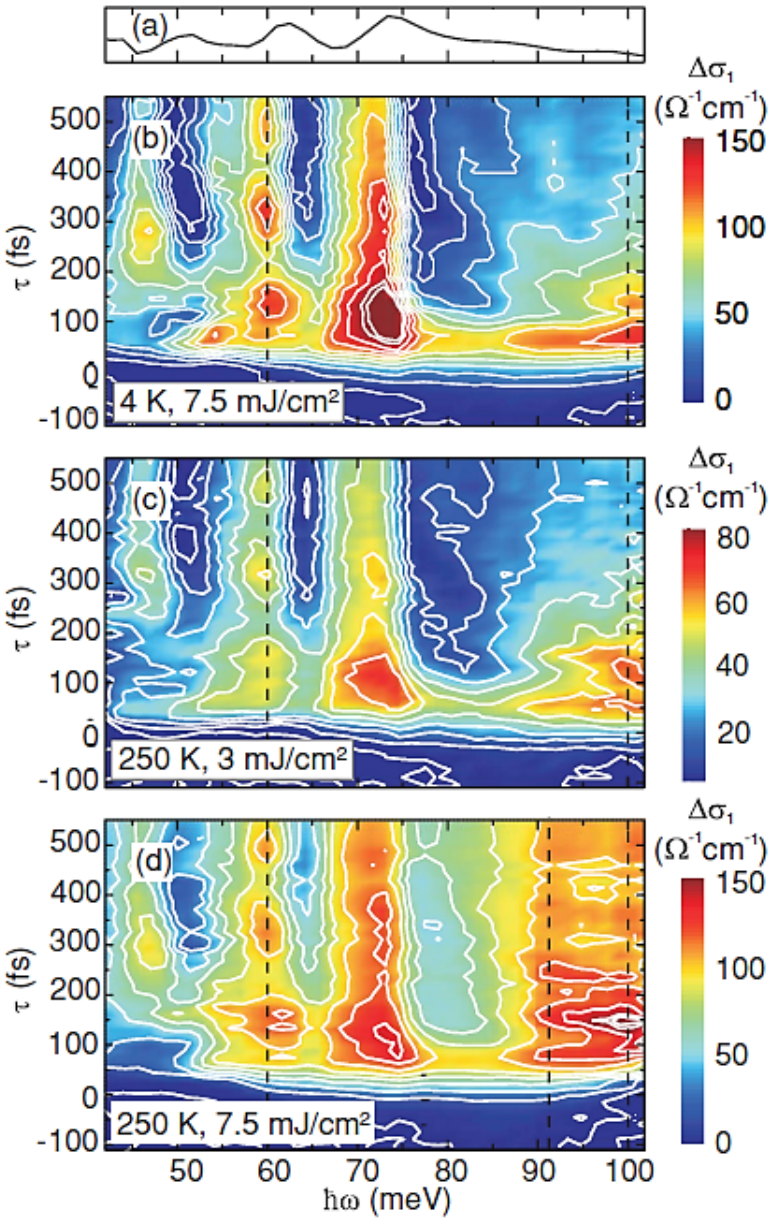


**Figure 1.38: 2D Optical Pump/Multi-THz Probe. (a)** Equilibrium conductivity of insulating $VO_2$. Color plots of the pump-induced changes of the conductivity: **(b)** at T = 4 K and an incident fluence of 7.5 mJ/cm$^2$; **(c)** at T = 250 K and pump fluence of 3 mJ/cm$^2$; **(d)** at T = 250 K and pump fluence of 7.5 mJ/cm$^2$. The broken vertical lines indicate the frequency positions of cross sections that will be used for figure 1.33.

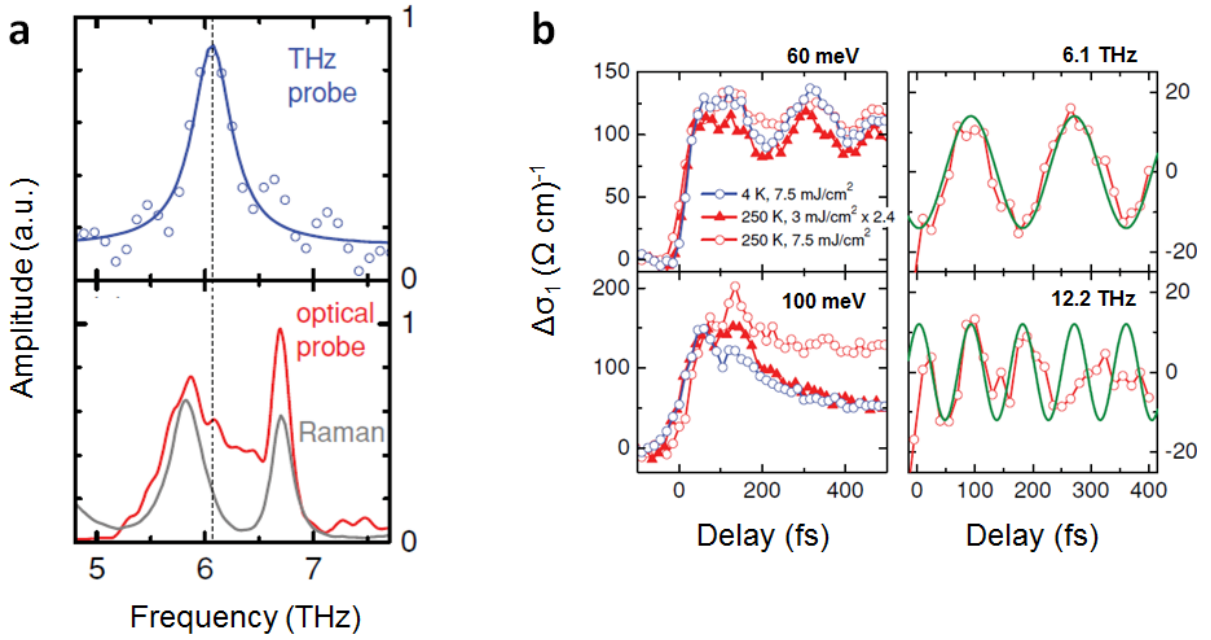


**Figure 1.39: Decay Dynamics of Optical Pump/THz-Probe Data. (a)** Spectrum of the oscillatory component and fit by a Lorentzian function (blue line). The spectrum of the oscillatory modulation observed in degenerate pump-probe experiment of [219] at 1.55 eV (red line) and the unpolarized spontaneous Raman spectrum[235](gray line). **(b)** Cross sections of figure 1.32 along the time axis for photon energies of 60 meV and 100 meV (left), along with the oscillating components of the cross sections through the 2D scans (right). Green solid lines are fit of the oscillating component by a cosine function with frequency of 6.1 THz (top) and at a doubled frequency of 12.2 THz (bottom).

This idea of a strong structural component of the phase transition mechanism has very recently (2012) been emphasized by Cocker *et al.* who described a critical-threshold model not only based on the critical density of electrons but also a critical density of coherently excited phonons, melting the Mott state while breaking the Peierls distortion respectively. Moreover, by providing the first phase diagram of the ultrafast photoinduced

IMT, a region of transient intermediate metallic state (metallic M1) was found at low temperatures (< 200 K), as shown in figure 1.34[236].

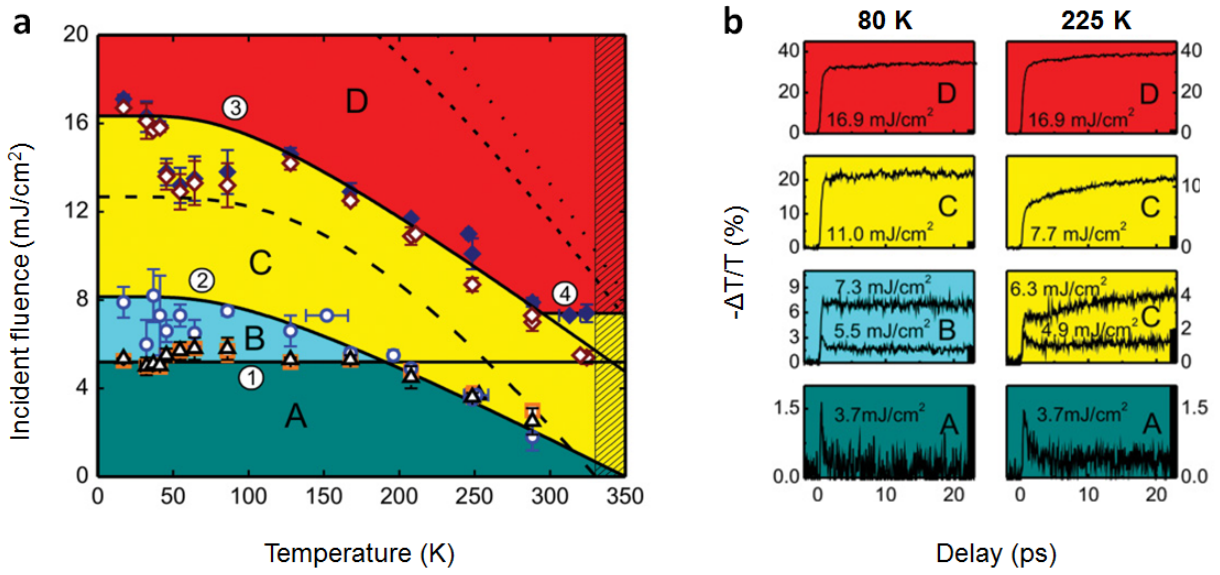


**Figure 1.40: Ultrafast Phase Diagram of $VO_2$. (a)** Phase diagram of the ultrafast IMT in $VO_2$. Regions A, B, C, and D depict the four characteristic conductivity dynamics. Line 1 corresponds to the incident pump fluence required to excite electron densities that correspond to the metallic state, while line 2 is the incident fluence that raises the front surface 6 THz phonon population to the critical density. Line 3 shows the incident fluence necessary for the 6 THz phonon modes to reach critical density and supply the latent heat for the structural transition at the back surface of the film. Finally, line 4 marks the incident fluence that corresponds to directly exciting the critical electron density at the back surface of the $VO_2$ film. Orange squares and black triangles represent the thresholds for metallic formation 5 ps and 25 ps after the pump pulse, respectively. Blue circles indicate thresholds for the onset of slow-rise dynamics. Filled navy blue diamonds in (a) show the ability to reach a fully metallic state ($-\Delta T/T \geq 33.5\%$) 5 ps following the excitation, while hollow brown diamonds indicate the fully metallic state is formed at 25 ps. Region A thus represents the insulating state while region C represents the photoinduced nucleation and growth of the metallic state. Region D represents the ultrafast (< 0.5 ps) photoinduced nucleation of the full metallic state throughout the film. Finally, region B shows the newly-

defined intermediate metallic state as described by Cocker *et al.* Moreover, the hatched pattern denotes the steady-state IMT region. **(b)** Vertical cuts of the phase diagram at 80 K and 225 K highlighting the THz conductivity dynamics of the VO2 film. The figure has been taken from reference [236].

The ability for $VO_2$ to switch at such ultrafast speeds while being operational at room-temperature has generated few novel applications such as potentially incorporating nanoparticles into optical fibers (at telecommunication wavelengths and with pulse energies as low as 250 $\mu J/cm^2$ for above band gap excitation[225]) as shown by Rini *et al*[237]. or use in thin-film form to probe and measure ultrafast pulses at the desired location, as demonstrated by Cilento *et al.*[145]. Recently, it has also been verified by Wegkamp *et al.* that broadband pulses of a record of about 10 fs in duration– generated by focusing pulses from an amplified Ti:Sapphire laser onto a YAG crystal – could be probed and consequently phase-corrected for the purpose of ultrafast pump-probe experiments. Some of these experimental results are highlighted in figure 1.35[238].

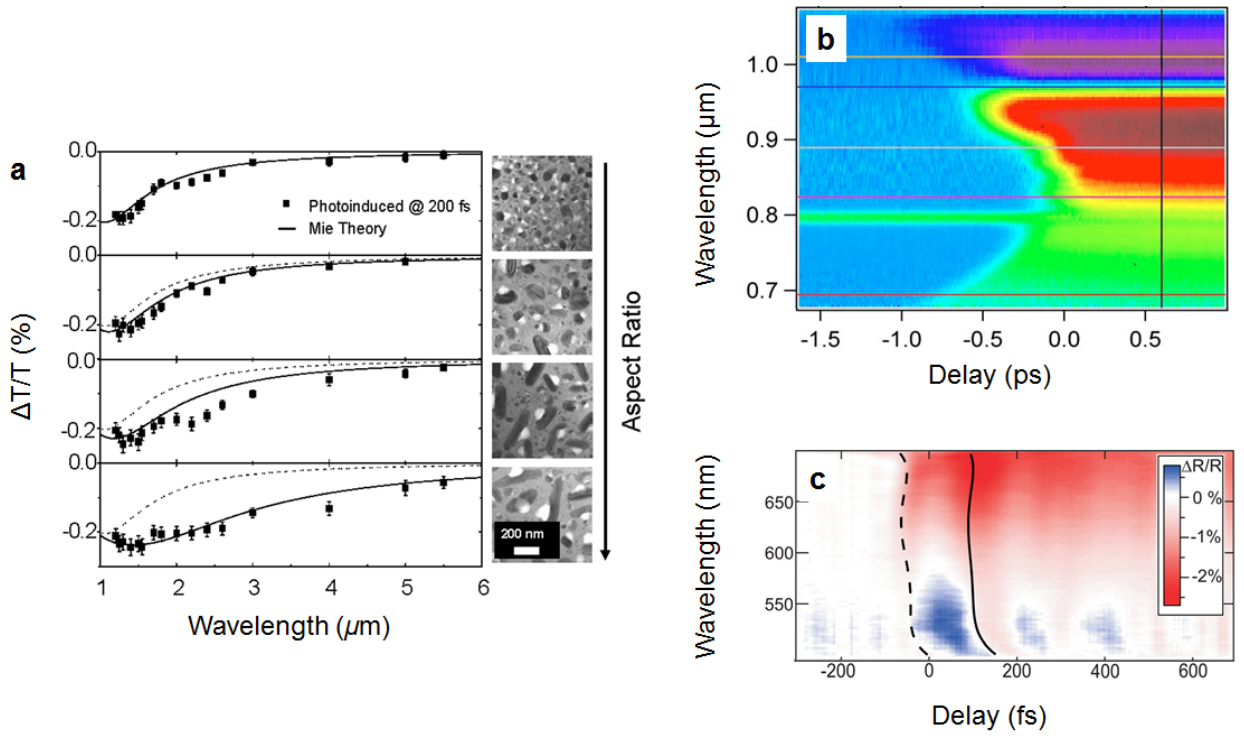


**Figure 1.41: Novel Ultrafast Applications of $VO_2$.** **(a)** Ultrafast switching of the intrinsic surface plasmon response of $VO_2$ nanoparticles with varying aspect ratio[237]. Thin film of $VO_2$ used **(b)** as an ultrafast broadband spectrograph[145] and **(c)** for phase-correction in ultrashort broadband probe pulses of ~ 10 fs in duration[238].

# CHAPTER 2

# PLASMONICS AT SINGLE NANOANTENNA LEVEL: THE $VO_2$ "WHISPERER"

"God runs electromagnetics by wave theory on Monday, Wednesday, and Friday,
and the Devil runs them by quantum theory on Tuesday, Thursday, and Saturday."
~ *William H. Bragg, 1915 Nobel Laureate*

## 2.1 INTRODUCTION

This chapter introduces the idea of hybrid nanostructures by combining a plasmonic nanostructure with PCM vanadium dioxide that undergoes a solid-solid phase transformation (*§1.3.1*). Although the ability to modulate the plasmonic response of a nanostructure using $VO_2$ has been demonstrated previously[239-241], we show experimentally for the first time that such large spectral shift can be achieved and detected at the single nanostructure level.

More importantly, we emphasize that the plasmonic nanostructure acts as a nanoscale antenna, probing its near-field nanoenvironment (for e.g. changes in the dielectric properties and interfacial effects such as grain boundaries). This is possible due to localized surface plasmons that can efficiently mediate electromagnetic energy transfer between the near- and far-field, thus registering information similar as an antenna but with much higher operating frequencies. Here we demonstrate that thermally controlled plasmon resonance modulation of a single gold nanoparticle on a $VO_2$ thin film by performing single-particle dark-field spectroscopy measurement during its phase

transformation process. The plasmon resonance of the nanoparticle significantly blue shifts when the $VO_2$ undergoes its characteristic IMT around 67$^{o}$C because of its drastic change in dielectric properties (figure 2.1). The nature of this near-field nanoantenna allows probing of the statistically and spatially varying domains (insulating, metallic and potential intermediate states). Consequently, monitoring the shift in the gold plasmon resonance shows a clear gradual "plasmonic" hysteresis that mimics the behavior of the underlying $VO_2$. Interestingly, plotting the scattering intensity at specific wavelengths of the Au nanostructure not only reveals the same hysteretic behavior but also displays a curious overshoot before (after) the insulator-metal (metal-insulator) PT of $VO_2$. Since this correspond to regions of the $VO_2$ phase diagram that are closely linked to strong correlation[129], this suggests the ability for plasmonic nanoantennas to probe effect associated with electron-electron correlations.

Furthermore, since in the present case modulation/detection was achieved at the single nanoparticle level, this chapter implies several technological implications such as the possibility of creating enhanced catalytic nanosensors and color nanosorters[242] that could be envisioned to operate as a single unit that is deep subwavelength in size.

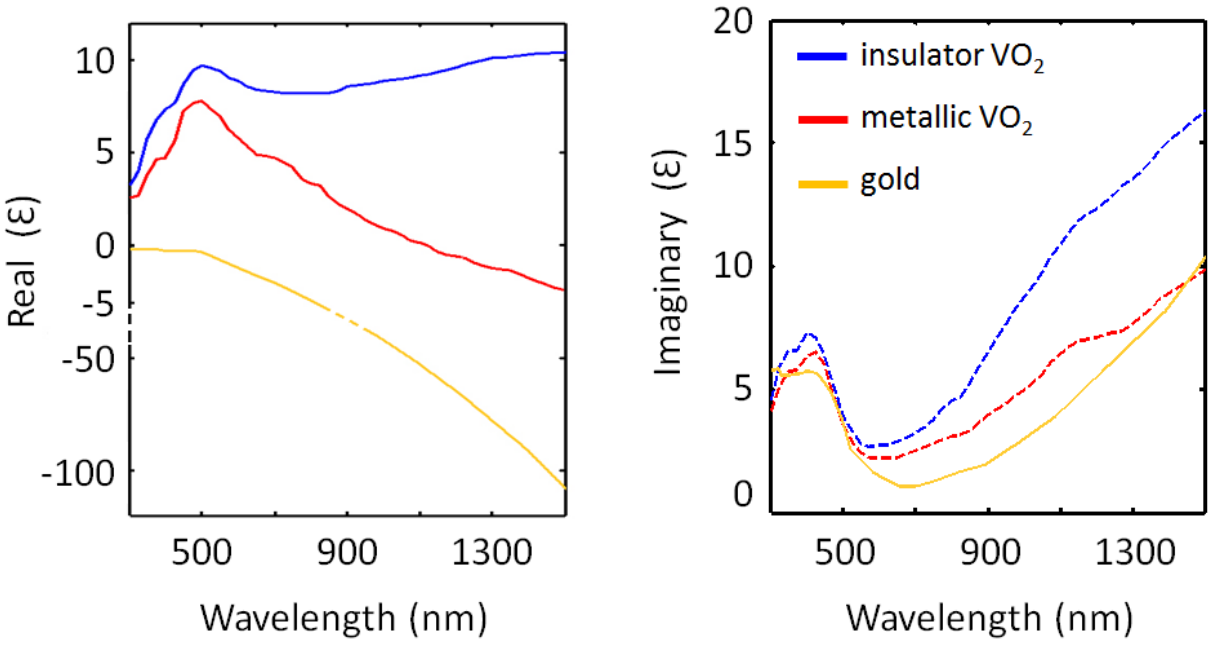


**Figure 2.1: Dielectric Properties of Gold and Vanadium Dioxide.** Real and imaginary part of the permittivity for gold (yellow) and insulating (blue) and metallic (red) $VO_2$ in the visible-NIR. The data has been extracted from references [114] and [243].

## 2.2 EXPERIMENTS AND DISCUSSION OF RESULTS

### 2.2.1 Sample Fabrication

A thin film of $VO_2$ with nominal thickness of 110 nm was fabricated on a thin (0.5 mm) glass substrate. A vanadium target was ablated using a pulsed laser deposition system (laser $\lambda$ = 248 nm, 25 ns pulse duration, ~ 3.9 mJ/cm$^2$ fluence and 10 Hz repetition rate) in an oxygen environment (10 mTorr), as shown in figure 2.2. The target-substrate distance was about 10 cm[167]. Subsequent annealing of the sample in 250 mTorr of oxygen rendered the film both crystalline, stoichiometric and switching. Following $VO_2$ thin film fabrication,

commercially purchased Au colloids of 100 nm diameter in deionized water were spin coated on the prepared film.

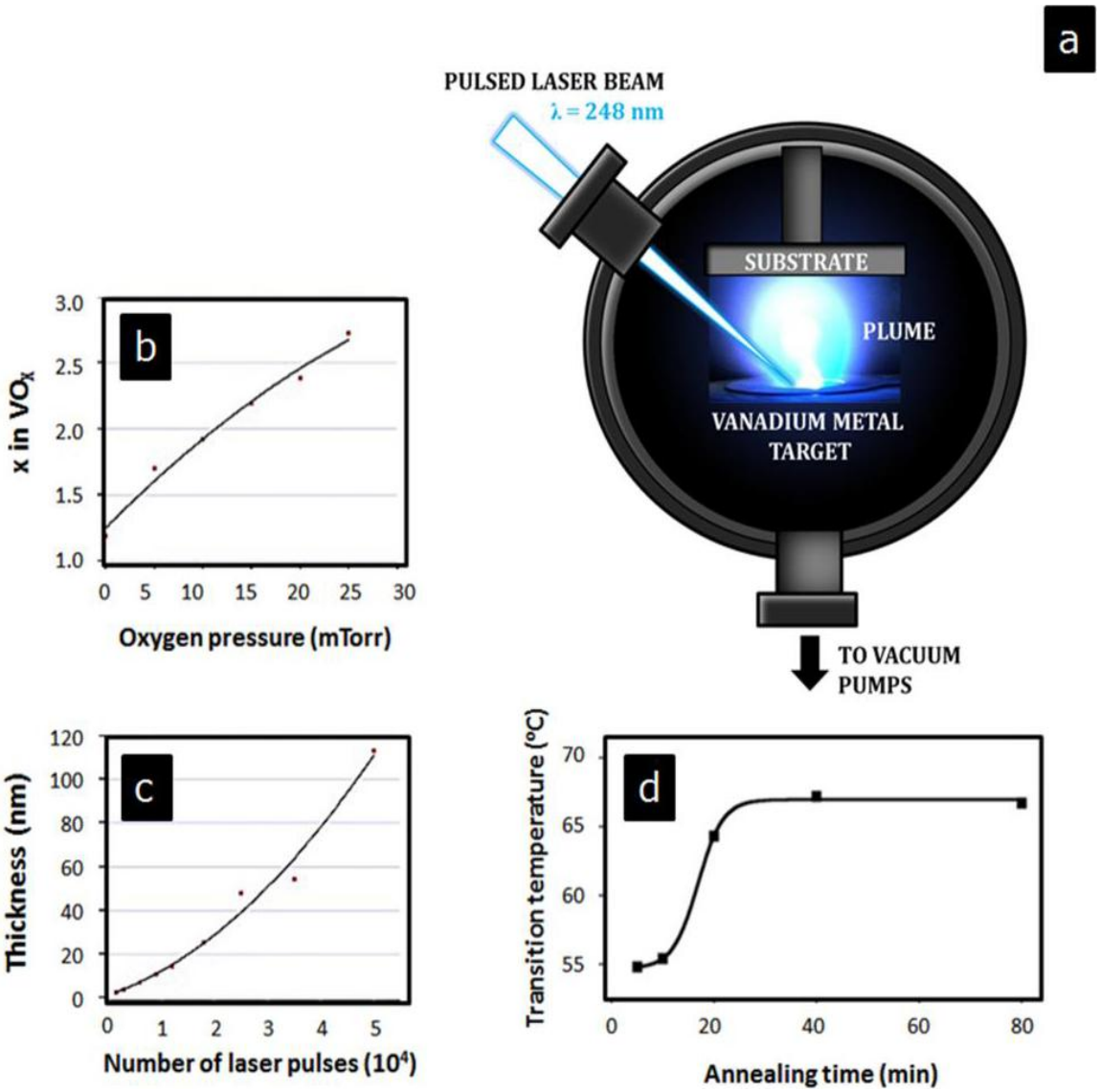


**Figure 2.2: Pulsed Laser Deposition of $VO_2$ Thin Film. (a)** Schematics of the PLD system. Depositions conditions such as **(b)** oxygen pressure, **(c)** number of laser pulses and **(c)** annealing time to render the $VO_2$ thin film crystalline, stoichiometric and switching. The data was extracted from reference [153]. The plume in the PLD schematics is an actual snapshot taken during the ablation process (courtesy of Dr. D. Ferrara).

### 2.2.2 Single Particle Spectroscopy

Single particle spectroscopy is used to characterize the optical properties of the Au colloid. The dark field configuration is operated in a spectroscopic setup as depicted in figure 2.3. In this dark field configuration, the sample is illuminated by a halogen bulb (100 W) with the light being shone at a high angle (> $60^{o}$) via a dark field condenser (Olympus LMPLFLN 100x BD, 0.8 NA)[244]. Here, only the light scattered in the focal plane is coupled to the detection path. A Peltier element[245] mounted on the sample stage was used for either heating or cooling the $VO_2$ film, which enables measurement of the Au particle plasmon resonance at different temperatures, thus mapping a hysteretic behavior.

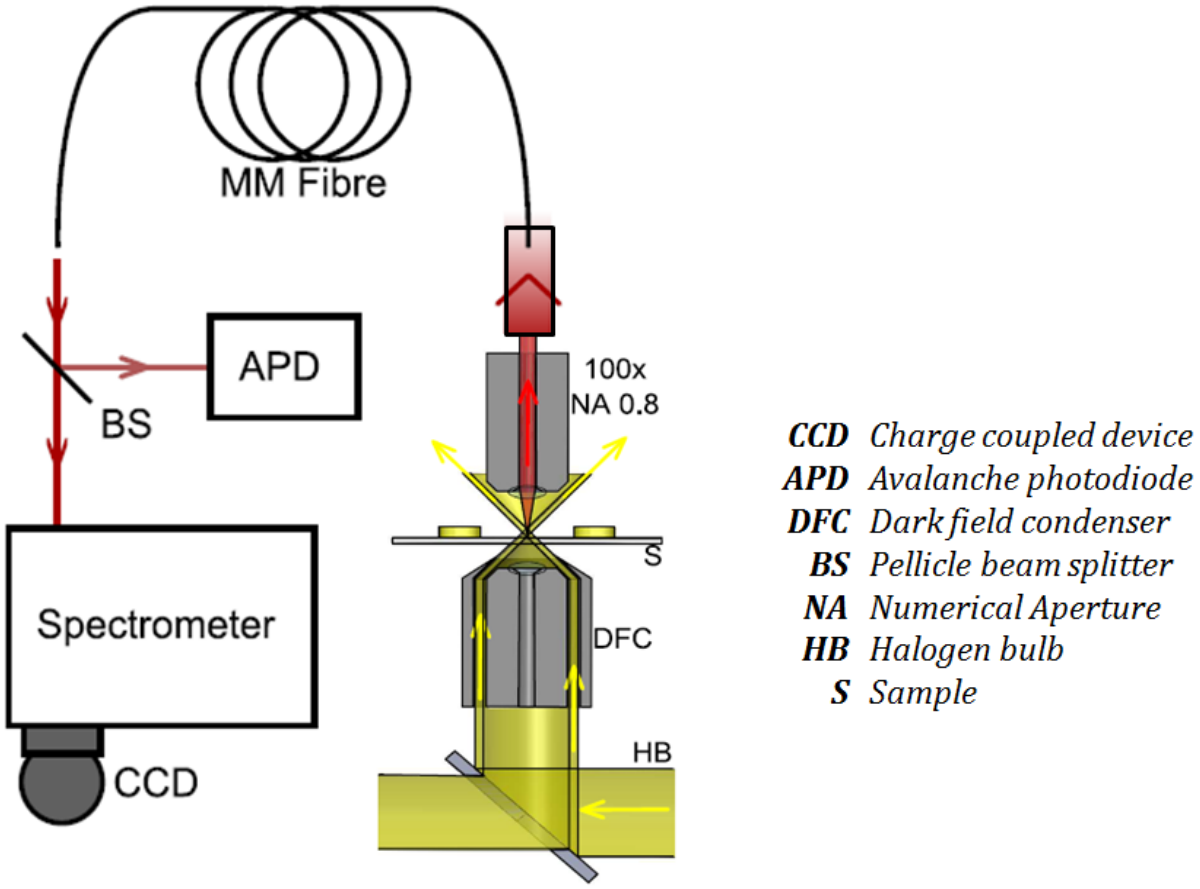


**Figure 2.3: Single-Particle Spectroscopy Setup.** Experimental setup of single particle dark field microscopy. Adapted from [246].

### 2.2.3 Hysteresis: Transmission *vs.* Plasmonic

From the above setup, the scattering spectra for a single Au colloid on the $VO_2$ thin film can be collected. Figure 2.4 shows the spectra when the film is in its metallic (red) and insulating (black) state, i.e. below (= 35°C) above (= 90°C) the transition temperature of ~ 67°C. From figure 2.4, it is clear that the plasmon resonance of the Au nanoparticle exhibits a blueshift up to 30 nm when increasing the temperature from 35 °C to 90 °C. As the $VO_2$

progresses through the phase transition, the gold nanoparticle experiences a change in its local dielectric environment, thereby causing the plasmon resonance to shift its peak position. This can be understood by a resulting change in the polarizability of the plasmonic material as its near field environment would undergo a change in its dielectric permittivity (*eqn 1.3*). More precisely, the dipole resonance condition for the Au colloid requires that the real part of the denominator in eqn 1.3 to vanish. Thus, the Au LSPR occurs in the near-IR region of the spectrum because the real part of the Au permittivity becomes negative enough to cancel out the $VO_2$ counterpart (the medium when insulating) that has values ranging between 8 and 10 at visible to near-IR wavelengths (figure 2.1). However , in the metallic state of $VO_2$, the real part of the permittivity is considerably lower than that in the insulating state, implying a less negative Au permittivity for the satisfying the resonance condition. Hence, the LSPR peak should appear at shorter wavelengths when the surrounding $VO_2$ becomes metallic. This means a blue-shift in the resonance.

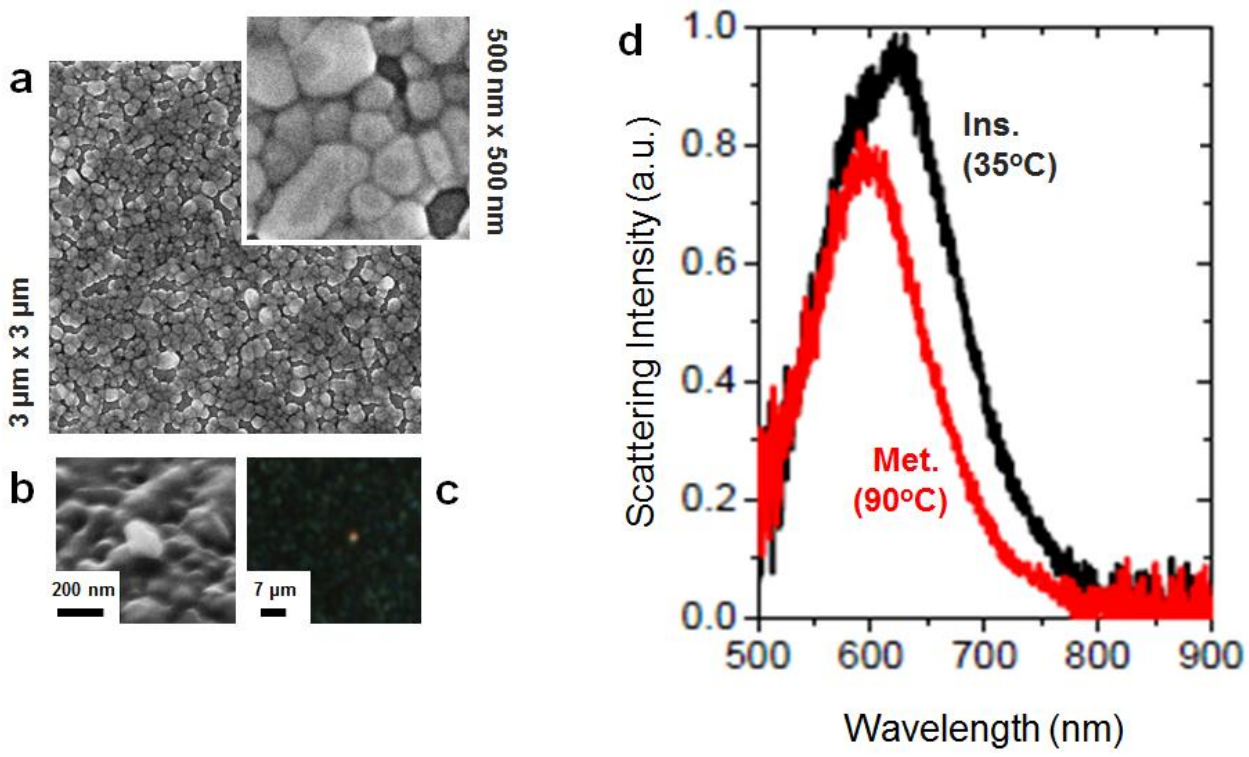


**Figure 2.4: Characterization of Hybrid Au Colloid/$VO_2$ Film. (a)** SEM of the $VO_2$ thin film used showing the grain structure. **(b)** SEM of single Au colloid on the corresponding film. **(c)** True color dark field image. **(d)** Spectra of scattered light from the gold colloid when the $VO_2$ is metallic (red) and insulating (black), depicting the blue shift.

Compared to the scattering spectrum at low temperature, there are two distinct features appearing in the high-temperature spectrum. First, the spectral linewidth at high temperature is narrower than that at low temperature, which is due to the substrate effect on the nanoparticle scattering spectra. This can be understood from the fact that the real part of the complex dielectric constant of the $VO_2$ film is smaller in its metallic phase than its insulating phase. Second, the scattering intensity at all wavelengths above 630 nm is lower at high temperature than low temperature. To gain deeper insights into the Au

plasmon resonance modulation, we measured the scattering spectra for an individual Au colloid when heating and cooling the $VO_2$ film at temperature intervals of 5 °C. By extracting the resonant wavelength from each spectrum, we were able to map the hysteresis curve of the Au plasmon resonance as a function of the external temperature, as shown in figure 2.5b. Moreover, we also carried out far-field transmission hysteresis measurement of the bare $VO_2$ film using an InGaAs photodetector. The integrated transmission intensity is plotted in figure 2.5a and shows the characteristic hysteretic response, indicating the temperature-dependent $VO_2$ dielectric functions. By comparing the two figures, one can clearly see that the hysteresis curve of Au plasmon resonance follows the transmission hysteresis of the $VO_2$ film closely.

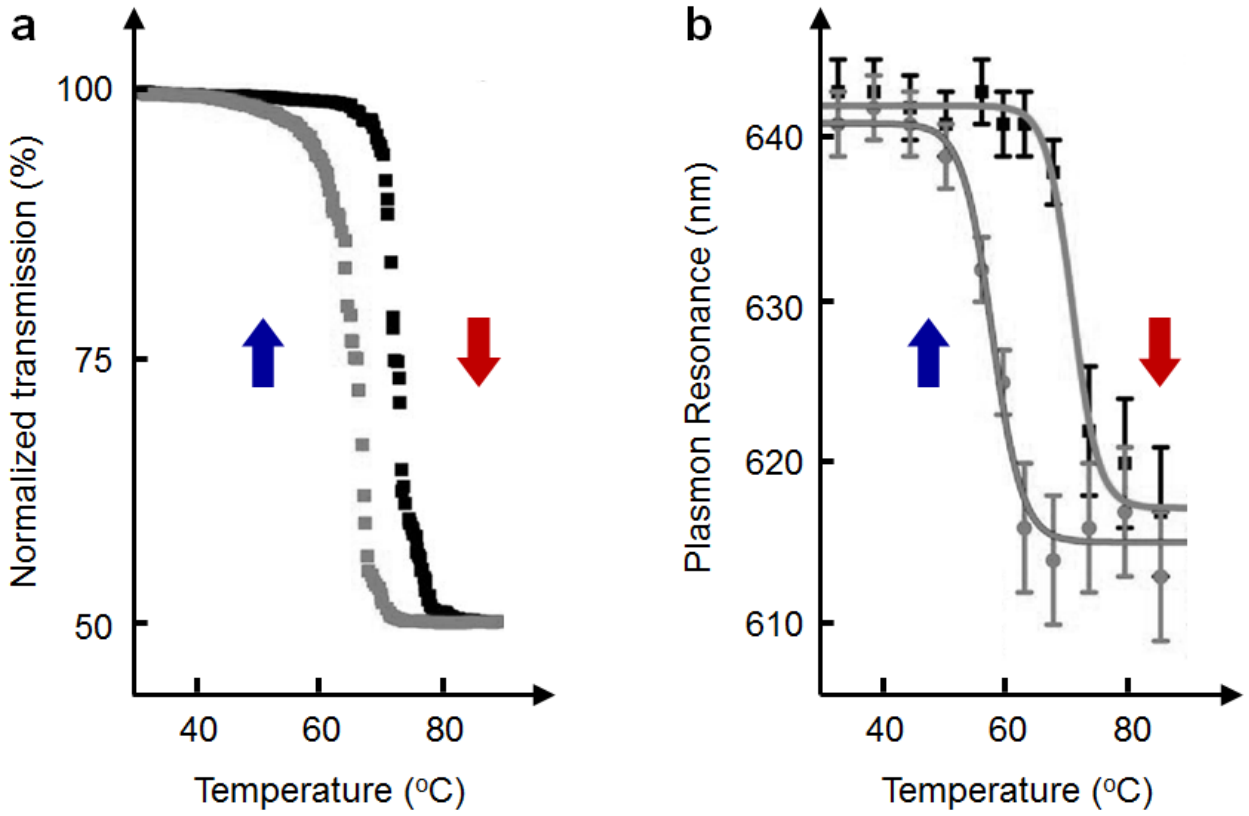


**Figure 2.5: Transmission Hysteresis vs. Plasmonic Hysteresis. (a)** Phase transition monitored by integrated white-light transmission of the thermally modulated 110 nm $VO_2$ film. **(b)** Phase transition of the same film monitored by plasmon resonance shift in a single gold nanoparticle. Red and blue arrows represent heating and cooling respectively.

At first glance, the hysteresis width in the transmission of $VO_2$ appears rather smaller than that in the plasmon resonance of the Au nanoparticle. However, one should not directly compare these two curves. The transmission from the bare $VO_2$ film was integrated by the photodetector over the wavelength range of the white-light probe, while the plasmon resonance of Au nanoparticle varies over a much smaller wavelength range from 600 to 630 nm. The dielectric function of the $VO_2$ film shows a strong dependence on

wavelength over the range included in the white-light spectrum[247]. More importantly, the transmission spectrum of the film was measured over a large area of the $VO_2$ film, while the Au nanoparticle plasmon resonance is governed only by the local change of the $VO_2$ dielectric response and is thus sensitive only to changes in the $VO_2$ film occurring within roughly the plasmon field decay length of order ~10–20 nm[248]. This highly localized response of the Au particle plasmon resonance to the change in its surrounding dielectric environment renders the nanoparticle a sensitive probe of the size effects in the metal–insulator phase transition of $VO_2$ nanoparticles in the proximity of Au particles. Therefore, while the white-light probe beam (transmission measurement) was interrogating a ~ 100 um diameter spot size, the plasmonic hysteresis represents the measurement of only a few $VO_2$ grains. Thus, the wider hysteresis width could potentially be due to a smaller volume of probed $VO_2$, corresponding to a smaller number of nucleation sites that can seed the PT in these domains (*§1.3.2c*).

### 2.2.4 Simulating the hybrid Au colloid/$VO_2$ thin film optical response

In order to understand the response of our hybrid system in greater details, we carry FDTD simulations using Lumerical Solutions package. In the first case, we simulate a gold colloid of diameter 100 nm that sits on the 110 nm of the $VO_2$ film. As shown in figure 2.6. the spectra shows similar response to the experimental one, with a blue shift when the film metallizes and a slightly narrower linewidth when metallic. However, we also note that both the spectral shift and the resonance position do not match exactly with the experimental ones. This is due to the fact that the gold colloid is in greater contact with the

film, due to the granular structure of our film. In order to confirm this hypothesis, FDTD simulations were performed for a gold colloid situated into the $VO_2$, as shown in figure 2.6. From these results, we see that indeed both the resonance position and the spectral shift agrees with the experimental one when such contact effect is accounted. This therefore shows that the gold is indeed interacting with few domains of the $VO_2$ and hence probes the near-field environment.

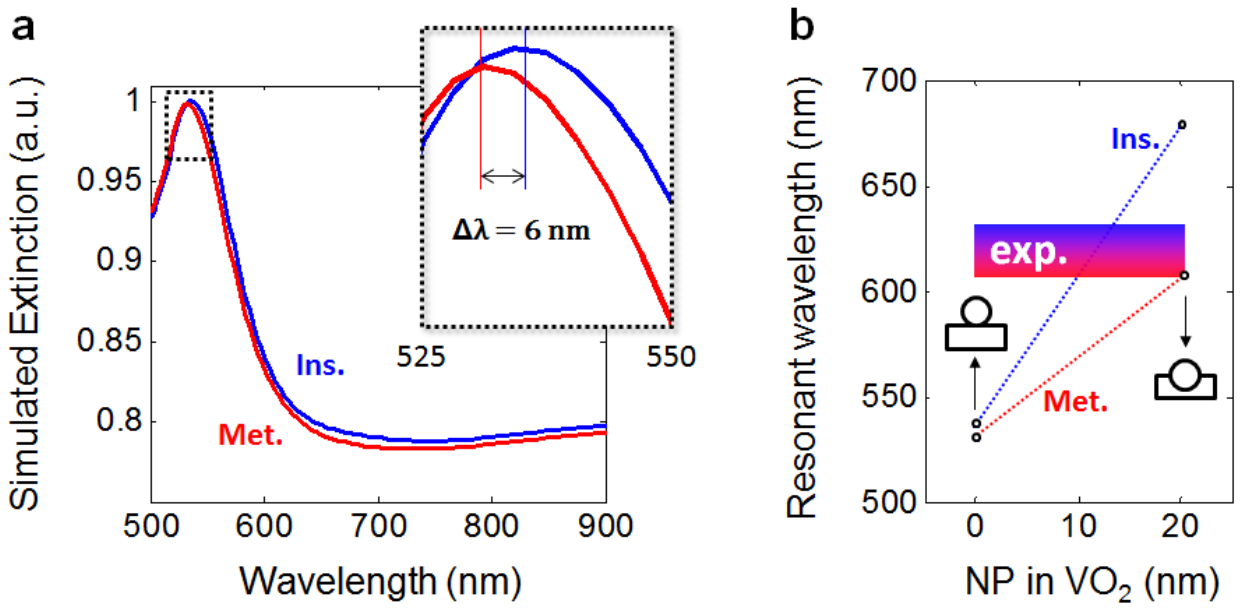


**Figure 2.6: Simulated Spectra of Hybrid Au Colloid/$VO_2$ Thin film. (a)** Simulated response of the gold nanoparticle with the gold colloid on the metallic (red) and insulating (blue) $VO_2$ film. The inset shows that the shift in resonance is only 6 nm (~ 30 nm experimentally). **(b)** Resonance position of the gold colloid when displaced from the top surface of the film (0 nm) to 20 nm deep into the $VO_2$. The experimental spectral shift is also overlaid (insulating blue to metallic red rectangle), confirming that the gold colloid is indeed not resting on the top surface but interacts more directly with the $VO_2$, due to the film grain structure.

### 2.2.5 Enhanced Scattering: The "Overshoot" Effect

Now we turn to the aforementioned finding that the scattering intensity of the Au particle at wavelengths above 630 nm is larger in the insulating phase of $VO_2$ than its metallic phase. To have a thorough understanding of this difference, we have plotted the temperature evolution of the scattering intensity at arbitrary wavelengths (640 nm, 700 nm and 740 nm) in figure 2.7. Note that we have excluded the average scattering contribution from $VO_2$ itself by subtracting the scattered signal of the bare $VO_2$ area in close proximity to the Au nanoparticle for each dark-field spectrum. A peculiar behavior is now observable for increasing wavelength: the scattering intensity exhibits a broad hysteresis loop with an overshoot emerging before the onset of the insulator–metal (heating) transition and after the completion of metal–insulator (cooling) transition of the $VO_2$ film. The overshoot is not a spike but exhibits a relatively symmetric shape and thus appears as "rabbit ears" superimposed on the hysteresis, as described in Lopez *et al.* work[111]. During the heating cycle, the scattering intensity shows a maximum at $T_c$ around 67 °C. During the cooling cycle, on the other hand, the maximum intensity occurs at a much lower temperature. A similar feature has previously been observed in a dark-field scattering measurement of $VO_2$ nanoparticle arrays[111]. However, in that case, the increased scattering intensity in the vicinity of the transformation from insulator to metal and back again was shown to be due to incoherent scattering from the nanoparticle arrays, because all the particles do not transform at a unique $T_c$ but instead have a probability of switching in a range of temperatures around $T_c$. In other words, at a certain temperature around $T_c$, all nanoparticles form a mixture of insulating and metallic phases and due to this order-

disorder-order phase transition, maximum incoherence occurred at about the mid-point of the PT. Adapting this idea to the present case, we note that the grain size of the $VO_2$ film (with characteristic domain sizes of approximately 70 ± 10 nm) is of the same order as the $VO_2$ nanoparticle dimensions in reference[111]. Thus, the Au nanoparticle potentially registers an average response of the statistical mixture of insulating and metallic grains of $VO_2$ within the short range of its plasmonic field, thereby leading to the strongest scattering at a temperature different from the critical temperature.

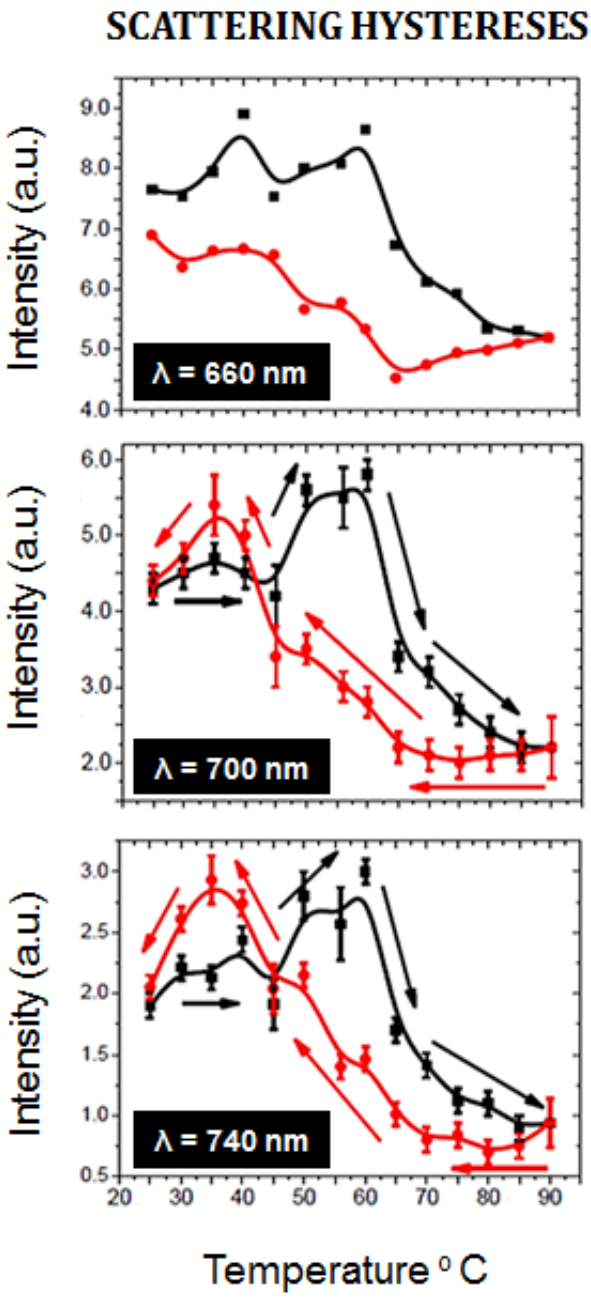


**Figure 2.7: Scattering Hysteresis at Varying Wavelengths.** The pronounced scattering effect at the onsets of the phase transition (heating and cooling) becomes more apparent at longer wavelengths due to a decreasing effect of the gold scattering as we move away from its resonance (~ 617-642 nm).

## 2.3 CONCLUSIONS

The appearance of these maxima in the hysteresis curves highlights the extremely localized character of our plasmonic probe when monitoring the PT. Although FDTD simulations can reproduce the spectral shift, with an agreement in the linewidth as well, these simulations cannot reproduce this enhanced scattering phenomena observed at the onsets of the phase transformation. This could be due to two things. First, the difficulty in simulating such phenomena could potentially arise due to the simplification of $\varepsilon(\boldsymbol{K} = 0, \omega) = \varepsilon(\omega)$ where the spatially local response has been averaged[249]. Although this simplification is valid for wavelength in the material that is significantly longer than all characteristic dimensions such as the size of the unit cell or the mean free path of the electrons, this might not be the case in $VO_2$, which is plague by grain boundaries and varying nanocrystals domain orientation. Second, this potentially suggests that these enhanced scattering effects could be associated to probing the strongly correlated nature of the $VO_2$, as has been observed previously in such $VO_2$ thin-film system (*§1.3.2b*) [129]. Similar to processes such as surface-enhanced Raman scattering (SERS) or emission enhancement, the plasmonic nanoparticle could potentially enhanced the $\text{electron}_{Au}$-$\text{electron}_{VO2}$ interaction as it undergoes the phase-transition. Such effect therefore cannot be accounted in the simulations. Consequently, further experimental and theoretical investigations will be required to gain a deeper understanding of this mechanism.

Nevertheless, we have shown that modulation at the single nanoparticle can clearly be achieved and that such single-particle plasmon resonance spectronanoscopy has the potential to probe the interfacial or domain-boundary scattering owing to the high

sensitivity of the scattered light to the environment. Our results show that the plasmon resonance has a reversible hysteresis that closely follows the transmission hysteresis of the underlying $VO_2$ film and therefore plasmonic memristors could potentially be demonstrated, underlying the memristive nature of the PCM-$VO_2$ itself[135,250].

## 2.4 ACKNOWLEDGEMENTS

The work presented in this chapter was supported by a research assistantship provided by the National Science Foundation (ECE-0801980). Portions of this work were performed (i) at the Vanderbilt Institute of Nanoscale Science and Engineering, using facilities renovated under NSF ARI-R2 DMR-0963361 and (ii) at Imperial College London and was sponsored by the Engineering and Physical Sciences Research Council (EPSRC) and the Leverhulme Trust (Dr. Dangyuan Lei, Dr. Yannick Sonnefraud and Prof. Stefan A. Maier).

# CHAPTER 3

# PLASMON RESONANCE SPECTROSCOPY: AN EXQUISITE TECHNIQUE FOR PROBING THE INTRINSIC PROPERTIES OF QUANTUM NANOSTRUCTURES

"God made the bulk; the surface was invented by the devil"

~ *Wolfgang Pauli, 1945 Nobel Laureate*

## 3.1 INTRODUCTION

Atomic and electronic reconstructions in vanadium dioxide and PCMs in general are increasingly considered for nanoscale data-storage, switching and photonics technologies. Such device technologies (ultrafast switches,[145] modulating barriers in multilayered spin switches,[146] Mott field-effect transistors[147] and novel solid-state memory devices.[148]) rely on switchable modification of the electrical and optical properties of PCMs when heat, laser pulses or electrical fields are applied to overcome the energy barrier to the phase transformation.[251] As these devices are scaled down, a deeper understanding of entangled structural and electronic effects is essential to tailoring the functionality of PCM devices. Of particular interest are surfaces, grain boundaries and interfaces of PCM nanostructures owing to their pronounced contribution at the nanoscale. Recent examples are conduction at an insulator surface,[252] superconductivity at oxide interfaces[253] and reduced switching energies in interfacial PCMs.[254]

This chapter illustrates the importance of understanding the effect of interfaces on the switching properties of $VO_2$. By considering the effect of size together with

homointerfaces, arising due to grain boundary, proper design consideration can thereafter be given when combining, more generally, a plasmonic material with a phase-changing material. At the heart of this modification in the phase-changing properties are defects, which are known to affect nanoscale phase transitions. However, their specific role in the metal-to-insulator transition in $VO_2$ has remained elusive. By combining here plasmon-resonance nanospectroscopy with density-functional calculations, we correlate decreased phase-transition energy with oxygen vacancies created by strain at grain boundaries. By measuring the degree of metallization in the lithographically-defined $VO_2$ nanoparticles we find that hysteresis width narrows with increasing size, thus illustrating the potential for domain-boundary engineering in phase-changing nanostructures.

Despite the simple stoichiometry and structure of $VO_2$ however, there are many unresolved puzzles about its metal-to-insulator transition (MIT). Recently, the nanoscale electronic and structural phase coexistence in thermally modulated $VO_2$ (*§1.3.2c*) [113] and the origins of size-dependent switching in $VO_2$ nanoparticles (NPs)[111,112] have been the subject of much debate. Although experiments to identify the mechanism of such size-dependent switching have been performed,[255, 112] following the initial observation by Lopez *et al.*,[111] the interpretation of the nanoscale $VO_2$ response, in particular distinguishing electronic and structural transitions, was complicated by the presence of a gold interface. In these experiments, owing to the low signal of pure $VO_2$ NPs, both in extinction (~10 times less than Au NPs) and Raman spectroscopy, gold nanostructures were employed either as SERS agents[255] or plasmonic nanosensors[112], illustrated in figure 3.1.

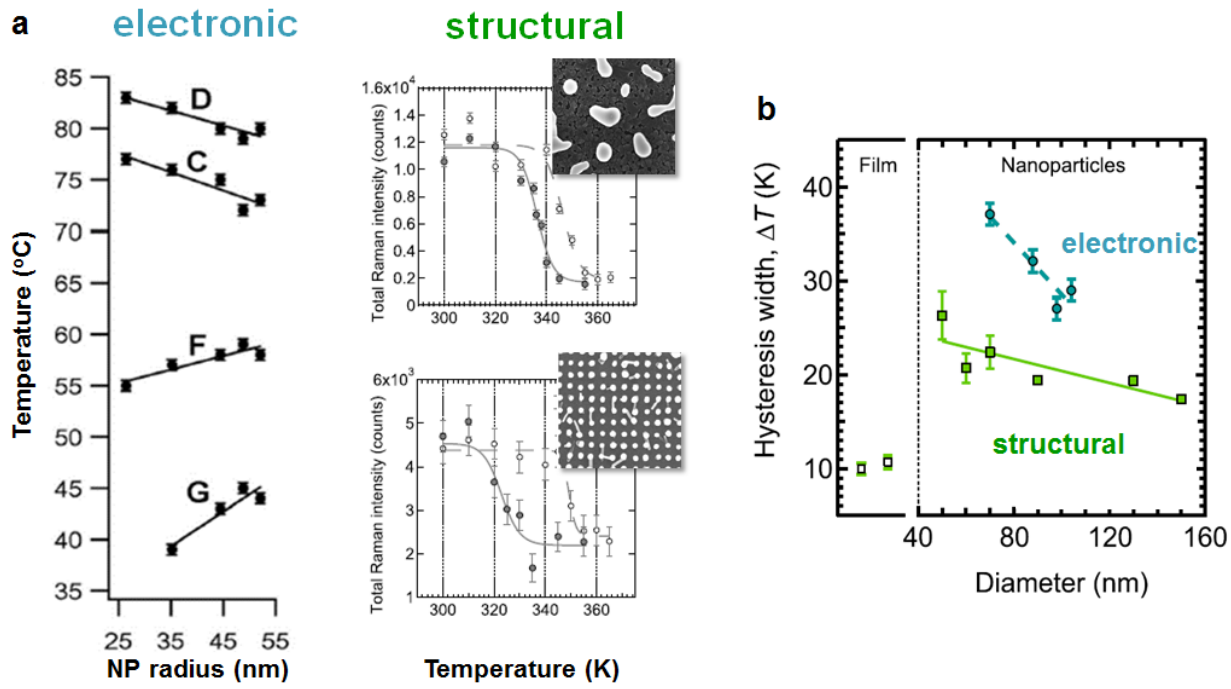


**Figure 3.1. Electronic *vs.* Structural Switching Signatures at Nanoscale. (a)** Electronic signatures of pristine $VO_2$ nanoparticles measured by monitoring the incoherent electron scattering response of each NP arrays while the structural signature was measured (in a different experiment) by monitoring the loss of Raman modes of the insulating $VO_2$ phase. Note that the bright colors in the SEM are gold nanoparticles used for surface enhancement. **(b)** Summary of both the electronic and structural phase transition (determined by their corresponding hystereses widths), displaying a non-congruence at the nanoscale.

Additionally, the specific origins of metallicity at grain boundaries have also emerged as a critical issue for PCM applications involving the transport and electrical properties of $VO_2$.[171,256-259] Unfortunately, it is precisely that knowledge of the specific point defects that nucleate this phase transition which is not available.

Here, we show that the most likely point defect nucleating the phase transition is an oxygen vacancy present at grain boundaries. By lithographically defining the size of the NPs, we constrain the number of grain boundaries in each NP from none to only a few, thus controlling the relative number of point defects that can be thermally activated in this heterogeneous nucleation process.[37] Here, in contrast to the recent work of Cao *et al.* showing the effect of mesoscopic twin boundaries on the MIT in strained $VO_2$ microbeams, we focus on determining the nature of the initiating point defect by tracking the MIT in $VO_2$ NPs that are few orders of magnitude smaller in volume than the microbeams.[144] Thus, interfacial effects *within* individual $VO_2$ NPs – solely due to grain boundaries and facet mismatch – can be evaluated from the switching properties of $VO_2$ PCM. By tracking the dipolar plasmonic response of the $VO_2$ NPs as they metallize near $T_c$ we observe a systematic decrease in hysteresis width with increasing particle size and number of grain boundaries (see pairs of arrows in figure 3.3b-d illustrating the definition of this width). This corresponds to a decreased energy barrier for the phase-transition.

The dipolar character of this plasmon resonance is confirmed by using 3D full-wave FDTD calculations. Density-functional calculations show that the strain associated with the larger NPs favors the formation of oxygen vacancies in grain boundaries as the defect responsible for heterogeneously nucleating the phase transformation.[260] These results have significant implications for the understanding not only of PCM properties at nanometer length scales, but also of polycrystalline and epitaxial thin films, where interaction among the various crystallites can have a profound macroscopic effect on the MIT character.

## 3.2 EXPERIMENTS AND DISCUSSION OF RESULTS

### 3.2.1 Sample Fabrication

We fabricated arrays of nanodisks with varying lateral dimensions on the same ITO-covered glass substrate by means of: (i) electron beam lithography (EBL: 10 kV accelerating voltage, 12.5 pA beam current and 95 $\mu C/cm^2$ nominal dosage) in a spin-coated layer of poly(methyl-methacrylate) (PMMA: 200 nm thick), followed by (ii) chemical removal of the exposed regions; (iii) pulsed-laser deposition (PLD: $\lambda$ = 248 nm, 25 ns pulse duration, 3.84 $mJ/cm^2$ fluence, 10 Hz repetition rate, vanadium metal target and 10 mTorr of $O_2$ gas) of amorphous, sub-stoichiometric vanadium dioxide (40 nm $VO_{X=1.7}$ nominal thickness); (iv) thermal anneal (450$^oC$, $O_2$ gas at 250 mTorr for 20 minutes) to render the NPs crystalline and stoichiometric. As the $VO_2$ NPs crystallized during the annealing process, they also acquired some individual variations in morphology[261] so as to contain a single domain or few grains, depending on the restriction imposed on their volume and shape by the lithographic process. Ordered arrays were used to enhance the signal-to-noise level while particle-particle interactions were minimized. This was achieved by keeping the grating period to ratio (L/r) constant and more than a factor of 5 (L/r ~ 6.0 here), which normalized the scattering cross-section per unit coverage area – proportional to $(r/L)^2$ – and minimized near-field interactions, respectively.[262-264] As shown from the SEMs in figure 3.2, the largest NPs (r = 105 nm) exhibit multiple grain boundaries within individual NPs that contain point defects, dislocations and other structural imperfections. For the array containing the smallest NPs (r = 48 nm) however, the NPs appear to consist mostly of single grains.

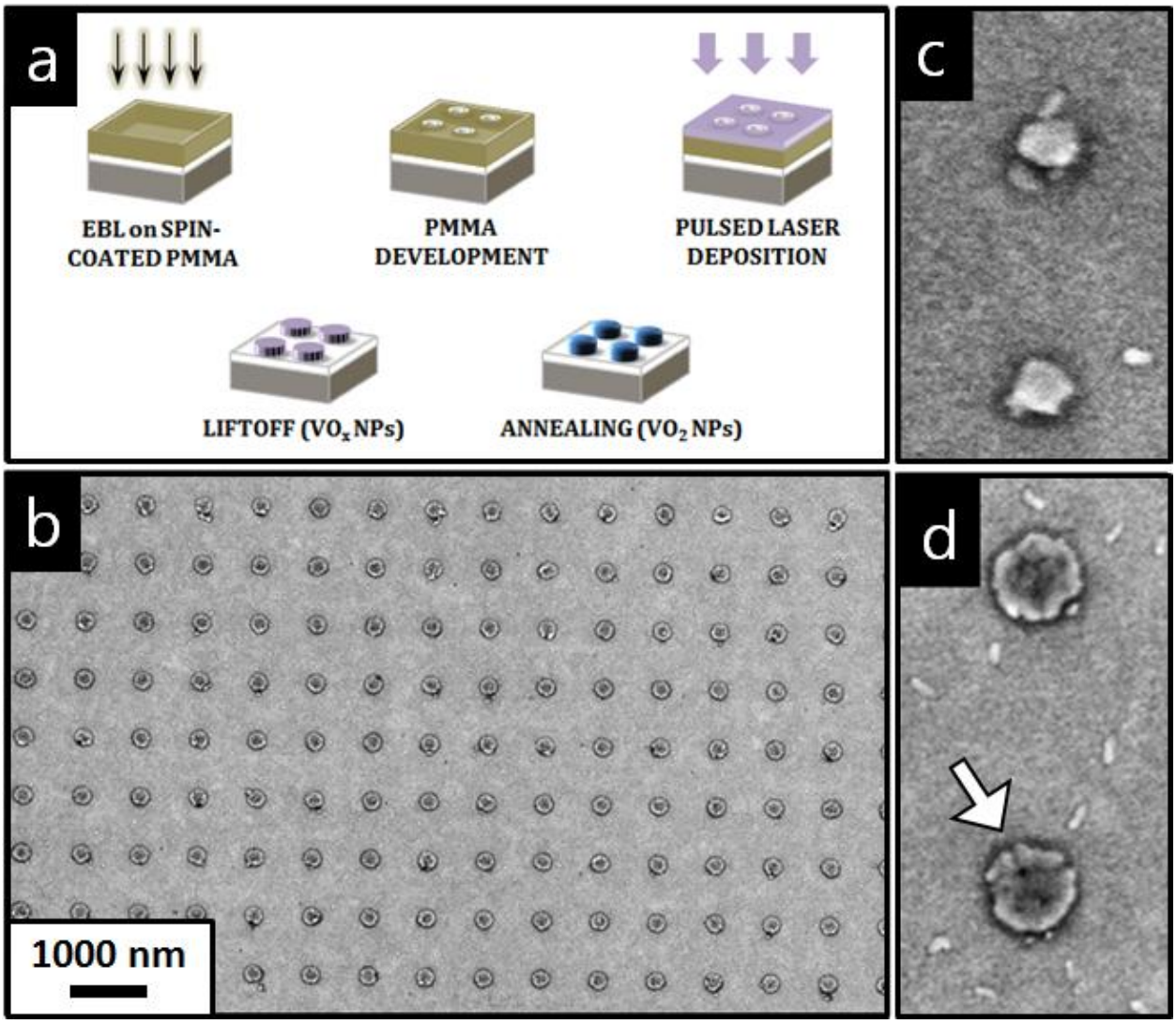


**Figure 3.2. Fabrication and Characterization of Pristine $VO_2$ Nanostructures. (a)** Schematic of the fabrication method. **(b)** Scanning electron micrographs of $VO_2$ NPs depicting integrity of the arrays. Panels **(c)** and **(d)** show the smallest (r = 48 nm) and largest (r = 105 nm) nanostructures in this study, respectively. Note not only the individual NP characteristics arising in the annealing process but also the presence of multiple grains/boundaries (dark line) in **(d)** indicated by the arrow. All SEMs were acquired at an accelerating voltage of 3 kV and working distance of 7 mm for better resolution of surface morphology.

### 3.2.2 Plasmon Resonance Spectroscopy of Pristine $VO_2$ NPs

The extinction spectrum of each array was acquired in an inverted optical microscope (Bruker Hyperion 2000) integrated with a Fourier-transform infrared spectrometer (Bruker Vertex 70) (*§2.2.1*) as follows: (i) the 100×100 $\mu m^2$ array of interest was positioned under white-light uniform illumination from a tungsten lamp, focused by a reflective objective (36X and NA 0.5) onto the substrate side of the sample; (ii) light transmitted through the array was selected by an aperture and collected by another reflective objective (36X and NA 0.5) that was also used to adjust the focus on the sample surface and detected by a InGaAs photodiode; (iv) the transmission spectrum from an uncoated area close to the particle array was also collected for normalizing the array measurement; (v) the sample was then heated using a Peltier cooler mounted on the stage or allowed to cool, and the measurement sequence was then repeated at the next temperature plateau where the focus was once again checked. Spectra were acquired at intervals of about $3^0$C, yielding about 30 data points per cycle for each array. Figure 3.3 depicts the resulting *intrinsic plasmonic hystereses* for the arrays.

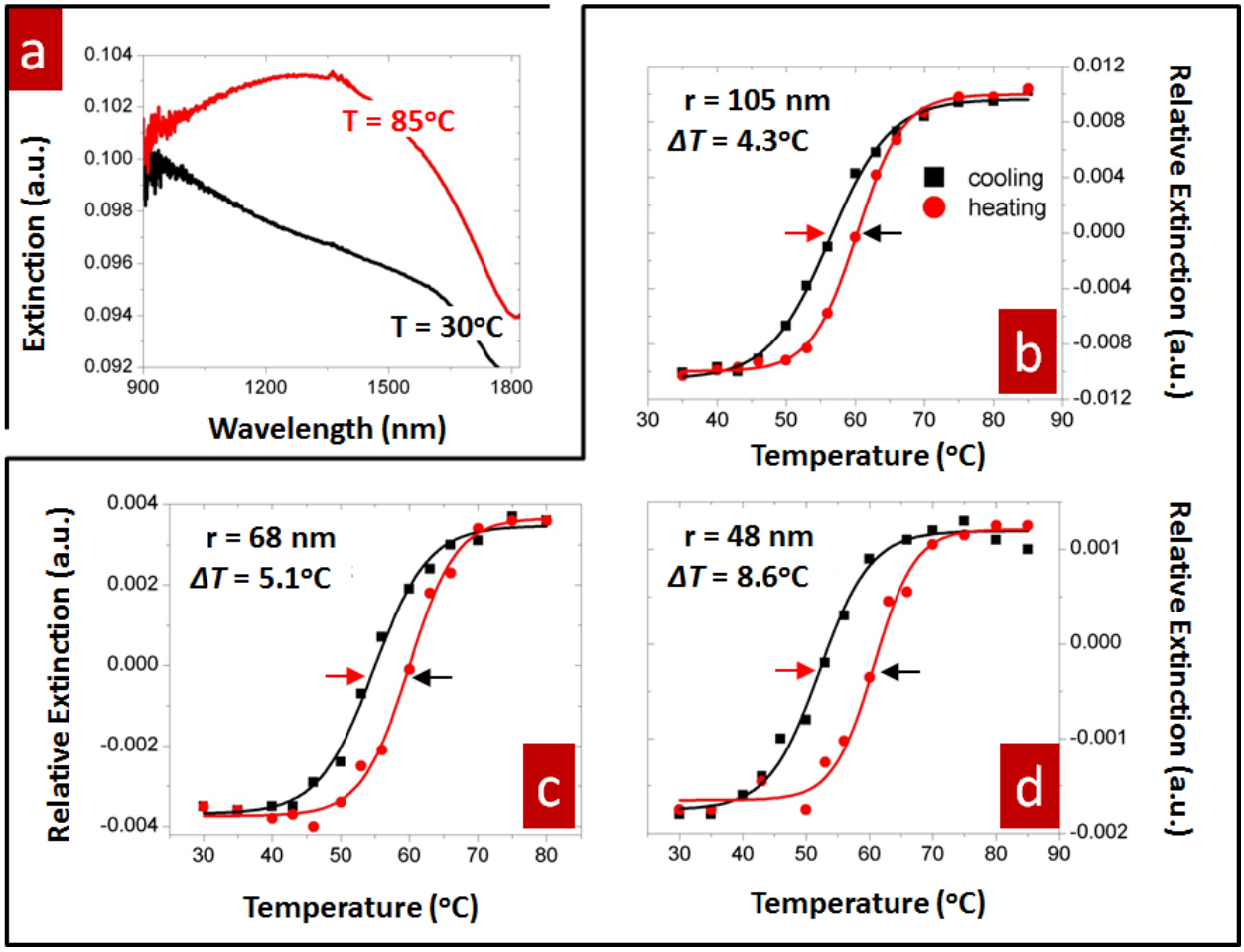


**Figure 3.3. Localized Surface Plasmon Resonance in $VO_2$ Nanostructures. (a)** Typical plasmonic response of $VO_2$ nanostructures as a function of wavelength in their metallic (red) and insulating (black) state for the r = 105 nm nanoparticle case. For each set of spectra, plasmonic hysteretic curves of the relative extinction intensities were plotted for the different nanoparticle arrays with nominal lateral dimension of **(b)** r = 105 nm **(c)** r = 68 nm and **(d)** r = 48 nm. The fits were obtained by using two sigmoidal functions, red for the heating sides and black for the cooling ones while pairs of arrows in **(b-d)** depict hysteresis widths obtained.

### 3.2.3 $VO_2$ Intrinsic Plasmonic Hystereses

In the metallic phase, the real part of the $VO_2$ dielectric function becomes negative around 1.1μm.[247] According to the Fröhlich condition in first approximation,[51] the dipolar plasmon resonance of $VO_2$ NPs occurs when $Re(\varepsilon_{VO2})=2\varepsilon_d$, where $\varepsilon_d$ is the dielectric constant of the nanoparticle environment. Here the effective $\varepsilon_d$ is between the dielectric constant of the substrate (~2.25) and air (~1), which leads to an expected dipolar plasmon mode for the $VO_2$ NPs between 1.3μm and 1.8μm, consistent with the experimentally observed response of the NPs. Figures 5.3b-d present hysteretic curves at the relative extinction intensity, defined as $\sigma = \sigma_{ext}(\lambda=\text{resonance}) - \sigma_{ext}$ (λ=1100 nm) that is the difference between the two extinction values at the on- and off-resonant wavelength.

It can be seen from figure 3.3b-d that the hysteresis width increases substantially as the nanoparticle radius decreases. This trend can be explained by the fact that defects and dislocations around the grain boundaries in bigger NPs act as nucleation sites for this heterogeneous phase transition, thus reducing the energy requirement as quantified by the width of the thermal hysteresis (*§1.3.2c*). In contrast to the work by Donev *et al.,*[261] highlighting the stochastic nature of the MIT in $VO_2$ through the study of single NPs, this work aims at understanding the *average effect* of size and homointerfaces. The effect of grain orientation (with respect to the substrate) has also been suppressed due to the non-preferential crystal growth orientation on glass substrate. In such an *array configuration*, the NPs domain alignment is randomized, that is their crystal-domains do not all align in the same direction. This minimizes consequently any strain contribution from the substrate.

### 3.2.4 Simulating the Dipolar Response of $VO_2$ Nanostructures

With the increase of nanostructure radius, the dipolar resonance substantially redshifts as plotted in figure 3.4c. Indeed, as the $VO_2$ nanostructures have transformed from their insulating to their metallic state, they behave similarly to metal nanoparticles with a characteristic plasmon resonance, albeit a strongly damped resonance. Thus, as the nanoparticles become larger, the retardation effect on the exciting field increases over the volume of the nanoparticle, leading to a shift in the plasmon resonance. Intuitively, this can also be understood by realizing that since the distance between the charges at opposite interfaces of the particle increases with size, a smaller restoring force is required, which lowers the resonance frequency and hence accounts for the observed redshift[51] (*§1.2.2b*).

In order to gain deeper understanding of the measured wavelength dependence of the dipolar plasmon resonance on the particle shape, FDTD simulations were carried out using Lumerical FDTD Solutions® (*§1.2.2c*). The FDTD calculations simulated a single $VO_2$ nanostructure (x, y, z = 0 nm) of varying radial dimensions with periodic boundary conditions and grid meshing size of 2 nm. While one monitor was placed above the nanostructure at z = 100 nm to record transmission of the white-light pulse (x polarized), another monitor (z = 10 nm) was used to record the spatial near-field enhancements. Since the three-dimensional morphology of the nanoparticle cannot be exactly determined, two independent sets of simulations were carried out to correlate the shape effect with the nanostructure plasmonic response. While the first set of simulations calculated the response of hemispherical nanoparticle, the second set simulated nanodisks. The thickness of both structures was set at 32 nm, the average value found by atomic force microscopy, as

shown in figure 3.4. The simulated spectra of figure 3.5a clearly reproduce the heavily damped dipole response of metallic $VO_2$ nanostructures (red curves) in the near IR region. As the nanoparticle size increases (from 96 nm to 210 nm in diameter), we observe the characteristic redshift with the increased size of the NPs. Moreover, the simulation matches well with Lopez *et al.* experiments,[111] with greater scattering amplitude in the visible for the nanoparticle in an insulating state (only shown here for the 96 nm insulating $VO_2$ NP – blue curve). As their plasmonic dipolar resonances – confirmed by the field plots in figure 3.5b – are plotted for the two sets of simulations in figure 3.5c, we find that the simulated hemispheroidal NPs better fit the experimental results for smaller NPs. However, as NP size increases, the discoidal simulations agree better with experiments. This suggests that annealing tends to round off the smaller NPs but retain the original disk-like shape for bigger NPs, possibly due to the variation in wetting behavior for the larger-area nanodisks. Again, such morphological changes due to annealing are also visible in the high-resolution atomic force micrographs of figure 3.4.

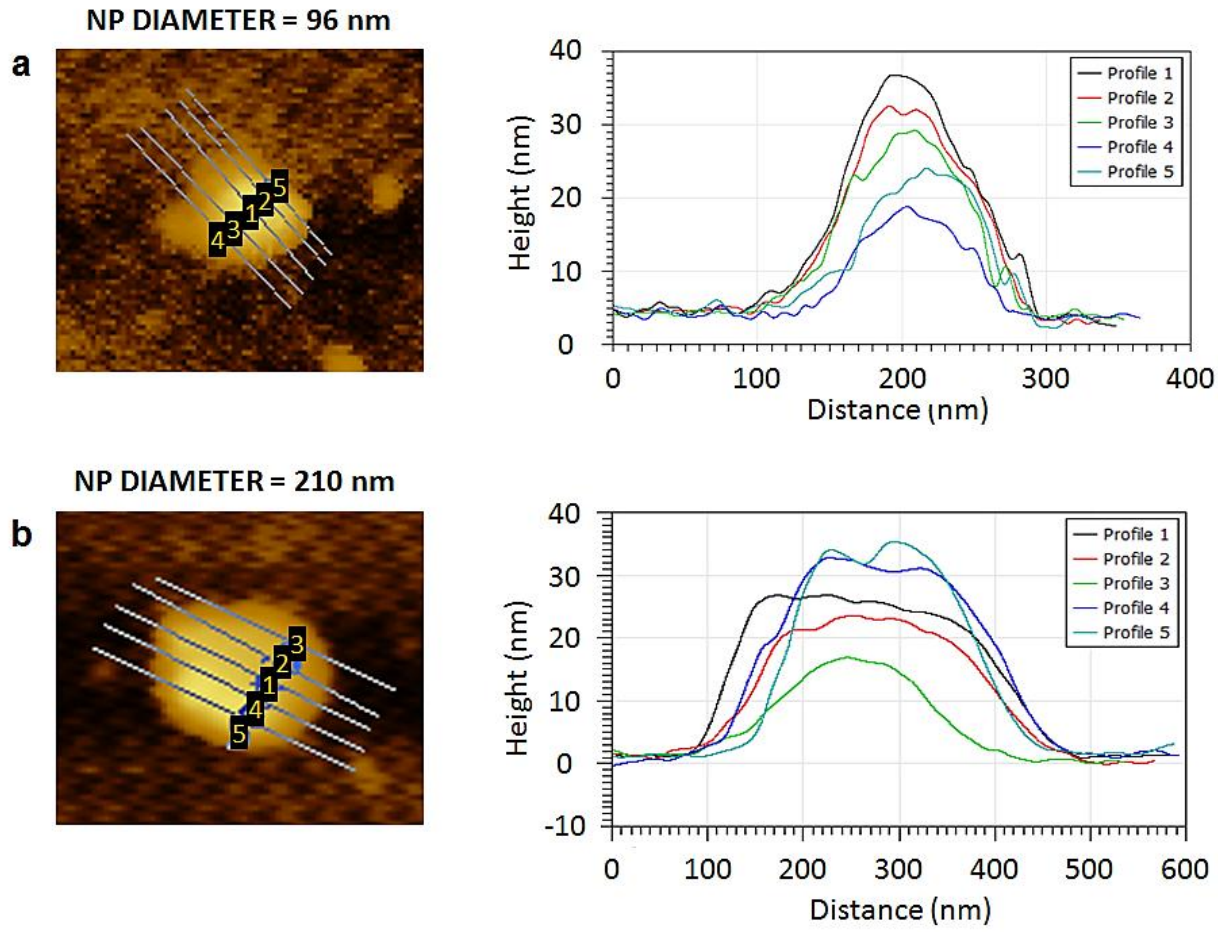


**Figure 3.4. High-Resolution Atomic Force Microscopy of Single $VO_2$ Nanostructures**. Atomic force micrographs for NSs with diameters of **(a)** 96 nm and **(b)** 210 nm. Height profiles depicting that for the smaller NSs, the annealing process rendered the nanoparticles hemispheroidal in shape, while the larger NPs show discoidal features. Note the dip in profile 5 for figure **(b)**, which agrees with the scanning electron micrographs of figure 3.1(d), that is the formation of a homointerface.

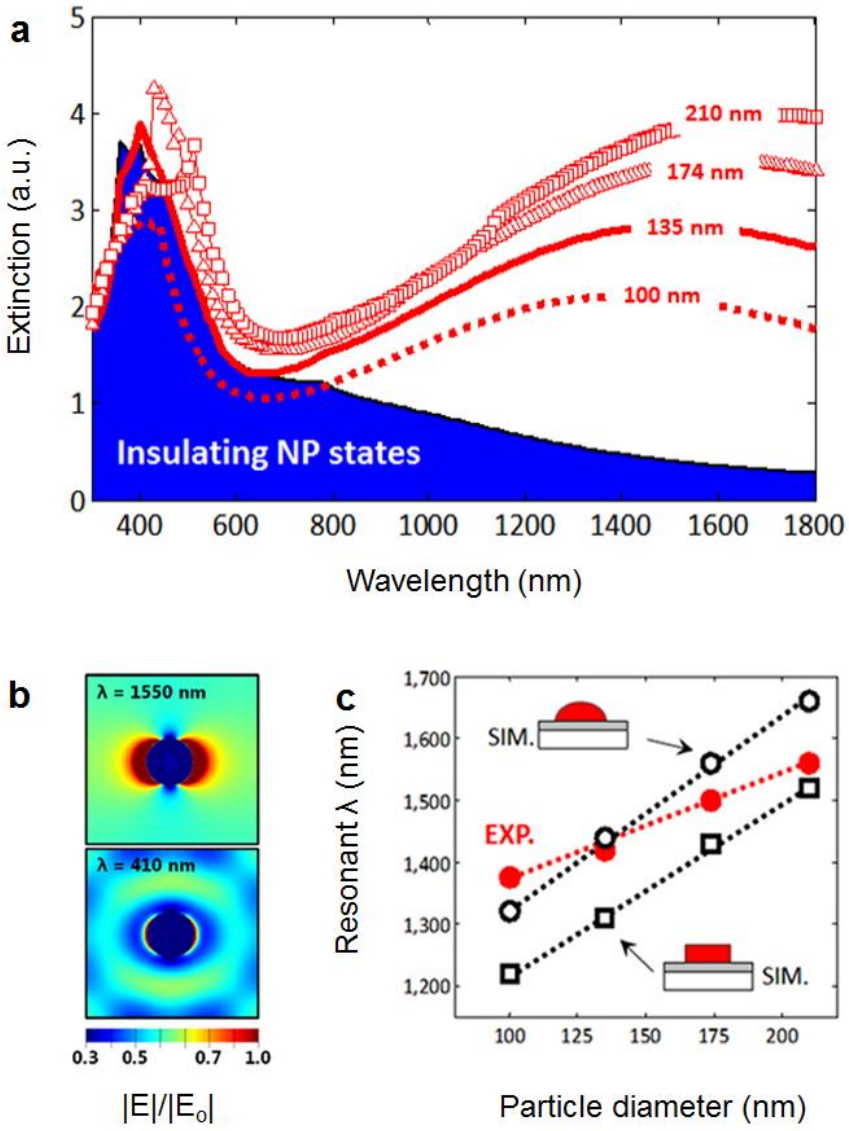


**Figure 3.5. Electromagnetic response of $VO_2$ nanostructures from FDTD simulations.** **(a)** Extinction spectra of $VO_2$ hemispheres in their metallic (red) and insulating (96 nm only shown, blue) states. **(b)** Nanoscale spatial distribution of electromagnetic fields at wavelengths of 410 nm and 1550 nm for the metallic $VO_2$ NPs depicting the two resonance modes of the system. **(c)** Plasmon resonance wavelength as a function of particle diameter for the two sets of simulations (hemispheroid and discoidal structures). Experimental measurements are superimposed in red. The $VO_2$ dielectric constants were extracted from reference [114].

### 3.2.5 Effect of interface on the electronic and structural hysteretic signatures

In order to gain insight about size and interface effects on switching, we plot in figure 3.6 the hysteresis widths – corresponding to the energy requirement – of the electronic (circles) and structural (squares) phase transitions as a function of the $VO_2$ volume for nanoparticles and thin-film samples grown using the same pulsed-laser deposition protocol.[153] First, one can clearly see that the structural signature always has a larger hysteresis width than its electronic counterpart, both in pristine (green, black and red) and gold-interfaced (yellow) $VO_2$ systems. Since the phenomenon occurs *even* at the single domain level, one might attribute this non-congruence to the intrinsic structure of the $VO_2$, and therefore not due to any dimensional effect. From a thermodynamic perspective, such a discrepancy also makes sense, because an atomic rearrangement should have a higher energy cost than a change in electronic structure. Also, since the mechanism represents a combination of the electronic-correlation (Mott-Hubbard) together with a structural (Peierls) contribution, this difference in energy expenditure corresponds potentially to the two correlation lengths of the phase transformation.[265]

Furthermore, an interfacial effect is clearly apparent in figure 3.6. In the single domain regime, for example, a gold heterointerface ($Au/VO_2$) has the effect of reducing the hysteresis width by about 25 K and 18 K for the structural and electronic transitions respectively. A similar interface effect is apparent in the multi-domain regime as well, where the homointerface ($VO_2$-$VO_2$ grain boundary) narrows the hysteresis width by about 22 K. We can deduce therefore that the formation of a single grain boundary is sufficient to lower the energy required to effect the transition, due to an increase of point defects that

can act as nucleation sites. The discrepancy in hysteresis widths between the smaller, single-domain NPs studied by Lopez *et al.* and the present experiment suggest that strain also increases with volume by creating additional point defects. This idea will be discussed later in conjunction with the density-functional calculations.

Another key feature of figure 3.6 is the rate of change of hysteresis width as a function of nanoparticle volume. The slope of this function for the electronic signature of the transition parallels its structural counterpart in *both* the single and multi-domain regimes. The significance of this result is twofold; first, it suggests the direct relationship between the number of intrinsic nucleation sites and the energy switching requirement for the NP, *in a given size range*. Second, the fact that the slope in the multi-domain regime is less steep than in the single-domain range suggests that the effect of grain boundaries is to create an enhanced defect concentration in the NP. This decrease in slope for multi-domain NPs implies once again that the first grain boundary to be formed dominates the nucleation process.

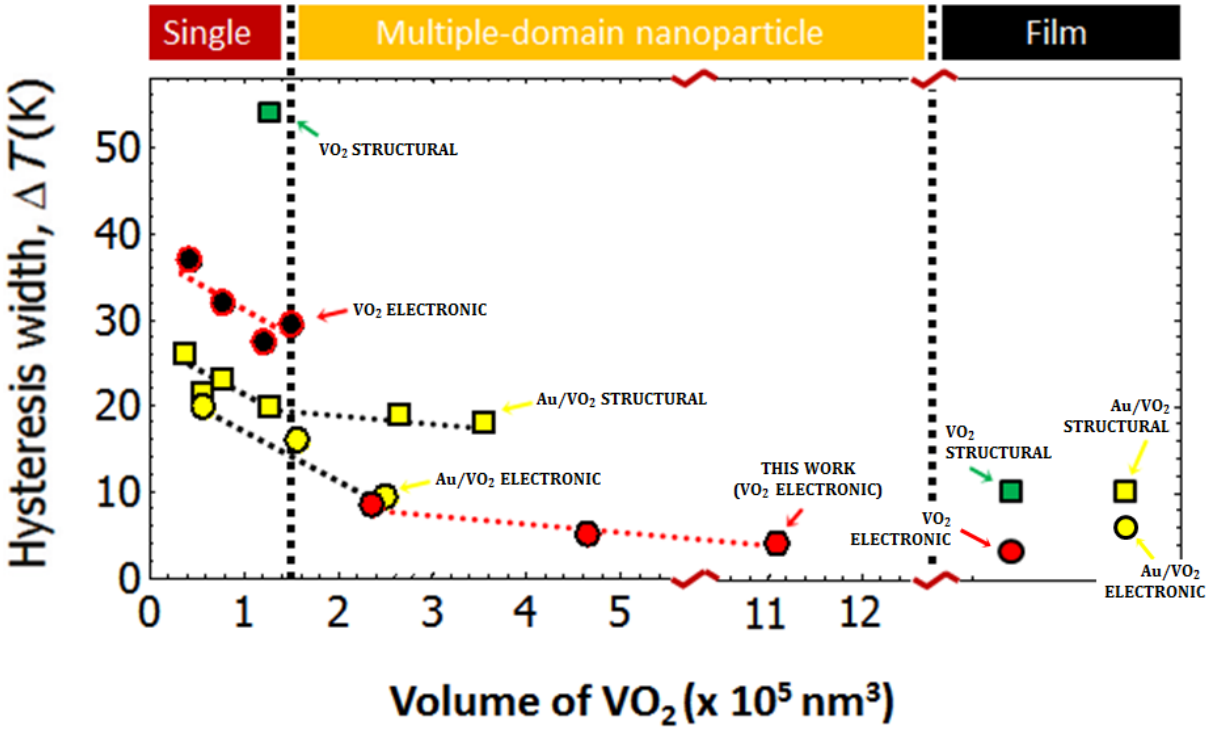


**Figure 3.6. Hysteresis widths as a function of $VO_2$ volume for three distinct regions: single-domain, multi-domain NPs and film, separated by bold, vertical dotted lines.** Circles represent data collected from measurements of the electronic transition (extinction or scattering) while square data were from measurements of the structural transition (Raman or XRD). In the single and multiple-domain nanoparticle regimes, data points were extracted from ref. [262] (circles, red border, black fill),[261] (square, green fill, black border),[255] (squares, yellow fill, black border) and [112] (circles, yellow fill, black border). In the film region (green and red fill) data were extracted from ref. [130] while the yellow-filled square and circle were obtained from refs. [255] and [266], respectively. The lines serve as guides to the eyes.

### 3.2.6 Density Functional Calculations: Exploring the Origins of the Phase Transition

To further substantiate this model of the interfacial effect, we explored the role of oxygen vacancies in nucleating the observed phase transformation by performing first-principles

density-functional calculations on the formation energy of these point defects at grain boundaries. This work was done by Dr. B. Wang and Prof. S. T. Pantelides at Vanderbilt University.

It has been shown previously that grain boundaries in polycrystalline materials induce local strains,[267-269] which have a drastic effect on the formation of point defects in metal oxides.[270] Similar effects are expected in $VO_2$. To simulate the strain induced by the grain boundaries, the bulk $VO_2$ was stretched in two dimensions, as in the work of Klie *et al.*[270] First-principles calculations were performed using the VASP package.[271] The PBE-GGA exchange-correlation potential[272] was used and electron-core interactions were treated in projector augmented wave (PAW) formalism.[273,274] A rotationally invariant DFT+U approach[275] was applied, and the effective parameters, U and J, to include the Hubbard on-site Coulomb repulsion, were specified as 4 eV and 0.68 eV, respectively.[276]

The formation energy of an oxygen vacancy was calculated in oxygen-rich conditions. To calculate the vacancy formation at a surface, we chose the (011) surface and used a 2×2 lateral periodicity. The thickness of the slab was 1.6 nm, corresponding to five O-$V_2O_2$-O trilayers. To simulate the vacancy in $VO_2$ bulk, a cell containing 27 unit cells was used. Only the $\Gamma$ point was used to sample the Brillouin zone. The formation energy of an oxygen vacancy was calculated as $E_{vac} = E_{defected} + \frac{1}{2}E_{O2} - E_{pristine}$, where $E_{pristine}$ and $E_{defected}$ are the total energy of pristine and defective $VO_2$, respectively, and $E_{O2}$ is the binding energy of $O_2$. The lattice parameters optimized in this calculation were a = 5.646 Å (5.743 Å), b = 4.553 Å (4.517 Å) and c = 5.390 Å (5.375 Å) with α = 122.1° (122.6°), in agreement with the experimental data of monoclinic $VO_2$ shown in parentheses.

The surface energy was calculated as $E_{surf} = ½ (E_{total} - n E_{bulk})$, where $E_{total}$ is the total energy of the slab consisting of n bulk unit cells and two surfaces, and $E_{bulk}$ is the total energy of unit cell $VO_2$. The slab thickness for the calculation of (011) surface was 3 nm, corresponding to nine O-$V_2O_2$-O trilayers. For other surfaces, *e.g*. (001), (100), (010), the thickness was set to ~ 4 nm. The cutoff energy was set to 400 eV and the Brillouin zone was sampled with a *k*-point (2×3) for the (011) surface. The *k*-points for other surfaces were adopted accordingly. During the optimization, all the atoms were relaxed until self-consistent forces reached 0.02 eV/Å.

As shown in figure 3.7, the formation energy of an oxygen vacancy in $VO_2$ bulk is 3.4 eV. By stretching the bulk crystal along the [100] and the [010] directions by 5%, we found a drop of 0.5 eV indicating that strain induced by the grain boundaries indeed facilitates the formation of oxygen-vacancy defects. For grain boundaries at surfaces, the formation energy of a surface oxygen vacancy on the (011) surface – the most stable surface of $VO_2$ as shown by the surface energy calculations – is 1.6 eV. In the presence of 5% tensile strain, the formation energy decreases to 1.3 eV. Therefore, due to the strain-reduced formation energy, one expects that in the multi-domain NPs more defects occur at the grain boundaries. The correlation between the increased defect concentration suggested by the calculations and the lower switching energy required in multi-domain NPs found experimentally suggests that vacancies may serve as the nucleation sites for this heterogeneous first order phase transition,[37,277] and consequently, provides an explanation for the reduced hysteresis width in multi-domain NPs.

In principle, delocalization of the strain field over the entire nanoparticle could potentially modify the character of the phase-transition. However, this possibility is excluded because strain fields around grain boundaries are short-ranged and localized, decreasing exponentially with distance from the boundary. The range of a grain-boundary strain-field can be estimated from the spacing (*D*) of the dislocations in the grain boundary,[278] by dividing the Burgers vector by the grain-boundary angle in radians.[279] For example, the Burger's vector for the (011) surface is about one unit cell length, that is about 5 Å. Therefore, for a small-angle grain boundary of 10 degrees, *D* is about 3 nm. For a large-angle grain boundary of about 60°, found by Yang *et al.* using transmission electron microscopy, we can estimate that the decay length for the strain field should be even smaller, of a few Ångstroms only.[256] This agrees nicely with the experimental findings of about 2 nm for $YBa_2Cu_3O_7$ as well. [278] Consequently, this phase-transition is driven mainly by the accumulation of point defects at grain boundaries.

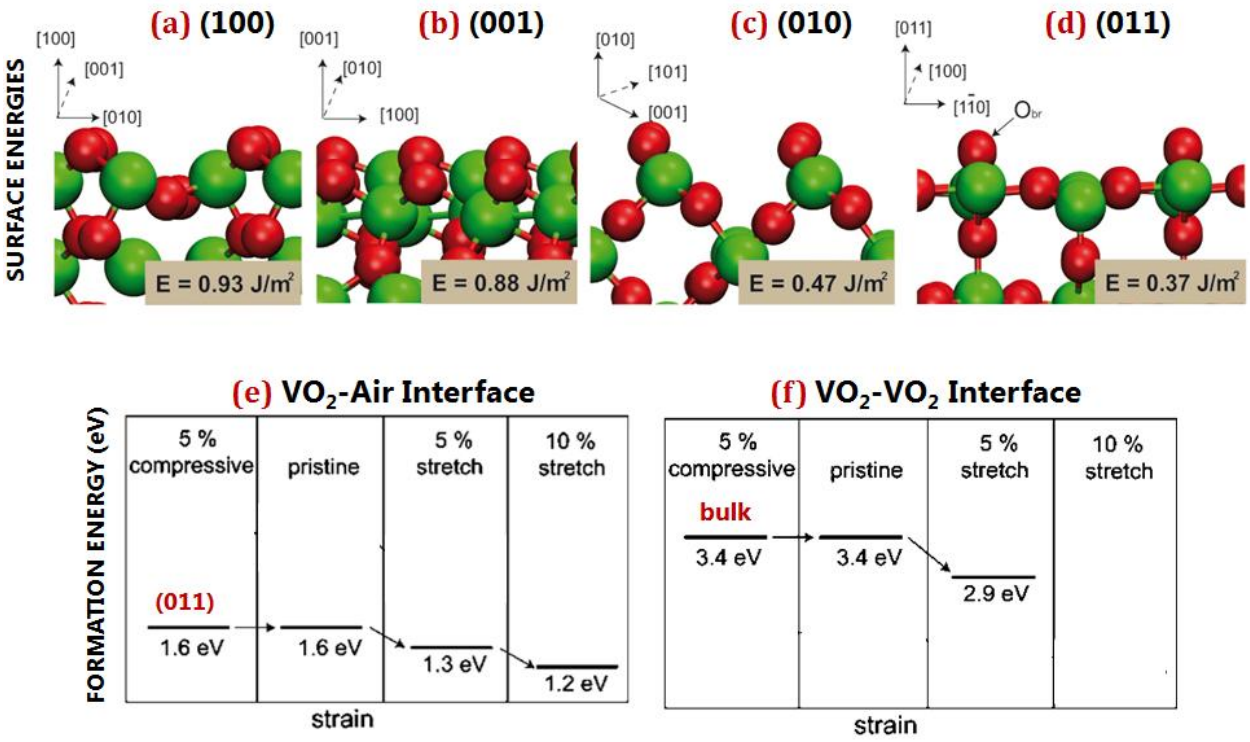


**Figure 3.7. First-principles density-functional calculations of the formation energy of oxygen vacancies.** First-principles calculations of surface energies of **(a)** (100) **(b)** (001) **(c)** (010) and **(d)** (011) surfaces of $VO_2$. The (011) surface with the lowest surface energy was the most stable and was used to calculate the formation energy of oxygen vacancies. Courtesy of Dr. Bin Wang.

## 3.4 CONCLUSION

Since its discovery in 2001 (*§1.3.2c*), few experiments have attempted to identify the mechanism of the size-dependent switching. As shown in this chapter, the interpretation of the nanoscale $VO_2$ response – in particular distinguishing the electronic and structural transitions – has been blurred by the presence of homointerfaces or heterointerfaces ($Au/VO_2$) as these previous experiments precluded detailed understanding of the mechanism or understanding of the specific point defect.

Taken all together, these new experimental and theoretical results make a strong case that the oxygen-vacancy defect triggers for the heterogeneous nucleation of the phase transition at the nanoscale. The case rests on three pillars: first, the lithographic fabrication of $VO_2$ nanoparticles that cover a range of sizes to contain single or multi-domain grain; second, the plasmon resonance nanospectroscopy which, combined with full electromagnetic field simulations shows how shape and size affect the dipolar plasmon resonance of the intrinsic $VO_2$ nanoparticle; and third, density-functional calculations show how mismatched or strained $VO_2$ at grain boundaries modifies the phase transition by reducing the energy required to form the oxygen-vacancy defects.

The implications of these results are twofold. First, since $VO_2$ was used here only as a prototypical insulator-to-metal transition, these point defects may suggest a new method for tailoring any general first-order phase transition by preferential nucleation at certain locations.[280] Second, one could also envision an ensemble of NPs of different sizes within one single device but whose properties could be driven individually and selectively, depending on an engineered interface or defect content. This opens the door for *domain boundary engineering*, which could be crucial for the development of nanoscale devices activated by phase transitions.

## 3.5 ACKNOWLEDGEMENTS

The work presented here was supported by a research assistantship provided by the National Science Foundation (ECE-0801980). Portions of this work were performed (i) at the Vanderbilt Institute of Nanoscale Science and Engineering, using facilities renovated

under NSF ARI-R2 DMR-0963361 (ii) at Imperial College London and was sponsored by the Engineering and Physical Sciences Research Council (EPSRC) and the Leverhulme Trust (Dr. Dangyuan Lei, Dr. Yannick Sonnefraud and Prof. Stefan A. Maier) and (iii) in collaboration with the theoretical group at Vanderbilt University (Dr. Bin Wang and Prof. Sokrates T. Pantelides) under the support of DTRA (HDTRA1-10-1-0047), the McMinn Endowment and the DoD Air Force Research Laboratory.

# CHAPTER 4

# PLASMONIC COUPLING GAME

"In a few years, all great physical constants will have been approximately estimated, and the only occupation which will be left to men of science will be to carry these measurements to another place of decimals.'

~ *James C. Maxwell*

## 4.1 INTRODUCTION

As described in Chapter 1, various methods have been designed to control the flow of light on subwavelength dimensions[281-286]. Most notably is the seminal work carried out by the Atwater Research Group[287] demonstrating that optical pulse propagation with a lateral mode confinement was possible via inter-nanostructure near-field coupling. Recently, progress in colloidal chemistry has also shown that such coupled EM energy could travel with similar propagation distances along quasi-self-assembled metallic chain via plasmonic dark-mode coupling[286]. These two design paradigms are illustrated in figure 4.1.

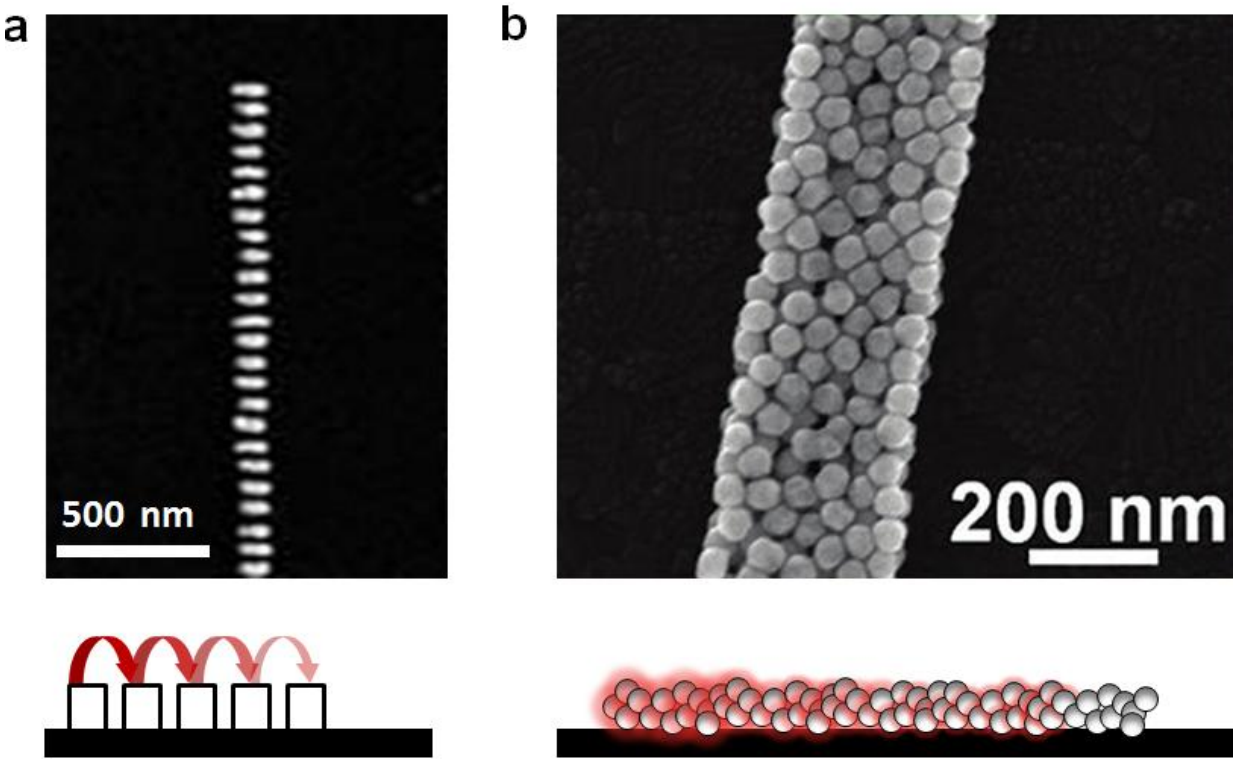


**Figure 4.1. Optical Pulse Propagation Schemes Below the Diffraction Limit. (a)** Lithographically prepared nanodisks and **(b)** nanoparticle chains that have chemically fabricated. In the latter, the interparticle distances are small enough to allow subradiant plamon modes to exist. Although more difficult to couple with light, such modes retain the energy due to reduction in loss, allowing for greater propagation lengths. Adapted from [283] and [286].

Here we focus our attention on understanding how modularity could be provided/integrated by studying the unit cell of plasmonic waveguides that were first presented by Maier *et al*[283].. This is because it provides a controlled testbed for understanding how reconfigurability can be achieved. The studies presented here will hopefully provide insights not only on the modulation capabilities of single hybrid

nanostructures but also on the difficulties and challenges related to the fabrication process. As emphasized in Chapter 2 and Chapter 3, great care should be taken to fabricate such hybrid nanostructures due to intrinsic size and interfacial effects that may respectively arise at the nanoscale.

## 4.2 STACKED HYBRID GOLD/$VO_2$ NANOSTRUCTURES

We investigate here the viability of fabricating and optically modulating hybrid sandwiched nanostructures, which are stacked nanodisks consisting of either Au or phase-changing $VO_2$. Although more difficult to fabricate, such hybrid nanostructures potentially offer several advantages over the Au nanoparticle/phase-change active substrate (figure 4.2). Such hybrid stacked nanostructures reduce drastically the absorption caused by the $VO_2$ film (less absorptive film in the light pathway) while still retaining the modulation capability of this active material. Moreover, if realizable, varying the size of such hybrid nanostructures would result in thermally tunable plasmonic nanomodulator dictated by the size-dependent switching property of $VO_2$ (*§ Chapter 3*).

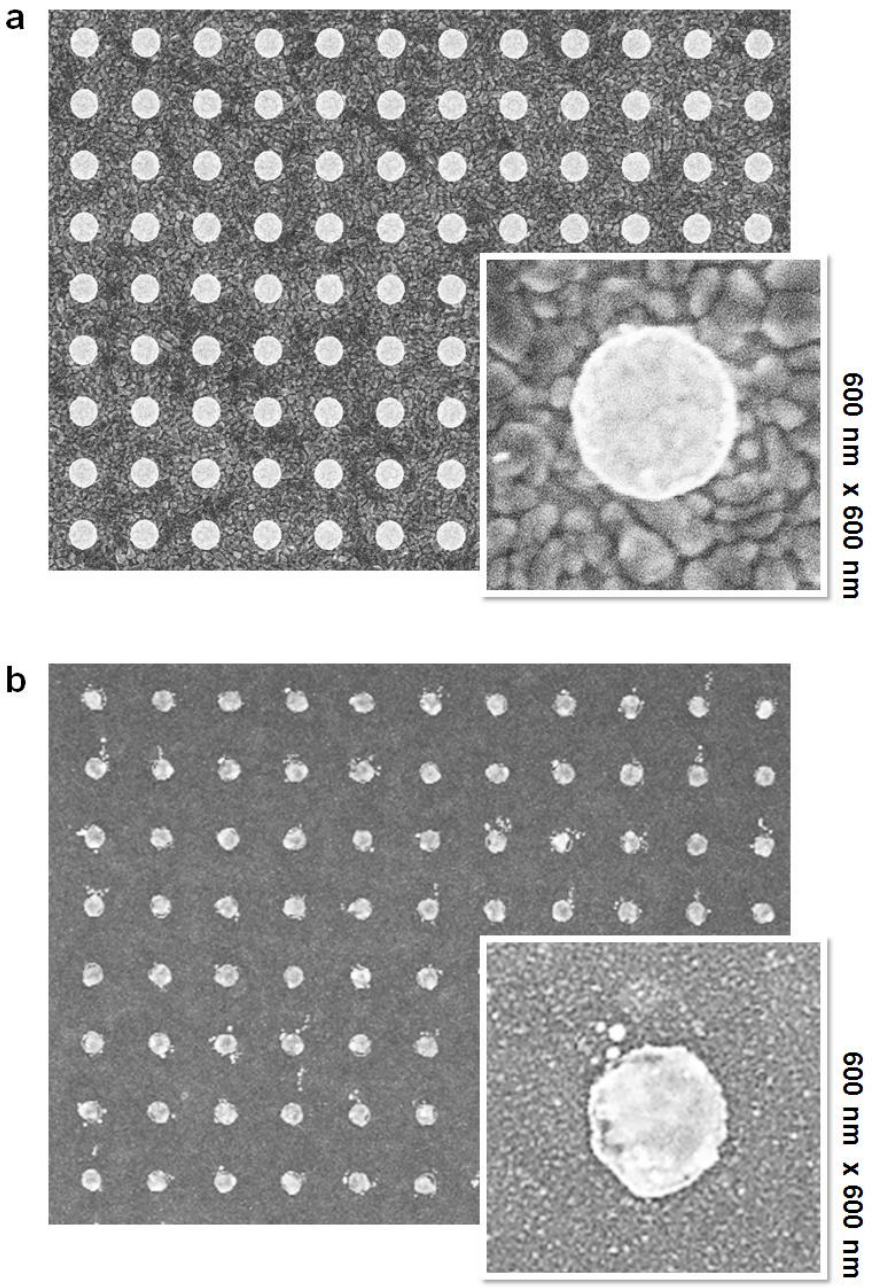


**Figure 4.2. Plasmonic-NS/PC-film *vs.* Plasmonic-NS/PC-NS Geometry. (a)** SEM micrographs of 20 nm thick Au nanodisks array on ~ 60 nm thin film of $VO_2$ and **(b)** 20 nm thick Au on ~ 40 nm thick $VO_2$ nanodisk array on ITO-covered glass substrate. The hybrid nanostructures in (b) acquire individual character due to the annealing process after liftoff. The roughness of the ITO substrate (few nanometers) is visible in (b) while the granular structure of the $VO_2$ film is seen in (a).

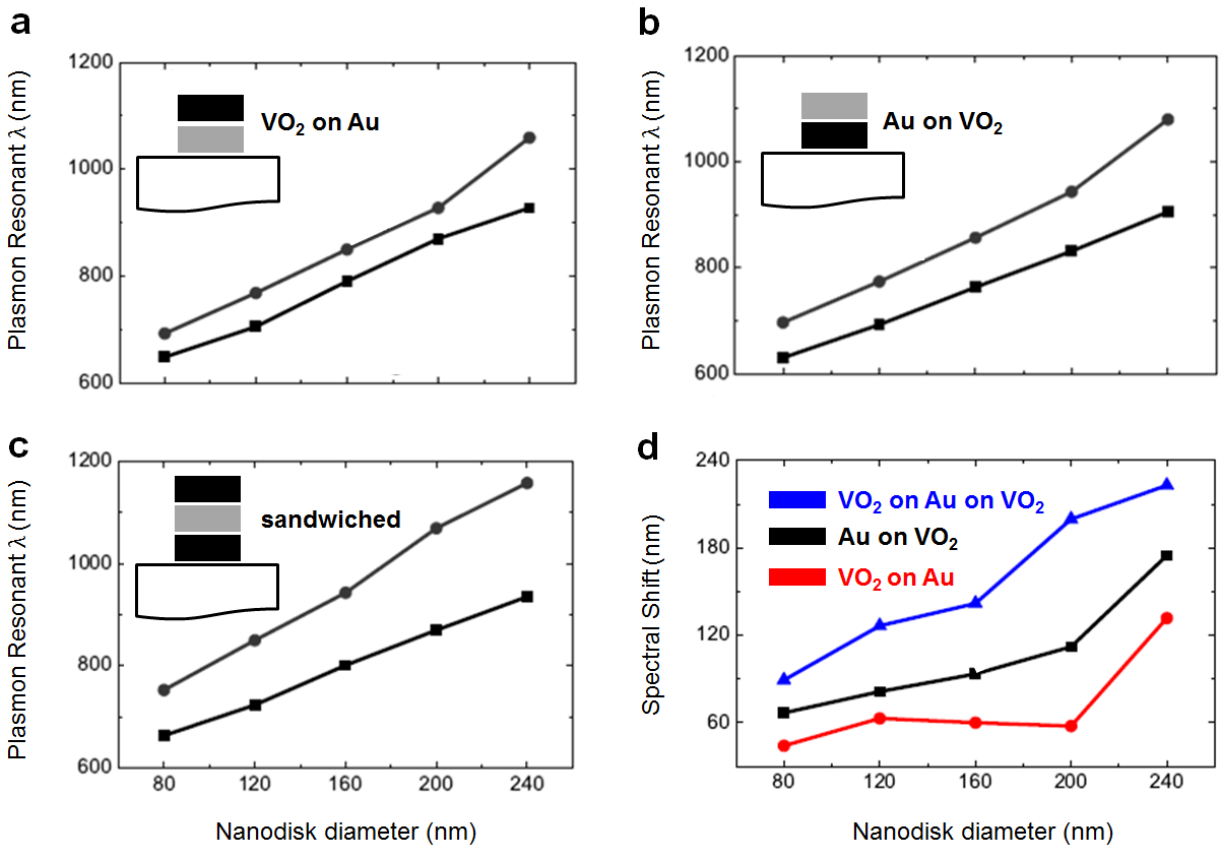


**Figure 4.3. Simulated Optical Response of Hybrid Plasmonic/$VO_2$ Nanostructures.** Plasmon resonant wavelength for **(a)** $VO_2$/Au **(b)** Au/$VO_2$ and **(c)** $VO_2$/Au/$VO_2$ (sandwiched) nanostructures as a function of nanodisk diameter when the $VO_2$ is insulating (grey) and metallic (black). **(d)** Spectral shift for the varying nanostructures under study as a function nanodisk diameter. Simulations were performed in close collaboration with Dr. Lei at Imperial College.

First, we examine three different hybrid geometries – Au/$VO_2$, $VO_2$/Au and $VO_2$/Au/$VO_2$ – on glass substrate using FDTD simulations. While the height of the nanostructures are kept constant (30 nm for Au and $VO_2$ nanodisks), the lateral dimensions are systematically varied, as shown in figure 4.3. Here, as expected, the sandwiched

nanostructures exhibit the greatest modulation. Intuitively, this can be understood by the fact that the larger the $VO_2$ volume (or switching material in contact with the oscillating electron gas of the plasmonic nanodisk), the larger the spectral shift. In this particular geometry, a maximum modulation of ~ 232 nm is observed. Moreover, we also note that the $Au/VO_2$ nanostructure shows a higher modulation contrast than its $VO_2/Au$ counterpart as the Au nanodisk experiences a greater effective dielectric shift in its environment due to a greater contact with a lower dielectric medium (air in this case).

In order to investigate the feasibility of creating such hybrid nanostructures, we experimentally demonstrate the fabrication of the former nanostructure, that is the $Au/VO_2$ stacked nanodisks (figure 4.4). Briefly, such hybrid $Au/VO_2$ nanostructures are fabricated in 100 x 100 $\mu m^2$ arrays with a grating constant of 1 μm on ITO-coated glass substrates by following standard electron-beam lithography process and thin film depositions ($VO_x$ followed by Au or vice-versa). A PMMA layer of 180 nm thick was spin-coated on the substrate and subsequently patterned with an electron-beam of 10 KeV accelerating voltage and ~ 11 pA beam current. The exposed areas were removed by the chemical developer MIBK/IPA (3:1 ratio) and the sample was then coated with a 40 nm $VO_2$ film by pulsed laser deposition of $VO_x$ and a 20 nm Au film by electron-beam evaporation. A chemical lift-off process of removing PMMA, $VO_x$ and Au nanostructures resulted in single hybrid $Au/VO_2$ nanoparticles on the substrate. A further thermal annealing process at $450^oC$ for about 20 minutes created stoichiometric and crystalline $VO_2$ nanodisks.

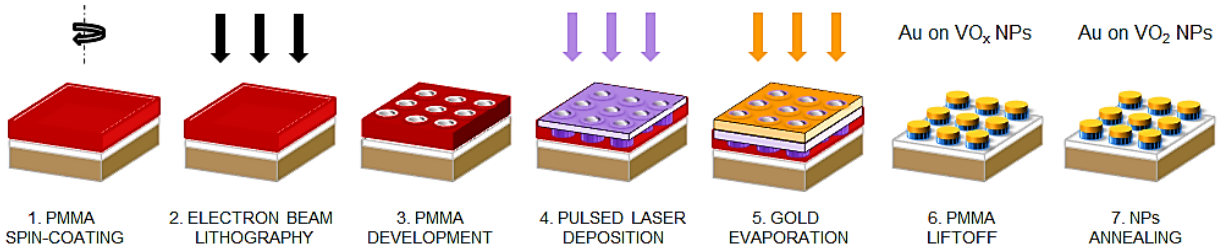


**Figure 4.4. Fabrication of Au/$VO_2$ Hybrid Stacked Nanostructures.** Fabrication of hybrid nanostructures by standard electron beam lithography. Step 4 and 5 can be interchanged to provide $VO_2$/Au nanostructures while an additional $VO_x$ deposition can be performed to provide the sandwiched nanostructures. Following liftoff, the sample is annealed at 450°C for 20 minutes to render the PC-$VO_2$ crystalline, stoichiometric and switching.

As shown in figure 4.5, we see the typical blue shift in the plasmonic resonance of the gold nanodisk as the underlying $VO_2$ nanodisk switches from its insulating to metallic state. We note however the considerable discrepancy between the observed experimental spectral shift (figure 4.5d) and the simulated ones (figure 4.3d) for the smaller nanodisk structures. This is potentially due to two things. First, the Au nanodisk on top could be mixing with the underneath $VO_2$ nanodisk during the annealing process and hence either lessen the $VO_2$ modulating capabilities due to damage or nanoparticulates of Au could be formed and get incorporated into the $VO_2$. These Au nanoparticles could potentially statically doped the $VO_2$ nanodisk, switching already portion of the $VO_2$[240]. Thus, this effect could potentially be more visible for the smaller nanodisks. Second and perhaps more difficult to solve is the fact that the underneath $VO_2$ may not be entirely stoichiometric. This could be due to a size-dependence in the annealing parameters. That is each nanoparticle

size would require a slightly different annealing conditions to be completely crystalline, stoichiometric and therefore switching.

In the light of this analysis, further optimization is required to achieve maximum modulation for smaller nanostructures. Moreover, other fabrication techniques can be implemented such as focused ion beam milling (i.e. $VO_2$ film deposition + annealing → gold film deposition → milling of the desired nanostructure)[53,54]. Also, with the novel electron-beam evaporation technique for $VO_2$ fabrication (*§ Appendix A*), a perhaps lower temperature and shorter duration for the annealing could be envisioned, thus reducing the potential effect of the gold doping or intermixing. Nevertheless, our results are very promising as we do experimentally achieve high modulation in hybrid nanostructures (~ 85 nm in spectral shift) for larger nanodisk structures and this agrees very well with FDTD simulations.

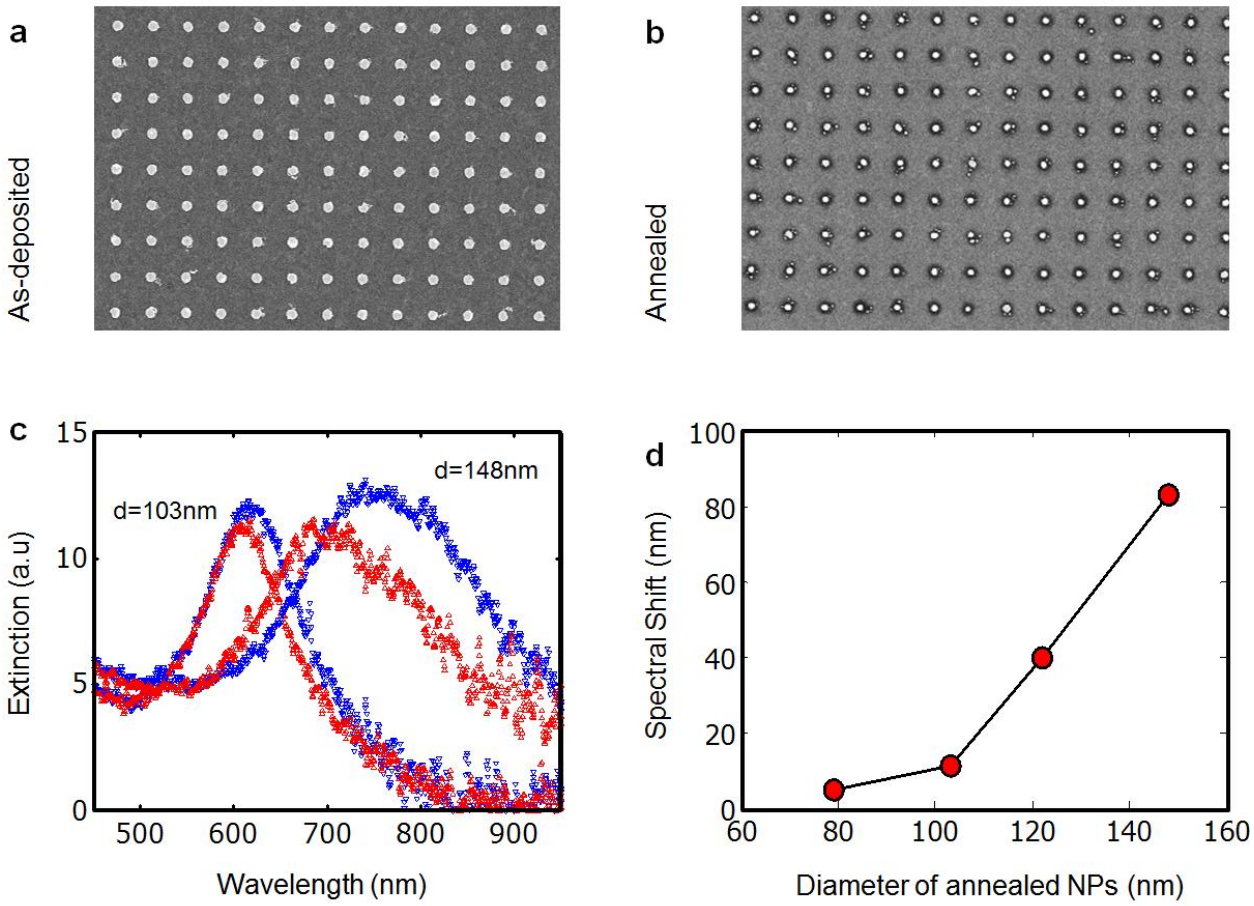


**Figure 4.5. Characterization of Au/$VO_2$ Nanostructures. (a)** SEM of hybrid nanostructures before annealed (after liftoff) and **(b)** after the annealing process. We note that there is a considerable decrease in the size of the nanostructures after the annealing process *(235 → **148** nm; 196 → **122** nm; 154 → **103** nm; 108 → **79** nm)*. The grating constant is 1000 nm. **(c)** Spectral response of Au/$VO_2$ nanostructures for two NS sizes (d = 103 nm and d= 148 nm) in the hot and cold state, i.e. when the $VO_2$ NS is metallic (red) and when the $VO_2$ NS is insulating (blue), respectively. Note the blue-shift in plasmonic resonance, as previously observed for the single Au colloid on $VO_2$ thin film as well. **(d)** Summary of the spectral shift as a function of nanostructure diameter (size after annealed).

## 4.3 METAMATERIAL SPLIT-RING RESONATORS: DEMONSTRATION OF TEMPERATURE-DEPENDENT, WAVELENGTH-SPECIFIC MODULATION

This section discusses designing plasmonic structures that exhibit anisotropic electronic oscillation in multi-mode resonance nanostructures and that can be optimize to interrogate nanoscale volumes of phase-changing material by spatial discrimination. In the present case, we demonstrate this principle by utilizing the size dependence of the solid-solid phase transformation in discrete nanoscale volumes of $VO_2$ combined with complex electron oscillation patterns in split-ring resonators. By monitoring the in-coupling plasmonic mode while thermally cycling through the insulator-to-metal transition, we show that plasmonic hysteresis width broadens with reduced interrogation volume. This is due to the decrease in the gap distance between the arms of the SRR, thus underlying the $VO_2$ switching mechanism that is dictated by the number of potent nucleation sites present in the domains (*§3.4*)).

This study provides the foundation for understanding hybrid plasmonic nanocomponents that could be one of the most promising approaches to nanophotonic technology based on signal modulation in confined nanoscale volumes.[251] Furthermore, consideration of phase transforming materials to be used for modulation should not only focus on composition, but close attention should also be paid to the question of size dependence in determining stable phases. This is because size plays a crucial role in determining the coupling with mechanical, optical, or thermal input required to effect the phase transformation.[288-290] As the domain size decreases to the nanoscale regime, interfacial boundary and strain can further affect the hysteretic behavior of the

transition[172,291], as highlighted in Chapter 3. Since hysteretic phenomena are of great importance from both technological (optical-memory-type applications and detectors) and basic research (mechanism of phase-transformation) perspectives, more attention should be devoted to such studies.[292] Also, with rapid progress in nanofabrication techniques, these size-dependent properties become relevant and systematic studies to assess both the role of nucleation in forming a new state and of the nanoscale dynamical effects are needed to achieve effective modulation, relying on the intrinsic switching mechanistic details of the PCM that is being integrated into the devices.

### 4.3.1 Fabrication of Split-Ring-Resonators

We fabricate arrays of SRRs with varying gap size on the same 0.5 mm thick glass substrate by means of: (i) electron beam lithography (EBL: 10 kV accelerating voltage, 52 pA beam current and nominal dosage of 95 $\mu C/cm^2$) in a spin-coated layer of poly(methyl methacrylate) (PMMA) 100 nm thick layer followed by chemical removal of the exposed regions; (ii) electron-beam evaporation of gold (Au, 21 nm thick) followed by chemical lift-off of the remaining PMMA, together with the Au overlayer. Figure 4.6 depicts the fabrication process, resulting in individual SRR unit cells having gaps of ~ 30, 50, and 80 nm and which constitute the nanosensor arrays. The lattice parameter for the arrays was kept at a constant value of 450 nm. Exact structural details of the sample used for this experiment is shown in figure 4.7.

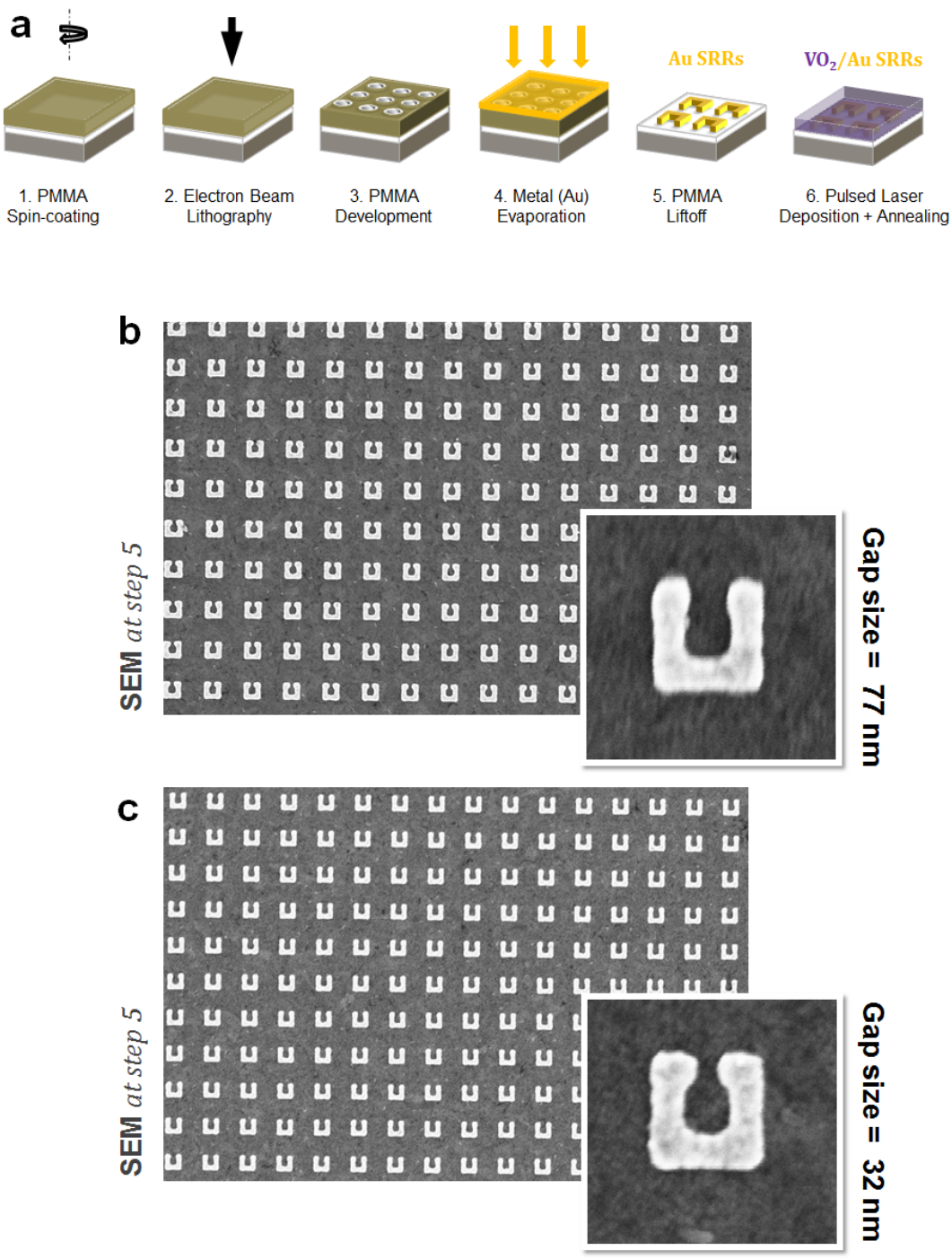


**Figure 4.6. Electron-Beam Lithography of Au Split-Ring Resonators. (a)** Fabrication protocol for Au SRRs followed by $VO_2$ thin film fabrication. SEMs of two metamaterials SRR arrays with varying gap dimensions, namely 77 nm **(b)** and 32 nm**(c)**.

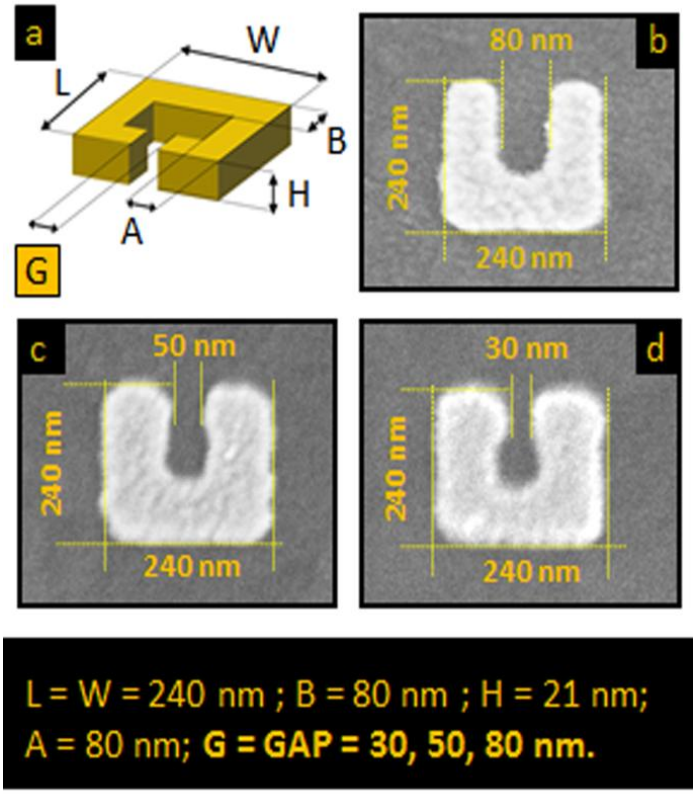


**Figure 4.7. Exact Structural Details of the Au Metamaterial Nanosensors. (a)** Schematic of the split-ring metamaterials with varying nominal gap sizes of 80, 50, and 30 nm. **(b-d)** SEM showing individual split-ring resonator unit cell which constitutes the three array sensors used in this study. The exact structural parameters are also depicted in the figures.

### 4.3.2 Optical Characterization of Split-Ring Resonators

Extinction measurements of each array were acquired as follows: (i) the sample was positioned using micrometer drives to bring the 100 x 100 μm array of interest under white light illumination (90 μm spot size and always polarized parallel to the gap for the purpose of these experiments) while concurrently being imaged onto a CCD camera in the

x-y plane; (ii) the focus (z-plane) was then visually adjusted by displacing the microscope objective; (iii) extinction at room temperature was then measured (integration time of 10 ms and average of 100). Figure 4.8 shows the measurement for the three different arrays with spectra shifted upward for clarity. The spectra for each array exhibit two plasmon resonances. The spectral feature arbitrarily labeled "Peak 1" is the significant one for this study and is attributed to the coupling of the two arms of the SRR, as shown in the simulation section. The red shift of this peak in these three samples is due to decreased inter-arm distance which facilitates coupling and lowers the interaction energy. "Peak 2," on the other hand, is due to the entire structure and, like the lower-order peak near 1500 nm previously thought to be the magnetic dipole resonance, has been extensively studied[293,294]. Most studies on SRRs have focused on the fundamental electric (~950 nm) and magnetic dipole (~1500 nm) modes associated with the entire structure.[17,250,293-295] In contrast, we examine here only the higher plasmonic modes associated with Mie resonances of the SRRs in view of their potential as selective sensors.[296] By systematically varying gap size, as defined by the arms of the SRRs (spectral features in the visible-near-IR region), we use the in-arm coupling resonance to monitor the metal-insulator transition in $VO_2$.

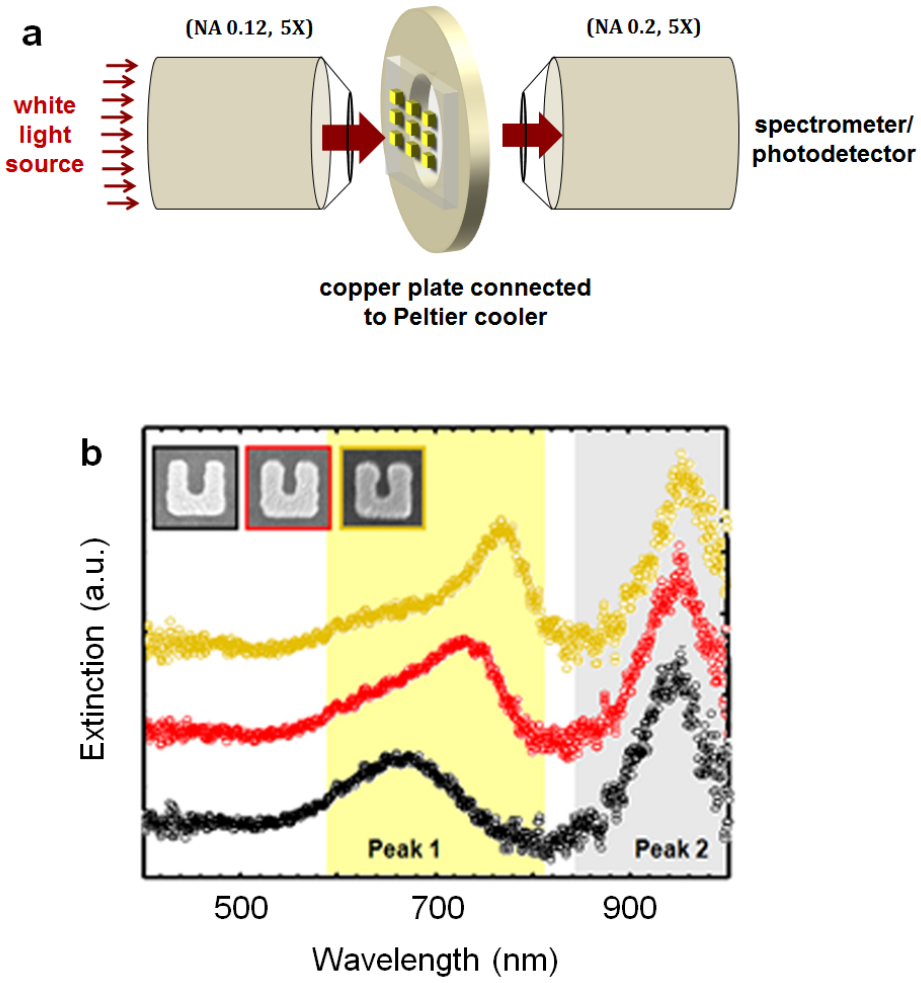


**Figure 4.8. Optical Characterization of Gold Metamaterial Nanosensors. (a)** Sketch of experimental setup used for investigating LSPR of the arrays of metamaterials with light polarized parallel to the gaps. **(b)** Extinction spectra for the 80 nm gap-SR (black), 50 nm (red), and 30 nm (orange). The insets depict the scanning electron micrograph of the respective split-ring structures. As discussed in the text, "Peak 1" is associated with coupling of the arms while "Peak 2" is attributed to a resonance of the entire metamaterial structure.

### 4.3.3 Simulating the Optical Response of SRR Metamaterials

To gain insight into the physical origin of the two resonances and their respective near-field distribution, FDTD simulations were carried out using Lumerical Solutions (*§1.2.2c*). As input for the structural parameters, SEMs of each SRR were used to determine the in-plane shape, while the thickness of the NPs was set to 21 nm. The FDTD calculation simulates a single SRR with periodic boundary conditions (unit cell 450 x 450 x 800 $nm^3$) and grid meshing size of 1 $nm^3$. While one monitor was placed above the SRR (z = 100 nm) to record transmission of the white-light pulse (x polarized), five other monitors were placed along the sagittal (x = 120 nm), coronal (y = base, center and along gap), and transverse (z = 12 nm) to record the spatial near-field enhancements. The simulated extinction spectra matched well with experimental ones, and for each identified peak, near-field distributions were plotted at the two resonant wavelengths. Figure 4.9 compares (i) SRRs having gap of 80 and 30 nm and (ii) spatial near-field distribution at the two resonances. For "Peak 1", the field is strongly localized between the two arms and strengthens as the distance between them is reduced. In the case of "Peak 2", the resonance is due to the entire structure with the region around its base having the strongest intensity. We note also that although the field penetrates into the substrate, the field within the gap for "Peak 1" appears well localized within the cavity of each structure, suggesting already its potential for selective interrogation of the material enclosed within the gap.

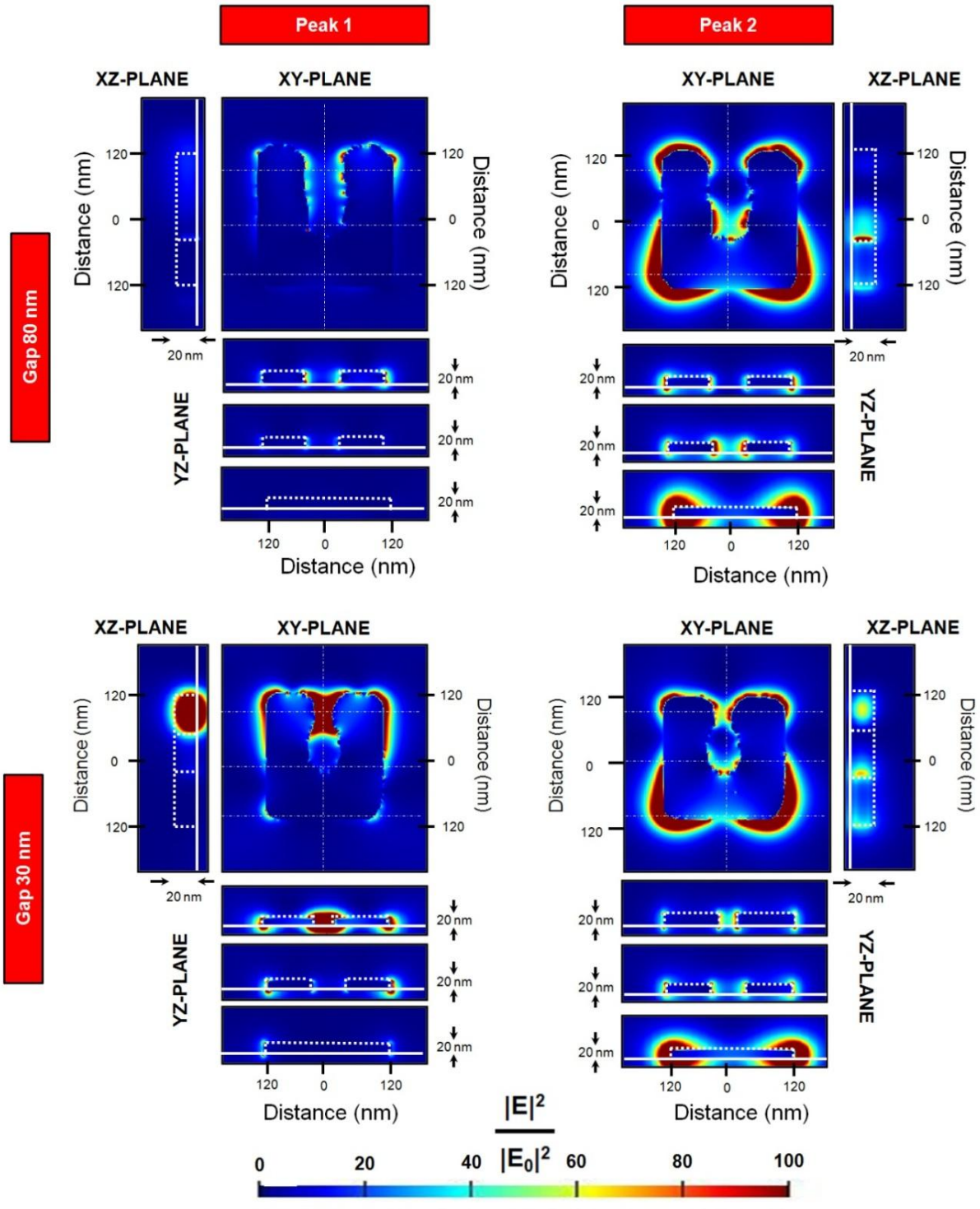


**Figure 4.9. Near-field Distributions of Split-Ring Resonator Metamaterials.** The top two figures represent near-field distribution for a single SRR with gap of 80 nm at the two

resonances (Peaks 1 and 2). Resonant peaks were identified by performing full field 3D FDTD with SEM images of the SRR as input for the structural parameters of the structure. The lower two plots show the electromagnetic distribution of the SRR with 30 nm gap. YZ-planes were added to strengthen the idea of strong confinement in the gap for the higher plasmonic modes (Peak 1). The bold (dotted) white lines represent the substrate/structure interface. Also, for ease of assessment, all near-fields plots were arbitrarily scaled to a maximum value of 100 with respect to the incident incoming plane wave.

### 4.3.4. Hybrid Au SRR/$VO_2$ Film Nanostructures: Temperature-Controlled, Wavelength-Specific Plasmonic Modulation

Following extinction measurements on the bare Au SRR arrays, $VO_2$ was deposited on the sample by means of: pulsed-laser deposition (PLD: $\lambda$ = 248 nm, vanadium metal target, O2 gas at 10 mTorr) of amorphous, sub-stoichiometric vanadium dioxide ($VO_X$ = 1.7, 50 nm thick); a thermal anneal (450$^o$C, $O_2$ gas at 250 mTorr) rendered the film crystalline and stoichiometric $VO_2$.[153] Extinction measurements of the SRR/$VO_2$ nanocomposites using the same protocol as described above were performed as follows (*§4.3.2*): (i) at a stabilized temperature during the heating or cooling stage, the array was moved away from the illumination spot and a flat-field spectrum of the $VO_2$ film was taken; (ii) the array was then brought back under illumination without alteration to the focus, and an average spectrum (integration time of 10 ms and average of 100 spectra) was recorded; (iii) the sample was then heated or allowed to cool using a Peltier cooler mounted on the stage, and the measurement sequence was then repeated at the next temperature point. To clearly demonstrate the size dependence of the plasmonic hysteresis widths, spectra were acquired at intervals of about 2$^o$. This procedure yielded about 40 data points per cycle for

each array. For each spectrum (and each array), the resonance position of "Peak 1" was identified and plotted as a function of the stabilized temperature at which that particular spectrum was taken. Figure 4.10 depicts the resulting plasmonic hystereses for the arrays studied. As the temperature was increased, the resonance blue-shifted (red curve), and when the sample was allowed to cool, the peak returned to its original position (blue curve). This phenomenon is well understood and is extensively discussed in reference[297] and in Chapter 3 (*§ 3*). Briefly, it is due to a considerable decrease in the real part of the permittivity of the $VO_2$ when it switches to its metallic state. As shown in Figure 4.7, the SRR arrays differ only in their interior dimensions and therefore in the volume of $VO_2$ that is contained within the gap after deposition.

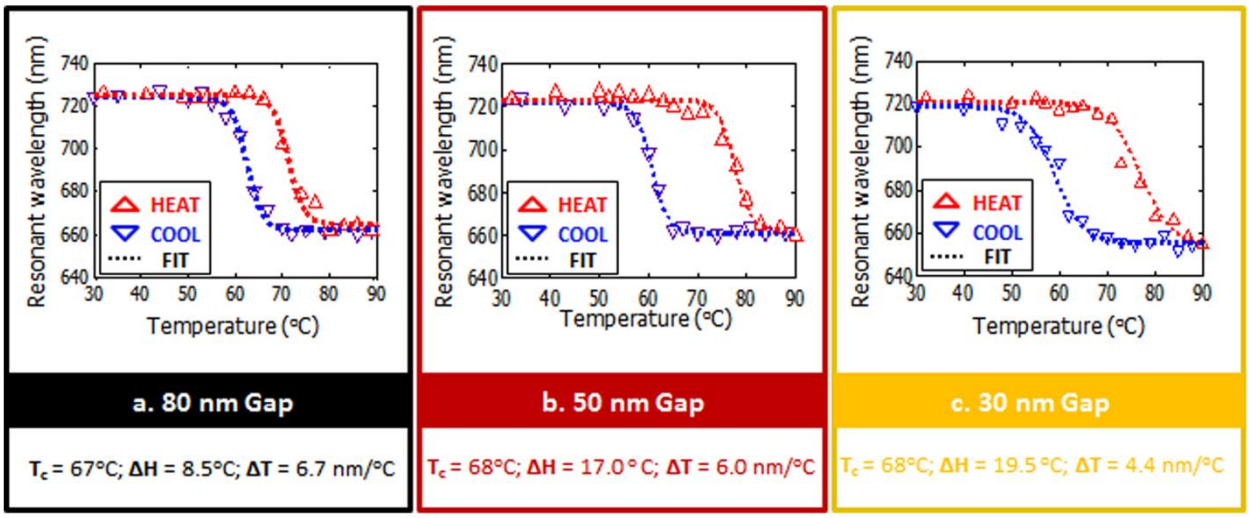


**Figure 4.10. Plasmonic Hystereses Depicting Nanoscale Size Effects of $VO_2$.** Hysteresis plots acquired by monitoring the peak plasmon resonance of the higher plasmonic mode of the SRRs as a function of controlled stepwise temperature interval (~ 2°C). The fit was obtained by using two sigmoidal functions, and each data point has an estimated error of ~ 2 nm. The table shows the various parameters $T_c$ (critical temperature), $\Delta H$ (width of hysteresis), and $\Delta T$ (sharpness of transition) which are used to define semi-quantitatively the hysteresis curves.[291]

In order to emphasize this point further, we have fabricated a similar nanosensor sample, but deposited *only* about 25 nm of $VO_2$. Figures 4.11-13 display high resolution AFM and SEM of that sample before and after the $VO_2$ deposition. Thus, by using Peak 1 as a plasmonic fingerprinting, we see that as the interrogation volume of $VO_2$ is decreased, the hysteresis width increases. Following Lopez *et al.*, this effect can be attributed to the fact that as the volume is decreased, the number of intrinsic nucleation sites necessary for switching the $VO_2$ is also reduced and this lowers the probability for phase transformation. This accounts for the widening of the hysteresis curves[298,299]. The sharpness ($\Delta T$) of the

transition, which is related to the overall defect content per unit volume, also decreases with a decrease in interrogated volume, consistent with the picture of Narayan *et al.*[291] Moreover, from the hysteresis plots, we see that there is no visible shift in $T_c$ despite the incorporation of Au into the system. We attribute this to the fact that the gold SRRs occupy less than 11% by volume of the $VO_2$-covered array. Thus, electron injection into the system would have a negligible effect on $T_c$.[300] Furthermore, the fact that $T_c$ is not shifted to lower temperatures also suggests that strain plays an insignificant role in the thermal hysteresis.[261,291]

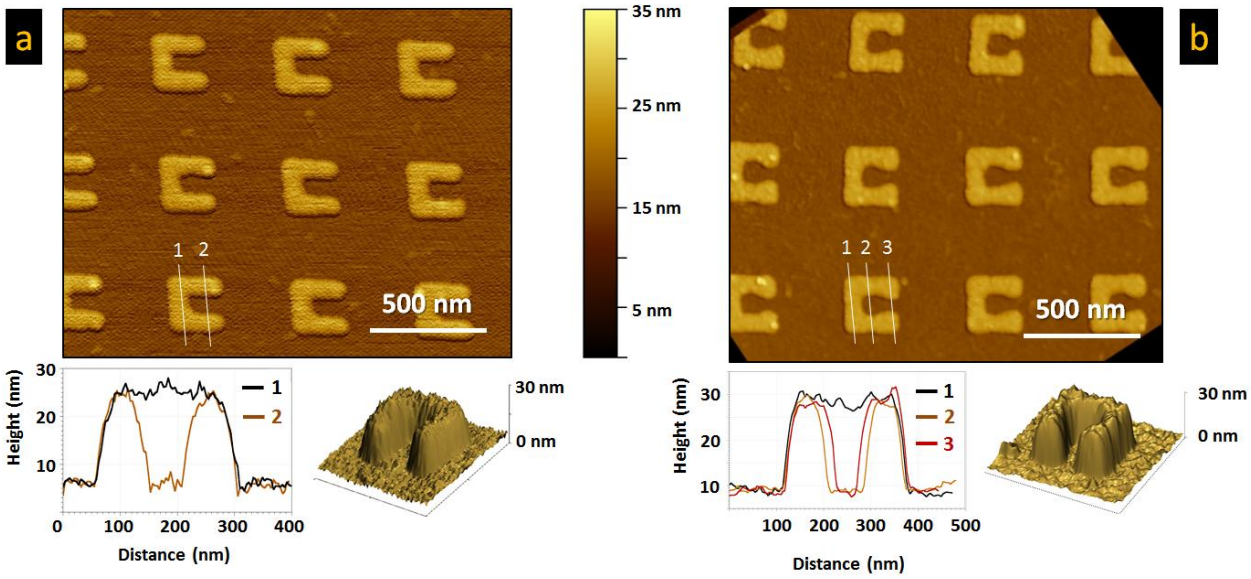


**Figure 4.11. High-Resolution Atomic Force Micrographs of SRRs Before $VO_2$ Deposition.** AFM of the **(a)** 80 nm and **(b)** 30 nm gap SRR arrays before deposition. The insets show the height profiles for the base (line # 1) and for the arms (line #2 and #3). The average step height is about 18 nm. The height profile graphs along with the 3D rendering depict the volume which will be interrogated after the deposition of $VO_2$.

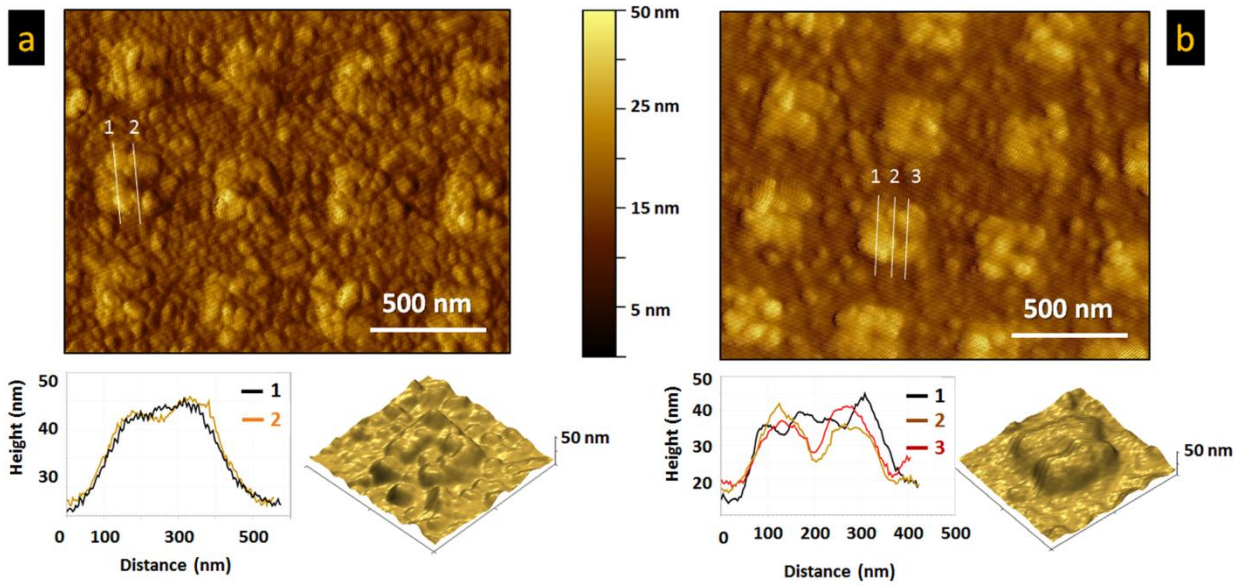


**Figure 4.12. High-Resolution Atomic Force Micrographs of SRRs After $VO_2$ Deposition.** AFM of the **(a)** 80 nm and **(b)** 30 nm gap SRRs arrays after deposition. The insets show the height profiles for the base (line # 1) and for the arms (line #2 and #3). The height profiles from both (a) and (b) show clearly filling of the gaps with the PCM.

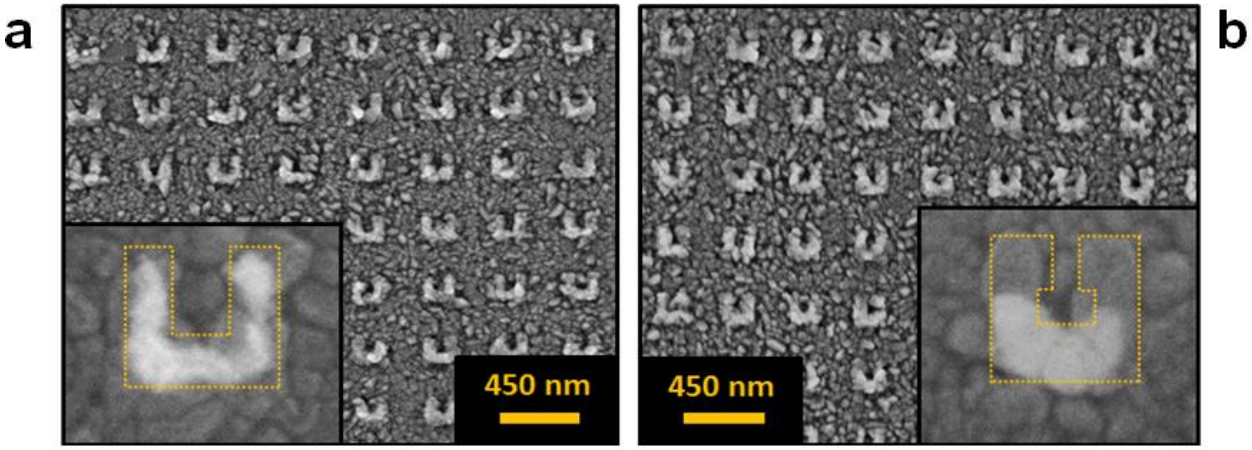


**Figure 4.13. SEM of SRRs After $VO_2$ Deposition.** SEM of the **(a)** 80 nm and **(b)** 30 nm gap SRRs arrays after deposition. The insets show not only the presence of $VO_2$ but also the

presence of multiple grains found within the 80 nm gap. In the 30 nm gap, SEM reveals the presence of single grains in the metamaterials nanosensors.

In addition, the pulsed laser deposition technique creates $VO_2$ films that are polycrystalline, and therefore the nanocrystals present within the gaps have a random crystallographic orientation. Thus, for the approximately 50,000 SRRs contained in each nanosensor array, the effect of strain along the sensitive rutile c axis for the phase transformation of $VO_2$ has been averaged out.[172,173] Owing to this averaging effect, no sharp transition is expected because the array comprising the SRR nanosensors is recording the statistically varying state of the nanocrystals being probed between the gaps in all 50,000 SRRs. Hence, given the inherently lower dynamic range associated with transmission measurement, avalanche phenomena have not been detected.[301] Furthermore, no effects of either electric field localization or morphology are observable; if these effects had been present, this would instead have resulted in a decrease of hysteresis width as the gap is decreased.[261,302] Moreover, in present case, both the volume to surface area ratio and the geometry for all three systems are very similar. From the work Donev *et al.* actually, we see that for a more strained object the hysteresis width would actually have been smaller. Here, we see that for gaps of 30 nm, the hysteresis is wider, implying a size effect instead. Also, thermal expansion of $VO_2$ and Au leading to strain should be considered. However, from an estimate of such expansion, we see that the differential change is only about 0.003% for the $VO_2$ and 0.07% for Au (assuming $VO_2$ and Au linear thermal expansion coefficients to be 5.70 x $10^{-6}/^oC$ and 14 x $10^{-6}/^oC$ respectively and a $50^oC$ change in temperature). Thus, when compared between the 80, 50 and 30 nm gap SRRs, this effect is

negligible and size is the dominant effect. Consequently, the results thus obtained can be attributed ***solely*** to a size-dependent property of the $VO_2$ enclosed between the arms.

### 4.3.4 Brief Digression: Selective Electronic and/or Structural Measurement of Strongly Correlated Material at the Nanoscale?

Although not the focus of this section, it is interesting to consider that the SRR metamaterials presented here could potentially be used to *selectively* and *simultaneously* probe the electronic and structural component of nanoscale strongly correlated material by spatially discriminating the region of interrogation. For example, concurrent extinction and resonant-Raman measurement could simultaneously interrogate nanoscale volumes of material; such deep subwavelength experiment would not have been feasible otherwise. Although the properties of the phase-change could be obscured by the presence of interfacial effect (Au for e.g.), this technique could provide a complementary method to recording the dual response (electronic *vs.* structural in this case) of a system.

As shown in figure 4.14, such electronic and structural response can be compared, albeit the fact that in this particular case the measurements were not taken simultaneously. Here hysteresis widths as a function of the calculated volume of $VO_2$ bounded by the SRR arms is plotted (red) and the measured hysteresis widths as seen here lie considerably below those of the pristine $VO_2$ nanodisks recorded in the scattering experiment by Lopez et al.[262] Since our experimental geometry is closer to the SERS experiment, the conjecture of Donev *et al.* that Au/$VO_2$ interface creates additional extrinsic nucleation sites can potentially be validated.[255] Thus, Au SRRs in contact with the $VO_2$ nanocrystals would have

therefore lowered the threshold for switching; consequently this would have resulted in a systematic decrease of the hysteretic widths in both Au/$VO_2$ experiments when compared to those of the pristine $VO_2$ nanodisks. Therefore, we see that such nanosensor template can provide a semi-quantitative way to relate all three measurements by comparing the relative slope of each experiment to determine if there is any correlation between the IMT and the SPT. Accordingly, in the region of single domains (i.e. for volumes of $VO_2$ smaller than 1.5 x $10^5$ $nm^3$), the slopes of all three measurements are almost identical, implying that both the electronic and structural transitions exhibit similar size dependence. The hysteresis widths decrease linearly as the number of potent sites available for nucleation increases. Also, figure 4.14 shows that the slope in the SPT hystereses (SERS data, gray line) seems to level off, asymptotically reaching a width of 10-15$^oC$ as observed in polycrystalline films. This might imply that in the case of the thin film limit (i.e. for large $VO_2$ volumes), SPT hystereses can be expected to be wider than those produced by the IMT.

Thus, as demonstrated, one can identify readily the discrepancy between the two responses (structural-grey and electronic-red data point) and the effect of a gold interface on the electronic one (red and yellow). This quantitative measurement of size-dependent switching in $VO_2$ below single-domain size suggests a number of extensions of this method: for example using specific plasmonic modes and structures to probe discrete volumes of other phase change materials.

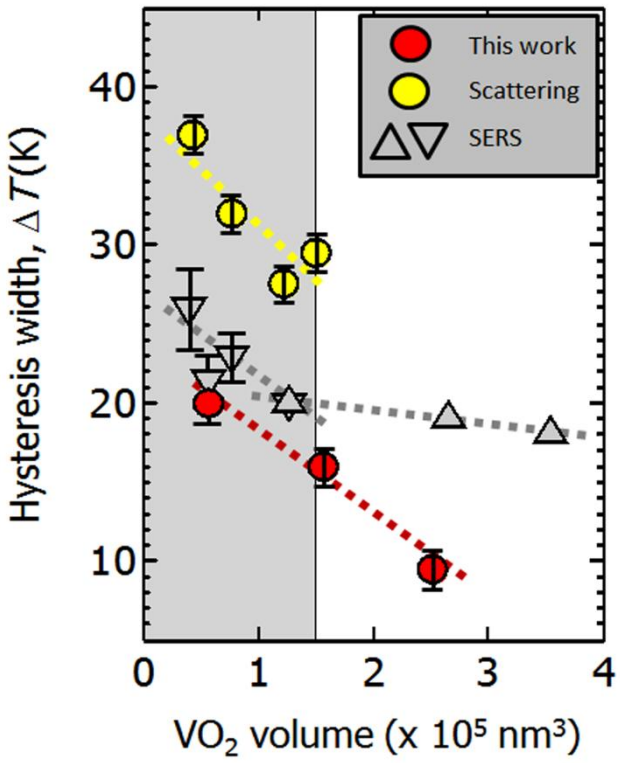


**Figure 4.14. Size-Dependent Hystereses.** Plot comparing results of hysteresis widths *vs.* $VO_2$ volume under investigation obtained from various experimental techniques. Donev *et al.* probed size effect structural phase transition using SERS of Au/$VO_2$ nanodisks while Lopez *et al.* probed the light-scattering properties of arrays of pristine $VO_2$ nanodisks. In this work (red circles), size-effect detection was efficiently achieved by monitoring incremental shifts in the plasmonic response of SRRs/$VO_2$ nanocomposite metamaterial as the sample is thermally driven to transition. The shaded region represents the approximate volume of a single domain nanocrystal.

### 4.3.5 Conclusions

We have demonstrated here that our hybrid Au-SRR/$VO_2$ film nanostructure can utilize the underlying size-dependent switching properties of the $VO_2$ to selectively modulate the resonance of SRRs. In other words, either by incorporating complex plasmonic structures

in a medium with a changing dielectric or by placing defined volumes of phase change material near a plasmonic component — e.g. in the gap or around the periphery of the SRR — we can envision single plasmonic components with distinct spectral responses each being modulated selectively depending on the size of the PCM being integrated.

### 4.4 POLARIZATION-DEPENDENT HYBRID NANOMODULATOR

As shown in sections 4.2 and 4.3, using a solid-solid phase transformation with high dielectric contrast between the parent and the product phase offers great tunability of the plasmonic nanostructure optical response. However, as discussed in those sections, there are several issues that are inherent and specific to the various nanostructure designs. In the stacked nanostructure case (i.e. Au-*NS*/$VO_2$-*NS*), contact of the Au nanostructure with the $VO_2$ can lead to poor switching efficiencies, especially because of the final annealing step. Moreover, smaller nanoparticles seem not to switch as efficiently as the bigger ones. This therefore places a restriction in the operating wavelength due to a limit in the size of the nanoparticle that can be used to provide enough modulation. In the case of the Au-*NS*/$VO_2$-*film*, although smaller nanoparticle can be switched effectively as was demonstrated in Chapter 1 while size-dependent switching in $VO_2$ can also be derived by using more complex nanostructures (*§ 4.3*), the high absorption of the $VO_2$ film, especially in the visible-NIR region, might not be suitable for every application. Thus, a more flexible design is required that can potentially cater for each of those specific technological requirements. One of such designs – coined hybrid nanomodulator – is proposed in this section and is illustrated in figure 4.15.

This design relies on spatially confining electromagnetic field on the nanometer scale using a plasmonic nanostructure while *simultaneously* tailoring the near-field environment of its optical nanofocus. As seen from figure 4.15, this hybrid nanomodulator consists of two nanodisks that are made of two different materials and positioned next to each other, but not touching. In this particular case, one is a Au plasmonic nanodisk while the other one is a PC-$VO_2$ nanodisk. On one hand, modulation of the bare $VO_2$ nanodisk can be achieved, but is restricted in its operating wavelength and modulation contrast, thus limited by its intrinsic dipole resonance when metallized. On the other hand, the plasmonic nanodisk spectral position and lineshape can be shifted easily by changing its size, shape or material, but however requires an active component to achieve modulation. Therefore, the synergy between these two nanoparticles provides greater room for reconfigurability. Although such design can now be easily realizable (and on a large scale) by a newly developed technique termed hole-colloid-mask lithography[303,304], we study here the precise effect of tailoring the near-field nanoenvironment of the plasmonic nanoparticle. Consequently, we employ electron-beam lithography to carefully and progressively approach the PC-$VO_2$ nanodisk in the reactive near-field of the Au nanodisk. In so doing, modulation is shown to be achieved not only when the PCM is in close proximity to the plasmonic near-field spot, but this interaction can be turned on and off by varying polarization of the incoming beam. In such a design, since modulation can occur "at a distance," this preserves the quality factor of the plasmonic nanoresonator as well. This concept paves the road towards ultrafast-all-optical signal modulation using a single hybrid

nanoswitch whose specificities can be exquisitely tuned by varying plasmonic geometries and the materials' intrinsic properties.

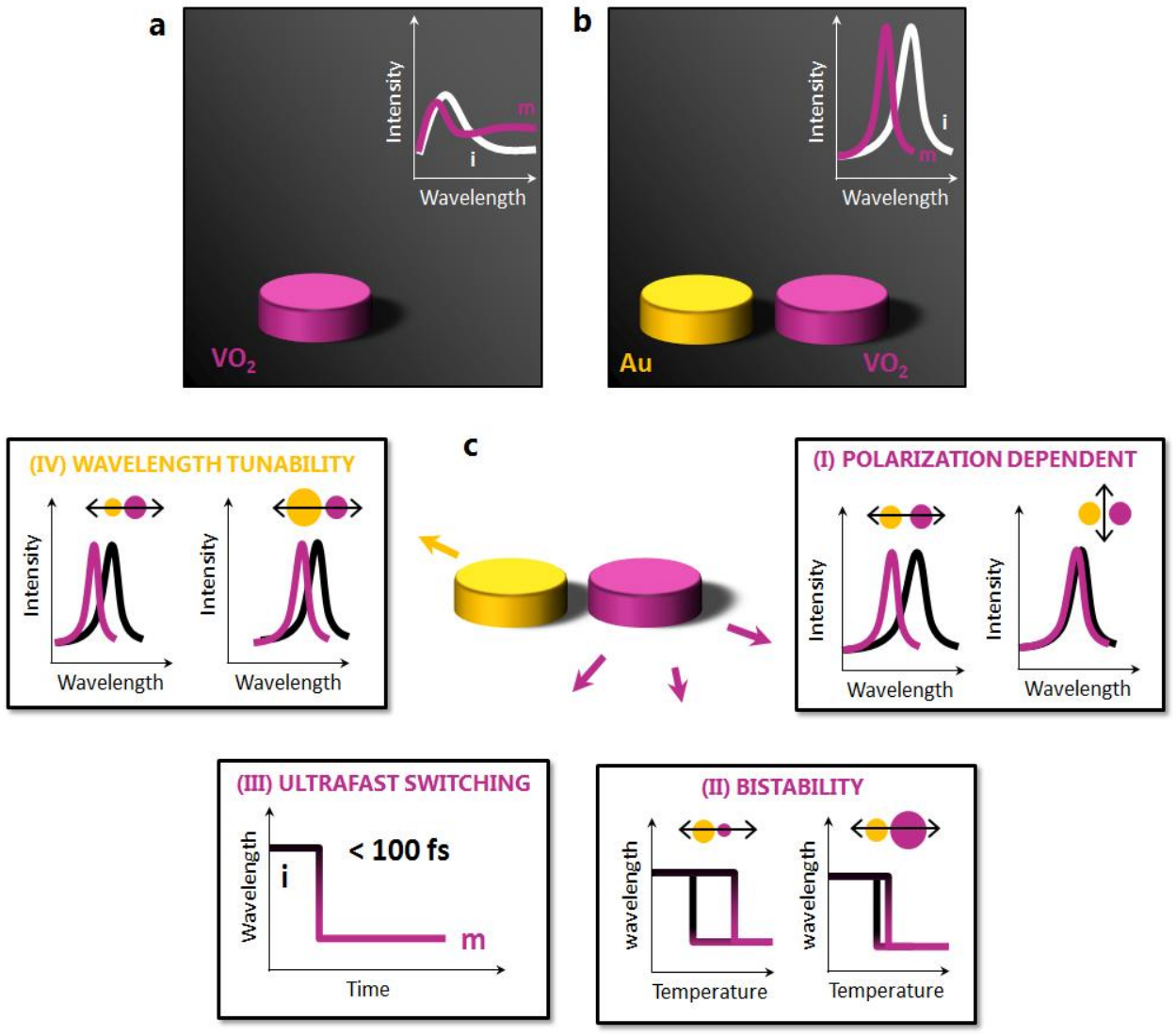


**Figure 4.15. Schematic Representation of a Hybrid Nanomodulator.** (a) Optical modulation of a single vanadium dioxide nanostructure by thermally triggering the phase-transition from its insulating (white) to metallic (magenta) state. The nanostructure alone shows a strongly damped localized surface plasmon resonance in the near-IR region with low signal-to-noise ratio. (b) Modulation using a resonant nanoantenna-enhanced scheme with the same $VO_2$ nanostructure but used as a tailored phase-changing nanoenvironment.

When positioned in the near-field region of a plasmonic antenna, here a gold nanodisk, greater tunability with larger signal is achieved. (c) By nanostructurally integrating these two materials, reconfigurability can be also achieved. Few examples are (I) polarization-dependent modulation, (II) bistable switching by utilizing the size-dependent switching properties of the PCM, (III) ultrafast switching of the intrinsic PCM and therefore the nanomodulator itself and (IV) tunability of this nanosystem by varying the plasmonic nanoantenna size and/or shape.

### 4.4.1 Fabrication of Hybrid Nanomodulators

In order to fabricate such nanostructures, a three-stage lithography is employed as follows and schematically depicted in figure 4.16: gold markers were lithographically fabricated on ITO coated glass substrate by means of (1) electron-beam lithography on PMMA, spun at 2500 r.p.m and baked at 180°C for 90 seconds; (2) e-beam evaporation of 20 nm of gold on the patterned substrate, measured by a quartz-crystal microbalance; (3) subsequent lift-off procedure using a Remover PG bath at 70°C for 20 min. The gold nanodisk lattices were fabricated using the same protocol, resulting in nanodisks of height 20 nm and unit cell of 600 nm, each plasmonic lattice having a footprint of 100 x 100 $\mu m^2$. Using the gold alignment markers, a third step of lithography was performed by coating once more PMMA resist on the sample and writing the phase-changing $VO_2$ lattice pattern at sub-20-nm level. Subsequently, the vanadium dioxide nanodisks were generated by (i) pulse laser ablation of a vanadium metal target (PLD: $\lambda$ = 248 nm, 25 ns pulse duration, 3.86 $mJ/cm^2$ fluence, 10 Hz repetition rate and 10 mTorr of $O_2$ gas) to render, after subsequent lift-off, nanodisks of amorphous, sub-stoichiometric vanadium dioxide (40 nm $VO_{X=1.7}$ nominal thickness); (iii)

thermal anneal of the sample (450°C, $O_2$ gas at 250 mTorr for 20 min) to render the NPs crystalline and stoichiometric.

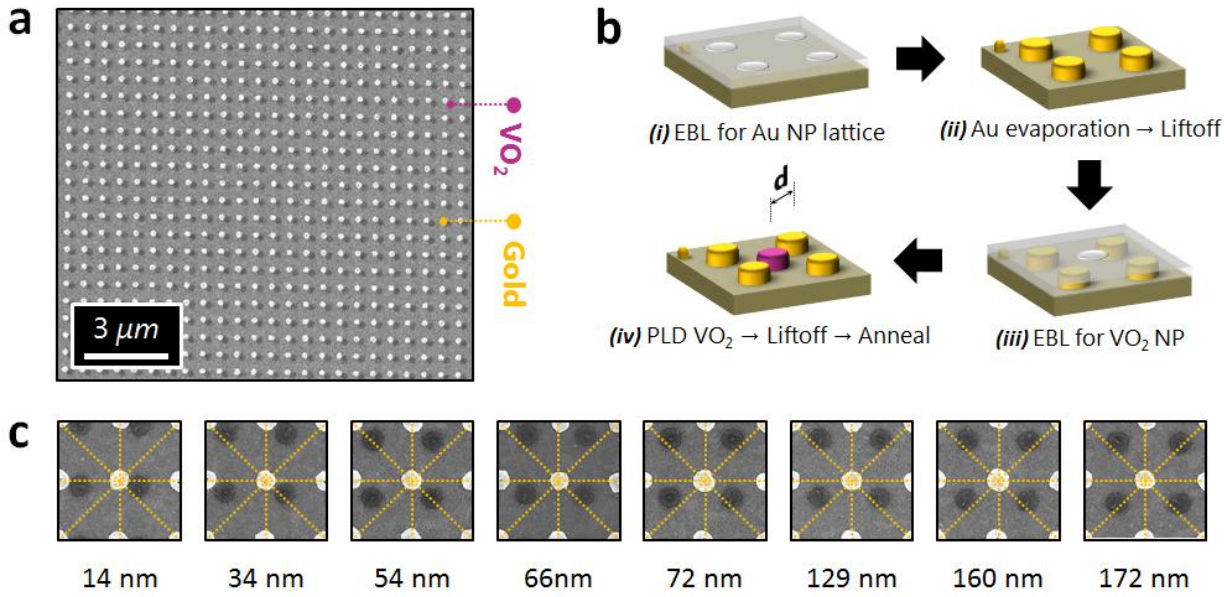


**Figure 4.16. Fabrication Protocol for the Hybrid Nanomodulator Arrays. (a)** SEM for the 14 nm separation hybrid nanostructured array. **(b)** Fabrication protocol of a planar plasmonic/phase-changing materials using a three step electron-beam lithography process including gold evaporation, pulsed laser deposition with subsequent lift-off procedures after each deposition method. A final annealing step that renders the vanadium dioxide nanocrystals crystalline and thus phase-switching is required (iv). **(c)** SEMs of the various arrays under study with varying separation (d nm) between the hybrid nanostructures.

### 4.3.2 Optical Characterization of Hybrid Nanomodulators

Extinction measurements were acquired as follows: (i) the 100 × 100 $\mu m^2$ plasmonic/phase-change lattice of interest was positioned using micrometer drives under white light illumination from a tungsten lamp (90 $\mu$m spot size and polarized at 45° (perpendicular) or 135° (parallel) to the interacting dimer) while concurrently being

imaged onto a CCD camera in the x-y plane; (ii) the focus (z-plane) was then visually adjusted by displacing the 5× microscope objective with a numerical aperture of 0.12; (iii) extinction at room temperature was then measured (integration time of 8 ms and average of 200) (iv) the sample was then heated to 95°C, well above the transition temperature of the $VO_2$ nanodisks, and extinction measurements for the various lattices were repeated. As flat-field, transmission spectra of the ITO-coated glass at room temperature and at 95°C were used when the $VO_2$ nanodisks were insulating and metallic respectively. Figure 4.17 shows the resulting spectra when the $VO_2$ nanodisk is switched from its insulating to metallic state. As seen from the spectra and corroborated with the SEM, an experimental minimum separation of ~ 14 nm is obtained corresponding to a modulation shift of ~ 10 nm. Although this is the lowest resolution achievable experimentally, the simulations (discussed in the next section) show that modulation of up to 50 nm can be reached. We note that such spectral shift has been obtained without any optimization of the plasmonic nanostructures (i.e. tailoring and focusing the near-field electromagnetic energy by using nanopyramids or nanotriangles for example).

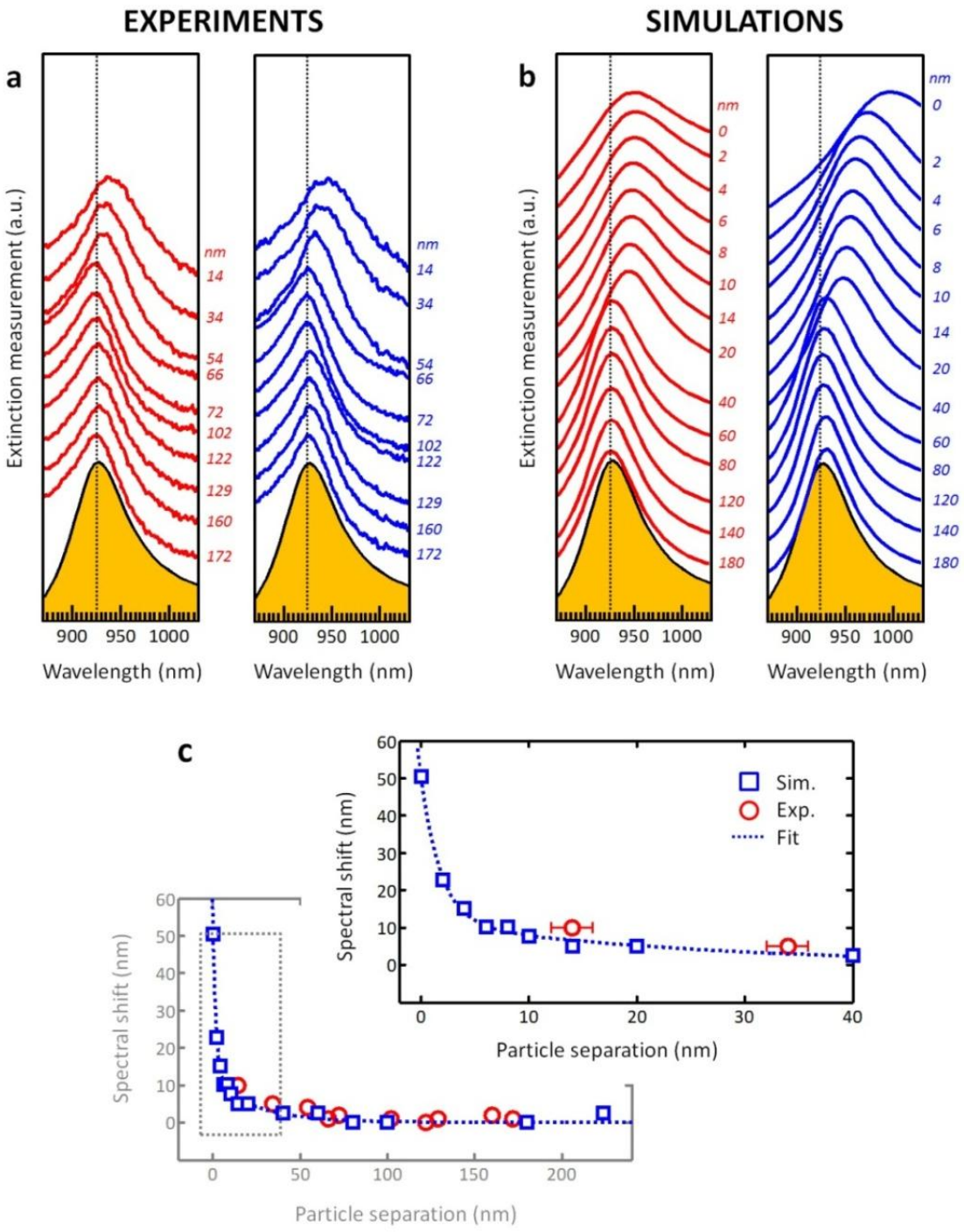


**Figure 4.17. Experimental and Simulated Optical Spectral Responses for the Nanomodulator Arrays. (a)** Experimental spectra for the 172, 160, 129, 122, 102, 72, 66, 54, 34, 14 nm interparticle separation arrays when the vanadium dioxide nanocrystals are

in the metallic (red) or insulating (blue) state. **(b)** Simulated spectra of the hybrid nanomodulator for interparticle separation of 180, 140, 120, 80, 60, 40, 20, 14, 10, 8, 6, 4, 2 and 0 nm when the $VO_2$ nanodisk is its metallic (red) and insulating (blue) state. The orange shaded plots in each figure represent the simulated optical response of the static gold lattices which match very closely both with the experimental results and with the case where the $VO_2$ nanostructures are not in the near-field region of the plasmonic nanoparticle. As the phase-switching nanostructures approach the active plasmonic near-field spot, the spectral signature can be substantially modulated. **(c)** Summary of spectral shifts comparing both experimental and simulated results. The error bar for the interparticle separation was estimated to be ~ 2 nm while the peak determination is assessed to be ~ 1 nm.

### 4.3.3 Simulating the Optical Response of Hybrid Nanomodulators

Similar to previous simulation sections, 3D full-field electromagnetic wave calculations were performed using Lumerical FDTD Solutions®. A unit cell of the plasmonic lattice structure (Au nanodisks of height 20 nm and radial dimension of 96 nm; $VO_2$ nanodisks of height 32 nm as averaged by atomic force microscopy on another sample and radial dimensions of about 96 nm), including the ITO-coated glass substrate, was simulated using periodic boundary conditions along the *x* and *y* axes and perfectly matched layers along the propagation of the electromagnetic waves. Broadband planes waves (700-1200 nm) were launched incident to the unit cell. While one monitor was placed in the glass substrate to record transmission (z = - 400 nm), another monitor (z = 10 nm) was used to record the spatial near-field enhancements. In all the simulations, we employed an auto-meshing accuracy of 3 together with an overriding cubic mesh size of 1 $nm^3$ around the nanoparticles and the gap. The dielectric functions for the Au was obtained from Johnson

and Christy's data while those of the $VO_2$, both insulating and metallic, were obtained from Verleur's paper.

As shown from figure 4.17b, we can clearly see that as the PC-$VO_2$ nanodisk approaches the near-field region of the plasmonic nanodisk, modulation can be achieved by varying its state (metallic or insulating). This region where modulation can occur (near-field) is estimated to be ~ 20 nm. In the extreme geometrical case of the kissing nanodisks (d = 0 nm) a plasmon spectral shift of ~ 50 nm is recorded. In order to study the coupling dynamics of this hybrid nanomaterial further, we investigate the near-field behavior of the system in two extreme cases – with the electric field polarization parallel and perpendicular with respect to the long axis of the system and for the two extreme cases in interparticle distance: the kissing nanodisks and when the $VO_2$ nanodisks are positioned almost at the center of each Au unit cell in the plasmonic lattice (d = 180 nm). As seen in figure 4.18b, when light is polarized parallel with respect to the long axis of the system, the Au nanodisk EM near-field is affected substantially while when the light is polarized perpendicularly, its near-field remains unaffected. Thus, this change in electron oscillation in the Au nanodisk when the neighboring $VO_2$ nanodisk is either metallic or insulating creates a shift in the plasmonic response. Interestingly, we note that no modulation is possible when the incoming light is polarized along the short axis of the system. Therefore, this effectively demonstrates the tight localization of the plasmonic near field as the latter is essentially myopic to changes in the $VO_2$ nanodisk (although almost in contact with the Au nanoparticle). This scenario has an identical effect to the $VO_2$ nanodisk placed at the center of the Au unit cell lattice because no modulation is possible.

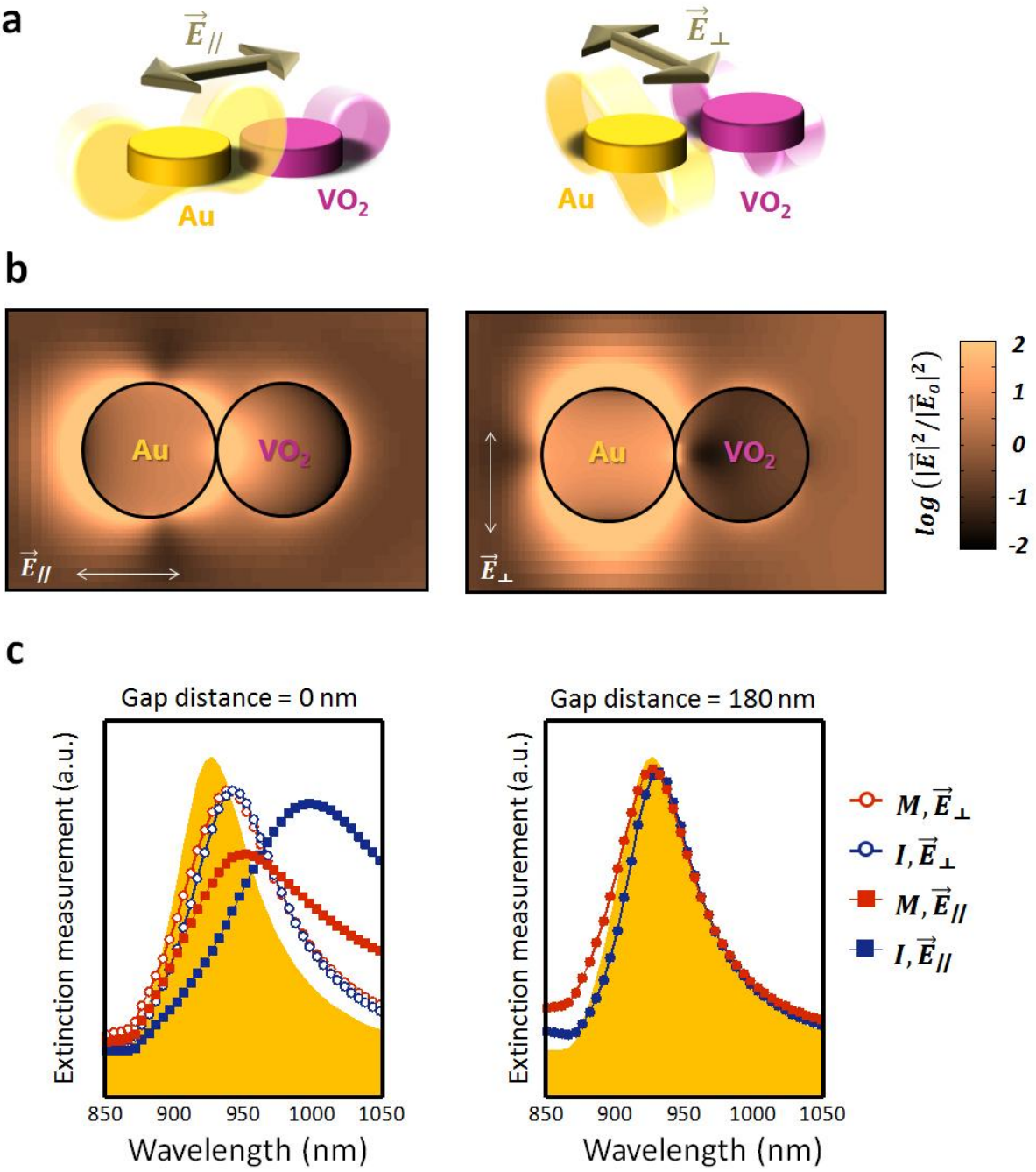


**Figure 4.18. Near-Field Polarization-Dependent Modulation. (a)** Schematic illustrating the ability of polarized nanoscale light fields to selectively interrogate the phase-changing nanoenvironment. When polarized perpendicularly, that is along the short axis of this nanosystem, modulation is drastically reduced, even for the extreme case of kissing hybrid

nanostructures. **(b)** Electromagnetic field enhancement profiles for a single hybrid nanomodulator (gap distance = 0 nm and $VO_2$ state is metallic) for both polarization cases. **(c)** Spectra for heterodimer gap distances of 0 and 180 nm when light is polarized parallel and perpendicular to the long axis of the dimer.

### 4.4.4 Conclusions

In summary, we have shown that hybrid heterodimers can potentially be a very flexible design not only allowing for control in the position of the plasmonic resonance but also at what temperature the modulation can be executed (by changing the size of the $VO_2$ nanoparticle). In addition, since our design is polarization sensitive, such hybrid plasmonic nanomodulator could potentially circumvent the slow switching off speeds that is inherent to $VO_2$ relaxation dynamics (tens to hundreds of ns). More specifically, one could think of an ultrafast switch that could be switched "on" using an ultrafast femtosecond pulse (for e.g. a 50 fs pulse from a Ti::Sapphire) while electro-acousto-optic effects could be used to change the polarization of the light, thus artificially switching "off" the nanomodulator in picoseconds. Thanks to this multi-step lithographic process, annealing issues that were inherent to the previous designs have now been solved as the $VO_2$ (crystalline, stoichiometric and switching) nanodisks can be fabricated first, followed by fabrication of the Au nanostructures.

At present, only two experiments (both published in 2011) were successful in fabricating such design, allowing the demonstration of enhanced gas sensing[3] and nanoscale spectral and spatial photon-sorting[242]. As mentioned previously, such designs can now be routinely fabricated on a wafer scale by a hole-colloid mask process[19]. Here we

have shown that our hybrid nanomodulator offers a versatile platform to control optical responses and careful material's choice along with specific plasmonic geometrical parameters open possibilities for a wide range of practical applications.

## 4.5 ACKNOWLEDGEMENTS

The work presented in section 4.2 was performed in close collaboration with Prof. Maier's research group at Imperial College London (Dr. Dang Yuan Lei and Dr. Yannick Sonnefraud) and sponsored by the Engineering and Physical Sciences Research Council (EPSRC) and the Leverhulme Trust.

The work present in sections 4.3 and 4.4 were performed in its entirety at Vanderbilt University and were supported by a research assistantship provided by the National Science Foundation (ECE-0801980). I thank B. K. Choi for assistance with gold evaporation and J. Nag for helpful discussions regarding vanadium dioxide.

# CHAPTER 5

# PLASMONIC HOT ELECTRON INJECTION AS A NOVEL TECHNIQUE FOR DRIVING ULTRAFAST PHASE TRANSITION

"The only reason for time is so that everything does not happen at once."

~ *Albert Einstein, 1921 Nobel Laureate*

## 5.1 INTRODUCTION

As discussed in Chapter 1 (*§1.3.3*), ultrafast photoinduced phase transitions could revolutionize data-storage and telecommunications technologies by modulating electron and photon transport in integrated nanocircuits at terahertz speeds. In quantum materials, phase transitions can provide functionality in nanophotonic devices[84,251] because the interplay among microscopic degrees of freedom such as charge, lattice and spin[107,305] conspires to generate macroscopic quantum phenomena such as multiferroicity[15], insulator-to-metal transition[16] and colossal magnetoresistance[14]. Although these interactions are well documented for bulk single crystals and thin films, little is known about the ultrafast dynamics of nanostructured PCMs and when interfaced with active plasmonic elements. Moreover, ultrafast optical excitation of PCMs provides the ultimate non-contact control over their properties by creating non-equilibrium states of matter not always accessible under equilibrium conditions.

Recently, such phase-transition (PT) events have been shown to occur on a timescale even shorter than a single phonon period, driven by electronic acceleration of

atomic motions caused by rapid modification of the lattice potential-energy surface[306,307], indicating that PT can be triggered potentially on an even faster timescale through ultrafast perturbation of the lattice potential. As shown in figure 5.1, such coherent phonons can be generated within the $VO_2$ lattice by pump pulses with fluences that are below the switching threshold. Fourier transform of the probed transmission revealed the various vibrational modes of the system as shown. At higher pump fluences, these Raman-active modes collapse and therefore *mark the onset* of phase transition of the $VO_2$ to its metallic state. Consequently, the appearance and disappearance of the coherent phonon modes is an accurate marker such that dynamical phase transitions can potentially be clearly identified.

Taking a step further, Wall *et al.* showed that at low pump fluence (below threshold), the coherent phonons could actually be controlled by constructive or destructive interference. This was made possible in a pump-pump-probe set-up where the delay between the two pump pulses was tuned to the intrinsic coherent vibration of the $VO_2$, that is $\sim$ 176 fs. The results are summarized in figure 5.2. Thus, not only can this technique be used to probe ultrafast processes by monitoring changes in the lattice potential, but this also demonstrates the ability to coherently control phase transition events, provided the proper pump fluence and wavelength are chosen[306].

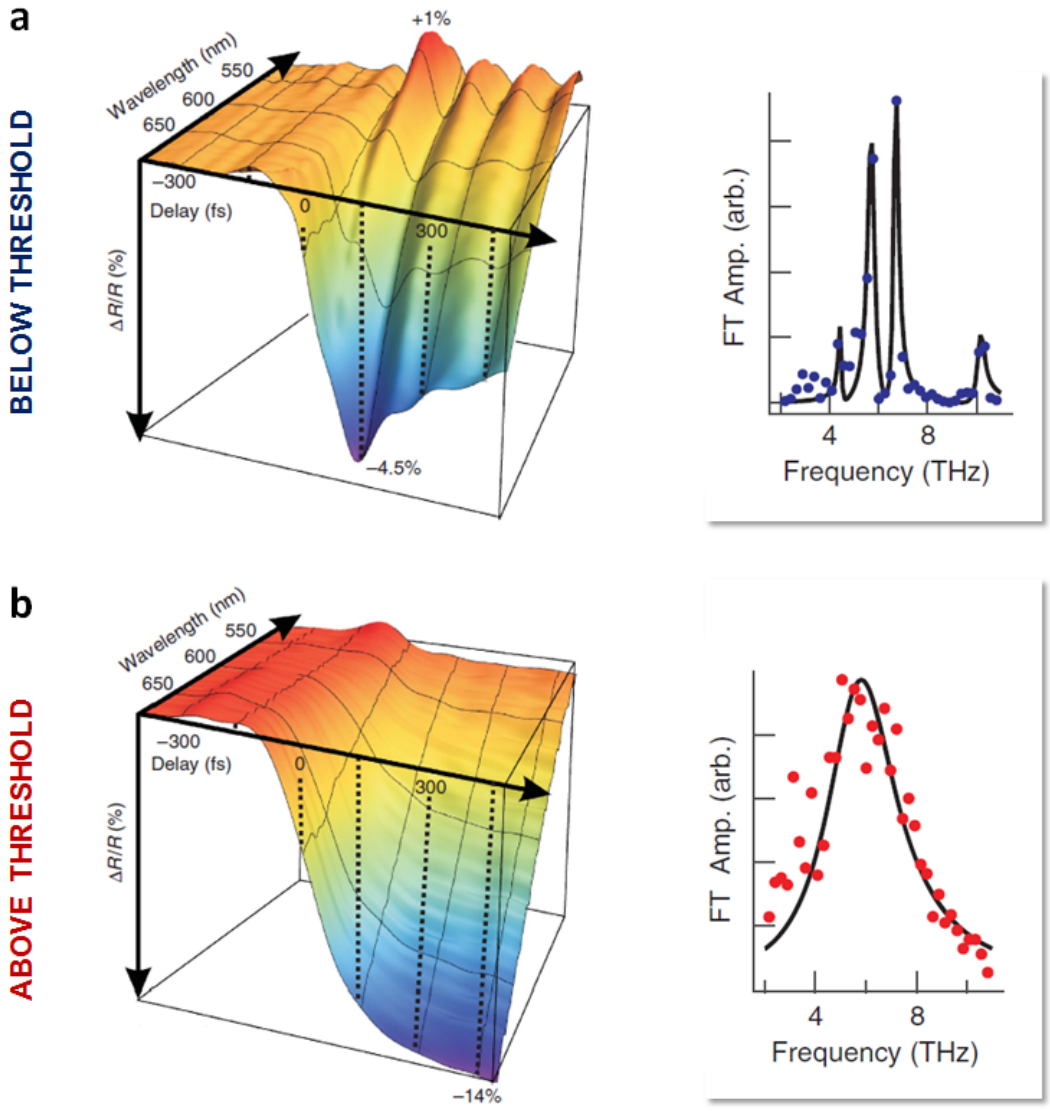


**Figure 5.1: Coherent optical phonons generation in $VO_2$. (a)** Ultrafast white-light reflectivity as a function of probe wavelength and delay below above the photoinduced phase transition threshold. Below threshold, signals at longer wavelengths are dominated by a large negative transient with the oscillations dominating the signal at shorter wavelengths. Below threshold the four lowest Raman active modes are clearly observed (solid line indicates the best fi t to four Lorentzian oscillators). **(b)** Ultrafast white-light reflectivity above threshold. We note that no oscillations are observed, showing that the phonon modes are lost over the entire visible spectrum with a single broad feature observed. Adapted from reference [306].

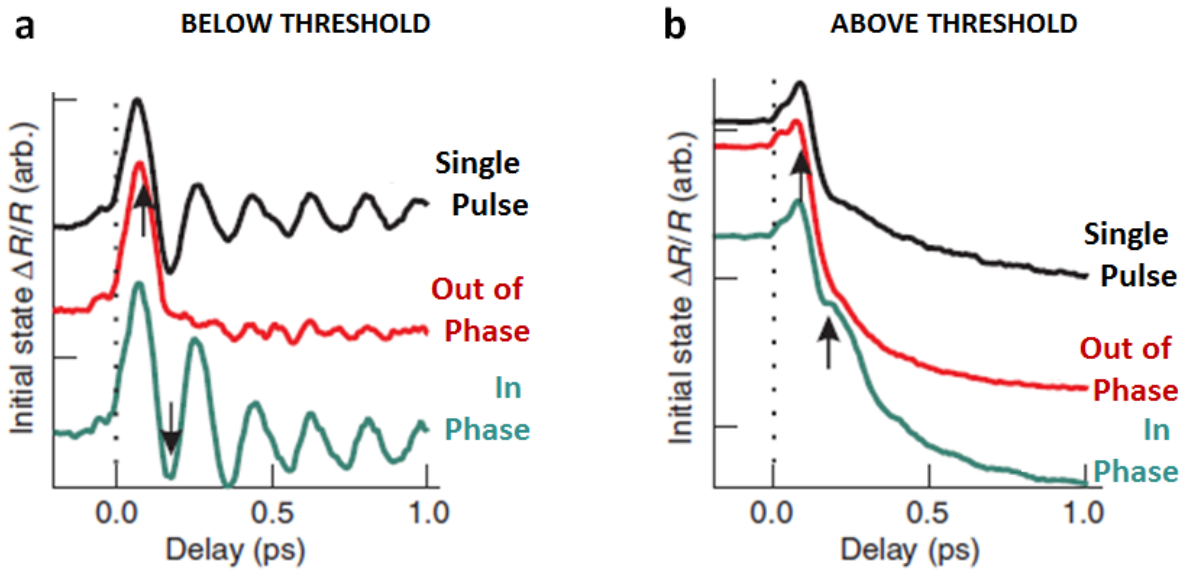


**Figure 5.2. Coherent control of optical phonons in $VO_2$.** Pump–pump probe measurements **(a)** below and **(b)** above threshold. Traces correspond to the transient reflectivity generated by a single pump pulse (black) and to a double-pulse excitation when the pump–pump delay is set to be out-of-phase, i.e. by π (red), and in-phase (green), i.e. by 2π, with the 5.7-THz phonon mode. The arrows indicate the arrival time of the second pump pulse. Adapted from reference [306].

Here we illustrate a novel generalizable *all-optical* method for triggering phase-transformation events on a femtosecond timescale (i.e. even faster that the $VO_2$ single phonon cycle itself) by photo-injecting hot electrons generated by surface-plasmon excitation into $VO_2$ nanoislands. In this particular example, plasmonic photoinjection process reduces the switching threshold by about five times. By exciting the surface-plasmon resonance in a sparse net of gold nanoparticles (hereinafter, Au-nanomesh) with ultrafast optical pulses, energetic electrons are injected ballistically across the Au/$VO_2$

interface. Density-functional calculations show that the injected electrons couple to the lattice to cause a catastrophic collapse of the $A_{1g}$ phonon mode of the $VO_2$ lattice. Moreover, the results show how plasmon damping by hot-electron effects – which is detrimental in plasmonic circuitry due to linewidth broadening[308] – can be harnessed for PT processes.

The response of the plasmonic/phase-change material is both thermodynamically and wavelength tunable; proper choice of ultrashort pulse duration, wavelength or multi-pulse sequencing can control the non-equilibrium thermodynamic evolution of the PT[25], while the plasmon resonance can be altered by selection of the nanostructure composition, size or shape[20,309]. The wavelength selectivity is demonstrated by tuning the plasmon resonance frequency of the Au-nanomesh (800 nm) to coincide with the center wavelength of the femtosecond laser pulse. The non-equilibrium thermodynamic character of the ultrafast phase transition is shown by the fact that the Au-nanomesh *does not affect* the critical switching temperature ($T_c$) of the IMT in the thermal equilibrium limit, as will be discussed in the next section. This demonstration of hot-electron-driven phase transition controlled by an *all-optical* ultrafast technique therefore represents a critical step towards developing hybrid plasmonic/PCMs with optimal switching thresholds.

## 5.2 EXPERIMENTS AND DISCUSSION OF RESULTS

### 5.2.1 Sample Fabrication

Samples of PCM $VO_2$ nanoislands on glass substrate were grown by a pulsed-laser deposition method[153]: Specifically here, (i) ablation of a vanadium metal target using a KrF excimer laser ($\lambda = 248$ nm; 25 ns pulse duration; 3.84 mJ cm$^{-2}$ fluence, 25 Hz repetition

rate, 40 nm nominal thickness) in 10 mTorr of $O_2$ environment; (ii) a subsequent thermal anneal was performed at 450°C in 250 mTorr of $O_2$ for 45 minutes to render the nanoislands stoichiometric, crystalline and switching. While one sample was used as control, the other sample was coated with 5 nm thick gold using electron-beam evaporation and monitored by a quartz crystal microbalance. Figure 5.3a,b show the schematics and SEMs of the resulting sample.

### 5.2.2 Equilibrium Limit

Hereafter, we compare $T_c$ of the two samples – pristine PCM-$VO_2$ nanoislands and the Au/$VO_2$ hybrid nanomaterial – by optical characterization. Broadband transmission hysteresis measurements were performed by focusing white-light from a 3000 K tungsten lamp using a 5x, 0.12 NA microscope objective onto the sample and collecting the transmitted light via a 5x, 0.20 NA microscope objective. An InGaAs photodiode placed at the back focal plane of the objective was used to collect the resultant transmitted light as the sample was thermally modulated by a Peltier Cooler. The temperature was monitored in situ by a K-type surface-mounted thermocouple. The integrated white-light transmission hysteresis curves exhibited switching temperatures of ~ 68.1°C and 68.7°C for pristine $VO_2$ and hybrid Au/$VO_2$ nanoislands, respectively. This is shown in figure 5.3c. Consequently, deposition of the Au-nanomesh on the PCM does not alter the equilibrium switching properties of the electronic or lattice configurations. This is in sharp contrast to a recent study whereby the $VO_2$ was doped by Au nanoparticles, which drastically modifies the thermal character of $VO_2$ PT[240]. Moreover, our results show that this is the case even for

nanoislands of $VO_2$, where greater contact electrification effects would in principle be noticeable due to strong dependence on effective contact area[310]. Next, extinction measurements were acquired by replacing the photodiode with a spectrometer in a quasi-confocal geometry. Spectroscopic measurements (figure 5.3d) depict characteristic properties of the $VO_2$, displaying a sharp but static feature at ~ 390 nm corresponding to a O2$p$→V3$d$ absorption peak and the appearance of a dipolar near-IR response in the $VO_2$ nanoislands when metallized (darker purple)[311]. When normalized to the pristine $VO_2$ nanoislands, the Au-nanomesh spectra display a plasmonic response centered at 800 nm, near the 790 nm pump wavelength. The resonance of the Au-nanomesh is broadened due to the large size distribution of the underlying $VO_2$ nanoislands and blue-shifts by ~ 3 nm when $VO_2$ undergoes its characteristic PT (figure 5.3e)[297].

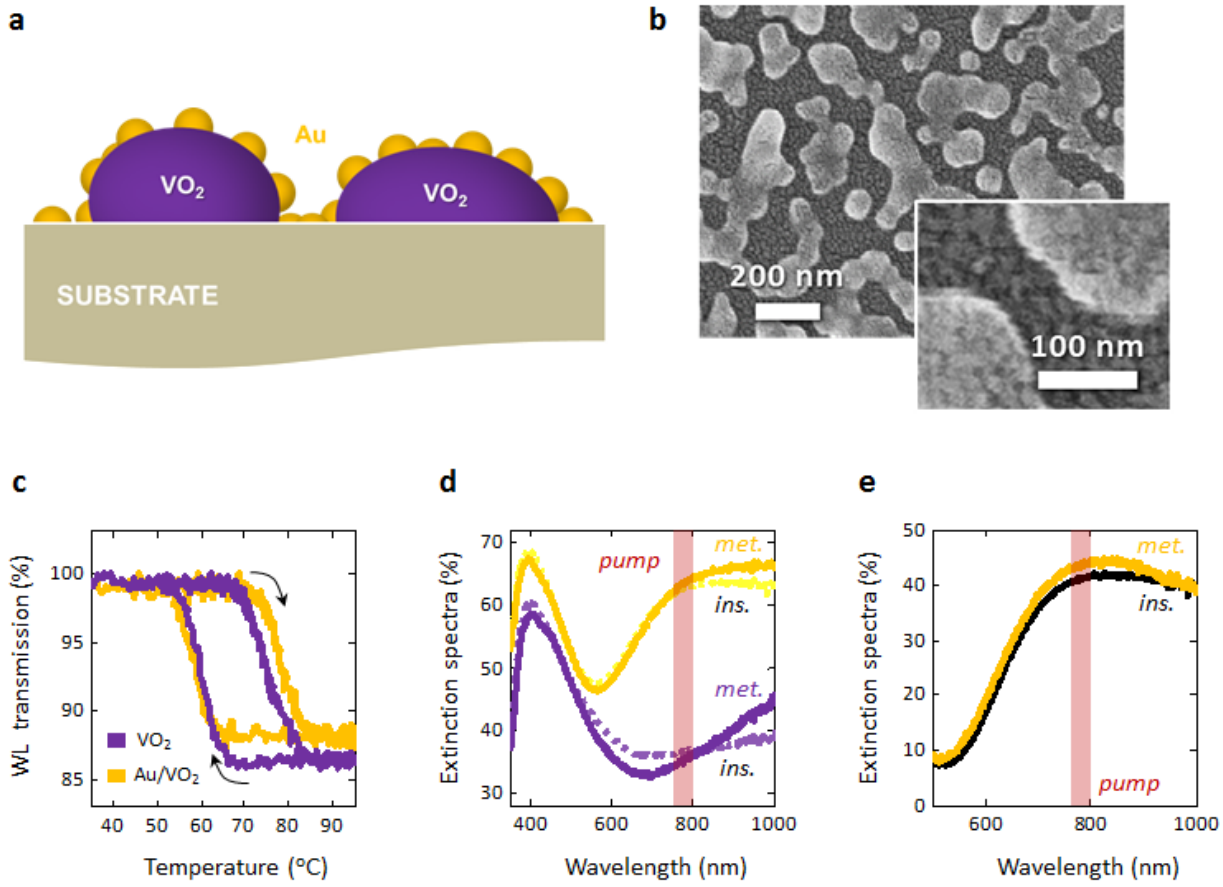


**Figure 5.3. Characterization of Hybrid Au/PCM-$VO_2$ Nanomaterial. (a)** Schematic of the hybrid nanomaterial with 5 nm thin Au-nanomesh coating the vanadium dioxide nanoislands core (40 nm nominal height). **(b)** Scanning electron micrograph of the hybrid nanomaterial. **(c)** White-light transmission hysteresis measurement of Au/$VO_2$ hybrid (yellow) and pristine $VO_2$ nanoislands (purple) samples when modulated thermally. Note that $T_c$ is $\sim$ 68°C in both cases. **(d)** Extinction spectra of the two samples (purple: pristine $VO_2$ and yellow: Au/$VO_2$) when at 25°C (insulating-$VO_2$) and 100°C (metallic-$VO_2$). Note the increase in extinction in both cases where the $VO_2$ switches metallic (darker yellow and darker purple) **(e)** Differential extinction spectra of figure (d), depicting the plasmonic response of the Au-nanomesh that slightly blue shifts when the $VO_2$ switches from insulating (black) to metallic (yellow).

### 5.2.3 Non-Equilibrium Limit

To reveal the ultrafast non-equilibrium character of the hybrid material, the differential transmission of both samples is compared (at 300 K) in a non-degenerate pump-probe scheme as a function of laser fluence (figure 5.4). A 50 fs, 790 nm (1.57 eV) pump pulse above the 0.67 eV $VO_2$ band-gap[225] excites a 67 μm-diameter spot at an angle of 12 degrees normal to the samples while a delayed probe pulse monitors the phase transformation. The probe, generated by optical parametric amplification, was tuned below the band gap to 3100 nm (0.4 eV) to maximize dielectric contrast between the "on" (metallic) and "off" (insulating) states, thus enabling detection of only a few 100 $\mu m^3$ of PCM-$VO_2$. The transmitted light was measured on a photodiode detector connected to a lock-in-amplifier and the experiment was carried out at a repetition rate of 100 kHz. The duration of the pulse was ~ 50 fs, measured by autocorrelation. Also, at a laser repetition-frequency of 100 kHz, the $VO_2$ nanoislands recover to their insulating phase between pulses, confirmed by the negligible background transmission signal at negative time delays.

### 5.2.3a Ultrafast spectroscopy of pristine $VO_2$ nanoislands

For the pristine $VO_2$ nanoislands, pump fluences below threshold result in a large transient transmission that decays rapidly to its original values (figure 5.4a-c). This fast-decaying signal resembling a typical semiconductor response is associated with the interaction of the laser field with the electronic system and is characterized by $\tau_e$, the electronic lifetime[306]. However, at a pump fluence of 1.13 mJ $cm^{-2}$ (figure 5.4d), a slowly decreasing transmission that reaches a minimum at ~ 75 ps is observed, signifying the initial

structural transformation of the $VO_2$ nanoislands, characterized by a lattice lifetime $\tau_l$. This fluence threshold corresponding here to one photon interacting with ~ 70 unit cells agrees with previous experimental findings when one accounts for $VO_2$ filling fraction, as calculated in the next section. This minimum in transmission is associated with the slower structural dynamics. It occurs sooner with increasing fluence and with intensities capable of creating electron densities of order ~ $10^{20}$-$10^{21}$ electrons/$cm^3$ in $VO_2$ – corresponding to the carrier density for the metallic state at thermal equilibrium – this produces an almost instantaneous transformation to the metallic phase with a characteristic step-like response in $VO_2$ PT. This fully metallic phase corresponds to the rutile (R) structural phase, described by Cavalleri *et al.* in ultrafast x-ray studies[219].

The enhanced speed of the monoclinic-rutile transformation with increasing fluence can be understood by a combination of two effects. First, the photogenerated electrons have sufficient densities to melt the Mott state via Coulomb screening due to charge redistribution following excitation. Second, the holes that are created in the 3d parallel bands destabilize the V-V dimers to create to local oscillations[228,230]. These local oscillations, corresponding to coherent 6 THz phonons, assist in breaking the Peierls-distortion component of the PT[109,236]. While these optical phonons can last for hundreds of picoseconds[229,233], the coherent structural response lasts for only few picoseconds and serves to accelerate the formation of the metallic phase throughout the laser-excited volume[236].

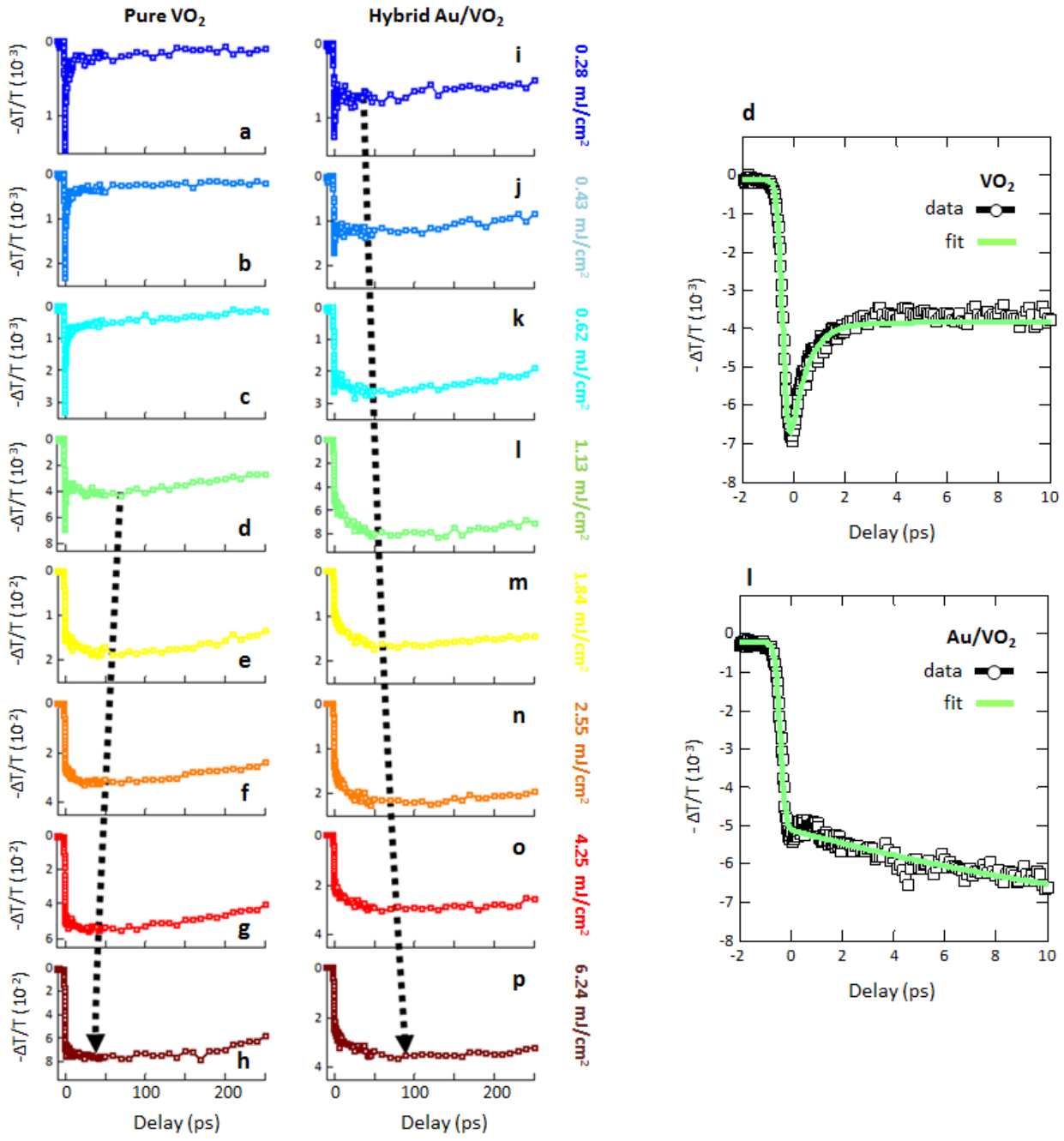


**Figure 5.4. Ultrafast Optical Measurements: Pristine vs. Hybrid.** Ultrafast differential transmission data taken at 300 K over 250 ps at all pump fluences for pristine $VO_2$ (**a-h**) and hybrid Au/$VO_2$ nanomaterial **(i-p)**. Ultrafast responses for an exciting pump fluence of 1.13 mJ $cm^{-2}$ for pristine $VO_2$ **(d)** and hybrid Au/$VO_2$ nanomaterial **(l)** during the first 10 ps. The empty squares are experimental data while the green lines are fits to the data. In **(l)**,

complete electronic and structural transformation is already achieved for the hybrid nanomaterial. The rise time for both the pristine $VO_2$ and hybrid nanomaterial samples is ~ 264 ± 28 fs and 289 ± 31 fs respectively, comparable within experimental variations. The dotted lines are guides to the eye depicting evolution in the minima in the relaxation curves representing the lattice system as a function of pump fluence.

### 5.2.3b Ultrafast spectroscopy of hybrid Au/$VO_2$ nanomaterial

In sharp contrast to pristine $VO_2$, the hybrid nanomaterial shows no sign of threshold-switching behaviour, suggesting that the structural PT component has already been initiated even at the lowest pump-fluence (figure. 5.4i and figure 5.7a,b). For example, comparing the first 10 ps dynamics for the 1.13 mJ $cm^{-2}$ case (figure 5.4d and l) reveals that the hybrid nanomaterial structural PT is triggered within the first picosecond. This marked difference is associated with non-equilibrium excited electrons from the Au-nanomesh that are injected into the PCM lattice faster than a phonon period (~ 176 fs)[306]. We note that this mechanism occurs in *addition* to the direct mechanism of exciting electrons and holes from the 3d parallel bands, as discussed in the previous section. During the 50 fs pump-pulse duration, electrons lying close to the Fermi surface in the Au-nanomesh are promptly excited via intraband transition (figure 5.5a)[312]. Since the Au-nanomesh thickness is less than the momentum relaxation length, hot electrons can propagate ballistically through the Au nanoparticles with Fermi velocities ($v_F$) of ~ $10^8$ cm/s and without experiencing large-angle scattering at the Au/$VO_2$ interface. Additionally, since the intrinsic length scale of the $VO_2$ nanoislands is comparable to e-e and e-p scattering lengths (~ 40-80 nm)[313] and is also smaller than the electron mean free path (~ 100 nm in s/p-band metals)[314], the electrons take only ~ 32 fs to travel through the $VO_2$ nanoislands, across the Schottky barrier formed

by the interfacial Au/$VO_2$ contact (figure 5.4b,c). Since $VO_2$ has a complex structure near the Fermi level[38], similar to that of other complex transition metal oxides, the injected electrons can couple efficiently to the lattice due to strong electron-phonon coupling, retaining much of the absorbed laser energy in the lattice[315]. At the lowest pump-fluence displaying traces of structural PT in the $VO_2$ nanoislands (figure 5.4i), each electron created by the Au-nanomesh interacts with $\sim$ 160 $\pm$ 20 unit cells, corresponding to electron densities of $\sim 5 \times 10^{19}\, cm^{-3}$ in $VO_2$. This estimate *excludes* direct photon-$VO_2$ lattice interactions that are estimated to be a photon interacting with $\sim$ 400 unit cells. Consequently, the additional injected electrons compensate for the lack of sufficient direct photon-lattice interaction (with the threshold estimated to be one photon per 70 unit cells). Thus, hot electron injection from the plasmonic Au-nanomesh element is the mechanism that triggers the sub-picosecond PT of $VO_2$, together with the lowering of the switching threshold.

Although not the primary focus of this chapter, it is noteworthy to mention that with different sub-systems evolving on multiple timescales, another distinctive feature of the hybrid nanomaterial dynamics (picosecond) is visible: with increasing fluence, it takes more time for the $VO_2$ nanoislands to reach maximum metallicity. For example, at a fluence of 6.24 mJ/cm$^2$, the pristine $VO_2$ nanoislands reach maximum metallicity at $\sim$ 25 ps while for its hybrid counterpart, maximum metallicity of the $VO_2$ occurs at $\sim$ 100 ps. The drastic increase in electrons being injected by the Au-nanomesh (together with the direct photon-lattice interaction as noted earlier), quenches the strength of the structural phonons in the $VO_2$ lattice due to electron-phonon scattering and this modifies the already complex

dynamics of the metallic formation in the $VO_2$ nanoislands[217]. As a consequence, complete transformation to the metallic phase for the nanoislands in presence of extra electrons is hindered until charge neutrality is restored at the metal/PCM interface. This electron recombination process at the interface occurs within tens of picoseconds[316]. Once recombination is achieved, the now charge-neutral $VO_2$ nanoislands can proceed along its transformation path, relying on thermal transport to reach its maximum metallicity for a given fluence. The thermal transport is derived mainly from electron-phonon scattering mechanism and occurs within hundreds of picoseconds.

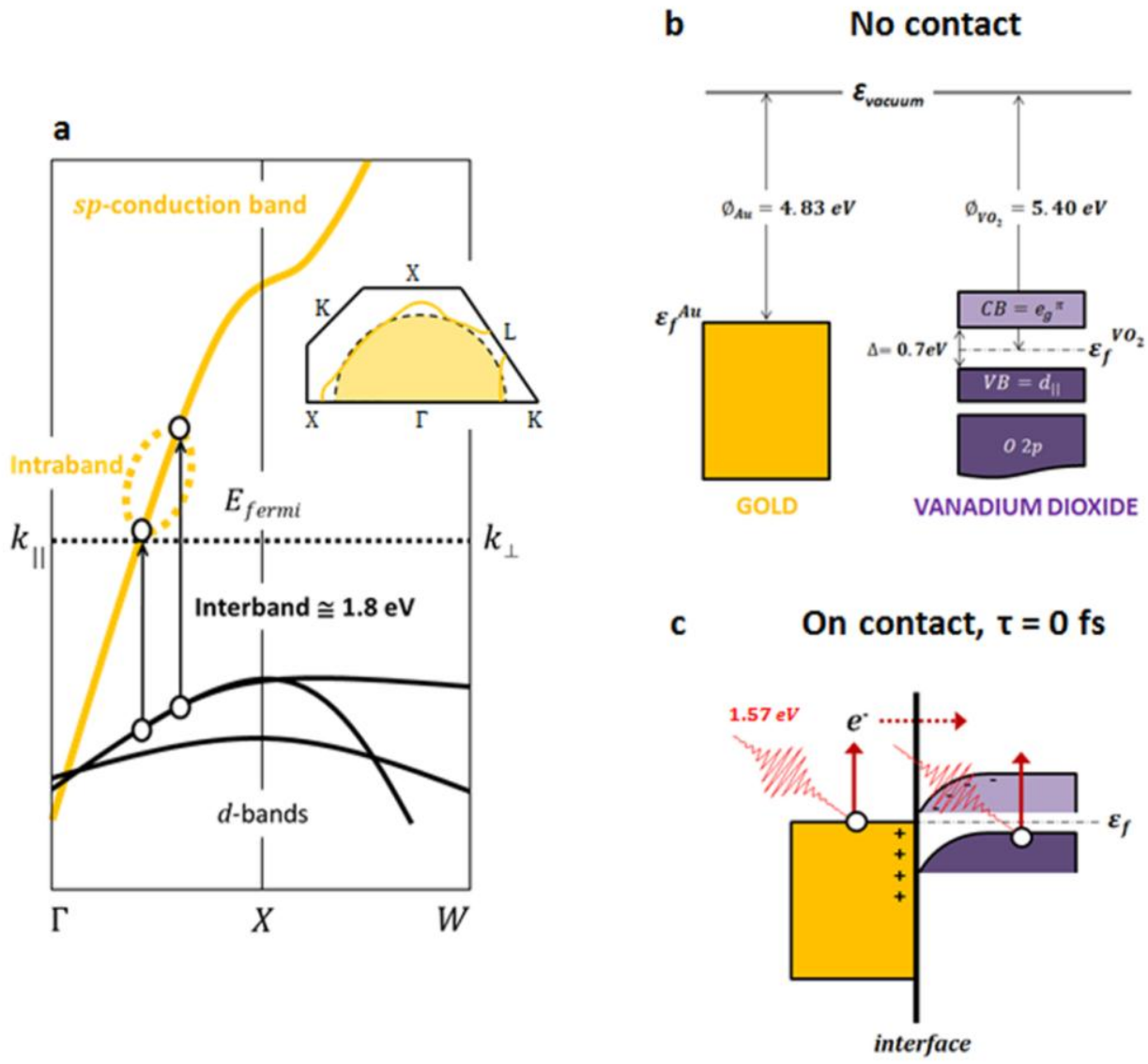


**Figure 5.5. Mechanism of Ultrafast Switching in Hybrid Au/$VO_2$ Nanomaterial. (a)** Band structure of gold near the Fermi Surface for the lowest possible interband transition; this hereby excludes the possibility of hole injection from *d*-bands by excitation with a 790 nm (1.57 eV) pump pulse[312]. **(b)** Energy band diagram of Au and $VO_2$ before contact with respective work functions adapted from Refs. [109,115,240]. **(c)** Schematics after contact at τ = 0 ps, when the pump pulse (50 fs, 1.57 eV) both creates hot electrons in Au via intraband transition and excites electrons from the $d_{//}$ valence band to the $e_g^{\pi}$ conduction band. The

hot electrons injected across the interface couple to the cold $VO_2$ lattice within the first picosecond to overcome the switching threshold and thereby trigger the structural phase transformation concurrently. Following excitation ($\tau > 2$ ps), an Ohmic contact is formed when $VO_2$ transforms from an insulator to a metal.

### 5.2.3c Calculations of fluence thresholds and injected electrons

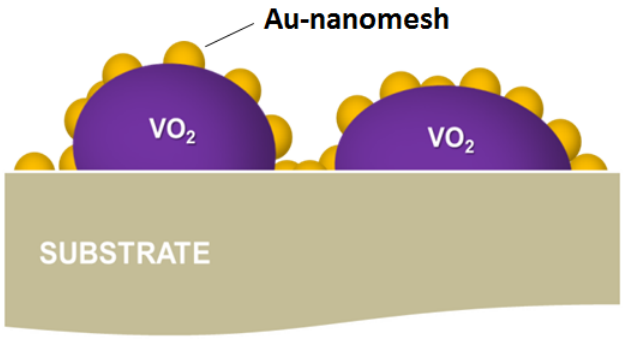


**Filling fraction Au = 52.5 %**

**Filling fraction $VO_2$ = 45.8 %**

| | n | k |
|---|---|---|
| $VO_2$ (790 nm) | 2.89 | 0.4230 |
| Gold (790 nm) | 0.15 | 4.8125 |

**Figure 5.6. Detail Schematics of Hybrid Sample.** Au-nanomesh (thickness of ~ 5 nm) on vanadium dioxide nanoislands (nominal thickness of ~ 40 nm) used for both experiments (section 5.2.1 and 5.2.2), i.e. thermal modulation and ultrafast switching. Filling fractions were derived from ImageJ software using scanning electron micrograph of figure 5.4b (top view).

***(I) Calculations of electrons excited in the $VO_2$ nanoislands:***

Number of photons generated in a pulse is:

$$= \frac{0.28 \times 10^{-3}}{2.51 \times 10^{-19}} \times \frac{1}{40 \times 10^{-7}} = 2.79 \times 10^{20}\ photons/cm^3$$

At a wavelength of 790 nm, the number of absorbed photons is:

$$= 0.32 \times (2.79 \times 10^{20}) = 8.9 \times 10^{19}\ photons/cm^3$$

Effective absorbed photons:

$$= 8.9 \times 10^{19} \times (0.525) \times (0.458) = 2.14 \times 10^{19}\ photons/cm^3$$

Therefore this corresponds to *one photon interacting with ~ 400 unit cells*.

We note that at a threshold fluence for the pristine $VO_2$ nanoislands of ~ 1.5 mJ/cm$^2$, this corresponds to about one photon interacting with 70 unit cells. This is in very good agreement with Rini *et al.* who found a threshold of one photon interacting with ~ 60 unit cells[225].

***(II) Calculations of extra electron density created by gold-nanomesh:***

From equation for penetration depth and using dielectrics of figure 5.6,

$$\delta_p = \frac{\lambda}{2\pi\kappa}$$

we find that the penetration depth for gold and $VO_2$ is 26 nm and 267 nm respectively. Since in both cases, $\delta_p > Au_{thickness}$ or $VO_{2,thickness}$ we assume uniform excitation from the 790 nm pulse and that each absorbed photon can excite one free electron from s-p conduction bands of Au via intraband excitation (figure 5.5a).

***(IIa) Number of electrons generated in the low fluence regime ($0.28\ mJ/cm^2$):***

Number of photons generated in a pulse is:

$$= \frac{0.28 \times 10^{-3}}{2.51 \times 10^{-19}} \times \frac{1}{5 \times 10^{-7}} = 2.23 \times 10^{21}\ photons/cm^3$$

At a wavelength of 790 nm, the number of absorbed photons is:

$$= 0.0241 \times (2.23 \times 10^{21}) = 5.37 \times 10^{19}\ photons/cm^3$$

Assuming one photon creates one excited electron, effective number of interacting electrons:

$$= 5.37 \times 10^{19} \times (0.525) \times (0.458) = 1.29 \times 10^{19}\ electrons/cm^3$$

To calculate the number of electrons interacting per unit lattice cell of $VO_2$, we assume that the nanoislands (from SEM) are hemi-ellipsoidal with lateral sizes ranging from 50 nm to 200 nm. Thus, we use $(\frac{1}{2}\left\{\frac{4}{3}\pi\left(\frac{a}{2} \times \frac{b}{2} \times 40\right)\right\})$, where $50\ nm \leq a = b \leq 200\ nm <$ 200nm.

Therefore, effective filling fraction of $VO_2$:

$$\frac{Vol_{ellipsoidal}}{2} = \frac{1}{2}\left\{\frac{4}{3}\pi\left(\frac{a}{2} \times \frac{b}{2} \times 40\right)\right\} = \frac{\pi}{6}\ (a^2 \times 40)$$

Hence, for any lateral ellipsoidal dimensions $50\ nm\ \leq a = b \leq 200\ nm$ :

$$Vol_{eff} = \frac{\frac{\pi}{6} \times (v)}{v} = 52.4\ \%$$

Consequently, the number of unit cell interacting with the electrons that are generated by the gold-nanomesh is:

Volume of 1 unit cell of $VO_2$ in monoclinic cell:

$$= 0.575\ nm\ \times 0.538(\sin\ 57.40)\ nm\ \times 0.456\ nm = 0.118\ nm^3$$

Number of $VO_2$ unit cell in $1\ cm^3$

$$= \frac{1\ \times\ 10^{21}}{0.118} = 8.47 \times 10^{21}$$

Therefore, number of $VO_2$ unit cells that actually interact with the injected electrons are:

$$=\ 8.47\ \times 10^{21}\ \times (0.458) \times (0.524) = 2.03\ \times 10^{21}\ unit\ cells/cm^3$$

Thus, in the low fluence, the number of unit cells that one electron interact with is:

$$= \frac{2.03\ \times 10^{21}}{1.29\ \times 10^{19}} = 157\ unit\ cells$$

*Therefore one electron interacts with ~ 157 unit cells of monoclinic M1 insulating $VO_2$.*

***(IIb) Number of electrons generated in the high fluence regime ($6.24\ mJ/cm^2$):***

Using the similar procedure as described above, in the high fluence case, *one electron interacts with ~ 7 unit cells.*

***(IIc) Error bars:***

Assuming that $VO_2$ thickness varies: $35\ nm \leq VO_{2,nominal\ thickness} \leq 45\ nm$, therefore, for the low fluence threshold:

*Upper limit is:*

$$= \frac{\left\{\frac{\pi}{6} \times (50 \times 50 \times 45)\right\} \times (0.458) \times 8.47 \times 10^{21}}{50 \times 50 \times 40} \cong 180\ unit\ cells$$

*Lower limit is:*

$$= \frac{\left\{\frac{\pi}{6} \times (50 \times 50 \times 35)\right\} \times (0.458) \times 8.47 \times 10^{21}}{1.29 \times 10^{19}} \cong 140\ unit\ cells$$

Therefore the in the low fluence threshold, *one electron interacts with ~ 160 ± 20 unit cells.*

### 5.2.3d Fitting procedure for the ultrafast data

Fits of figure 5.4b with accompanied lifetimes in figures 5.7a and b were obtained by fitting the data with a function of the form:

$$\frac{\Delta T(t)}{T} = \Theta(t)\left[T_e\, e^{\left(\frac{-t}{\tau_e}\right)} + T_l\left(1 - e^{\left(\frac{-t}{\tau_e}\right)}\right)e^{\left(\frac{-t}{\tau_l}\right)}\right]$$

where $\Theta(t)$ is an error function defined as $\frac{1}{2}\left[1 + \mathrm{erf}\left(\frac{t}{\tau_c}\right)\right]$ depicting the rising edge of the signal due to the pump and probe cross-correlation and governed by $\tau_c$, the laser pulse duration of 50 fs. $T_i$ and $\tau_i$ $(i = e, l)$ are fit parameters representing the amplitude and recovery rate of the electronic and structural dynamics, respectively. For the hybrid case in figure 5.4b, 5.7a and b, an additional amplitude ($T_{Au,e}$) and lifetime ($\tau_{Au,e}$) term was introduced to represent the electronic relaxation of the Au-nanomesh with a fitting function of the form:

$$\frac{\Delta T(t)}{T} = \Theta(t)\left[T_e e^{\left(\frac{-t}{\tau_e}\right)} + T_{Au,e}\, e^{\left(\frac{-t}{\tau_{Au,e}}\right)} + T_l\left(1 - e^{\left(\frac{-t}{\tau_l}\right)}\right)\left(1 - e^{\left(\frac{-t}{\tau_{Au,e}}\right)}\right)e^{\left(\frac{-t}{\tau_l}\right)}\right].$$

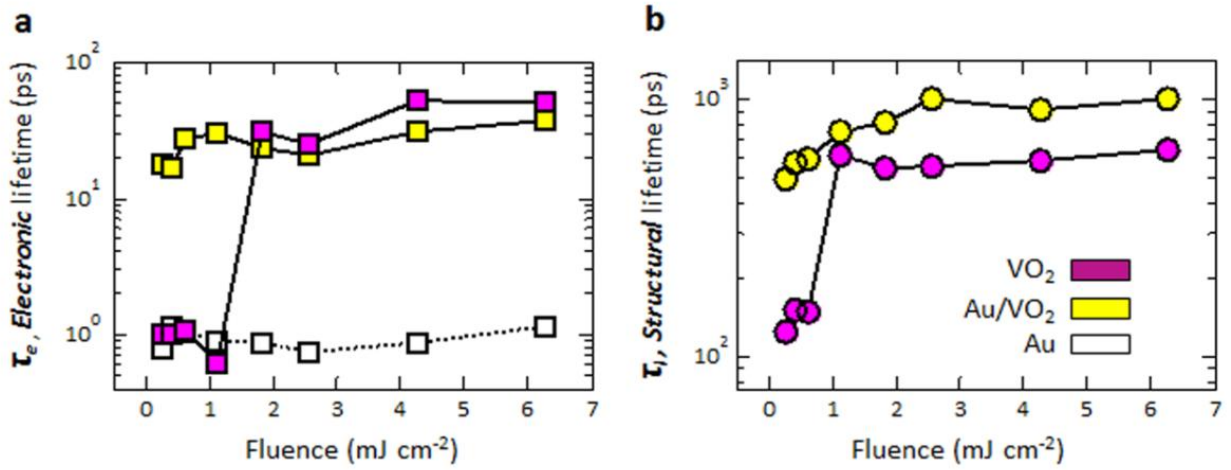


**Figure 5.7. Electronic and Structural Lifetimes. (a)** Electronic decay lifetimes for the Au (empty squares), pristine $VO_2$ (purple filled squares) and Au/$VO_2$ nanomaterial (yellow filled squares). Note that (i) the electronic lifetime for the Au has a relatively constant value of ~ 1 ps and (ii) the pristine $VO_2$ has a switching threshold at about 1.2 mJ cm$^{-2}$. **(b)** Structural lifetimes for $VO_2$ with (yellow filled circles) and without (purple filled circles) Au-nanomesh. In both **(a)** and **(b),** the electronic and structural lifetimes of the Au/$VO_2$ nanomaterial are already higher than those of the pristine $VO_2$. In this case, no threshold at the lowest fluences is found, suggesting an already switched state. We note that a nonlinear least squares fitting procedure was used and all the extracted lifetimes were within the 95% confidence bounds.

## 5.3 DENSITY FUNCTIONAL CALCULATIONS: INSIGHTS ABOUT THE ULTRAFAST COUPLING MECHANISM

To further elucidate this mechanism at microscopic level, density functional calculations were carried out to determine the exact role played by the injected electrons. This work was performed by Dr. Bin Wang and Prof. S. T. Pantelides at Vanderbilt University.

First-principles calculations based on density functional theory (DFT) were performed using the VASP package.[271] The PBE-GGA exchange-correlation potential[272] was used and electron-core interactions were treated in the projector augmented wave (PAW) formalism.[273,274] A rotationally invariant DFT+U approach[275] was applied, and the effective parameters, U and J, to include the Hubbard on-site Coulomb repulsion, were 4 eV and 0.68 eV, respectively. The plane-wave kinetic-energy cutoff was set to 400 eV. Gaussian smearing (width = 0.01 eV) was used to calculate the partial occupancies. Calculations were performed using a supercell consisting of 27 unit cells. Γ point in the Brillouin zone was used to compute the density of states and the forces. The phonon calculations were carried out by calculating force constants in real space using Density functional Perturbation Theory (DFPT).[317] In the phonon calculations of excited systems, electrons were removed from the valence band maximum and positioned at the conduction band minimum, and the occupancies were kept fixed throughout run.

First, the effect of electron-hole pairs excitation in a $VO_2$ supercell, consisting of 27 monoclinic M1 unit cells is examined. This represents experiment of photoexciting the pristine $VO_2$ nanoislands only. As shown in figure 5.8, excitation of a single e-h pair shows softening of the 6 THz mode at the Γ point. Moreover, exciting four electrons leads to a negative frequency in its phonon spectrum, corresponding to a destabilization of the $VO_2$ system. Since the creation of holes has been demonstrated to facilitate the V-V dimer structural relaxation[221], the phonon spectrum is also calculated when an electron is removed from the valence band to simulate hole creation. As in the case of exciting electrons, a similar concentration of holes is required for the 6 THz phonon to reach

negative frequencies. Close inspection of the induced electron density difference shows that the removed electrons are mainly located on $d_{xy}$ orbitals of V atoms, corresponding to the orbitals that are responsible for the V-V dimer binding states[115].

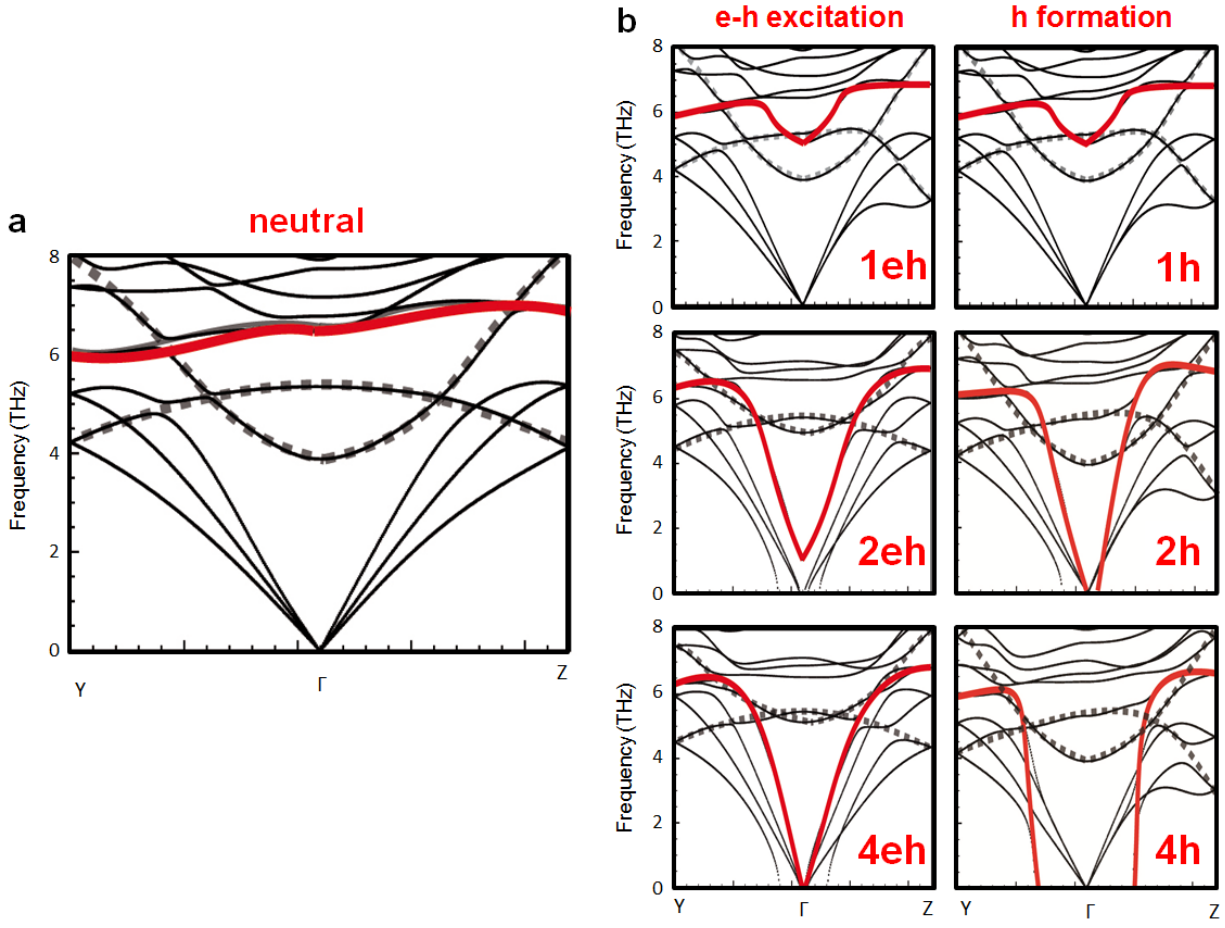


**Figure 5.8. Phonon Spectrum for e-h Pairs Excitation and Holes Formation. (a)** Phonon spectrum of a neutral VO2 supercell consisting of 27 monoclinic M1 unit cells. **(b)** Resulting phonon spectra during **(i)** electron-hole (eh) pair excitation and **(ii)** hole (h) creation process. Data collected by Dr. Bin Wang.

Hereafter, calculations to simulate the injection process (corresponding to experiment of the hybrid nanomaterial) were performed. The calculations were based on

the same periodically-repeated supercell so that the addition of electrons is automatically compensated by a uniform positive background. Since the latter has no effect on phonons, we expect the calculation to correspond to electron injection. Addition of up to 16 electrons results in virtually no change of the phonon spectrum of the normal bulk material. However, adding an additional electron to the system (now 17 extra electrons) shows clear sign of the 6 THz softening at the Γ point (highlighted in red in figure 5.9) and with just one more injected electron, this results in a *catastrophic phonon collapse* to a negative frequency (figure 5.9a). This excess of electrons corresponds to electron densities of $10^{21}$ $cm^{-3}$, similar to experimental values at saturation level (that is when the *entire* $VO_2$ has switched). While changes to other phonon modes are rather subtle, the collapse of the 6 THz is clearly visible. Its atomic motions correspond to the two V atoms forming V-V dimer vibrating along the [010] direction and perpendicular to the c-axis, as schematically depicted in figure 5.9b.

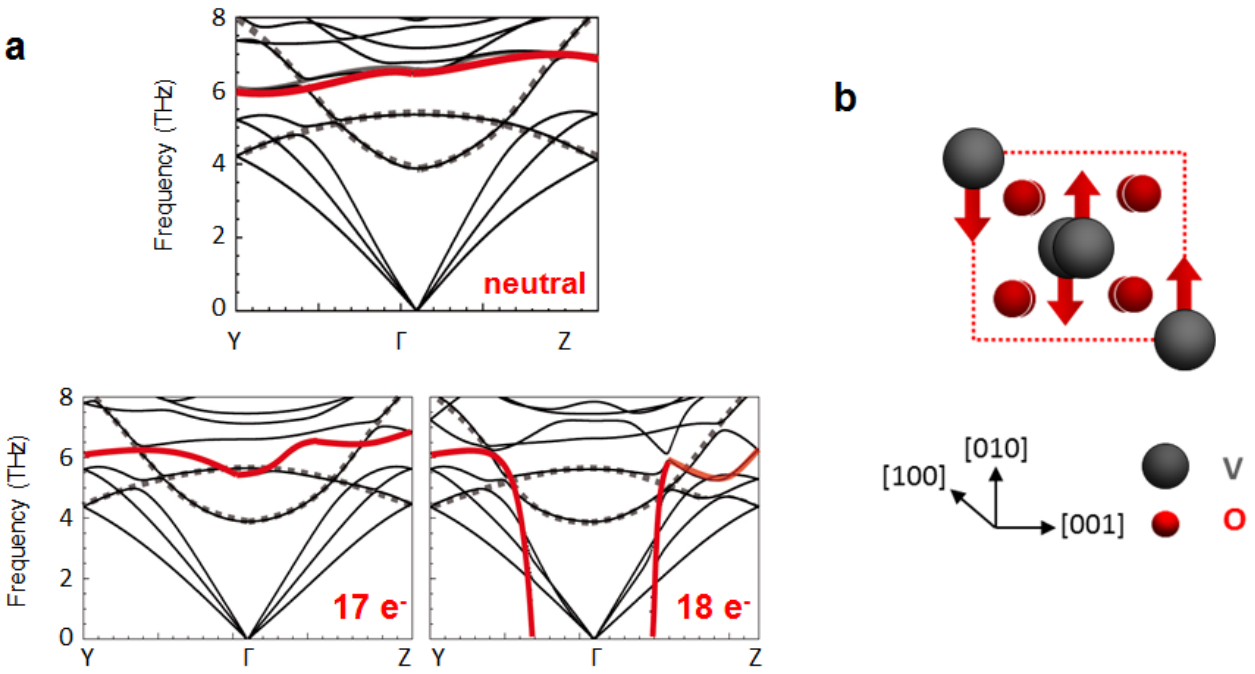


**Figure 5.9. Phonon Spectra Resulting from Electron Injection. (a)** Density functional calculations of phonon spectrum of neutral VO2, 17 and 18 electrons injected into VO2 supercell corresponding to an electron density of ~$10^{21}$ cm-3. **(b)** Schematic of the critical phonon mode at 6 THz. Data collected by Dr. Bin Wang.

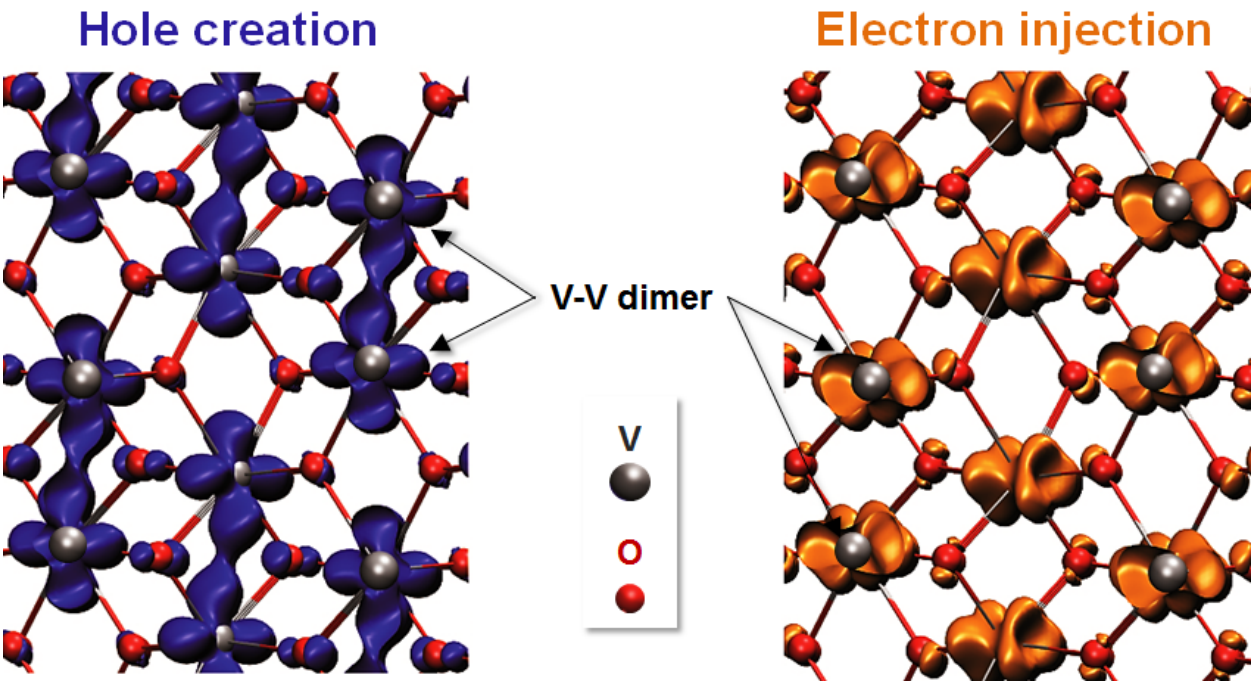


**Figure 5.10. Induced Electronic Charge Difference in $VO_2$ Lattice for Hole Formation and Electron Injection.** Charge difference in the $VO_2$ lattice when (i) an electron is removed (hole creation) and (ii) the $18^{th}$ electron is injected (i.e. $18^{th}$-$17^{th}$ electron density). Courtesy of Dr. Bin Wang.

Excitation of these 6 THz phonons has been shown in previous experimental work to be critical in triggering the structural phase transition of $VO_2$[219,228,236]. These calculations show for the first time how the catastrophic phonon collapse of the critical 6 THz phonon is a direct consequence of electron injection and photo-excitation as well, supporting the present experimental finding of ultrafast phase transition by electron injection. Although not as effective as directly removing an electron from the orbitals bonding the V-V dimer, the DFT calculations confirmed that injecting electrons into the spatially extended

conduction band also relaxes the monoclinic structure, resulting in a catastrophic phonon collapse and therefore the $VO_2$ phase transition.

## 5.4 CONCLUSIONS

The overall change in dynamics when $VO_2$ is interfaced with a plasmonic element illustrates the delicate balance that exists in these complex phase-changing materials and suggests the need for careful tailoring of the hybrid nanomaterial to achieve fast-acting switches. More importantly, our results elucidate the correlation between electron injection and its coupling to the lattice. Here, the electron injection process provides both a means to melt the Mott-insulating character of $VO_2$ but also a means to break Peierls-distortion by selective phonon mode collapse.

The analysis presented here demonstrates that hot electrons can be harnessed to increase the efficiency with which a phase transformation is triggered on an ultrafast timescale. Furthermore, multiple plasmonic materials with lower work functions together with optimized nano-photocathode designs can now be explored. Ultimately, these studies will enable the design of materials to fabricate all-optical modulators operating at optimal switching threshold for next-generation nanophotonic devices and whose non-equilibrium transient states can be manipulated by dynamic charge doping.

More broadly, since $VO_2$ serves as a prototypical PCM, ultrafast electron-injection provides an additional method to tailor other phase-transition phenomena and also to understand their properties via dynamic tuning of the Fermi level. Detailed studies of hybrid nanomaterials will be necessary to reveal novel physical processes that do not

typically occur within one class of material even under equilibrium conditions. Moreover, by examining the effect of plasmonics nanostructures with increased absorption efficiency on other transition-metal oxides, this opens the possibility of efficient optically induced electronics[20], controlling and manipulating materials properties via selective, wavelength-dependent ultrafast creation of non-equilibrium states. Hybrid nanomaterials thus have the potential to create new ultrafast phase-diagrams, revealing novel dynamic emergent phenomena.

## 5.5 ACKNOWLEDGEMENTS

The work presented in this chapter was performed and supported in part by (i) the Office of Science, US Department of Energy (DE-FG02-01ER45916) and DTRA (HDTRA1-10-1-0047), (ii) the Vanderbilt Institute of Nanoscale Science and Engineering, using facilities renovated under NSF (ARI-R2 DMR-0963361) (iii) a collaboration with the University of Alabama at Birmingham (Nate Brady and Prof. David J. Hilton) funded under the support from the US Dept. Education GAANN Fellowship (P200A090143) (iv) a collaboration with the theoretical group at Vanderbilt University (Dr. Bin Wang and Prof. Sokrates T. Pantelides) under the support of DTRA (HDTRA1-10-1-0047), the McMinn Endowment and the DoD Air Force Research Laboratory (v) the Center for Integrated Nanotechnologies (Dr. Minah Seo and Dr. Rohit P. Pransankumar), a U.S. Department of Energy, Office of Basic Energy Sciences user facility at Los Alamos National Laboratory (Contract DE-AC52-06NA25396), Sandia National Laboratories (Contract DE-AC04-94AL85000) and by the Laboratory Directed Research and Development Program.

# CHAPTER 6

# CONCLUSION AND FUTURE DIRECTIONS

"One day Sir, you may tax it."

*~ Michael Faraday to British Minister of Finance, William Gladstone, when asked about the practical worth of electricity.*

## 6.1 INTRODUCTION

The overall goal of this dissertation is to provide a framework for understanding how coupling (electron and the lattice or plasmonic nanostructures) occurs both at nanometer length scales and on femtosecond time scales in hybrid quantum nanomaterials and nanostructures. This work not only identifies the various parameters at play, but also demonstrates how light can be controlled on a subwavelength scale by using the kinetics and dynamics of $VO_2$, a canonical quantum material. In conventional optoelectronic devices, functionality is driven by tuning steady-state material properties. In contrast, this dissertation describes a novel category of hybrid nanomaterials and nanostructures whose functionality relies on collective interactions between electrons and the crystal lattice.

By demonstrating hybrid plasmonic/phase-change nanostructures in varying architectures, we have developed a generalizable methodology for reconfiguring nanodevices that relies intrinsically on the atomic properties of the quantum material used. Thus, since our hybrid nanomaterial combines prototypical plasmonic (gold) and phase-changing ($VO_2$) components, this dissertation can potentially be generalizable to other

hybrid systems, combining other plasmonic nanoarchitectures with phase-changing elements exhibiting other extraordinary macroscopic quantum phenomena (ferromagnetism, paramagnetism and superconductivity to name a few). More specifically, the major accomplishments of the research efforts in the dissertation are:

- Demonstrating that modulation can be achieved at the single nanoparticle level and, that the plasmonic response of a single nanoantenna can track and thus mimic the phase-transition of the $VO_2$ when thermally modulated.

- Assessing for the first time the importance of the surface roughness due to $VO_2$ grain structure on the plasmonic response of an antenna by means of FDTD simulations.

- Developing a new methodology that combines electron-beam lithography, plasmon-resonance nanospectroscopy and density-functional theory to pin-point a possible cause of phase transition in vanadium dioxide: oxygen defects created at grain boundaries due to strain effects.

- Connecting the electronic *vs.* structural response of the $VO_2$ across various volumes, thus demonstrating the importance of interface and grain boundaries on the $VO_2$ phase transition, driven by heterogeneous nucleation.

- Evaluating various hybrid plasmonic/phase-change nanoarchitectures that can achieve superior wavelength modulation ($\Delta\lambda \sim 230$ nm) capability while still being experimentally achievable.

- Describing a three-stage electron-beam lithographic process that allows one to fabricate nanostructures of varying material on the same planar substrate (for e.g. heterodimers), allowing for not only spatial control of EM near-fields, but spatially controlling the reactive near-field nanoenvironment as well.

- Performing the first ultrafast experiment on a hybrid quantum nanomaterial both at nanometer length scales and on femtosecond time scales simultaneously, thus demonstrating the complexity that arises from coupling of the injected charge carriers to the crystal lattice (Chapter 5).

- Reporting ballistic electron injection due to resonant plasmonic excitation as a novel mechanism that can trigger a phase transition event on a timescale faster that the intrinsic phonon cycle of the $VO_2$ while lowering the fluence threshold for switching.

- Developing, in collaboration with Robert Marvel, Joyeeta Nag and Bo Choi, a reliable, cost-effective method to fabricate $VO_2$ thin films using electron-beam evaporation as an alternative to pulsed laser deposition.

- Developing a scheme for extracting the response function of hybrid nanostructures using an interferometric autocorrelation setup.

Thanks to a collaboration with Professor Sokrates Pantelides and Dr. Bin Wang, we have also learned how density functional theory can help to elucidate the mechanism responsible for the phase transition in the hybrid nanomaterial, that is the electron-lattice coupling dynamics along with the observation of a catastrophic collapse of a specific 6 THz phonon mode, corresponding to local oscillations of the V-V dimer. This collapse thus marks the onset of the phase transition of $VO_2$. Using density functional theory to describe theoretically for the first time the importance of hole creation in destabilizing the V-V dimer, thus triggering the phase transition.

Although this dissertation shed much light on the intrinsic properties of hybrid nanostructures and on the ability to control their optical responses both spatially and temporally, it perhaps serves more importantly one of the most fundamental aspects of research, as expressed by Thorstein Veblen, namely that "the outcome of any serious research can only be to make two questions grow where only one grew before." In the following sections, we highlight few research avenues that could potentially aid to better understand $VO_2$ and develop better intuition with regards to the intimate coupling that exists between plasmonic and PCM. This would surely help to further increase the chance of such hybrid class of materials to be integrated into current nanodevice technologies.

## 6.2 ENGINEERING AT THE ATOMIC SCALE

From Chapter 2 and 3, one has seen how homogeneous or heterogeneous interfaces tend to obscure the dynamics of the $VO_2$. Therefore, new fabrication schemes in conjunction with novel detecting strategies should be devised to understand the effect of electron correlation and structural changes during the phase transition, potentially pin point its microscopic physical origins. In such cases, molecular beam epitaxy or atomic layer deposition could potentially be an important route to fabricating layered $VO_2$ oxides that are separated by a non-interacting oxide with low lattice mismatch such as $TiO_2$ for example. As demonstrated very recently, such "digital superlattice oxides" in another class of quantum material, combined with angle-resolved photoemission spectroscopy provided tremendous physical insights about the nature of electron localization in such system[318] and thus, such technique could potentially be implemented to elucidate the mechanistic details of the $VO_2$ phase-transition. This experiment is illustrated in figure 6.1. Interestingly, the concept of layering the $VO_2$ has been suggested theoretically as well whereby an exact number of $VO_2$ on $TiO_2$ layers (5:3 ratio) was found to result in a semi-Dirac point at the Fermi surface, thus having spinless charge carriers that are effective mass-like along one principal axis but are massless along the other[319,320].

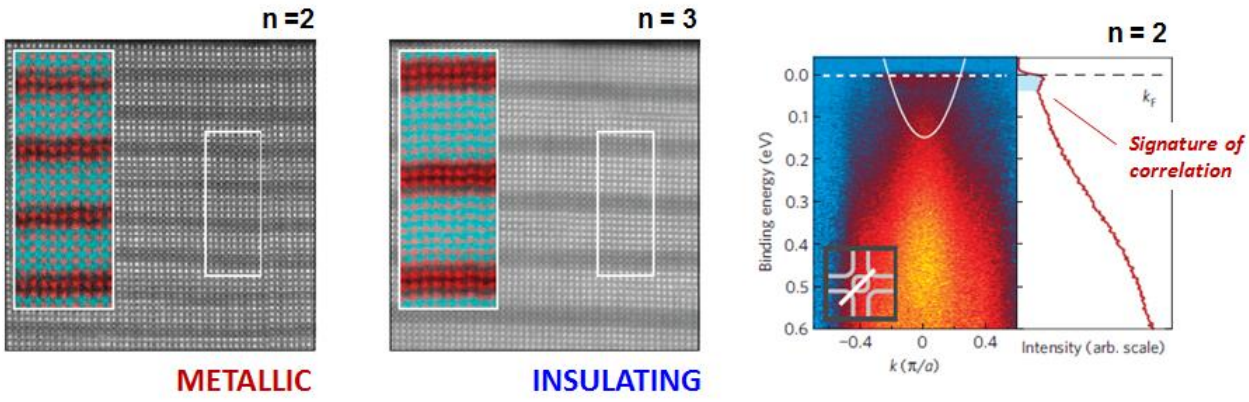


**Figure 6.1. Digital Oxide Superlattices.** By fabricating atomically abrupt interfaces, the electronic structure of superlattices of Mott insulator $LaMnO_3$ and the band insulator $SrMnO_3$ show how enhancement in quantum many-body interactions can be interfacial engineered. Renormalized ARPES spectrum showing the formation of the quasiparticle peak, signature of electron correlation. Adapted from reference [318].

Although we now know that the most probable sites for nucleation are oxygen vacancies, a deeper understanding of the heterogeneous nucleation process to switch the entire $VO_2$ volume is still needed. Moreover, the question of what is the *fundamental size limit* at which the phase transition can occur is still unknown. In order to attempt answering such questions, one could think of a similar experiment demonstrated by the Alivisatos group, namely using high-resolution transmission electron microscopy to study the growth of nanocrystals that are trapped in a liquid embedded between atom-thick graphene sheets. With progress in the micro/nanobeam community in fabricating defect-free $VO_2$ crystals, one could think of embedding the $VO_2$ nanobeams in such graphene cells to study the phase-transition process at an atomic scale[21].

Moreover, since both nanoscale and interfacial effects can impact performance of optoelectronic devices, it is necessary to understand how these parameters can modify macroscopic properties. Thus, experiments aimed at understanding the electronic properties (for e.g. carrier mobility, percolation) are also required. For example, one could think of growing epitaxial $VO_2$ films with a certain grain structure in specific device geometries so as to measure the effect of interface and grain boundaries on the electrical properties as a function of thermal switching. Such an experiment is depicted in figure 6.2.

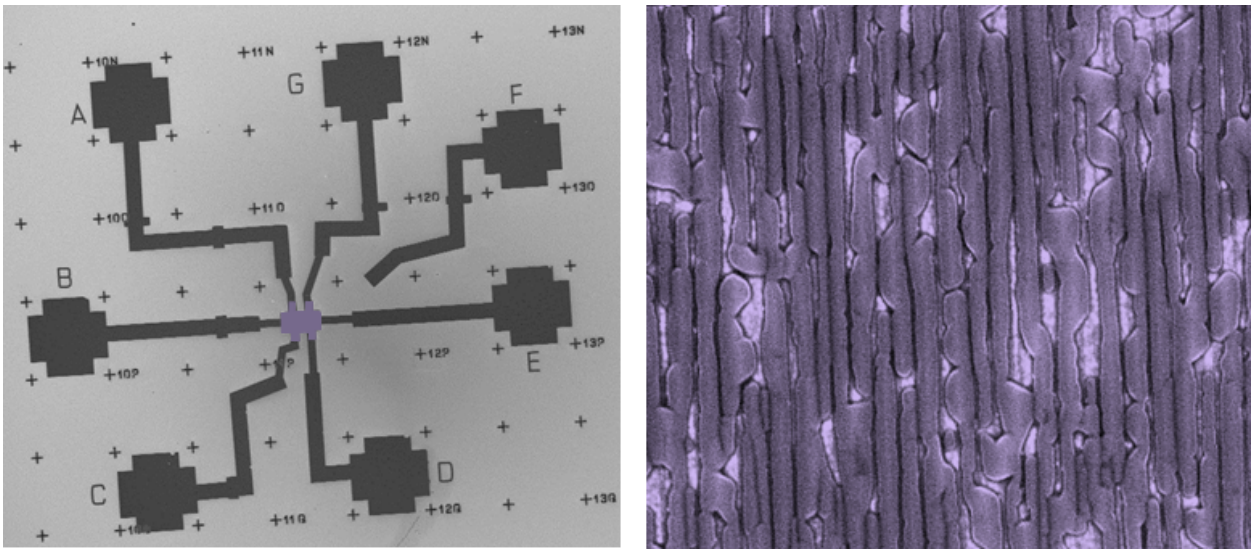


**Figure 6.2. Effect of Grain Boundaries on $VO_2$ Electrical Properties.** Hall bar devices can be fabricated on a-cut sapphire with the $VO_2$ (purple) grain structure (~ 125 nm wide grains) along or across the drain-source path. Thus, a correlation can be drawn between switching performance and the effect of the interface, potentially highlighting the bifunctionality of such nanodevices. Initial experiments were performed in collaboration with the Bolotin group at Vanderbilt University.

## 6.3 COMPLEX COUPLING MECHANISM IN HYDRID NANOSTRUCTURES

Although Chapter 4 provides an exhaustive treatment of plasmonic modulation using $VO_2$, our hybrid nanostructures provide a versatile test bed for understanding other physical optical phenomena. For example, phase-changing $VO_2$ could be used to modulate electromagnetically induced transparency[321-323] by creating the hybrid nanostructures shown in figure 6.3. Also, due to the narrow linewidth (or Q-factors) that are created by Fano-type interference, such nanostructures could potentially provide a more sensitive probe of the phase transition in $VO_2$. One could also implement of a more complex scheme in which the broad highly damped dipole plasmonic resonance created when a $VO_2$ nanodisk metallizes could interact with a sharp dipole resonance of a heptamer nanostructure geometry to create Fano-like interference[324-328]. This could potentially provide greater flexibility and modularity to the optical response of the hybrid nanostructures (figure 6.4).

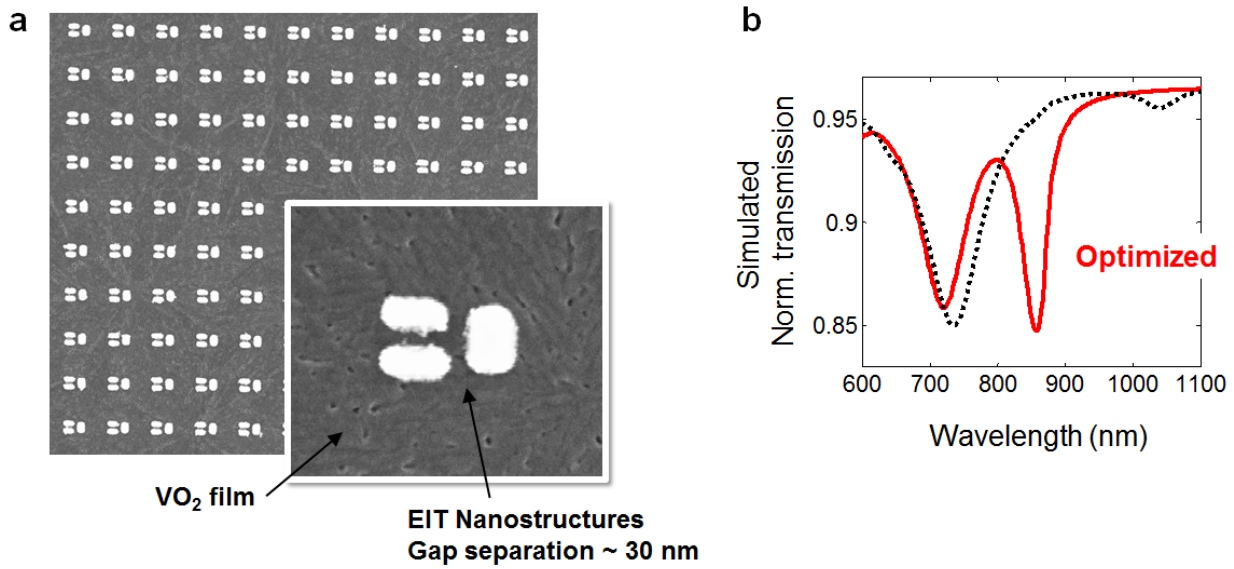


**Figure 6.3. Modulating Electromagnetically Induced Transparency in Plasmonic Nanostructures. (a)** SEM of hybrid Au-EIT/$VO_2$-film plasmonic nanostructures. The dipole (vertical bar) and quadrupole (horizontal bars) resonances interact to form a narrow transparency window in the extinction spectrum of this plasmonic nanostructure. The inset shows the underlying smooth ~ 40 nm $VO_2$ film fabricated by electron-beam evaporation. **(b)** Simulated transmission spectra of 20 nm thick Au EIT nanostructures (without $VO_2$) showing that transmission increase can be optimized at specific wavelength (~ 800 nm in this case).

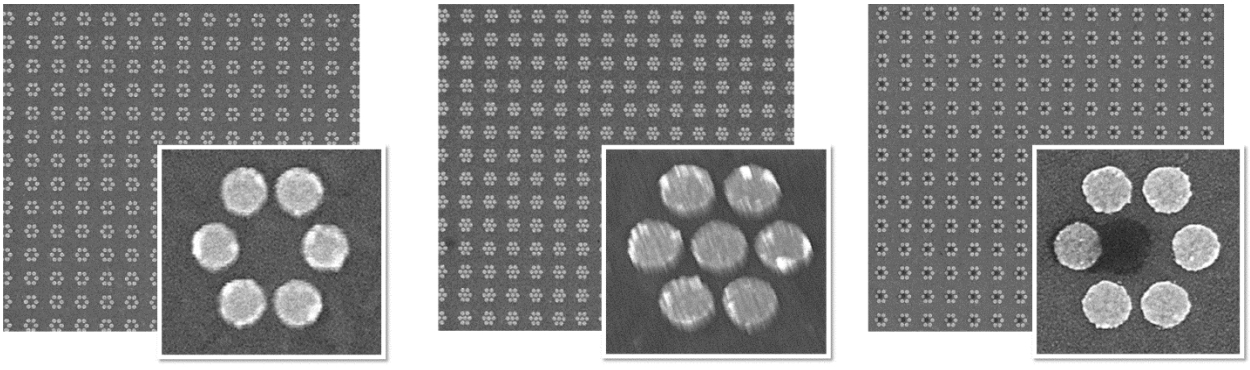

**Figure 6.4. Fano Resonance in Complex Nanostructures.** Increasing complexity of near field interaction: SEM displaying a hexamer of Au nanostructures (for a single-peak

resonance at ~ 600 nm), a heptamer (for a dip in the extinction due to a Fano resonance) and a hybrid Au/$VO_2$ heptamer (for tuning the Fano resonance by varying the phase of the nanoparticle). The nanodisks have an average diameter of 160 nm and the edge-to-edge separations are ~25-30 nm.

Potentially even more rewarding, albeit more demanding, is to incorporate a phase-changing material into the recently developed nanostructure designs of the Capasso group[329,330] for beam steering and beam modulation in plasmonic antennas for quantum-cascade lasers. Since the plasmonic antennas themselves are purely passive, the incorporation of a phase-changing material such as $VO_2$ would make possible active optical or electrical control of the antenna. If modulation of both the amplitude and phase in the optical response of a hybrid plasmonic nanoparticle is achieved by optimizing its shape and size, one could potentially think of 2D planar geometries that can control the propagation of laser light through the plasmonic interface. Effects such as active steering or focusing of a beam and creation of optical vortices could then be realized due to modulation of the phase discontinuity at that interface. Although using $VO_2$ thin film as the active substrate might be too absorptive, the three-stage electron-beam lithography process could potentially be used to optimize simultaneously the plasmonic and phase-changing properties. Thus, the Au/$VO_2$ hybrid nanostructures would be conceived as entities whose sizes and shapes vary as a function of spatial position on the planar substrate (figure 6.5).

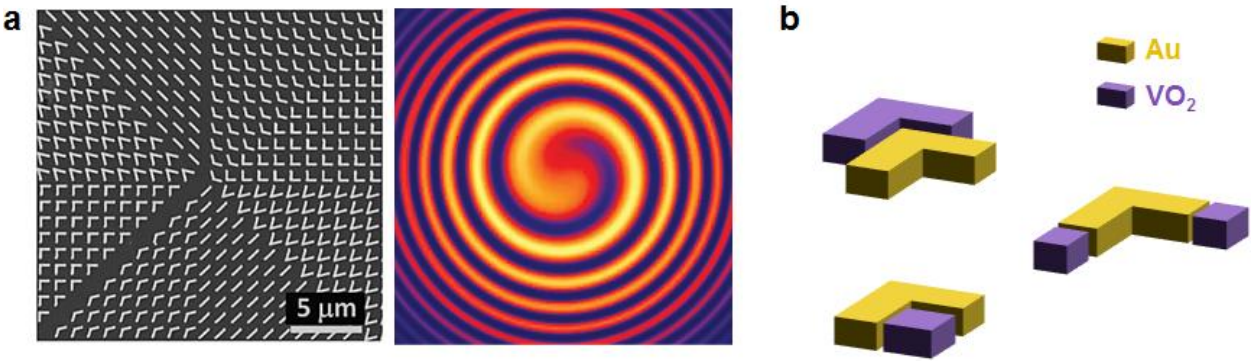


**Figure 6.5. Modulation of Interfacial Phase Discontinuity. (a)** Demonstration of static Au structures used to create optical vortex. From reference [329]. **(b)** Suggested potential hybrid nanostructures whose phase and amplitude can be modulated to achieve effect such beam steering or beam focusing.

## 6.4 ULTRAFAST DYNAMICS OF COUPLED SYSTEM

As illustrated in Chapter 5, the hybrid nanomaterials display rich ultrafast physics due to the various electron-electron or electron-phonon coupling mechanism taking place at various length scales but also evolving on various time scales. Although the study of hybrid nanomaterials is still in its infancy, one can already see that the complexity of such systems has many ramifications for the ultrafast (femtosecond/picosecond) dynamics of condensed matter, including the potential to control electronic and vibrational pathways so as to maximize a specific product phase.

Since electron injection has been shown to modify the coupling dynamics, one can now consider how doping could affect the intrinsic switching properties of phase-changing material, beyond the obvious lowering of the fluence threshold to trigger the phase-transition. Indeed, as shown in Chapter 5, the presence of extra electrons in the $VO_2$ lattice can complicate the formation of metallicity and thus it would be interesting to know the

exact mechanistic details for such an observation. This could perhaps shed light on the charge recombination effect at the interface. Here ultrafast THz experiments on such hybrid nanomaterial (plasmonic/$VO_2$ or doped $VO_2$) could be designed to understand the complex dynamics of metallic grain formations[217].

As eluded previously, one of the main drawbacks of using $VO_2$ as the phase-change material is its slow relaxation time, ranging from hundreds of picoseconds to tens of nanoseconds. For technological applications this may be unacceptable and more understanding is needed of ways to reducing relaxation time. As initially demonstrated by Lysenko *et al*.[331], relaxation time is highly dependent on substrate and therefore, one could think of using low lattice mismatched substrate to efficiently couple the energy out of the $VO_2$ lattice, thus relaxing the structure faster. Also, we note that there have not been any experiments performed on the size-effect of $VO_2$ in the ultrafast regime.

Last but not least are the results by Wall *et al.* that showed how coherent control of the $VO_2$ phase transition can be achieved fluences below the threshold at which the $VO_2$ becomes not only metallic but also rutile[306]. These results are very important in so far that they show the potential to coherently control the state of the $VO_2$, thus potentially "switching off" the material on the timescale of its phonon cycle ($\sim$ 176 fs). One important part of this puzzle however is to extract the dielectric properties of $VO_2$ in the time domain to understand how the dielectric functions evolve temporally as $VO_2$ loses it monoclinic character after (or during) ultrafast excitation. Hopefully, one might not need to *completely* transform the $VO_2$ from metallic to insulating phase to obtain a drastic change in dielectrics, necessary for photonic applications.

## 6.5 AND THIS LIST GOES ON…

As one can infer from this dissertation, there are many research projects suggested by thinking about applications of hybrid nanomaterials that are yet to be explored. The most interesting experiments are the ones that demonstrate the ability to control simultaneously both the spatial and temporal properties of the phase-changin material. One could think of using plasmonic near-field interferometry[332] to achieve phase transformation for example or even using ultrafast excitation combined with spatial light modulation to tune the dielectrics of a PCM with a predetermined spatial pattern that can evolve on an ultrafast timescale, depending on the relaxation properties of the excited material.

# APPENDIX A

# ROBUST AND COST-EFFECTIVE FABRICATION OF ACTIVE HYBRID PLASMONIC NANOSTRUCTURES

## A.1 INTRODUCTION

We describe here the initial experiments required to fabricate efficiently and on a large scale crystalline and switching vanadium dioxide using electron-beam evaporation. Combined with a cost-effective and reliable lithography method coined hole-mask colloidal lithography by Fredriksson *et al.*[303], this process has the ability to create large areas (several $cm^2$) of hybrid nanostructures (stacked nanodisks, gold nanostructures on phase-change film and even the heterodimers as described in sections *§4.2*, *§2.1*, *§4.4* respectively). Moreover, other complex structures with nanoscale features such as holes, disc, ring and crescent-shaped can also be fabricated, with tunable optical responses yet to be determined.

## A.2 ELECTRON-BEAM EVAPORATION OF VANADIUM DIOXIDE

In contrast to expensive method of fabricating $VO_2$ such as pulsed laser deposition and chemical vapor deposition[167], electron-beam evaporation is a less expensive method that typically requires the use of inexpensive powder or pellet targets.

Here crystalline, stoichiometric and switching $VO_2$ was fabricated at room temperature as follows: $VO_2$ films were deposited on glass substrates by electron-beam evaporation of a commercially available (Materion) crystalline $VO_2$ powder (mesh of 100)

using a laboratory-built evaporator system with 5 keV electron gun and 130 mA average beam current. The system pressure before evaporation was ~ $4 \times 10^{-7}$ Torr while during the evaporation, the vacuum was maintained at ~ $1 \times 10^{-4}$ Torr, with a typical deposition rate of 0.3 Å/s as monitored by quartz crystal microbalance (QCM). We deposited 100 nm thin film on glass confirmed using profilometric measurement. After deposition but before annealing, the films were characterized by XRD, AFM and SEM. In addition, optical transmission and reflection were measured with a white-light source (tungsten filament) and InGaAs photodetector (700– 1800 nm). Measurements were taken while thermally cycling through the phase transition (~ 25–100°C) using a Peltier cooler. XRD measurements were taken using a Scintag XGEN-4000 with copper Kα radiation of 0.154 nm; θ–2θ scans from 10 to 90 degrees were acquired in 0.05-degree steps with 30-second integration time. A Nanoscan III AFM was used to determine morphology and to measure RMS surface roughness. To study the sample surface morphology, corresponding SEM images were taken with a Raith e-Line microscope system. After the initial characterization, the $VO_{x\sim2}$ thin film samples were annealed at 450°C with 250 mTorr oxygen pressure. Annealing durations were varied (5, 10, 20, 30, 40, 60 and 90 minutes) for optimization purposes while all other parameters were held constant. SEM images of the film surface after deposition show no grain structure as pictured in figure 1.29, in good agreement with AFM measurements. XRD analysis performed on glass samples prior to annealing did not show any peaks consistent with $VO_2$; only a broad peak attributed to the substrate was observed, indicating the absence of significant crystal structure in the films prior to annealing. White-light transmission measurements confirm the lack of sizable $VO_2$

domains, with no change in intensity observed across the transition temperature range. To determine the stoichiometry of as-deposited films, x-ray photoelectron spectroscopy (XPS) was performed. The vanadium-to-oxygen ratio was measured to be 1.00:1.98 for the as-deposited film (before annealing) with $V_2O_5$, $VO_2$ and $V_2O_3$ oxides observed to be present. Prior to annealing the films are believed to be amorphous because no XRD peaks were observed. Analysis of the powder precursor by XPS shows the presence of $V_2O_5$ and $VO_2$ in the amounts required to produce $VO_{2.4}$ stoichiometry. The short annealing time needed to produce good quality $VO_2$ films is quite reasonable given the near perfect stoichiometry after deposition. After annealing, SEM was used to examine the morphology. This was shown figure 1.29, displaying the increasing granular structure of the $VO_2$ with increasing annealing durations. Longer annealing times (> 40 min) clearly reveals the presence of rod-like structures, likely due to Ostwald ripening. AFM measurements show a linear increase in surface roughness with annealing time and the presence of rod-shaped grains. White-light transmission measurements were also performed after annealing to confirm that all the samples switched. We note that no trend in hysteresis width as a function of increasing grain size is observed, implying the same average number of potent nucleation sites. The formation of rod-like grains after 40 minutes might suggest degradation of the film optical performance due to a possible conversion of the stoichiometric $VO_2$ to $V_2O_5$[153]; however, the switching contrast remains fairly constant. To further investigate the composition of these films, XRD analysis was performed on all samples. We observe that there is no shift in peak position nor appearance of new peak is observed, demonstrating that our films are stable to varying annealing conditions.

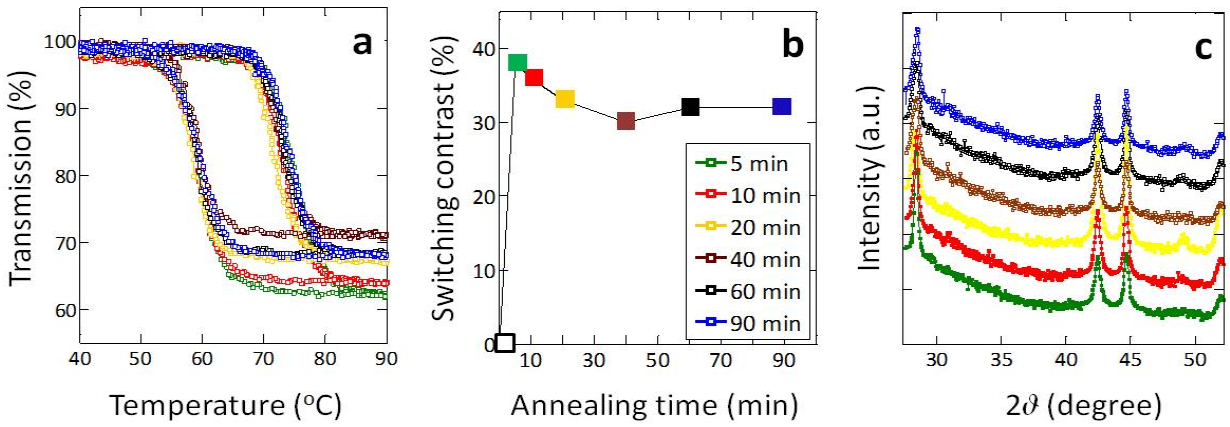


**Figure A.1. Characterization of $VO_2$ Thin films on Glass Substrate. (a)** White-light transmission measurements showing the hysteresis curves with an average switching temperature of about 68 °C. **(b)** Switching contrast as a function of annealing time. **(c)** XRD measurements depicting the consistent composition of the thin films, with curves shifted for clarity. The three prominent peaks are indexed from left to right as the $VO_2$ (011), (212) and (012), (021).

From figure A.1., we see that the optical performance decreases only slightly with increasing annealing times, suggesting perhaps that the film morphology could be responsible for this transmission decrease. This can also be inferred by the fact that no new crystal phases have been formed during annealing. Thus, we performed simulations to understand VO2 morphologies (due to increasing annealing times) can affect the switching contrast. FDTD simulations were used to link the changes in morphology to the observed optical switching performance. To do so, we simulated the interaction of a white light with two different $VO_2$ structures: a chain of three nanoparticles and a rod-like structure. The simulated structure is surrounded by a total-field/scattered-field (TFSF) source with 2 fs pulse duration. The spectral range used was from 300 to 1800 nm and the source was

injected with the polarization aligned parallel to the long axis of the structures. Two sets of power monitors were used, one located inside the TFSF region, providing the absorption cross-section, while another was located outside the TFSF source, giving information on the scattering cross section. The entire simulation region was meshed using 2-nm grid spacing and surrounded with PML boundary conditions.

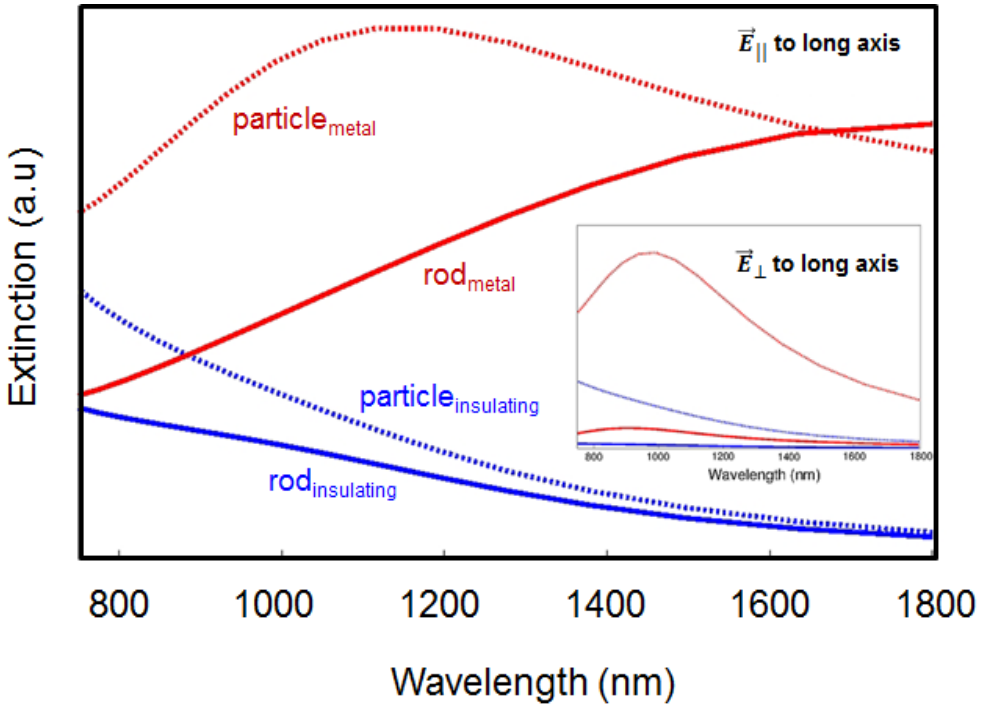


**Figure A.2. Effect of Film Morphology on the Optical Response. (a)** Simulated extinction response for the $VO_2$ rod-like grain and nanoparticle chain structures in insulating and metallic states. We note that the chain of nanoparticles have greater extinction in both metallic and insulating state within the detector range.

Figure A.2 shows that for both the insulating and metallic states of $VO_2$, the extinction is greater for the nanoparticle chain than for the nanorods; the same relationship being observed when polarization is perpendicular to the long axis of the

system (inset of figure A.2.). The broad peak observed at 1150 nm is due the dipole resonance of the structure when it metallizes, as described in Chapter 3. We compare the smooth morphology of the rod structure to the morphology of the film annealed for five minutes: the scattering is more specular in nature, the result of smoother edges on the rod and corresponding to a smoother film with less well-defined grain boundaries. As the annealing time increases, the grain boundaries become more sharply defined, as simulated by the chain of nanoparticles, resulting in more diffuse scattering of light. This corresponds to the negative slope between 5 and 40 minutes in figure A.1 and is due to the transition from a smooth to a granular-like film and consequently from a specular to diffuse scattering. After 40 minutes, the switching contrast increases and levels off. This is possibly due to the competition between the diffuse scattering of the sharply defined grain boundaries and the specular scattering from the larger, rod-shaped domains.

In conclusion, we have demonstrated a robust, reproducible protocol for electron-beam evaporation that produces $VO_2$ films on glass with optical switching characteristics that do not exhibit a strong dependence on annealing time. In addition, the near-perfect stoichiometry of the as-deposited films, a result of the powder precursor, requires short annealing times and produces films with smooth morphology. Converting the as-deposited films to high-quality $VO_2$ requires only a short time at conditions under which $VO_2$ is the preferred oxide. This is in sharp contrast to deposition processes that produce films with a composition that deviate strongly from the preferred $VO_2$ stoichiometry. Thus, such films require longer times for oxygen diffusion and crystallization to the correct VO2 stoichiometry. Possible extensions of this work include doping (W, Ti or Cr), epitaxial

growth on various substrates, and more importantly perhaps fabrication of VO2 nanoparticles since they are more resistant to annealing times. Finally, we see that electron-beam evaporation shows the potential to produce very smooth films for annealing times of less than five minutes, making it an excellent low-thermal-budget deposition method for $VO_2$ films (and potentially nanoparticles as well) in optical and electronic applications.

### A.3 HOLE-MASK COLLOIDAL LITHOGRAPHY

The following fabrication protocol follows very closely that of the first experiment demonstrated by Fredriksson *et al.*[19]. Schematics of the protocol are illustrated in figure A.3 and A4.

Glass substrates were spin coated with PMMA film (Microchem Coorporation, 2 or 4 wt % PMMA diluted in anisole, MW = 950000, RPM of 4000[333]) onto a clean surface and baking (180 °C for 90 seconds on a hotplate). Reactive oxygen plasma treatment (2 seconds) of the PMMA to decrease the polymer film hydrophobicity and avoid dewetting of this surface during subsequent polyelectrolyte and particle deposition steps, which might cause particle inhomogenity in the particle distribution. We then provide a net charge to the PMMA surface by pipetting a solution containing a positively charged polyelectrolyte onto the film (poly-diallyl-dimethyl ammonium (PDDA) MW 200000–350000, Sigma Aldrich, 0.2 wt % in Milli-Q water, Millipore), followed by gentle rinsing with de-ionized water in order to remove excess PDDA and subsequent drying in an air/nitrogen stream. Deposition by way of spin coating (RPM 500 for 1 minute) of a water suspension containing

negatively charged polystyrene particles (sulfate latex, Interfacial Dynamics Coorporation, 0.2 wt % in Mili-Q water; microsphere diameter of 84 nm), followed by drying in a similar fashion as before. This leave the PMMA surface covered with uniformly distributed PSS (figure A.3. – step 4).

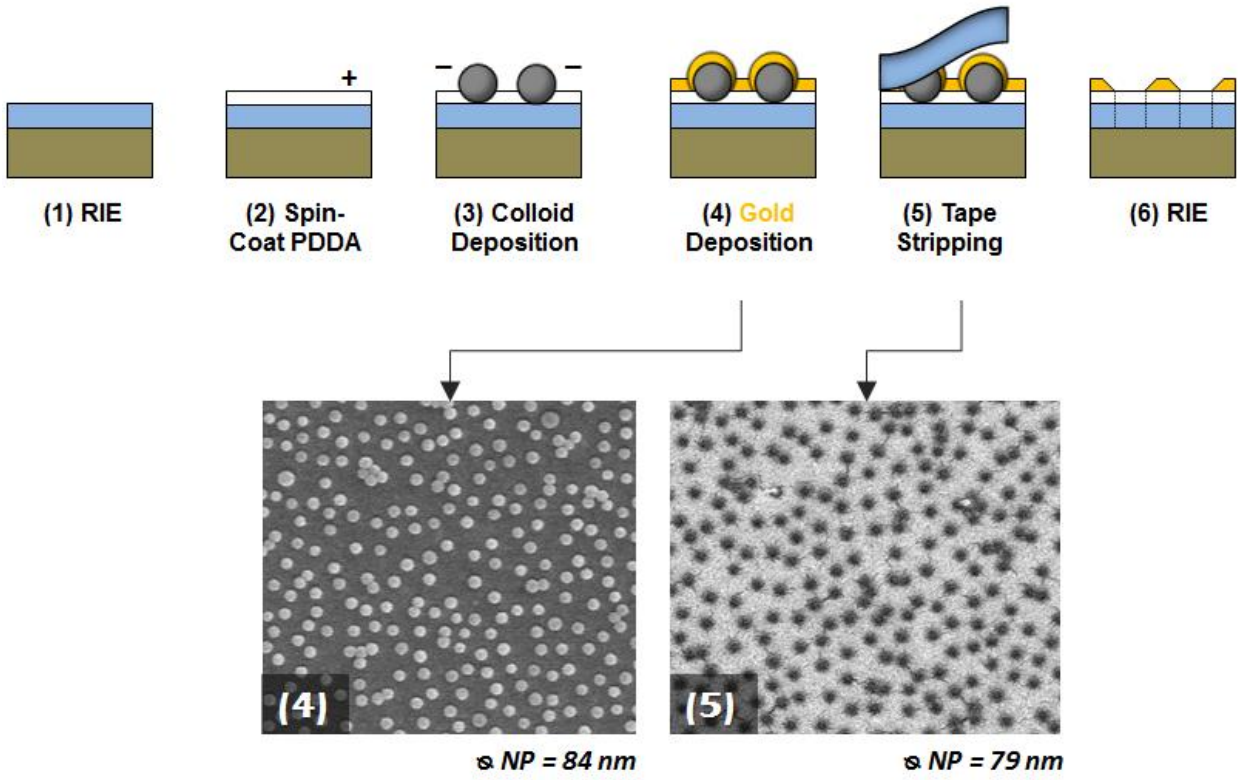


**Figure A.3. Fabrication Protocol for the Hole-Mask Colloid.** Explanation of each step is found in the text. SEM of step 4 and 5 and are shown, depicting the uniformity in the size of the nanospheres and the resulting mask after tape stripping. The size of the NPs that are fabricated relies completely on the size (and size distribution) of the PSS.

Evaporation of a thin, oxygen plasma resistant film such as Au (20 nm) for example is performed. The PSS are then removed by tape stripping (SWT-10 tape, Nitto Scandinavia AB). This results in a mask with holes arranged in a pattern determined by the self-

assembled colloidal particles. Transfer of the hole-mask pattern into the sacrificial layer via an oxygen plasma treatment that effectively removes all PMMA situated underneath the holes in the film, leaving the surface covered with a thin film mask supported on the perforated PMMA film. In this step, careful optimization is required so as to exactly remove the desired PMMA thickness. Such a calibration is performed as shown in figure A.5, noting that this procedure is specific to the equipment used and the number of samples placed in the chamber.

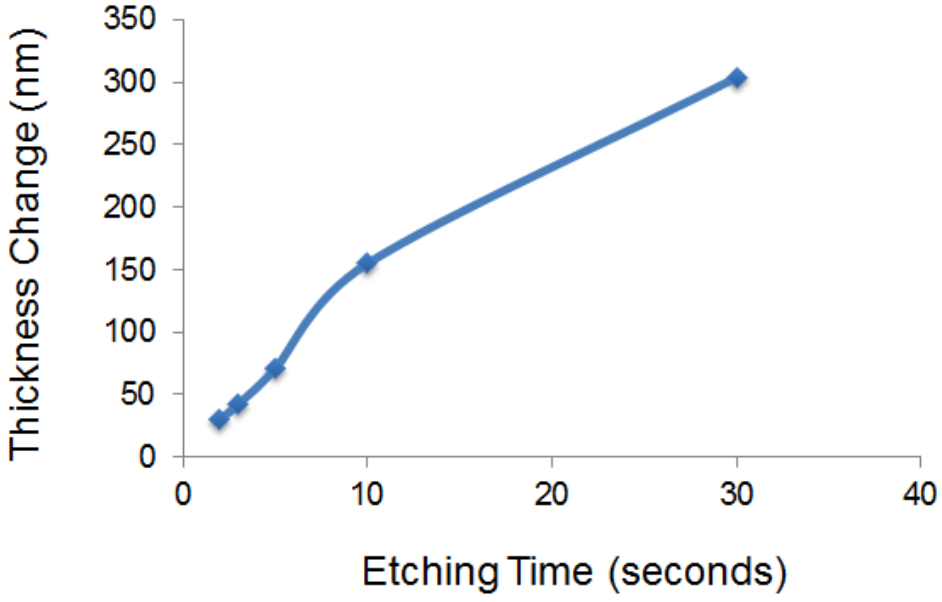


**Figure A.4. Etching Rate of PMMA.** The etching was performed at VINSE with etching conditions of 150 W, 25 mTorr, 98 sccm $O_2$. Data collected by Yuanmu Yang.

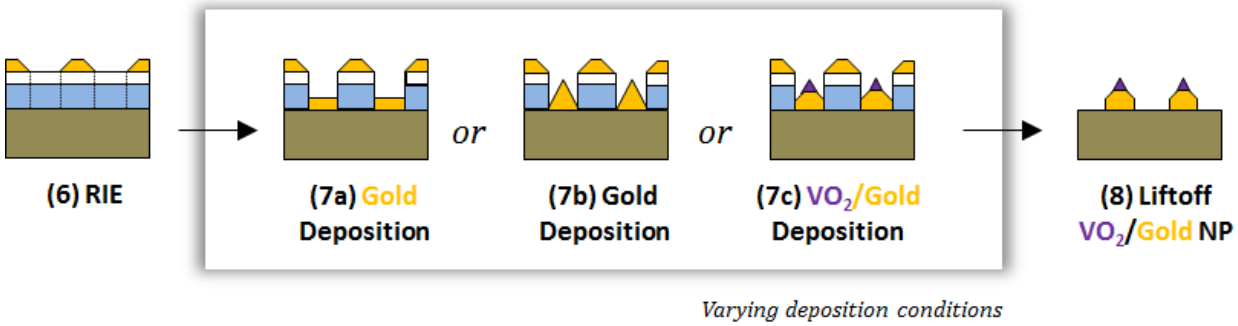


**Figure A.5. Fabrication of Hybrid Nanostructures by Hole-Mask Colloidal Lithography.** Varying the deposition conditions (material sequence, angle of deposition and thickness) can result in fabricating a large assortment of hybrid nanostructures.

Following this etching step (6), deposition of the plasmonic material (or phase-change) is performed, followed by standard liftoff process, as elaborated in Chapter 3 and 4. Such a sample, where only 10 nm of gold was deposited is shown in figure A.6.

In conclusion, we have discussed a relatively simple bottom-up fabrication process that can be used to create hybrid nanostructures at wafer scale. Although not attempted yet, this technique has the potential to create complex functional nanoarchitectures such as those shown in reference and . In addition, a major advantage of this method is that all the nanoparticles fabricated on the same sample have a very narrow size distribution as they have undergone the same physical or chemical treatment.

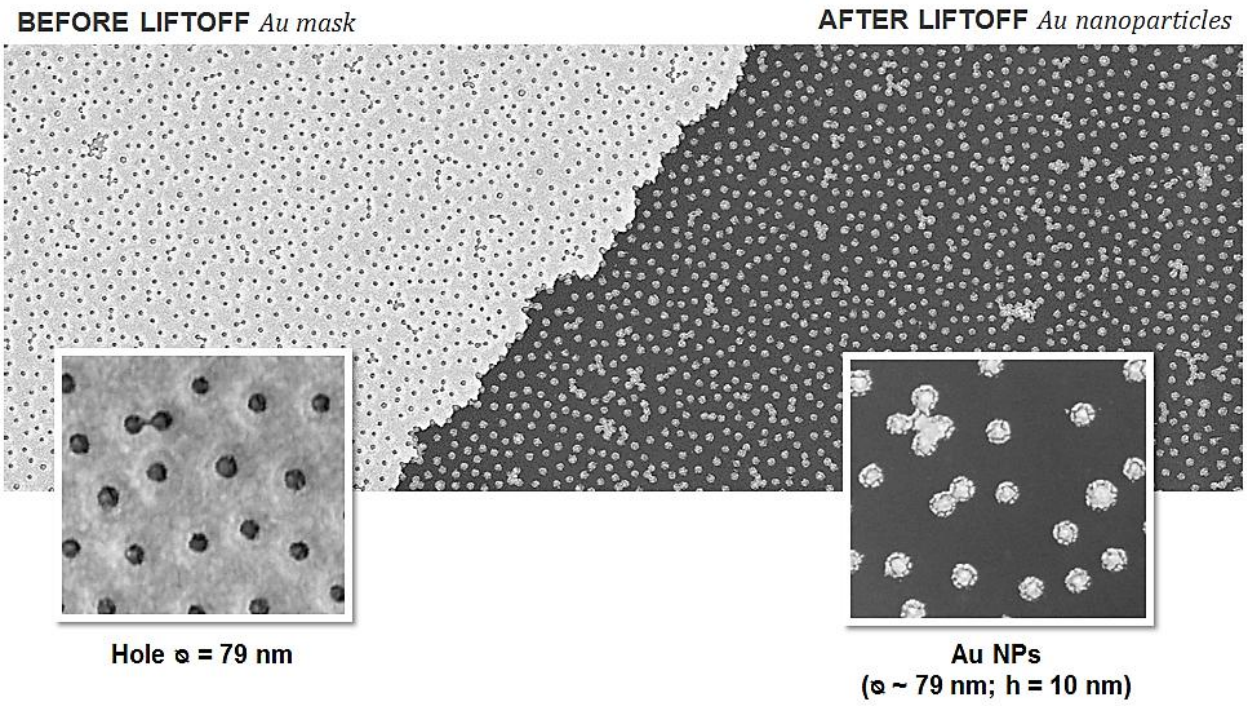


**Figure A.6. Effect of Film Morphology on the Optical Response. (a)** Simulated extinction response for the $VO_2$ rod-like grain and nanoparticle chain structures in insulating and metallic states. We note that the chain of nanoparticles have greater extinction in both metallic and insulating state within the detector range.

## A.4 CONCLUSIONS

Although the stage of combining these two techniques (electron-beam evaporation of $VO_2$ with HMCL) is still at its infancy, one can already see the potential for fabrication of such cost-effective, reliable active substrate. Moreover, slight variations in the deposition conditions (for e.g. thickness, deposition angle and materials) can provide highly tunable template spanning the visible-NIR spectral range. More importantly perhaps, by varying the size of the PSS used, fabrication of samples having varying $VO_2$ nanoparticle sizes can be easily realized, accompanied by its corresponding size-dependent switching properties.

## A.5 ACKNOWLEDGEMENTS

Part of the work presented here was performed in collaboration with Luke Andrea, Yuanmu Yang, Robert E. Marvel, Joyeeta Nag and Bo Choi at the Vanderbilt Institute for Nanoscale Science and Engineering.

# APPENDIX B

# STUDIES OF DEPHASING ($T_2$) IN ACTIVE HYBRID NANOSTRUCTURES: PROBING ELECTRON DYNAMICS BY TIME-RESOLVED SPECTROSCOPY

## B.1 INTRODUCTION

For a better modulation or sensing scheme, one needs to understand the fundamental interaction between a metallic nanostructure and its (phase-changing) environment (*eqn 1.8*). As mentioned before, the resonance condition for collective electron oscillations in plasmonic metallic nanostructure is determined by the shape, size and dielectric function of the metal and the surrounding environment. The spectral linewidth, if measured at the single nanoparticle level,[70] provides a quantitative measure of the electronic dephasing – one of the fastest processes governing the first few-femtosecond initial interaction of the optical field with the metal.[334,335] As an alternative to single-particle nanospectroscopy for extracting indirectly the homogeneous linewidth in the frequency-domain (discussed extensively in §1.2.2b and Chapter 1), such measurements can be carried out also in a time-resolved fashion and on arrays of similar nanostructures using second-order interferometric autocorrelation. From such a measurement, one can obtain the homogeneous linewidth of the system, its corresponding Q-factor and the electromagnetic enhancement.

In the following sections, we report on initial studies of dephasing measurements showing how to fit and interpret the experiments. This may provide a general scheme for understanding the dynamics of hybrid nanostructures on the most fundamental timescale.

## B.2 EXPERIMENTAL SETUP

In order to accurately record ultrafast processes such as dephasing with a characteristic lifetime of about 10 fs, two-pulse interferometric autocorrelation[336,337] is required to probe directly the coherent electron oscillations of the plasmonic nanoparticle. The setup is depicted in figure B.1. and B.2. To ensure accurate timing of electron dephasing, the two identical pulses that are used must have fluences below 25 μJ/cm$^2$ so as to minimize the risk of free-electron heating[201,207].

As shown in figure B.2, we use a BBO crystal to record the resulting second harmonic that is created in the crystal as the two pulses interact. Since the BBO response may be considered to be instantaneous, the second harmonic measurement provides an accurate temporal measurement of the pulse. However, the correct deconvolution requires a few assumptions about the pulse shape as discussed in the next section. In addition, a novel technique to retrieve information about short pulses without any assumptions about the pulse profile and its duration will be presented. This technique is termed interferometric frequency resolved optical gating (*i*FROG) and was developed during the same time frame as the work by Anderson *et al.*[335].

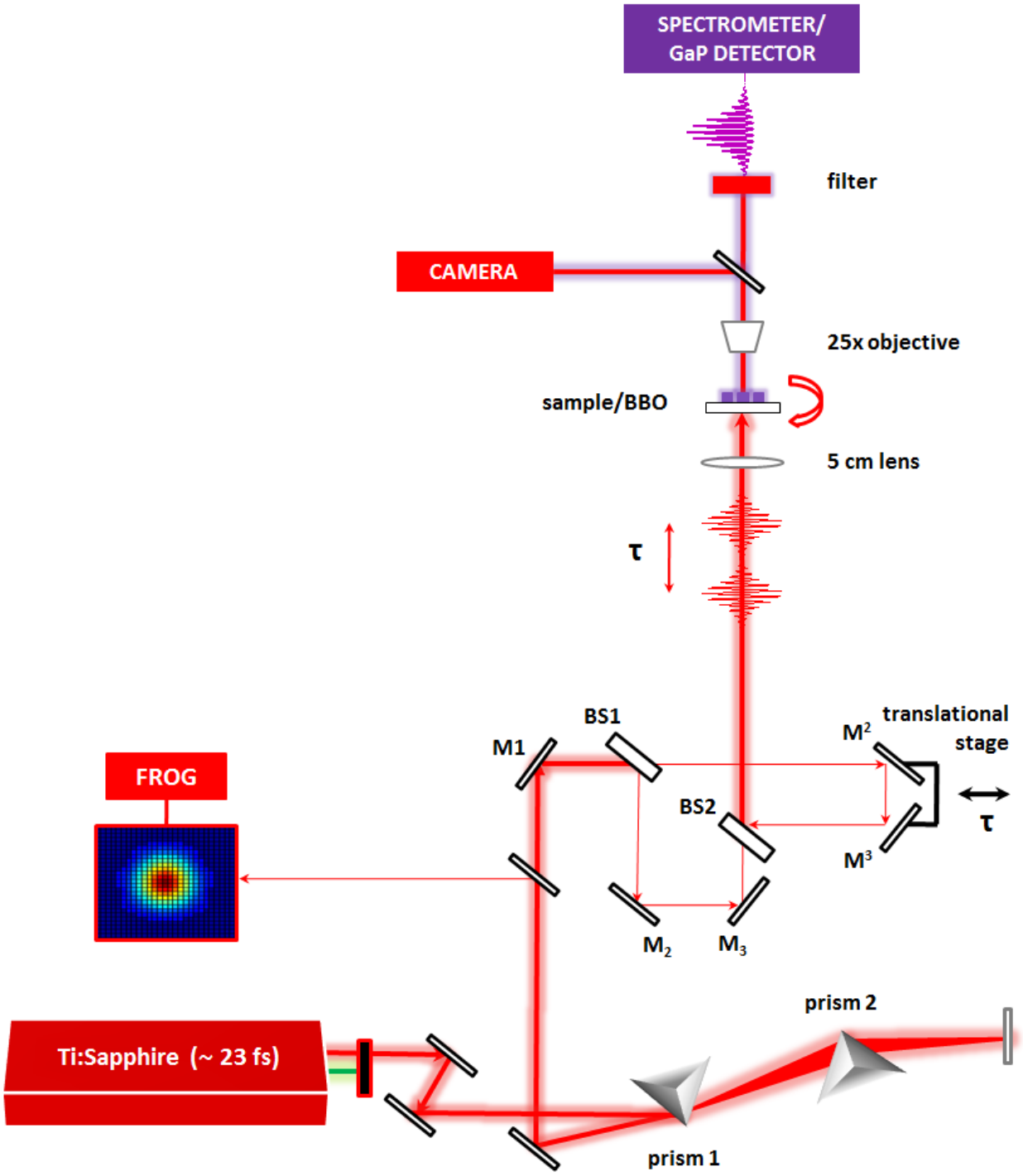


**Figure B.1. Schematics of the Second-Order Interferometric Autocorrelation Setup.** This is similar to the photograph of figure B.1. Also, the frequency resolved optical gating

(FROG) measurement can be compared to the second-harmonic generation of the BBO crystal in the interferometric autocorrelation scheme.

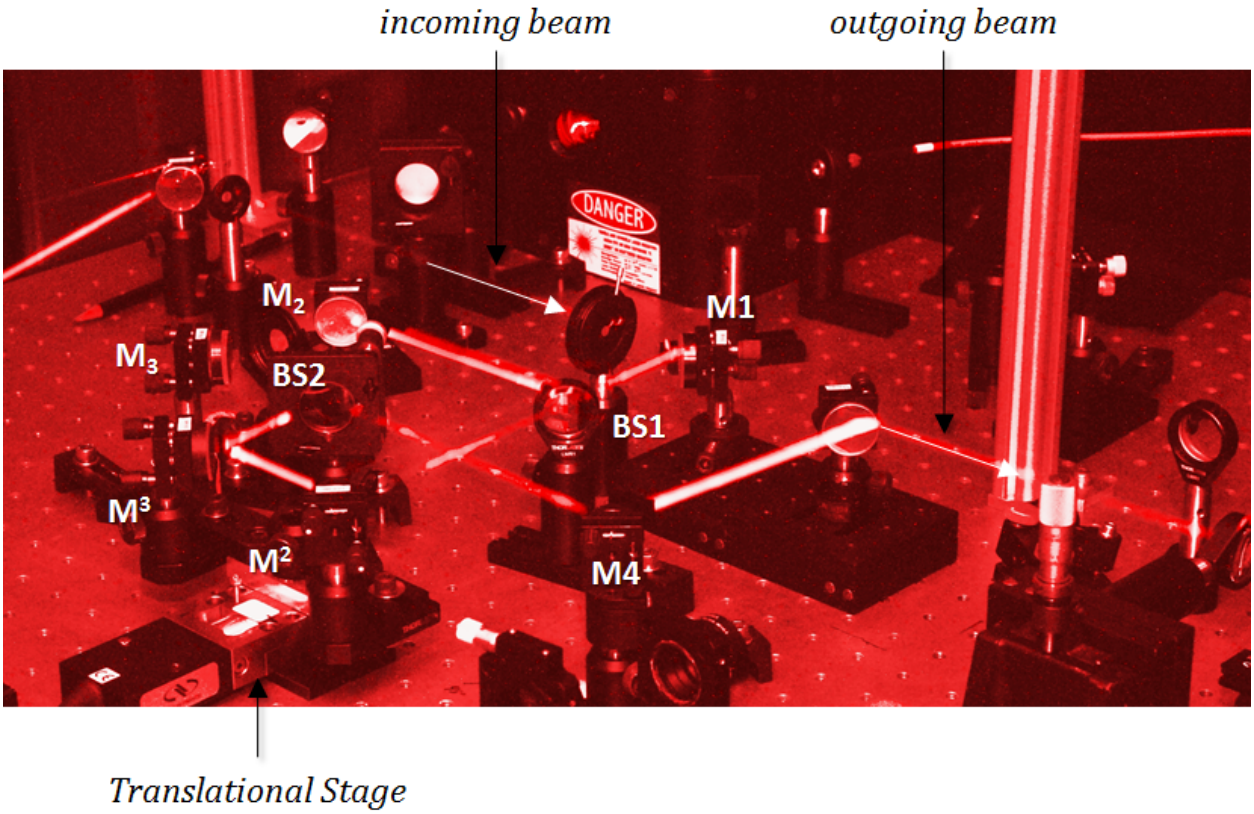


**Figure B.2. Photograph of the Second-Order Interferometric Autocorrelation Setup.** The incoming beam is split into two identical pulses of equal energy at beam splitter BS1. While one of the pulses follow the path BS1→$M_2$→$M_3$→BS2, the other one follows BS1→$M^2$→$M^3$→BS2. Since, $M^2$ and $M^3$ are found on a translational stage, the path length of the later pulse can be changed very precisely. The pulses with collinear path thereafter interact at BS2.

After this pair of pulses has been characterized, the BBO is then replaced by the plasmonic sample of interest. For these experiments, we typically fabricate a 100 x 100 $\mu m^2$ array of non-centrosymmetric "L-shaped" Au nanostructures (*l = 150 nm; w = 75nm; h = 23 nm*) that

is resonant with our 808 nm laser wavelength. Example of such a nanostructure is depicted in figure B.3. Such nanostructures are chosen to achieve high second-harmonic generation efficiencies with low excitation fluences. Although the signal is very weak, it is still detectable in the forward direction and accurately measures the dephasing time of plasmonic nanostructures. Here a similar deconvolution process is used as before to extract the lifetimes, with only one additional component: incorporating the response function of the resonant nanoparticle when driven by the laser pulse. One can think of such a process as a plasmon near-field interferometry that is dictated by the intrinsic lifetime of the nanostructures when driven resonantly by the electric field of the laser pulse.

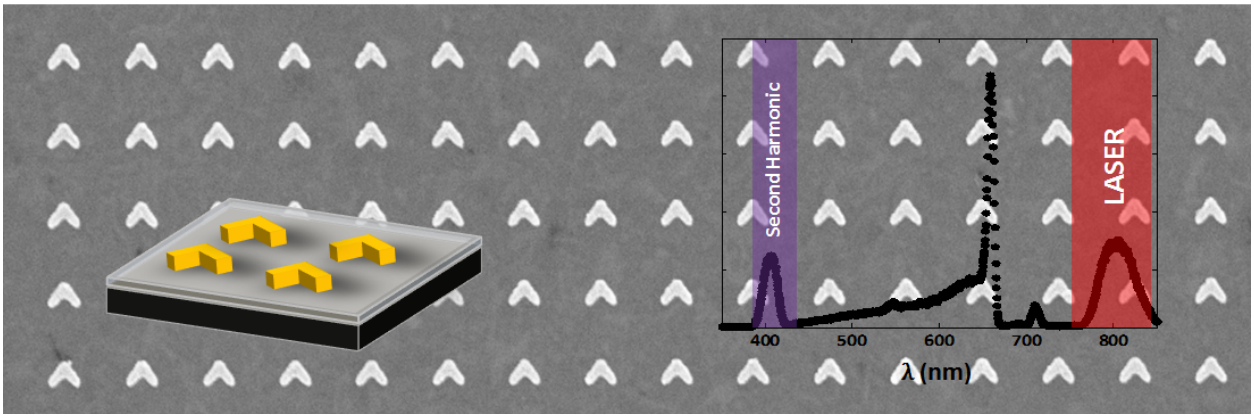


**Figure B.3. Non-Centrosymmetric Second-Harmonic Generating Nanostructures.** SEM of "L-shaped" Au nanostructures with typical length and width of 150 nm and 75 nm, respectively. Second-harmonic spectrum of those nanostructures. Note the very small leakage of the 808 nm laser light.

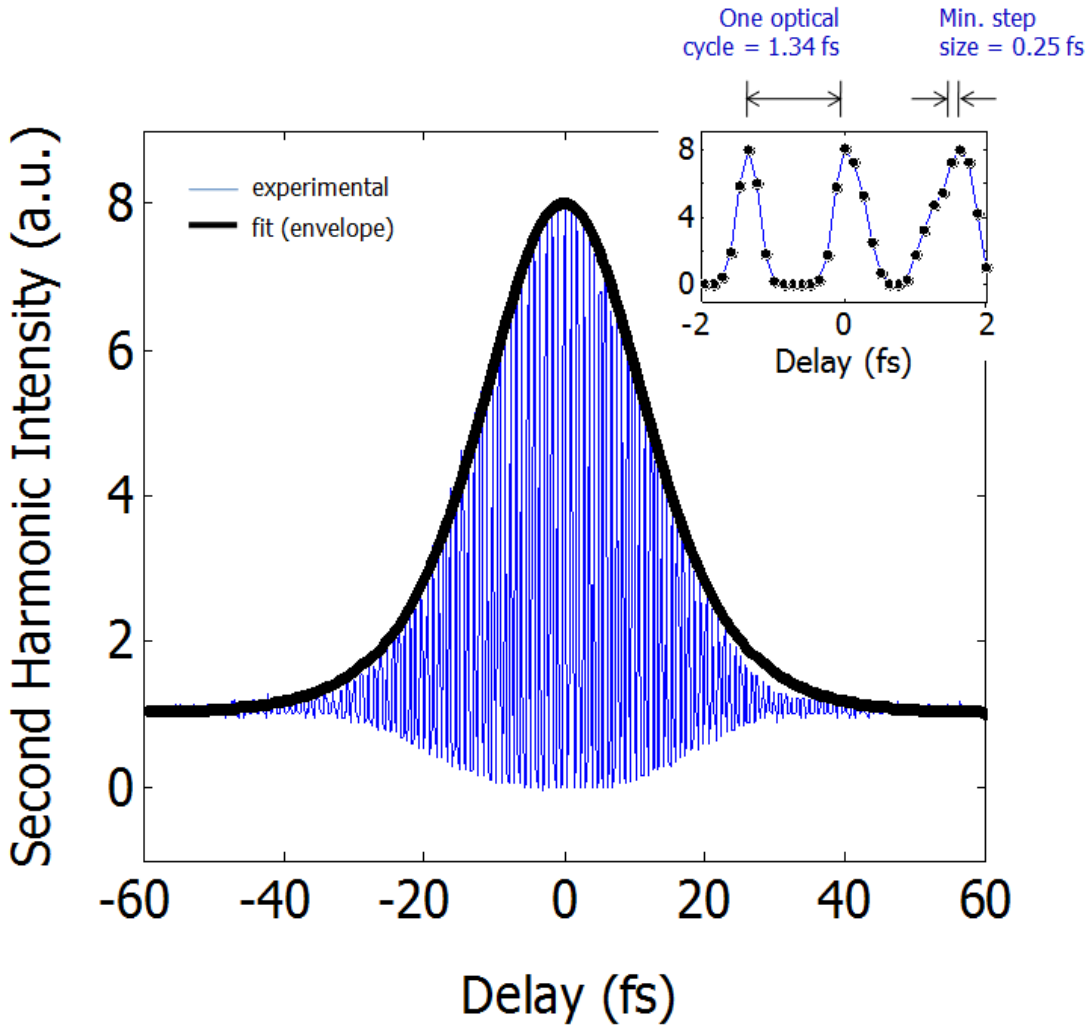


**Figure B.4. Experimental Interferometric Second-Harmonic Trace Generated by BBO Crystal.** Second harmonic intensity as a function of delay stage between interferometer arms normalized to the background SH. The inset shows a magnified region in time domain displaying the perfect constructive and destructive interference obtained at the zero delay and at half the optical cycle, respectively. Note that the stage resolution also satisfies the Nyquist limit (~ 0.5 fs) and appropriate sampling of the SH signal is therefore carried out.

## B.3 SIMULATING SECOND-ORDER INTERFERROMETRIC AUTOCORRELATION

### B.3.2 Theoretical Background

In this section, we discuss the key equations that lead to the code for plotting the second-order interferometric autocorrelation. This derivation has been compiled from several references, including mainly work done by Diels *et al*[336,338]., Lampretch et al. [49,50,71,72,334,339]and Steinmeyer et al. [340-344].

First, consider a balanced Michelson interferometer where the input pulse has been split equally and the electric fields of the two pulses interact with each other.

The electric field takes the form:

$$\tilde{E}^{+}(t) = \frac{1}{2}\mathcal{E}(t)e^{i\varphi_0}e^{i\varphi(t)}e^{i\omega_\ell t} = \frac{1}{2}\tilde{\mathcal{E}}(t)e^{i\omega_\ell t}$$

where $\omega_l$ is defined as the carrier frequency, $\theta$(t) is a time-dependent phase, $\tilde{\mathcal{E}}(t)$ is the complex-valued electric field and $\mathcal{E}$(t) is the real field envelope. The constant phase $e^{i\theta o}$ is typically referred to as the carrier to envelope phase.

One can solve for the intensity at the output due to the interference of the real fields on the detector by using $E = E_1(t-\tau) + E_2(t)$, where $\tau$ is the time delay. Therefore, the intensity at the output of the interferometer averaged over one optical cycle T, is given by:

$$I(t,\tau) = \epsilon_0 cn \frac{1}{T} \int_{t-T/2}^{t+T/2} [E_1(t'-\tau) + E_2(t')]^2 dt'$$

$$= 2\epsilon_0 cn[\tilde{E}_1^+(t-\tau) + \tilde{E}_2^+(t)][\tilde{E}_1^-(t-\tau) + \tilde{E}_2^-(t)]$$

$$= \frac{1}{2}\epsilon_0 cn \left\{ \mathcal{E}_1^2(t-\tau) + \mathcal{E}_2^2(t) \right.$$

$$\left. + \tilde{\mathcal{E}}_1^*(t-\tau)\tilde{\mathcal{E}}_2(t)e^{i\omega_\ell \tau} + \tilde{\mathcal{E}}_1(t-\tau)\tilde{\mathcal{E}}_2^*(t)e^{-i\omega_\ell \tau} \right\}$$

Realizing that the measured signal has been averaged over the slow detector response, the equation above simplifies to the average intensity ($\bar{I}$) where the pulse fluctuations have also been averaged out:

$$\bar{I}(\tau) = \frac{\epsilon_0 cn}{4} \left\{ \langle \tilde{\mathcal{E}}_1^2 \rangle + \langle \tilde{\mathcal{E}}_2^2 \rangle + \left\langle \tilde{\mathcal{E}}_1^*(t-\tau)\tilde{\mathcal{E}}_2(t)e^{i\omega_\ell \tau} + \tilde{\mathcal{E}}_1(t-\tau)\tilde{\mathcal{E}}_2^*(t)e^{-i\omega_\ell \tau} \right\rangle \right\}$$

$$= \epsilon_0 cn \left\{ A_{11}(0) + A_{22}(0) + \tilde{A}_{12}^+(\tau) + \tilde{A}_{12}^-(\tau) \right\}.$$

The correlation $\tilde{A}_{12}^+$ and $\tilde{A}_{12}^-$ arise due to the interaction of the two electric fields acting on each other. This correlation is called the first-order field correlation, while the $n^{th}$ correlation has the general form of:

$$A_n(\tau) = \int_{-\infty}^{\infty} I(t) I^n(t-\tau) dt$$

Therefore, the first order autocorrelation function is given by:

$$G_1(\tau) = \tilde{A}_{12}^+(\tau) + c.c = \frac{1}{4} \int_{-\infty}^{\infty} \tilde{\mathcal{E}}_1(t) \tilde{\mathcal{E}}_2^*(t-\tau) e^{i\omega_\ell \tau} dt + c.c.$$

Since the Fourier transform of this autocorrelation only provides only information about the spectral intensity of the pulse, a first-order autocorrelation provides no other information that a spectrometer would. On the other hand, if we now add to this detecting scheme a second harmonic crystal (while filtering the electric field from the fundamental beam), we obtain the second-order interferometric autocorrelation, that is given by:

$$G_2(\tau) = \int_{-\infty}^{\infty} \left\langle \left| [E_1(t-\tau) + E_2(t)]^2 \right|^2 \right\rangle dt$$

This can be solved (replacing by the electric field and performing the averaging) to yield the following:

$$G_2(\tau) = A(\tau) = A_0(\tau) + \mathrm{Re}\left[A_1(\tau)e^{-i\omega_\ell \tau}\right] + \mathrm{Re}\left[A_2(\tau)e^{-2i\omega_\ell \tau}\right]$$

where the various correlation functions are now given by:

$$A_0(\tau) = \int_{-\infty}^{\infty} \left[\mathcal{E}_1^4(t-\tau) + \mathcal{E}_2^4(t) + 4\mathcal{E}_1^2(t-\tau)\mathcal{E}_2^2(t)\right] dt$$

$$A_1(\tau) = 4\int_{-\infty}^{\infty} \mathcal{E}_1(t-\tau)\mathcal{E}_2(t)\left[\mathcal{E}_1^2(t-\tau) + \mathcal{E}_2^2(t)\right] e^{i[\varphi_1(t-\tau)-\varphi_2(t)]} dt$$

$$A_2(\tau) = 2\int_{-\infty}^{\infty} \mathcal{E}_1^2(t-\tau)\mathcal{E}_2^2(t) e^{2i[\varphi_1(t-\tau)-\varphi_2(t)]} dt.$$

The purpose of this deconvolution is to emphasize the fact that there are three terms. While $A_o(\tau)$ contains the background and the intensity autocorrelation, the term $A_1(\tau)$ and $A_2(\tau)$ contain information about the phase of the pulse and is used to determine the degree

of chirp in a pulse. In order to gain deeper insights into this, let's look at two extreme conditions, that is when $\tau = 0$ and$\tau = \infty$, resulting respectively into $16 \times \int \mathcal{E}^4(t)dt$ and $2 \times \int \mathcal{E}^4(t)dt$, as plotted in figure B.5. This results in a *systematic* peak to background ratio of 8:1 for the second-order interferometric autocorrelation. In the case of the intensity autocorrelation alone, this corresponds to a 3:1 ratio. Thus, correlation of the second-harmonic fields adds to this ratio and contains the required information about the phase of the pulse. This second-order autocorrelation signature (as for every autocorrelation actually) is symmetric and the shape and phase sensitivity can be used to test whether or not phase modulation is present in the field (linear or quadratic chirp).

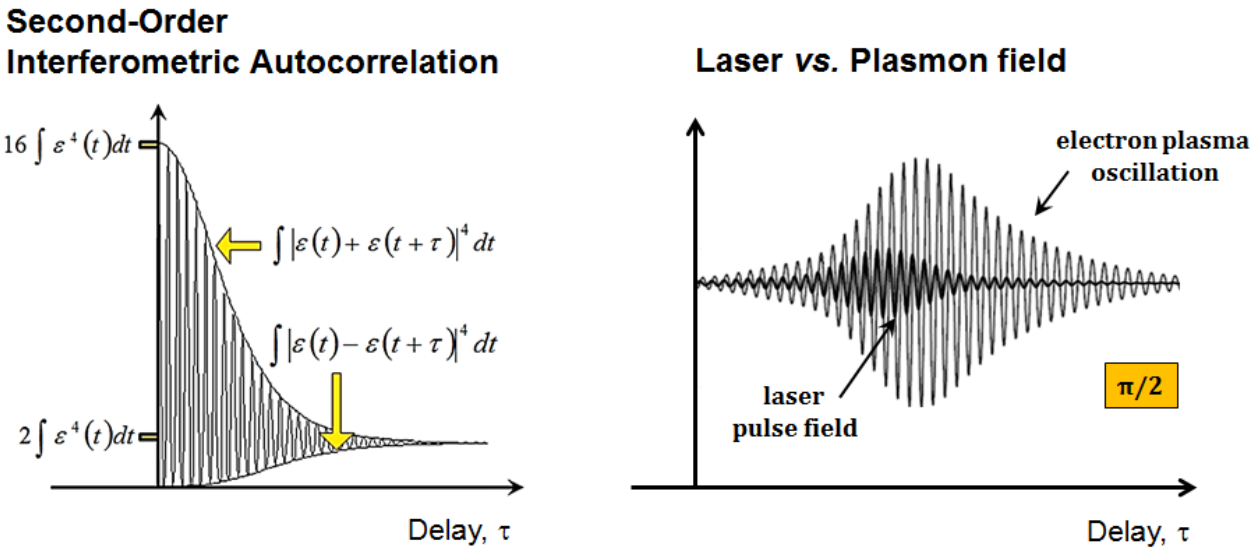


**Figure B.5. Autocorrelation fields.** Second-order interferometric autocorrelation highlighting that the ratio between its peak to its background is 8:1. The plot to the right is a comparison between the electric field of the laser and the resonant nanoparticle.

From this electric-field/electric-field interaction, one can now add the resonant response of the nanoparticle as it reacts to the field and interfere coherently. Such plasmon interferometry, first treated by Lampretch *et al.*, can be described as follows:

$$\mathrm{I}_{SHG} = \int_{-\infty}^{\infty} \left\langle \left| \left[ \int_{\infty}^{t} \frac{1}{\omega_0} E_{pulse1}\left(t^*\right) e^{-\gamma\left(t-t^*\right)} sin\left[\omega_0\left(t-t^*\right)\right] dt^* \right.\right.\right.$$

$$+$$

$$\left.\left.\left. \int_{\infty}^{t} \frac{1}{\omega_0} E_{pulse2}\left(t^*+\tau\right) e^{-\gamma\left(t-t^*\right)} sin\left[\omega_0\left(t-t^*\right) dt^*\right] \right]^2 \right|^2 \right\rangle dt$$

where (i) $E_{pulse1} = E_{pulse2}$ = secant square pulse with a duration of 23 fs and (ii) $\gamma = 1/2\tau$ ($\tau$ is the oscillator energy decay time). This equation is hereby implemented in the code below, treating both the resonant and non-resonant cases of the nanoparticle.

### B.3.2 Code

We present here the Matlab code that can be used to generate n$^{th}$ -order interferometric autocorrelation pattern. Here we focus mostly on the second order one.

```
%%%%%%%%%%%%%%%%%%%%%%%%%%%%%%%%%
% CODE START: Parameters for the laser - Secant hyperbolic
%%%%%%%%%%%%%%%%%%%%%%%%%%%%%%%%%
 c = 3e8;          % Speed of light [m/s]
fs = 1e-15;       % For time conversion
```

```
nm = 1e-9;      % For length conversion
AC_order = 2;          %nth order autocorrelation
tp = 23*fs;            % pulse duration of Ti:Sapphire
wavelength = 808;   % give wavelength in nm
wl =  2*pi*c/(wavelength*nm); % center frequency for the laser
phiO = 0 ;                    %the pulse interaction with matter depends on phi0
phi = 0;                      % phase dependent pulse


%%%%%%%%%%%%%%%%%%%%%%%%%%%%%%%%%%%%%%%%%%%%%%%%%%%%%%%%%%%%%%%%%%%%%%%%%%%%
%
% Parameters for the NP dephasing time
%
%%%%%%%%%%%%%%%%%%%%%%%%%%%%%%%%%%%%%%%%%%%%%%%%%%%%%%%%%%%%%%%%%%%%%%%%%%%%
wavelengthReso = 808;                 % give wavelength in nm
w0 = (2*pi*c)/(wavelengthReso*nm);  % center wavelength for the NP
dephasingTime = 10*fs;
gamma = 1/(dephasingTime);

%%%%%%%%%%%%%%%%%%%%%%%%%%%%%%%%%%%%%%%%%%%%%%%%%%%%%%%%%%%%%%%%%%%%%%%%%%%%
%
% Parameters for the "translation stage"
%
%%%%%%%%%%%%%%%%%%%%%%%%%%%%%%%%%%%%%%%%%%%%%%%%%%%%%%%%%%%%%%%%%%%%%%%%%%%%
delay_step = 0.25;      %  STAGE DELAY in fs
delay_spread = 200;
tStage = (-delay_spread:delay_step:delay_spread)*fs;
time_spread = 400;    % Time window that we integrate over
time_step = 1;
t = (-time_spread:time_step:time_spread)*fs;
```

```
%%%%%%%%%%%%%%%%%%%%%%%%%%%%%%%%%%%%%%
%
% Initialization of data vectors
%
%%%%%%%%%%%%%%%%%%%%%%%%%%%%%%%%%%%%%%
G2 = zeros(1,length(tStage));
PLT = zeros(1,length(tStage));
PL = zeros(1,length(t));

%%%%%%%%%%%%%%%%%%%%%%%%%%%%%%%%%%%%%%
%
% Testing just the autocorrelation calculation
%
%%%%%%%%%%%%%%%%%%%%%%%%%%%%%%%%%%%%%%
for p1 = 1:length(tStage)
        tdelay = tStage(p1);
EPulse_1 =
(1/2).*(1./cosh(1.763.*(t./tp))).*exp(1i*phiO).*exp(1i*wl.*t).*exp(1i*phi.*t)+
(1/2)*(1./cosh(1.763*(t./tp))).*exp(-1i*phiO).*exp(-1i*wl.*t).*exp(-1i*phi.*t);
EPulse_2 =
(1/2).*(1./cosh(1.763.*((t-tdelay)./tp))).*exp(1i*phiO).*exp(1i*wl.*(t-
tdelay)).*exp(11i*phi.*(t-tdelay))+ (1/2)*(1./cosh(1.763*((t-tdelay)./tp))).*exp(-
1i*phiO).*exp(-1i*wl.*(t-tdelay)).*exp(-1i*phi.*(t-tdelay));

G2_pa = (((EPulse_1 + EPulse_2).^AC_order)).^2;
G2(p1) = sum(G2_pa)/length(G2_pa);
end

figure(1),clf
```

```
plot(tStage,G2/G2(1))
%%%%%%%%%%%%%%%%%%%%%%%%%%%%%%%%%%%%%
%
%  Calculation including plasmon field
%
%%%%%%%%%%%%%%%%%%%%%%%%%%%%%%%%%%%%%
for p1 = 1:length(tStage)
        tdelay = tStage(p1);
for p2 = 1:length(t)
        tt = t(1:p2);

EPulse_1s =
(1/2).*(1./cosh(1.763.*(tt./tp))).*exp(1i*phiO).*exp(1i*wl.*tt).*exp(1i*phi.*tt)+
(1/2)*(1./cosh(1.763*(tt./tp))).*exp(-1i*phiO).*exp(-1i*wl.*tt).*exp(-1i*phi.*tt);
EPulse_2s =
(1/2).*(1./cosh(1.763.*((tt-tdelay)./tp))).*exp(1i*phiO).*exp(1i*wl.*(tt-
tdelay)).*exp(11i*phi.*(tt-tdelay))+ (1/2)*(1./cosh(1.763*((tt-tdelay)./tp))).*exp(-
1i*phiO).*exp(-1i*wl.*(tt-tdelay)).*exp(-1i*phi.*(tt-tdelay));

plf = exp(-gamma.*(t(p2)- tt)).*sin(w0*(t(p2)- tt));
plf_total = (EPulse_1s + EPulse_2s).*plf;
PL(p2) = sum(plf_total);
end

PL2 = (PL.^AC_order).^2;
PLT(p1) = sum(PL2)/length(PL2);
end

av = sum(PLT(1:30))/30;
figure(2), clf
```

```
plot(tStage,PLT/av)

%%%%%%%%%%%%%%%%%%%%%%%%%%%%%%%%%%%%%%%
% CODE END
%%%%%%%%%%%%%%%%%%%%%%%%%%%%%%%%%%%%%%%
```

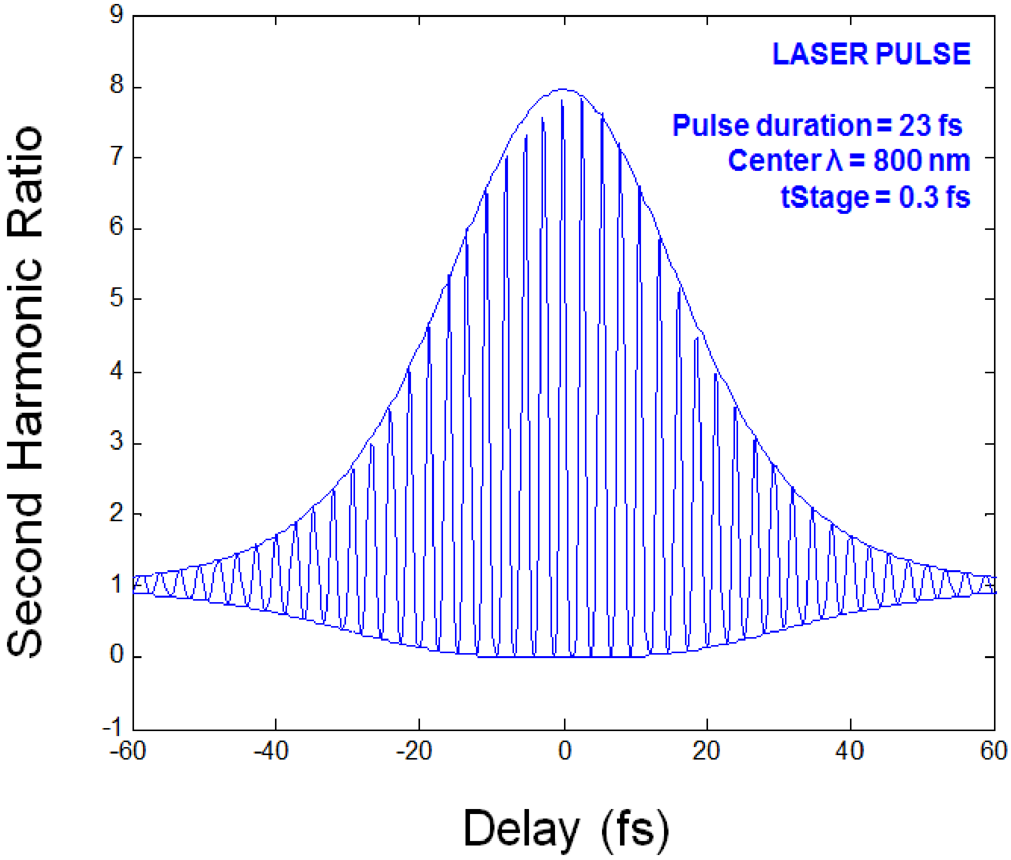

**Figure B.6. Simulated IFRAC of an Optical Pulse.** Simulated interferometric autocorrelation (envelope + fringes) of an 800 nm light pulse of 23 fs in duration. The stage step size was set to 0.3 fs.

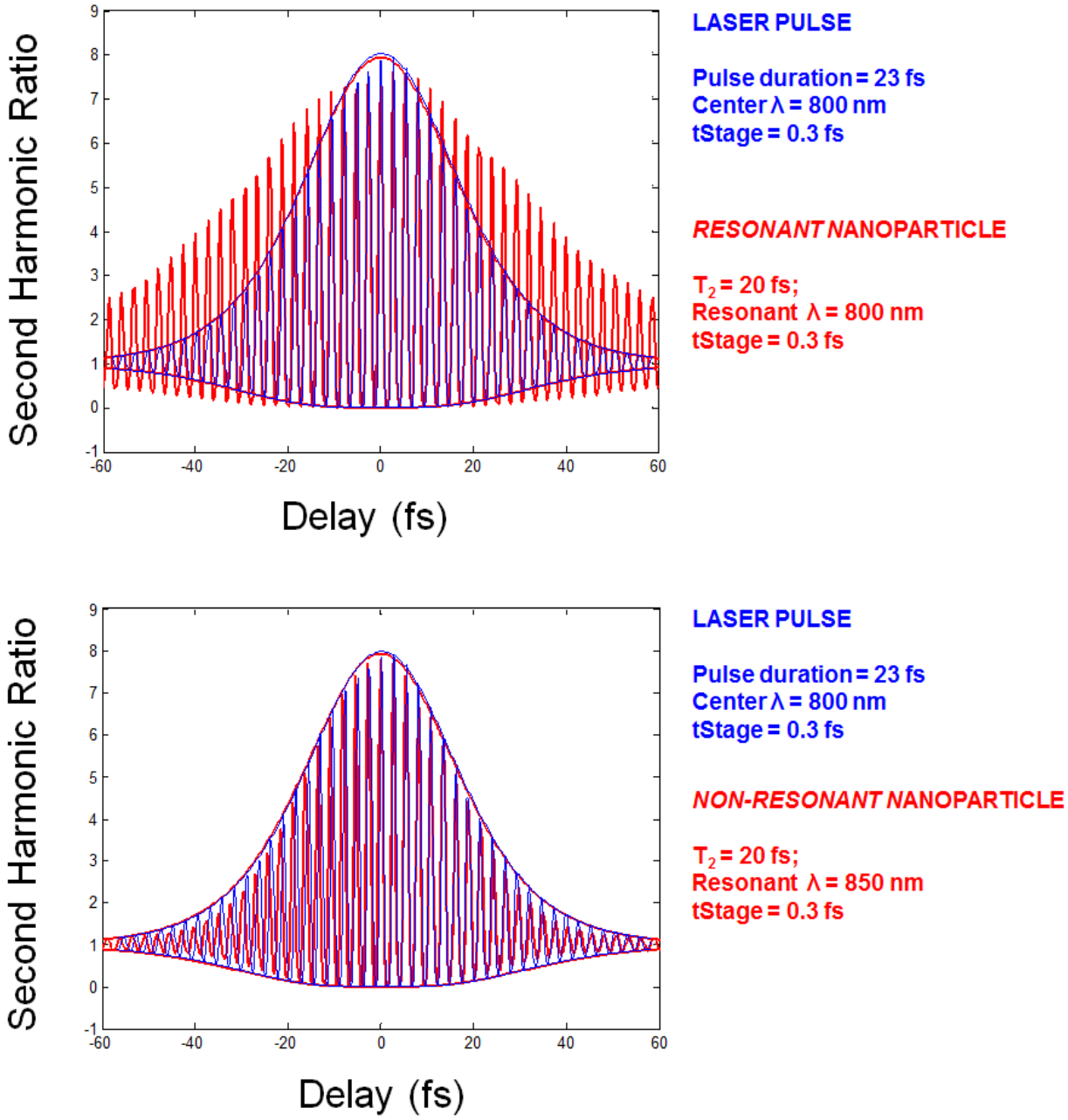


**Figure B.7. Resonant vs. Non-Resonant Response of Nanostructures.** Simulated optical responses for a nanoparticle on and off resonance (red) with a characteristic dephasing lifetime of 20 fs when interacting with a laser light of 800 nm (blue). We note that in the case of the resonant nanoparticle, the lifetime is dictated by its intrinsic lifetime while in the off-resonant case, the response resembles that of the driving laser pulse.

## B.4 PROBING INTRINSIC ELECTRON DYNAMICS OF NANOSTRUCTURES

As mentioned before, such time-resolved experiments are designed to understand the dynamical processes in nanostructures of thin films with minimum assumption about the near field environment. Here we discuss the beginnings of two experiments aim at understanding size effect and variation of the nanoenvironment on the coherent electron oscillation of plasmonic nanostructures.

In the first experiment, we perform interferometric autocorrelation on quantum size metallic (Au) nanoparticles. Due to the very low second harmonic yield, the nanoparticles were arranged in a superlattice geometry and had an average size distribution, centered at $\sim$ 2, 4 and 8 nm[345,346]. Due to the asymmetry of the nanoparticles and slight variation in their size distribution, a weak but detectable second-harmonic generation could be recorded in the forward direction. Thus, time-resolved second harmonic measurement could be obtained as shown in figure B.8. Extracting the second harmonic only at its central wavelength (thus at its maximum as well) and analyzing the data in a similar fashion as described in the previous section, we obtain a dephasing time of $\sim$ 8 fs for the 4 nm Au nanoparticle. This is in good agreement with previous results and future experiments will investigate the dephasing lifetimes of smaller sized nanoparticles (2, 4 and 8 nm). In these cases, the goal will be assess the role of both chemical interface damping and increased electron scattering at the boundary, known to be of upmost importance at this length scale.

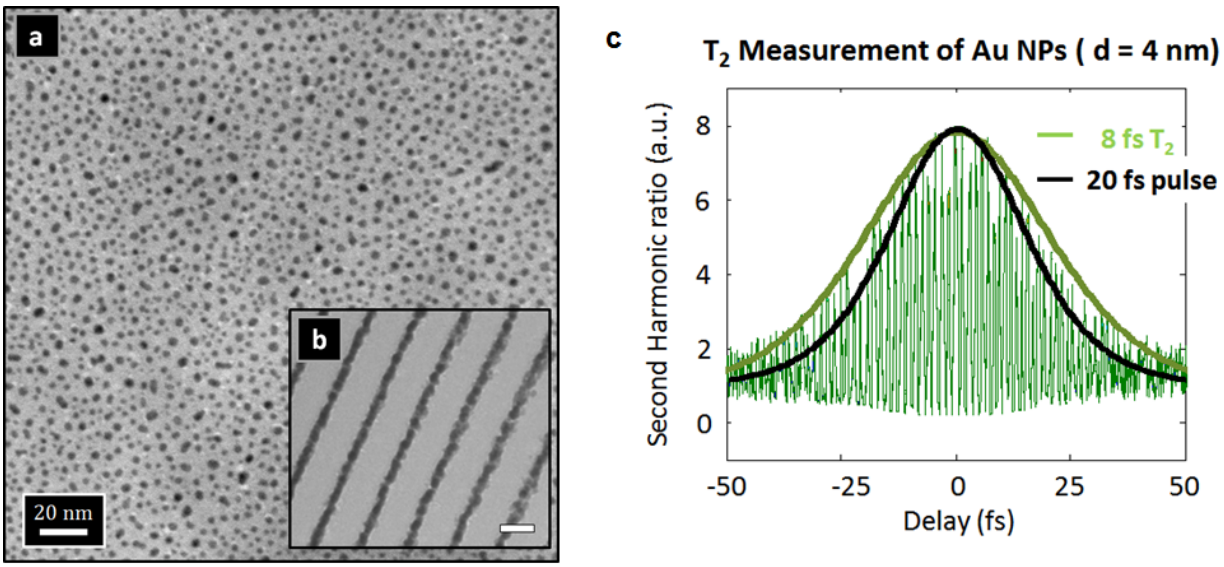


**Figure B.8. Dephasing Measurement of Au Superlattices.** **(a)** TEM of the 4 nm Au superlattice in top and **(b)** side view configuration. **(c)** Dephasing measurement of the sample. The black line is the envelope of a chirp-free pulse (20 fs) necessary for the correct timing. Dephasing time of ~ 8 fs were obtained for this sample.

In the second experiment, we investigate how spatial fluctuations of the nanoenvironment can affect the optical response of the nanoparticle (or nanoantenna). Here as a means of spatially varying the nanoenvironment of the nanoparticle we use $VO_2$ that can, at the onset of the phase-transition, have metallic and insulating domains coexisting, as shown in Figure B.9 (*§ 1.3.2c*). Thus, at each temperature point during the phase transition, second-harmonic interferometric autocorrelation measurements will be taken to extract the dephasing lifetime of the nanoparticle. Since the measurement directly connects to dynamic due to its time-domain specificity (in contrast to frequency measurement), an array of similar nanoparticles can be used. This serves therefore as a complement to the single nanoparticle studies of Chapter 2. Thus, this potentially could provide insights on the

physical mechanism at play for the peculiar enhanced scattering observed at the onset of the phase-transition (Chapter 2). Although time-resolved measurement is necessary to obtain conclusive analysis about the change in homogeneous linewidth of such hybrid system, initial static measurements on the plasmon resonance wavelength and of its corresponding FWHM linewidth of the gold particle plasmon at various temperatures between the cold (insulating) and hot (metallic) states of the $VO_2$ clearly shows an increased linewidth at the onsets of the phase transition. This corresponds to a decrease in the lifetime of the coherent electron oscillation, potentially suggesting the change in oscillation pattern by spatial alteration of the surrounding medium.

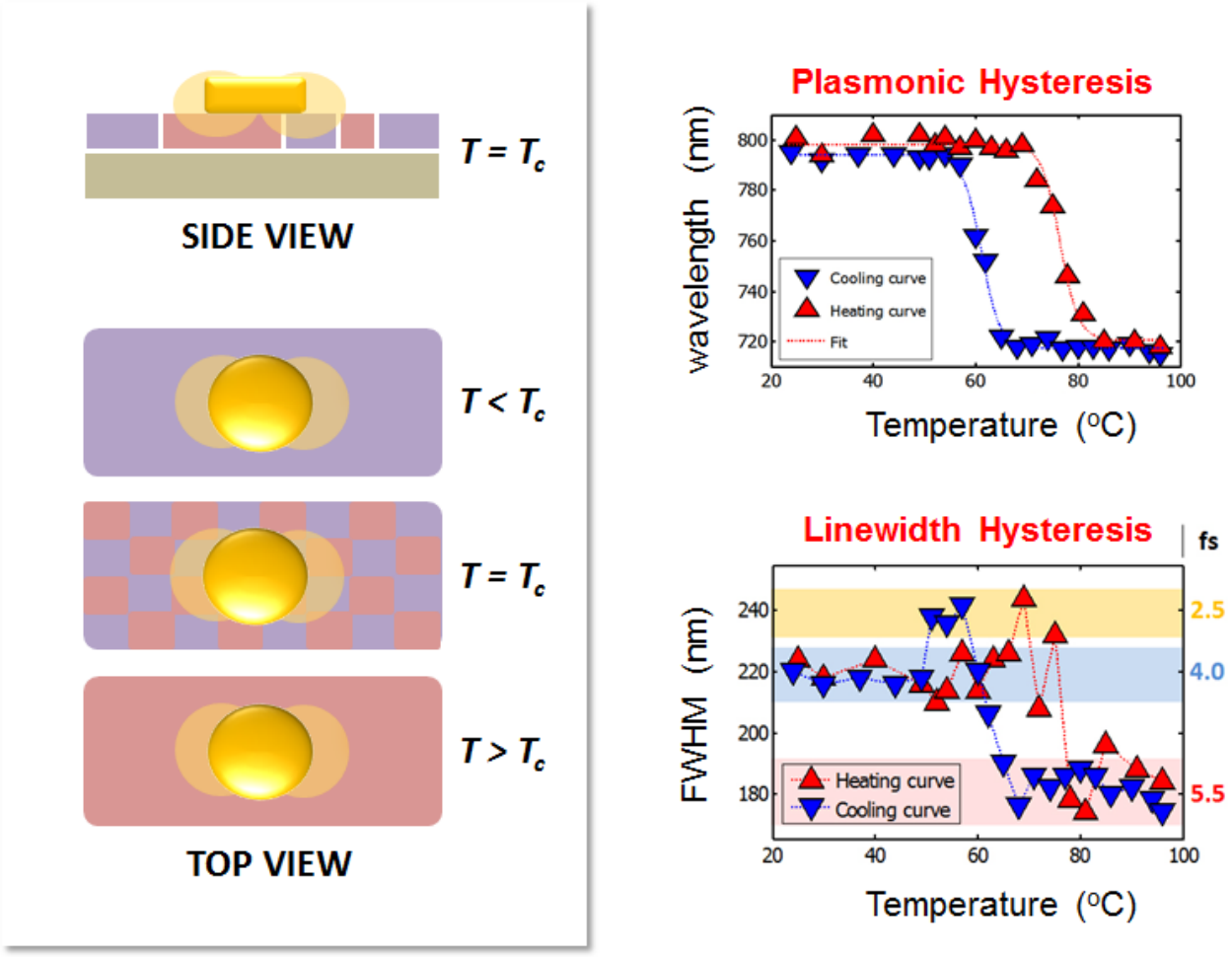


**Figure B9. Linewidth Hysteresis of Hybrid Nanostructures.** (a) Schematics depicting the spatially varying domains of $VO_2$ (metallic or insulating) as a means to spatially alter the electron oscillation in the plasmonic nanoantenna. While the plasmonic hysteresis mimics the $VO_2$ phase transition, the FWHM linewidth shows an increase at the onset of the phase transition. This corresponds to a decreased in the dephasing time of the nanoparticles.

## B.5 GENERAL SCHEME FOR INTERFERROMETRIC 2nd-ORDER AUTOCORRELATION FOR SECOND HARMONIC GENERATING NANOSTRUCTURES

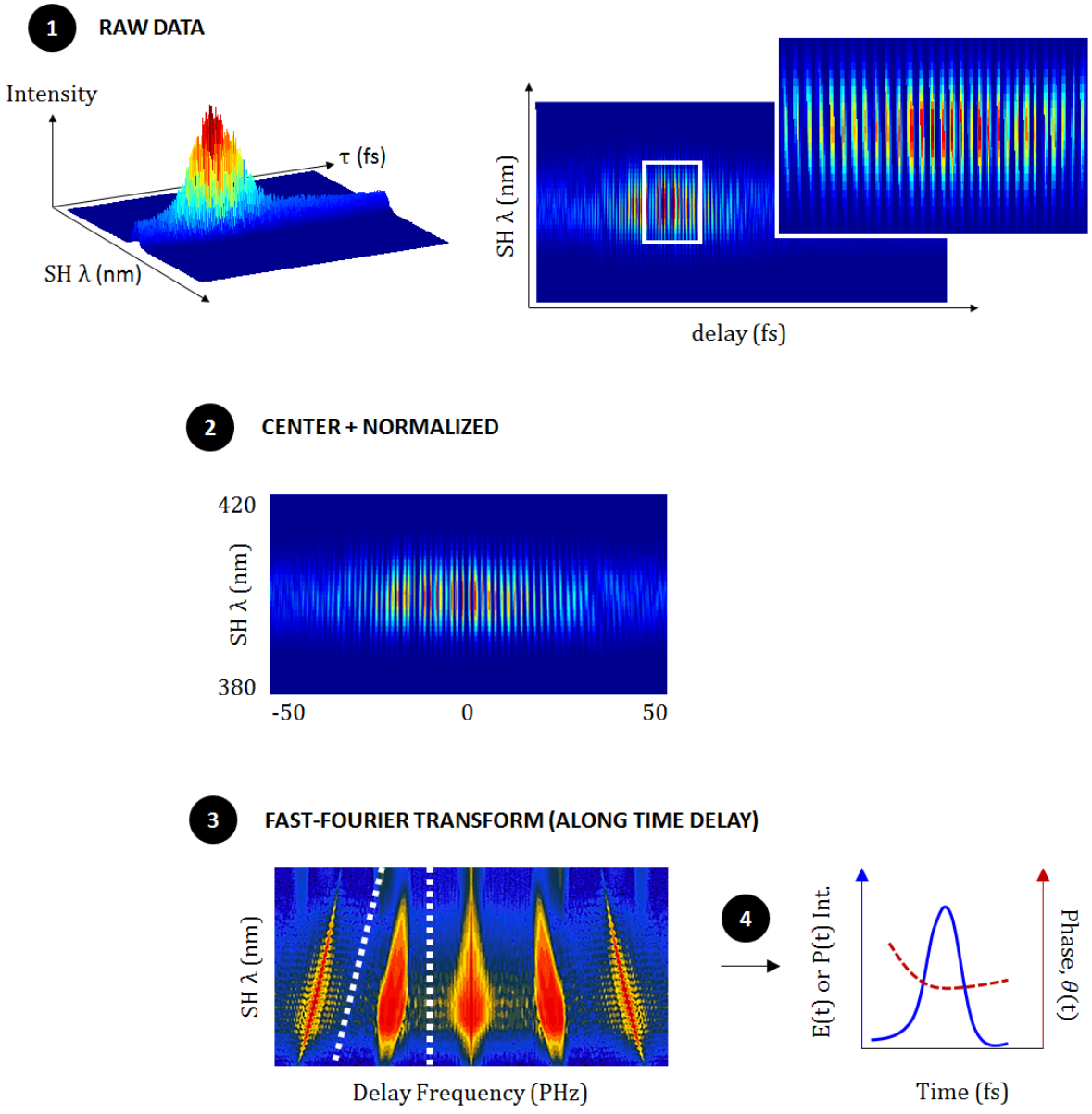


**Figure B9. iFROG Scheme for Extracting Response Function of Nanostructures.** (1) Second harmonic raw data is collected as a function time delay. (2) The data is centered, normalized and Fourier filtered. (3) A Fast-Fourier Transform (iFFT) algorithm is used along the delay to extract only the DC baseband. (4) This selected data (dotted lines) set

undergoes thereafter an iFFT and is used as the input into a typical frequency resolved optical gating software (for e.g. FROG3) to evaluate the electric field and response function of the nanostructures.

In the previous sections of Appendix B, experimental interferometric second-harmonic measurements (BBO or nanostructures) were obtained either by averaging the second harmonic response (use of PMT or GaP detector) or by extracting only its center wavelength (when using a spectrometer), while assumptions were made about the driving laser pulse as well to extract dephasing lifetime. In the scheme presented here, we take into account the entire bandwidth of the pulse and its corresponding generated second harmonic bandwidth to extract the lifetime. Thus no assumptions are made about our exciting pulse and its corresponding interaction with the nanoparticle. This characterization technique was first developed by Steinmeyer for use in laser diagnostic only. However, this concept to retrieve the nanostructure response by such interferometric fashion is more robust and provides greater physical insights about the response of complex hybrid nanostructures, both its phase and intensity, as shown in figure B.10.

**B.6 ACKNOLEDGEMENTS**

We thank Dr. A. Halabica for providing the superlattice samples and for help with the MATLAB code and Dr. J. Nag for initial sample fabrication of the non-centrosymmetric L-shaped nanostructures.

# BIBLIOGRAPHY


1 Novotny, L. & Hetch, B. *Principles of Nano-Optics*. (Cambridge University Press, 2006).

2 Grigorenko, A. N., Roberts, N. W., Dickinson, M. R. & Zhang, Y. Nanometric optical tweezers based on nanostructured substrates. *Nat. Photonics* **2**, 365-370, (2008).

3 Liu, N., Tang, M. L., Hentschel, M., Giessen, H. & Alivisatos, A. P. Nanoantenna-enhanced gas sensing in a single tailored nanofocus. *Nat. Mater.* **10**, 631-636, (2011).

4 Valentine, J. *et al.* Three-dimensional optical metamaterial with a negative refractive index. *Nature* **455**, 376-U332, (2008).

5 Gansel, J. K. *et al.* Gold Helix Photonic Metamaterial as Broadband Circular Polarizer. *Science* **325**, 1513-1515, (2009).

6 Ma, R. M., Oulton, R. F., Sorger, V. J., Bartal, G. & Zhang, X. A. Room-temperature sub-diffraction-limited plasmon laser by total internal reflection. *Nat. Mater.* **10**, 110-113, (2011).

7 Gather, M. C. & Yun, S. H. Single-cell biological lasers. *Nat. Photonics* **5**, 406-410, (2011).

8 Curto, A. G. *et al.* Unidirectional Emission of a Quantum Dot Coupled to a Nanoantenna. *Science* **329**, 930-933, (2010).

9 Liu, N., Hentschel, M., Weiss, T., Alivisatos, A. P. & Giessen, H. Three-Dimensional Plasmon Rulers. *Science* **332**, 1407-1410, (2011).

10 Liu, M. *et al.* A graphene-based broadband optical modulator. *Nature* **474**, 64-67, (2011).

11 Taminiau, T. H., Stefani, F. D., Segerink, F. B. & Van Hulst, N. F. Optical antennas direct single-molecule emission. *Nat. Photonics* **2**, 234-237, (2008).

12 Valentine, J., Li, J. S., Zentgraf, T., Bartal, G. & Zhang, X. An optical cloak made of dielectrics. *Nat. Mater.* **8**, 568-571, (2009).

13 Fausti, D. *et al.* Light-Induced Superconductivity in a Stripe-Ordered Cuprate. *Science* **331**, 189-191, (2011).

14 Millis, A. J., Shraiman, B. I. & Mueller, R. Dynamic Jahn-Teller effect and colossal magnetoresistance in $La_{1-x}Sr_xMnO_3$. *Physical Review Letters* **77**, 175-178, (1996).

15 Hur, N. *et al.* Electric polarization reversal and memory in a multiferroic material induced by magnetic fields. *Nature* **429**, 392-395, (2004).

16 Imada, M., Fujimori, A. & Tokura, Y. Metal-insulator transitions. *Rev. Mod. Phys.* **70**, 1039-1263, (1998).

17 Enkrich, C. *et al.* Magnetic metamaterials at telecommunication and visible frequencies. *Physical Review Letters* **95**, (2005).

18 Karaveli, S. & Zia, R. Spectral Tuning by Selective Enhancement of Electric and Magnetic Dipole Emission. *Physical Review Letters* **106**, (2011).

19 Fredriksson, H. *et al.* Hole-mask colloidal lithography. *Adv. Mater.* **19**, 4297, (2007).

20 Fang, Z. *et al.* Plasmon-Induced Doping of Graphene. *ACS Nano*, (2012).

21 Yuk, J. M. *et al.* High-Resolution EM of Colloidal Nanocrystal Growth Using Graphene Liquid Cells. *Science* **336**, 61-64, (2012).

22 Scholl, J. A., Koh, A. L. & Dionne, J. A. Quantum plasmon resonances of individual metallic nanoparticles. *Nature* **483**, 421-U468, (2012).

23 Maier, S. A. *et al.* Plasmonics - A route to nanoscale optical devices. *Adv. Mater.* **13**, 1501-+, (2001).

24 Brongersma, M. L. & Shalaev, V. M. APPLIED PHYSICS The Case for Plasmonics. *Science* **328**, 440-441, (2010).

25 Orenstein, J. Ultrafast Spectroscopy of Quantum Materials. *Physics Today* **65**, 44-50, (2012).

26 Ritchie, R. H. Plasma Losses by Fast Electrons in Thin Films. *Physical Review* **106**, 874-881, (1957).

27 Ritchie, R. H. & Marusak, A. L. Surface plasmon dispersion relation for an electron gas. *Surf. Sci.* **4**, 234-+, (1966).

28 Atwater, H. A. The promise of plasmonics. *Sci.Am.* **296**, 56-63, (2007).

29 Veselago, V. G. Electrodynamics of substances with simultaneously negative values of sigma and mu. *Soviet Physics Uspekhi-Ussr* **10**, 509-&, (1968).

30 Shelby, R. A., Smith, D. R. & Schultz, S. Experimental verification of a negative index of refraction. *Science* **292**, 77-79, (2001).

31 Shelby, R. A., Smith, D. R., Nemat-Nasser, S. C. & Schultz, S. Microwave transmission through a two-dimensional, isotropic, left-handed metamaterial. *Applied Physics Letters* **78**, 489-491, (2001).

32 Smith, D. R. & Kroll, N. Negative refractive index in left-handed materials. *Physical Review Letters* **85**, 2933-2936, (2000).

33 Smith, D. R., Padilla, W. J., Vier, D. C., Nemat-Nasser, S. C. & Schultz, S. Composite medium with simultaneously negative permeability and permittivity. *Physical Review Letters* **84**, 4184-4187, (2000).

34 Morin, F. J. Oxides Which Show a Metal-to-Insulator Transition at the Neel Temperature. *Physical Review Letters* **3**, 34-36, (1959).

35 Cavalleri, A. *et al.* Femtosecond structural dynamics in $VO_2$ during an ultrafast solid-solid phase transition. *Physical Review Letters* **87**, (2001).

36 Lopez, R., Boatner, L. A., Haynes, T. E., Haglund, R. F. & Feldman, L. C. Enhanced hysteresis in the semiconductor-to-metal phase transition of $VO_2$ precipitates formed in $SiO_2$ by ion implantation. *Applied Physics Letters* **79**, 3161-3163, (2001).

37 Lopez, R., Haynes, T. E., Boatner, L. A., Feldman, L. C. & Haglund, R. F. Size effects in the structural phase transition of $VO_2$ nanoparticles. *Physical Review B* **65**, 224113, (2002).

38 Eyert, V. $VO_2$: A Novel View from Band Theory. *Physical Review Letters* **107**, 016401, (2011).

39 Raether, H. *Surface Plasmons on Smooth and Rough Surfaces and on Gratings*. (1988).

40 Ebbesen, T. W., Lezec, H. J., Ghaemi, H. F., Thio, T. & Wolff, P. A. Extraordinary optical transmission through sub-wavelength hole arrays. *Nature* **391**, 667-669, (1998).

41 Pendry, J. B. Negative refraction makes a perfect lens. *Physical Review Letters* **85**, 3966-3969, (2000).

42 Barber, D. J. & Freestone, I. C. An investigation of the origin of the color of the Lycurgus Cup by analytical transmission electron-microscopy. *Archaeometry* **32**, 33-45, (1990).

43 Zhou, W. *et al.* Atomically localized plasmon enhancement in monolayer graphene. *Nat. Nanotechnol.* **7**, 161-165, (2012).

44 Jackson, J. B. & Halas, N. J. Surface-enhanced Raman scattering on tunable plasmonic nanoparticle substrates. *Proc. Natl. Acad. Sci. U. S. A.* **101**, 17930-17935, (2004).

45 Huang, X., Jain, P. K., El-Sayed, I. H. & El-Sayed, M. A. Gold nanoparticles: interesting optical properties and recent applications in cancer diagnostic and therapy. *Nanomedicine* **2**, 681-693, (2007).

46 Jain, P. K., Huang, X., El-Sayed, I. H. & El-Sayed, M. A. Noble Metals on the Nanoscale: Optical and Photothermal Properties and Some Applications in Imaging, Sensing, Biology, and Medicine. *Accounts of Chemical Research* **41**, 1578-1586, (2008).

47 Pan, L. *et al.* Maskless Plasmonic Lithography at 22 nm Resolution. *Scientific Reports* **1**, (2011).

48 Wang, S. *et al.* Subcellular Resolution Mapping of Endogenous Cytokine Secretion by Nano-Plasmonic-Resonator Sensor Array. *Nano Letters* **11**, 3431-3434, (2011).

49 Lamprecht, B. *et al.* Surface plasmon propagation in microscale metal stripes. *Applied Physics Letters* **79**, 51-53, (2001).

50 Weeber, J. C. *et al.* Near-field observation of surface plasmon polariton propagation on thin metal stripes. *Physical Review B* **64**, (2001).

51 Maier, S. A. in *Plasmonics: Fundamentals and Applications* 248 (Springer, 2007).

52 Fox, M. *Optical Properties of Solids*. (Oxford Master Series in Condensed Matter Physics, 2008).

53 Suh, J. Y., Donev, E. U., Lopez, R., Feldman, L. C. & Haglund, R. F. Modulated optical transmission of subwavelength hole arrays in metal-VO2 films. *Applied Physics Letters* **88**, (2006).

54 Donev, E. U. *et al.* Optical properties of subwavelength hole arrays in vanadium dioxide thin films. *Physical Review B* **73**, (2006).

55 Chan, G. H., Zhao, J., Schatz, G. C. & Van Duyne, R. P. Localized surface plasmon resonance spectroscopy of triangular aluminum nanoparticles. *J. Phys. Chem. C* **112**, 13958-13963, (2008).

56 Lawrie, B. J., Kim, K. W., Norton, D. P. & Haglund, R. F. Plasmon–Exciton Hybridization in ZnO Quantum-Well Al Nanodisc Heterostructures. *Nano Letters*, (2012).

57 Lal, S., Link, S. & Halas, N. J. Nano-optics from sensing to waveguiding. *Nat. Photonics* **1**, 641-648, (2007).

58 Jackson, J. B. & Halas, N. J. Silver nanoshells: Variations in morphologies and optical properties. *J. Phys. Chem. B* **105**, 2743-2746, (2001).

59 Knight, M. W. & Halas, N. J. Nanoshells to nanoeggs to nanocups: optical properties of reduced symmetry core-shell nanoparticles beyond the quasistatic limit. *New Journal of Physics* **10**, (2008).

60 Landes, C. F., Link, S., Mohamed, M. B., Nikoobakht, B. & El-Sayed, M. A. Some properties of spherical and rod-shaped semiconductor and metal nanocrystals. *Pure and Applied Chemistry* **74**, 1675-1692, (2002).

61 Hulteen, J. C. & Vanduyne, R. P. Nanosphere lithography - a materials general fabrication process for periodic particle array surfaces. *Journal of Vacuum Science & Technology a-Vacuum Surfaces and Films* **13**, 1553-1558, (1995).

62 Bastys, V., Pastoriza-Santos, I., Rodriguez-Gonzalez, B., Vaisnoras, R. & Liz-Marzan, L. M. Formation of silver nanoprisms with surface plasmons at communication wavelengths. *Advanced Functional Materials* **16**, 766-773, (2006).

63 Sun, Y. G. & Xia, Y. N. Shape-controlled synthesis of gold and silver nanoparticles. *Science* **298**, 2176-2179, (2002).

64 Wang, H., Brandl, D. W., Le, F., Nordlander, P. & Halas, N. J. Nanorice: A hybrid plasmonic nanostructure. *Nano Letters* **6**, 827-832, (2006).

65 Hao, F., Nehl, C. L., Hafner, J. H. & Nordlander, P. Plasmon Resonances of a Gold Nanostar. *Nano Letters* **7**, 729-732, (2007).

66 Mie, G. Beiträge zur Optik trüber Medien, speziell kolloidaler Metallösungen (Contributions to the optics of turbid media, particularly colloidal metal suspensions). *Ann. Phys.-Berlin* **25**, (1908).

67 Meier, M. & Wokaun, A. Enhanced fields on large metal particles - dynamic depolarization. *Opt. Lett.* **8**, 581-583, (1983).

68 Link, S. & El-Sayed, M. A. Shape and size dependence of radiative, non-radiative and photothermal properties of gold nanocrystals. *Int. Rev. Phys. Chem.* **19**, 409-453, (2000).

69 Link, S. & El-Sayed, M. A. Spectral properties and relaxation dynamics of surface plasmon electronic oscillations in gold and silver nanodots and nanorods. *J. Phys. Chem. B* **103**, 8410-8426, (1999).

70 Klar, T. *et al.* Surface-plasmon resonances in single metallic nanoparticles. *Physical Review Letters* **80**, 4249-4252, (1998).

71 Lamprecht, B., Leitner, A. & Aussenegg, F. R. Femtosecond decay-time measurement of electron-plasma oscillation in nanolithographically designed silver particles. *Appl. Phys. B-Lasers Opt.* **64**, 269-272, (1997).

72 Lamprecht, B., Krenn, J. R., Leitner, A. & Aussenegg, F. R. Particle-plasmon decay-time determination by measuring the optical near-field's autocorrelation: influence of inhomogeneous line broadening. *Appl. Phys. B-Lasers Opt.* **69**, 223-227, (1999).

73 Sonnichsen, C. *et al.* Drastic reduction of plasmon damping in gold nanorods. *Physical Review Letters* **88**, (2002).

74 Aeschlimann, M. *et al.* Coherent Two-Dimensional Nanoscopy. *Science* **333**, 1723-1726, (2011).

75 Boltasseva, A. & Atwater, H. A. Low-Loss Plasmonic Metamaterials. *Science* **331**, 290-291, (2011).

76 West, P. R. *et al.* Searching for better plasmonic materials. *Laser Photon. Rev.* **4**, 795-808, (2010).

77 Kreibig, U. & Vollmer, M. *Optical Properties of Metal Clusters*. (Springer Series in Materials Science, 1995).

78 Ashcroft, N. W. & Mermin, N. D. *Solid State Physics*. 848 (Brooks Cole, 1976).

79 Yee, K. S. Numerical solution of initial boundary value problems involving Maxwells equations in isotropic media. *IEEE Trans. Antennas Propag.* **AP14**, 302-&, (1966).

80 Taflove, A. & Brodwin, M. E. Numerical-solution of steady-state electromagnetic scattering problems using time-dependent Maxwells equations. *IEEE Trans. Microw. Theory Tech.* **23**, 623-630, (1975).

81 Taflove, A. & Hagness, S. C. *Computational Electrodynamics: The Finite-Difference Time-Domain Method, 3rd ed.*, (Artech House Publishers, 2005).

82 Courant, R., Friedrichs, K. & Lewy, H. Uber die partiellen differenzengleichungen der mathematischen physik *Math. Ann.* **100**, (1928).

83 *Lumerical Solutions*, <http://www.lumerical.com/tcad-products/fdtd/>

84 Krasavin, A. V. & Zheludev, N. I. Active plasmonics: Controlling signals in Au/Ga waveguide using nanoscale structural transformations. *Applied Physics Letters* **84**, 1416-1418, (2004).

85 Nikolajsen, T., Leosson, K. & Bozhevolnyi, S. I. Surface plasmon polariton based modulators and switches operating at telecom wavelengths. *Applied Physics Letters* **85**, 5833-5835, (2004).

86 Liu, J. *et al.* Waveguide-integrated, ultralow-energy GeSi electro-absorption modulators. *Nat. Photonics* **2**, 433-437, (2008).

87 Green, W. M. J., Rooks, M. J., Sekaric, L. & Vlasov, Y. A. Ultra-compact, low RF power, 10 gb/s silicon Mach-Zehnder modulator. *Optics Express* **15**, 17106-17113, (2007).

88 Smalley, J. S. T. *et al.* High contrast modulation of plasmonic signals using nanoscale dual-frequency liquid crystals. *Opt. Express* **19**, 15265-15274, (2011).

89 Pacifici, D., Lezec, H. J. & Atwater, H. A. All-optical modulation by plasmonic excitation of CdSe quantum dots. *Nat. Photonics* **1**, 402-406, (2007).

90 Pala, R. A., Shimizu, K. T., Melosh, N. A. & Brongersma, M. L. A nonvolatile plasmonic switch employing photochromic molecules. *Nano Letters* **8**, 1506-1510, (2008).

91 Dionne, J. A., Diest, K., Sweatlock, L. A. & Atwater, H. A. PlasMOStor: A Metal-Oxide-Si Field Effect Plasmonic Modulator. *Nano Letters* **9**, 897-902, (2009).

92 Sorger Volker, J., Lanzillotti-Kimura Norberto, D., Ma, R.-M. & Zhang, X. Vol. 1 17 (2012).

93 Samson, Z. L. *et al.* Chalcogenide glasses in active plasmonics. *Phys. Status Solidi-Rapid Res. Lett.* **4**, 274-276, (2010).

94 MacDonald, K. F. & Zheludev, N. I. Active plasmonics: current status. *Laser Photon. Rev.* **4**, 562-567, (2010).

95 Caspers, J. N., Rotenberg, N. & van Driel, H. M. Ultrafast silicon-based active plasmonics at telecom wavelengths. *Optics Express* **18**, 19761-19769, (2010).

96 Chen, H. T. *et al.* Tuning the Resonance in High-Temperature Superconducting Terahertz Metamaterials. *Physical Review Letters* **105**, (2010).

97 Haertling, G. H. PLZT electrooptic materials and applications - a review. *Ferroelectrics* **75**, 25-55, (1987).

98 Adachi, H., Mitsuyu, T., Yamazaki, O. & Wasa, K. Ferroelectric (PB,LA)(ZR,TI)$O_3$ epitaxial thin-films on sapphire grown by rf-planar magnetron sputtering. *Journal of Applied Physics* **60**, 736-741, (1986).

99 Taylor, T. R. *et al.* Impact of thermal strain on the dielectric constant of sputtered barium strontium titanate thin films. *Applied Physics Letters* **80**, 1978-1980, (2002).

100 Lei, D. Y. *et al.* Spectroscopic ellipsometry as an optical probe of strain evolution in ferroelectric thin films. *Optics Express* **20**, 4419-4427, (2012).

101 Kim, D.-Y. *et al.* Electro-optic characteristics of (001)-oriented $Ba_{0.6}Sr_{0.4}TiO_3$ thin films. *Applied Physics Letters* **82**, 1455-1457, (2003).

102 Bethe, H. Theorie der Beugung von Elektronen an Kristallen. *Ann. Phys.-Berlin* **392**, 55-129, (1928).

103 Bloch, F. Bemerkung zur Elektronentheorie des Ferromagnetismus und der elektrischen Leitfähigkeit. *Zeitschrift für Physik A Hadrons and Nuclei* **57**, 545-555, (1929).

104 Sommerfeld, A. Z. Elektrochem. . *Angew. Phys. Chem.* **34**, (1928).

105 Mott, N. F. & Peierls, R. Discussion of the paper by de Boer and Verwey. *Proceedings of the Physical Society of London* **49 (4S)**, (1937).

106 de Boer, J. H. & Verwey, E. J. W. Semi-conductors with partially and with completely filled 3d-lattice bands. . *Proceedings of the Physical Society of London* **49 (4S)**, (1937).

107 Basov, D. N., Averitt, R. D., van der Marel, D., Dressel, M. & Haule, K. Electrodynamics of correlated electron materials. *Reviews of Modern Physics* **83**, 471-541, (2011).

108 Yang, Z., Ko, C. Y. & Ramanathan, S. in *Annual Review of Materials Research, Vol 41* Vol. 41 *Annual Review of Materials Research* (eds D. R. Clarke & P. Fratzl) 337-367 (Annual Reviews, 2011).

109 Pashkin, A. *et al.* Ultrafast insulator-metal phase transition in $VO_2$ studied by multiterahertz spectroscopy. *Physical Review B* **83**, 195120, (2011).

110 Tselev, A. *et al.* Symmetry Relationship and Strain-Induced Transitions between Insulating M1 and M2 and Metallic R phases of Vanadium Dioxide. *Nano Letters* **10**, 4409-4416, (2010).

111 Lopez, R., Feldman, L. C. & Haglund, R. F. Size-Dependent Optical Properties of $VO_2$ Nanoparticle Arrays. *Physical Review Letters* **93**, 177403, (2004).

112 Appavoo, K. & Haglund, R. F. Detecting Nanoscale Size Dependence in VO2 Phase Transition Using a Split-Ring Resonator Metamaterial. *Nano Letters* **11**, 1025-1031, (2011).

113 Qazilbash, M. M. *et al.* Nanoscale imaging of the electronic and structural transitions in vanadium dioxide. *Physical Review B* **83**, 165108, (2011).

114 Verleur, H. W., Barker, A. S. & Berglund, C. N. Optical Properties of $VO_2$ between 0.25 and 5 eV. *Physical Review* **172**, 788, (1968).

115 Eyert, V. The metal-insulator transitions of $VO_2$: a band theoretical approach. *Ann. Phys.-Berlin* **11**, 650-702, (2002).

116 Cavalleri, A. *et al.* Picosecond soft x-ray absorption measurement of the photoinduced insulator-to-metal transition in VO2. *Physical Review B* **69**, (2004).

117 Goodenough, J. 2 components of crystallographic transition in $VO_2$. *Journal of Solid State Chemistry* **3**, 490, (1971).

118 Bray, J. W. *et al.* Observation of a Spin-Peierls Transition in a Heisenberg Antiferromagnetic Linear-Chain System. *Physical Review Letters* **35**, 744-747, (1975).

119 Kaxiras, E. *Atomic and Electronic Structure of Solids*. (Cambridge University Press, 2003).

120 Kotliar, G. & Vollhardt, D. Strongly correlated materials: Insights from dynamical mean-field theory. *Physics Today* **57**, 53-59, (2004).

121 Zylbersztejn, A. & Mott, N. F. METAL-INSULATOR TRANSITION IN VANADIUM DIOXIDE. *Physical Review B* **11**, 4383-4395, (1975).

122 Wentzcovitch, R. M., Schulz, W. W. & Allen, P. B. $VO_2$ - Peierls or Mott-Hubbard - a view from band theory. *Physical Review Letters* **72**, 3389-3392, (1994).

123 Iori, F., Gatti, M. & Rubio, A. Role of nonlocal exchange in the electronic structure of correlated oxides. *Physical Review B* **85**, (2012).

124 Shin, S. *et al.* Vacuum-ultraviolet reflectance and photoemission study of the metal-insulator phase transitions in $VO_2$, $V_6O_{13}$, and $V_2O_3$. *Physical Review B* **41**, 4993-5009, (1990).

125 Okazaki, K. *et al.* Photoemission study of the metal-insulator transition in $VO_2/TiO_2(001)$: Evidence for strong electron-electron and electron-phonon interaction. *Physical Review B* **69**, 165104, (2004).

126 Heyd, J., Scuseria, G. E. & Ernzerhof, M. Hybrid functionals based on a screened Coulomb potential. *J. Chem. Phys.* **118**, 8207-8215, (2003).

127 Weber, C. *et al.* Vanadium Dioxide: A Peierls-Mott Insulator Stable against Disorder. *Physical Review Letters* **108**, (2012).

128 Haverkort, M. W. *et al.* Orbital-Assisted Metal-Insulator Transition in $VO_2$. *Physical Review Letters* **95**, 196404, (2005).

129 Qazilbash, M. M. *et al.* Mott transition in $VO_2$ revealed by infrared spectroscopy and nano-imaging. *Science* **318**, 1750-1753, (2007).

130 Nag, J., Payzant, A., More, K. & Haglund, R. F. J. *submitted to Journal of Applied Physics*, (2011).

131 Tao, Z. *et al.* Decoupling of Structural and Electronic Phase Transitions in VO2. *Physical Review Letters* **109**, (2012).

132 Landau, L. D. & Lifshitz, E. M. *Statistical Physics*. (Pergamon Press, 1959).

133 Ehrenfest, P. Phasenumwandlungen im ueblichen und erweiterten Sinn, classifiziert nach den entsprechenden Singularitaeten des thermodynamischen Potentiales. *Proceedings Koninklijke Akademie van Wetenschappen* **36**, 153-157, (1933).

134 Ortin, J., Planes, A. & Delaey, L. *Hysteresis in Shape-Memory Materials in "The Science of Hysteresis"*. Vol. 3 467 (Elsevier, 2005).

135 Driscoll, T., Kim, H. T., Chae, B. G., Di Ventra, M. & Basov, D. N. Phase-transition driven memristive system. *Applied Physics Letters* **95**, (2009).

136 Driscoll, T. *et al.* Memory Metamaterials. *Science* **325**, 1518-1521, (2009).

137 Berglund, C. N. & Guggenhe.Hj. Electronic properties of $VO_2$ near semiconductor-metal transition. *Physical Review* **185**, 1022-&, (1969).

138 Donev, E. U. *Metal-semiconductor transitions in nanoscale vanadium dioxide thin-films, subwavelength holes, and nanoparticles* Ph. D. thesis, Vanderbilt University, (2008).

139 Rao, C. N. R. & Rao, K. J. *Phase transitions in solids: an approach to the study of the chemistry and physics of solids*. (McGraw-Hill, 1978).

140 Aliev, R. A. *et al.* Effect of grain sizes on the metal-semiconductor phase transition in vanadium dioxide polycrystalline thin films. *Physics of the Solid State* **48**, 929-934, (2006).

141 Aliev, R. A. & Klimov, V. A. Effect of synthesis conditions on the metal-semiconductor phase transition in vanadium dioxide thin films. *Physics of the Solid State* **46**, 532-536, (2004).

142 Klimov, V. A. *et al.* Hysteresis loop construction for the metal-semiconductor phase transition in vanadium dioxide films. *Technical Physics* **47**, 1134-1139, (2002).

143 Tu, K. N., Mayer, J. W. & Feldman, L. C. *Electronic Thim Film Science for Electrical Engineers and Material Scientists*. (Macmillan Publishing Company, 1992).

144 Fan, W. *et al.* Large kinetic asymmetry in the metal-insulator transition nucleated at localized and extended defects. *Physical Review B* **83**, 235102, (2011).

145 Cilento, F. *et al.* Ultrafast insulator-to-metal phase transition as a switch to measure the spectrogram of a supercontinuum light pulse. *Applied Physics Letters* **96**, 021102, (2010).

146 Yin, W. *et al.* The metal-insulator transition in vanadium dioxide: A view at bulk and surface contributions for thin films and the effect of annealing. *Journal of Applied Physics* **105**, 114322-114322-114327, (2009).

147 Yang, Z., Ko, C. & Ramanathan, S. Oxide Electronics Utilizing Ultrafast Metal-Insulator Transitions. *Annual Review of Materials Research* **41**, 337-367, (2011).

148 Kim, H. T. *et al.* Mechanism and observation of Mott transition in VO2-based two- and three-terminal devices. *New Journal of Physics* **6**, 52, (2004).

149 Katzke, H., Toledano, P. & Depmeier, W. Theory of morphotropic transformations in vanadium oxides. *Physical Review B* **68**, (2003).

150 Loehman, R. E., Rao, C. N. R. & Honig, J. M. Crystallography and defect chemistry of solid solutions of vanadium and titanium oxides. *Journal of Physical Chemistry* **73**, 1781-&, (1969).

151 Morinaga, M. & Cohen, J. B. Defect structure of $VO_x$ (I). Ordered phase, $VO_{1.30}$. *Acta Crystallographica Section A* **35**, 745-756, (1979).

152 Ladd, L. A. & Paul, W. OPTICAL AND TRANSPORT PROPERTIES OF HIGH QUALITY CRYSTALS OF V2O4 NEAR METALLIC TRANSITION TEMPERATURE. *Solid State Communications* **7**, 425-&, (1969).

153 Suh, J. Y., Lopez, R., Feldman, L. C. & Haglund, R. F. Semiconductor to metal phase transition in the nucleation and growth of $VO_2$ nanoparticles and thin films. *Journal of Applied Physics* **96**, 1209-1213, (2004).

154 Ruzmetov, D., Senanayake, S. D. & Ramanathan, S. X-ray absorption spectroscopy of vanadium dioxide thin films across the phase-transition boundary. *Physical Review B* **75**, (2007).

155 Sambi, M., Sangiovanni, G., Granozzi, G. & Parmigiani, F. Growth and the structure of epitaxial VO2 at the TiO2(110) surface. *Physical Review B* **55**, 7850-7858, (1997).

156 Nag, J., Payzant, E. A., More, K. L. & Haglund, R. F., Jr. Enhanced performance of room-temperature-grown epitaxial thin films of vanadium dioxide. *Applied Physics Letters* **98**, (2011).

157 Cao, J. *et al.* Strain engineering and one-dimensional organization of metal-insulator domains in single-crystal vanadium dioxide beams. *Nat. Nanotechnol.* **4**, 732-737, (2009).

158 Strelcov, E., Lilach, Y. & Kolmakov, A. Gas Sensor Based on Metal-Insulator Transition in VO2 Nanowire Thermistor. *Nano Letters* **9**, 2322-2326, (2009).

159 Sohn, J. I. *et al.* Direct observation of the structural component of the metal-insulator phase transition and growth habits of epitaxially grown VO2 nanowires. *Nano Letters* **7**, 1570-1574, (2007).

160 Baik, J. M., Kim, M. H., Larson, C., Wodtke, A. M. & Moskovits, M. Nanostructure-dependent metal-insulator transitions in vanadium-oxide nanowires. *J. Phys. Chem. C* **112**, 13328-13331, (2008).

161 Fuls, E. N., Hensler, D. H. & Ross, A. R. Reactively sputtered vanadium dioxide thin films. *Applied Physics Letters* **10**, 199-&, (1967).

162 Kim, D. H. & Kwok, H. S. Pulsed laser deposition of $VO_2$ thin-films. *Applied Physics Letters* **65**, 3188-3190, (1994).

163 Chae, B. G. *et al.* Highly oriented VO2 thin films prepared by sol-gel deposition. *Electrochemical and Solid State Letters* **9**, C12-C14, (2006).

164 Chae, B. G., Kim, H. T. & Yun, S. J. Characteristics of W- and Ti-doped VO(2) thin films prepared by sol-gel method. *Electrochemical and Solid State Letters* **11**, D53-D55, (2008).

165 Maruyama, T. & Ikuta, Y. Vanadium dioxide thin-films prepared by chemical-vapor-deposition from vanadium (III) acetylacetonate. *Journal of Materials Science* **28**, 5073-5078, (1993).

166 Sahana, M. B., Subbanna, G. N. & Shivashankar, S. A. Phase transformation and semiconductor-metal transition in thin films of $VO_2$ deposited by low-pressure metalorganic chemical vapor deposition. *Journal of Applied Physics* **92**, 6495-6504, (2002).

167 Nag, J. & Haglund, R. F., Jr. Synthesis of vanadium dioxide thin films and nanoparticles. *J. Phys.-Condes. Matter* **20**, (2008).

168 Cao, J. *et al.* Extended Mapping and Exploration of the Vanadium Dioxide Stress-Temperature Phase Diagram. *Nano Letters* **10**, 2667-2673, (2010).

169 Wu, J. *et al.* Strain-induced self organization of metal-insulator domains in single-crystalline $VO_2$ nanobeams. *Nano Letters* **6**, 2313-2317, (2006).

170 Guiton, B. S., Gu, Q., Prieto, A. L., Gudiksen, M. S. & Park, H. Single-crystalline vanadium dioxide nanowires with rectangular cross sections. *Journal of the American Chemical Society* **127**, 498-499, (2005).

171 Tselev, A. *et al.* Mesoscopic Metal–Insulator Transition at Ferroelastic Domain Walls in $VO_2$. *ACS Nano* **4**, 4412-4419, (2010).

172 Gu, Y. J., Cao, J. B., Wu, J. Q. & Chen, L. Q. Thermodynamics of strained vanadium dioxide single crystals. *Journal of Applied Physics* **108**, (2010).

173 Pouget, J. P., Launois, H., Dhaenens, J. P., Merenda, P. & Rice, T. M. Electron localization induced by uniaxial stress in pure $VO_2$. *Physical Review Letters* **35**, 873-875, (1975).

174 Marvel, R., Appavoo, K., Choi, B., Nag, J. & Haglund, R. Electron-beam deposition of vanadium dioxide thin films. *Applied Physics A: Materials Science & Processing*, 1-7, (2012).

175 Pouget, J. P. *et al.* Dimerization of a linear heisenberg chain in insulating phases of $V_{1-X}Cr_XO_2$. *Physical Review B* **10**, 1801-1815, (1974).

176 Ghedira, M., Vincent, H., Marezio, M. & Launay, J. C. Structural aspects of metal-insulator transitions in $V_{0.985}Al_{0.015}O_2$. *Journal of Solid State Chemistry* **22**, 423-438, (1977).

177 Wei, J., Ji, H., Guo, W., Nevidomskyy, A. H. & Natelson, D. Hydrogen stabilization of metallic vanadium dioxide in single-crystal nanobeams. *Nat. Nanotechnol.* **7**, 357-362, (2012).

178 Liu, M. *et al.* Terahertz-field-induced insulator-to-metal transition in vanadium dioxide metamaterial. *Nature* **487**, 345-348, (2012).

179 Kim, H. T. *et al.* Mechanism and observation of Mott transition in $VO_2$-based two- and three-terminal devices. *New Journal of Physics* **6**, (2004).

180 Stefanovich, G., Pergament, A. & Stefanovich, D. Electrical switching and Mott transition in $VO_2$. *J. Phys.-Condes. Matter* **12**, 8837-8845, (2000).

181 Kim, B.-J., Lee, Y. W., Choi, S., Yun, S. J. & Kim, H.-T. $VO_2$ Thin-Film Varistor Based on Metal-Insulator Transition. *IEEE Electron Device Letters* **31**, 14-16, (2010).

182 Chen, C. H., Wang, R., Shang, L. & Guo, C. Gate-field-induced phase transitions in $VO_2$: Monoclinic metal phase separation and switchable infrared reflections. *Applied Physics Letters* **93**, (2008).

183 Chudnovskiy, F., Luryi, S. & Spivak, B. Switching device based on first-order metal insulator transition induced by external electric field. 148-155 (Wiley Interscience, 2002).

184 Nakano, M. *et al.* Collective bulk carrier delocalization driven by electrostatic surface charge accumulation. *Nature* **487**, 459-462, (2012).

185 Zhou, Y. & Ramanathan, S. Relaxation dynamics of ionic liquid-$VO_2$ interfaces and influence in electric double-layer transistors. *Journal of Applied Physics* **111**, (2012).

186 Ko, C., Yang, Z. & Ramanathan, S. Work Function of Vanadium Dioxide Thin Films Across the Metal-Insulator Transition and the Role of Surface Nonstoichiometry. *Acs Applied Materials & Interfaces* **3**, 3396-3401, (2011).

187 Yang, Z., Ko, C., Balakrishnan, V., Gopalakrishnan, G. & Ramanathan, S. Dielectric and carrier transport properties of vanadium dioxide thin films across the phase transition utilizing gated capacitor devices. *Physical Review B* **82**, (2010).

188 Ruzmetov, D., Gopalakrishnan, G., Ko, C., Narayanamurti, V. & Ramanathan, S. Three-terminal field effect devices utilizing thin film vanadium oxide as the channel layer. *Journal of Applied Physics* **107**, (2010).

189 Ruzmetov, D., Gopalakrishnan, G., Deng, J., Narayanamurti, V. & Ramanathan, S. Electrical triggering of metal-insulator transition in nanoscale vanadium oxide junctions. *Journal of Applied Physics* **106**, (2009).

190 Ko, C. & Ramanathan, S. Dispersive capacitance and conductance across the phase transition boundary in metal-vanadium oxide-silicon devices. *Journal of Applied Physics* **106**, (2009).

191 Kittiwatanakul, S., Lu, J. & Wolf, S. A. Transport Anisotropy of Epitaxial $VO_2$ Films near the Metal-Semiconductor Transition. *Applied Physics Express* **4**, (2011).

192 Chollet, M. *et al.* Gigantic photoresponse in 1/4-filled-band organic salt (EDO-TTF)(2)PF6. *Science* **307**, 86-89, (2005).

193 Roach, W. R. & Balberg, I. Optical induction and detection of fast phase transition in $VO_2$. *Solid State Communications* **9**, 551-555, (1971).

194 Roach, W. R. Holographic storage in $VO_2$. *Applied Physics Letters* **19**, 453, (1971).

195 Museum, S. F. *"Sallie Gardner at a Gallop" by Eadward Muybridge*, <http://www.sfmuseum.org/hist3/sallie.html>

196 Gearheart, L. A. *et al.* Sodium-ion binding to DNA: Detection by ultrafast time-resolved stokes-shift spectroscopy. *Journal of the American Chemical Society* **125**, 11812-11813, (2003).

197 Zewail, A. H. LASER Femtochemistry. *Science* **242**, 1645-1653, (1988).

198 Zewail, A. H. Femtochemistry: Atomic-scale dynamics of the chemical bond. *Journal of Physical Chemistry A* **104**, 5660-5694, (2000).

199 Siwick, B. J., Dwyer, J. R., Jordan, R. E. & Miller, R. J. D. An atomic-level view of melting using femtosecond electron diffraction. *Science* **302**, 1382-1385, (2003).

200 Borri, P. *et al.* Ultralong dephasing time in InGaAs quantum dots. *Physical Review Letters* **87**, (2001).

201 Ogawa, S., Nagano, H., Petek, H. & Heberle, A. P. Optical dephasing in Cu(111) measured by interferometric two-photon time-resolved photoemission. *Physical Review Letters* **78**, 1339-1342, (1997).

202 Ichikawa, H. *et al.* Transient photoinduced 'hidden' phase in a manganite. *Nat. Mater.* **10**, 101-105, (2011).

203 Dienst, A. *et al.* Bi-directional ultrafast electric-field gating of interlayer charge transport in a cuprate superconductor. *Nat. Photonics* **5**, 485-488, (2011).

204 Shank, C. V., Auston, D. H., Ippen, E. P. & Teschke, O. Picosecond time resolved reflectivity of direct gap semiconductors. *Solid State Communications* **26**, 567-570, (1978).

205 Shank, C. V., Yen, R. & Hirlimann, C. Time-resolved reflectivity measurements of femtosecond-optical-pulse induced phase-transitions in silicon. *Physical Review Letters* **50**, 454-457, (1983).

206 von der Linde, D. *et al.* 'Ultrafast' extended to X-rays: Femtosecond time-resolved X-ray diffraction. *Zeitschrift Fur Physikalische Chemie-International Journal of Research in Physical Chemistry & Chemical Physics* **215**, 1527-1541, (2001).

207 Petek, H. & Ogawa, S. Femtosecond time-resolved two-photon photoemission studies of electron dynamics in metals. *Progress in Surface Science* **56**, 239-310, (1997).

208 Lehmann, J. *et al.* Surface plasmon dynamics in silver nanoparticles studied by femtosecond time-resolved photoemission. *Physical Review Letters* **85**, 2921-2924, (2000).

209 Knoesel, E., Hotzel, A. & Wolf, M. Temperature dependence of surface state lifetimes, dephasing rates and binding energies on Cu(111) studied with time-resolved photoemission. *Journal of Electron Spectroscopy and Related Phenomena* **88**, 577-584, (1998).

210 Perfetti, L. *et al.* Ultrafast electron relaxation in superconducting $Bi_2Sr_2CaCu_2O_8$+delta by time-resolved photoelectron spectroscopy. *Physical Review Letters* **99**, (2007).

211 Perfetti, L. *et al.* Time evolution of the electronic structure of 1T-$TaS_2$ through the insulator-metal transition. *Physical Review Letters* **97**, (2006).

212 Rini, M. *et al.* Control of the electronic phase of a manganite by mode-selective vibrational excitation. *Nature* **449**, 72-74, (2007).

213 Foerst, M. *et al.* Nonlinear phononics as an ultrafast route to lattice control. *Nature Physics* **7**, 854-856, (2011).

214 Lysenko, S. *et al.* Light-induced ultrafast phase transitions in $VO_2$ thin film. *Applied Surface Science* **252**, 5512-5515, (2006).

215 Lysenko, S., Rua, A., Vikhnin, V., Fernandez, F. & Liu, H. Insulator-to-metal phase transition and recovery processes in VO2 thin films after femtosecond laser excitation. *Physical Review B* **76**, (2007).

216 Lysenko, S., Vikhnin, V., Fernandez, F., Rua, A. & Liu, H. Photoinduced insulator-to-metal phase transition in VO2 crystalline films and model of dielectric susceptibility. *Physical Review B* **75**, (2007).

217 Hilton, D. J. *et al.* Enhanced photosusceptibility near T(c) for the light-induced insulator-to-metal phase transition in vanadium dioxide. *Physical Review Letters* **99**, (2007).

218 Cavalleri, A., Rini, M. & Schoenlein, R. W. Ultra-broadband femtosecond measurements of the photo-induced phase transition in $VO_2$: From the mid-IR to the hard x-rays. *Journal of the Physical Society of Japan* **75**, (2006).

219 Cavalleri, A., Dekorsy, T., Chong, H. H. W., Kieffer, J. C. & Schoenlein, R. W. Evidence for a structurally-driven insulator-to-metal transition in $VO_2$: A view from the ultrafast timescale. *Physical Review B* **70**, (2004).

220 Abbate, M. *et al.* Soft-x-ray-absorption studies of the electronic-structure changes through the $VO_2$ phase-transition. *Physical Review B* **43**, 7263-7267, (1991).

221 Cavalleri, A. *et al.* Band-selective measurements of electron dynamics in $VO_2$ using femtosecond near-edge x-ray absorption. *Physical Review Letters* **95**, (2005).

222 Kim, H. T. *et al.* Raman study of electric-field-induced first-order metal-insulator transition in VO2-based devices. *Applied Physics Letters* **86**, (2005).

223 Brinkman, W. F. & Rice, T. M. Application of Gutzwiller's variational method to the metal-insulator transition. *Physical Review B-Solid State* **2**, 4302-4304, (1970).

224 Kim, H. T. Extension of the Brinkman-Rice picture and the Mott transition. *Physica C* **341**, 259-260, (2000).

225 Rini, M. *et al.* Optical switching in $VO_2$ films by below-gap excitation. *Applied Physics Letters* **92**, (2008).

226 Paquet, D. & Lerouxhugon, P. Electron correlations and electron-lattice interactions in the metal-insulator, ferroelastic transition in $VO_2$ - a thermodynamical study. *Physical Review B* **22**, 5284-5301, (1980).

227 Pashkin, A. *et al.* Ultrafast insulator-metal phase transition in $VO_2$ studied by multiterahertz spectroscopy. *Physical Review B* **83**, (2011).

228 Kuebler, C. *et al.* Coherent structural dynamics and electronic correlations during an ultrafast insulator-to-metal phase transition in $VO_2$. *Physical Review Letters* **99**, (2007).

229 Kim, H.-T. *et al.* Monoclinic and correlated metal phase in $VO_2$ as evidence of the Mott transition: Coherent phonon analysis. *Physical Review Letters* **97**, (2006).

230 Biermann, S., Poteryaev, A., Lichtenstein, A. I. & Georges, A. Dynamical singlets and correlation-assisted peierls transition in $VO_2$. *Physical Review Letters* **94**, (2005).

231 Huber, R. *et al.* 12-fs pulses from a continuous-wave-pumped 200-nJ Ti : sapphire amplifier at a variable repetition rate as high as 4 MHz. *Opt. Lett.* **28**, 2118-2120, (2003).

232 Kubler, C., Huber, R., Tubel, S. & Leitenstorfer, A. Ultrabroadband detection of multi-terahertz field transients with GaSe electro-optic sensors: Approaching the near infrared. *Applied Physics Letters* **85**, 3360-3362, (2004).

233 Hada, M., Okimura, K. & Matsuo, J. Characterization of structural dynamics of $VO_2$ thin film on c-$Al_2O_3$ using in-air time-resolved x-ray diffraction. *Physical Review B* **82**, (2010).

234 Hada, M., Okimura, K. & Matsuo, J. Photo-induced lattice softening of excited-state $VO_2$. *Applied Physics Letters* **99**, (2011).

235 Petrov, G. I., Yakovlev, V. V. & Squier, J. Raman microscopy analysis of phase transformation mechanisms in vanadium dioxide. *Applied Physics Letters* **81**, 1023-1025, (2002).

236 Cocker, T. L. *et al.* Phase diagram of the ultrafast photoinduced insulator-metal transition in vanadium dioxide. *Physical Review B* **85**, (2012).

237 Rini, M. *et al.* Photoinduced phase transition in $VO_2$ nanocrystals: ultrafast control of surface-plasmon resonance. *Opt. Lett.* **30**, 558-560, (2005).

238 Wegkamp, D. *et al.* Phase retrieval and compression of low-power white-light pulses. *Applied Physics Letters* **99**, (2011).

239 Dicken, M. J. *et al.* Frequency tunable near-infrared metamaterials based on VO2 phase transition. *Optics Express* **17**, 18330-18339, (2009).

240 Xu, G. *et al.* Electron injection assisted phase transition in a nano-Au/$VO_2$ junction. *Applied Physics Letters* **93**, (2008).

241 Xu, G., Huang, C.-M., Jin, P., Tazawa, M. & Chen, D.-M. Nano-Ag on vanadium dioxide. I. Localized spectrum tailoring. *Journal of Applied Physics* **104**, (2008).

242 Shegai, T. *et al.* A bimetallic nanoantenna for directional colour routing. *Nature Communications* **2**, (2011).

243 Johnson, P. B. & Christy, R. W. Optical constants of noble metals. *Physical Review B* **6**, 4370-4379, (1972).

244 *Microscope Objective*, <http://www.olympus-ims.com/en/microscope/lmplfln-bd/>

245 *TE Technologies*, <http://www.tetech.com/Peltier-Thermoelectric-Cooler-Modules.html>

246 Lei, D. Y. *Superfocusing, Biosensing and Modulation in Plasmonics* Ph. D. thesis, Imperial College London, (2011).

247 Verleur, H. W., Barker, A. S. & Berglund, C. N. Optical properties of $VO_2$ between 0.25 and 5 eV. *Physical Review* **172**, 788-&, (1968).

248 Larsson, E. M., Alegret, J., Kall, M. & Sutherland, D. S. Sensing characteristics of NIR localized surface plasmon resonances in gold nanorings for application as ultrasensitive biosensors. *Nano Letters* **7**, 1256-1263, (2007).

249 Jackson, J. D. *Classical Electrodynamics, 3rd ed.*, (Wiley, 1998).

250 Driscoll, T. *et al.* Tuned permeability in terahertz split-ring resonators for devices and sensors. *Applied Physics Letters* **91**, (2007).

251 Zheludev, N. All change, please. *Nat. Photonics* **1**, 551-553, (2007).

252 Santander-Syro, A. F. *et al.* Two-dimensional electron gas with universal subbands at the surface of SrTiO3. *Nature* **469**, 189-193, (2011).

253 Reyren, N. *et al.* Superconducting Interfaces Between Insulating Oxides. *Science* **317**, 1196-1199, (2007).

254 Simpson, R. E. *et al.* Interfacial phase-change memory. *Nat. Nanotechnol.* **6**, 501-505, (2011).

255 Donev, E. U., Ziegler, J. I., Haglund, R. F. & Feldman, L. C. Size effects in the structural phase transition of VO2 nanoparticles studied by surface-enhanced Raman scattering. *Journal of Optics a-Pure and Applied Optics* **11**, (2009).

256 Yang, T. H., Jin, C. M., Zhou, H. H., Narayan, R. J. & Narayan, J. Role of twin boundaries in semiconductor to metal transition characteristics of VO(2) films. *Applied Physics Letters* **97**, 072101 - 072101-072103, (2010).

257 Yin, W. *et al.* The metal-insulator transition in vanadium dioxide: A view at bulk and surface contributions for thin films and the effect of annealing. *J. Appl. Phys.* **105**, 114322, (2009).

258 Nagashima, K., Yanagida, T., Tanaka, H. & Kawai, T. Interface effect on metal-insulator transition of strained vanadium dioxide ultrathin films. *Journal of Applied Physics* **101**, 026103, (2007).

259 Viswanath, B., Ko, C. H., Yang, Z. & Ramanathan, S. Geometric confinement effects on the metal-insulator transition temperature and stress relaxation in VO(2) thin films grown on silicon. *Journal of Applied Physics* **109**, 063512, (2011).

260 Goncalves-Ferreira, L., Redfern, S. A. T., Artacho, E., Salje, E. & Lee, W. T. Trapping of oxygen vacancies in the twin walls of perovskite. *Physical Review B* **81**, 024109, (2010).

261 Donev, E. U., Lopez, R., Feldman, L. C. & Haglund, R. F. Confocal Raman Microscopy across the Metal-Insulator Transition of Single Vanadium Dioxide Nanoparticles. *Nano Letters* **9**, 702-706, (2009).

262 Lopez, R., Feldman, L. C. & Haglund, R. F. Size-Dependent Optical Properties of VO_{2} Nanoparticle Arrays. *Physical Review Letters* **93**, 177403, (2004).

263 Zhao, L., Kelly, K. L. & Schatz, G. C. The Extinction Spectra of Silver Nanoparticle Arrays: Influence of Array Structure on Plasmon Resonance Wavelength and Width†. *The Journal of Physical Chemistry B* **107**, 7343-7350, (2003).

264 Kelly, K. L., Coronado, E., Zhao, L. L. & Schatz, G. C. The Optical Properties of Metal Nanoparticles: The Influence of Size, Shape, and Dielectric Environment. *The Journal of Physical Chemistry B* **107**, 668-677, (2002).

265 Pergament, A. Metal-insulator transition: the Mott criterion and coherence length. *J. Phys.-Condes. Matter* **15**, 3217-3223, (2003).

266 Lei, D. Y., Appavoo, K., Sonnefraud, Y., Haglund, R. F. & Maier, S. A. Single-particle plasmon resonance spectroscopy of phase transition in vanadium dioxide. *Opt. Lett.* **35**, 3988-3990, (2010).

267 Ke, M., Hackney, S. A., Milligan, W. W. & Aifantis, E. C. Observation and measurement of grain rotation and plastic strain in nanostructured metal thin-films. *Nanostruct. Mater.* **5**, 689-697, (1995).

268 van der Laan, D. C., Haugan, T. J. & Barnes, P. N. Effect of a Compressive Uniaxial Strain on the Critical Current Density of Grain Boundaries in Superconducting $YBa_2Cu_3O_{7-delta}$ Films. *Physical Review Letters* **103**, 027005, (2009).

269 Wang, B., Puzyrev, Y. & Pantelides, S. T. Strain enhanced defect reactivity at grain boundaries in polycrystalline graphene. *Carbon* **49**, 3983-3988, (2011).

270 Klie, R. F. *et al.* Enhanced current transport at grain boundaries in high-T-c superconductors. *Nature* **435**, 475-478, (2005).

271 Kresse, G. & Furthmuller, J. Efficient iterative schemes for ab initio total-energy calculations using a plane-wave basis set. *Physical Review B* **54**, 11169-11186, (1996).

272 Perdew, J. P., Burke, K. & Ernzerhof, M. Generalized Gradient Approximation Made Simple. *Physical Review Letters* **77**, 3865, (1996).

273 Kresse, G. & Joubert, D. From ultrasoft pseudopotentials to the projector augmented-wave method. *Physical Review B* **59**, 1758, (1999).

274 Blochl, P. E., Jepsen, O. & Andersen, O. K. Improved tetrahedron method for brillouin-zone integrations. *Physical Review B* **49**, 16223-16233, (1994).

275 Liechtenstein, A. I., Anisimov, V. I. & Zaanen, J. Density-functional theory and strong interactions: Orbital ordering in Mott-Hubbard insulators. *Physical Review B* **52**, R5467, (1995).

276 Biermann, S., Poteryaev, A., Lichtenstein, A. I. & Georges, A. Dynamical Singlets and Correlation-Assisted Peierls Transition in VO_{2}. *Physical Review Letters* **94**, 026404, (2005).

277 Maiti, A., Pantelides, S. T., Chisholm, M. F. & Pennycook, S. J. Damage nucleation and vacancy-induced structural transformation in Si grain boundaries. *Applied Physics Letters* **75**, 2380-2382, (1999).

278 Zhi-Xiong Cai, Y. Z. *Microstructures and Structural Defects in High-Temperature Superconductors*. (World Scientific Pub Co Inc, 1998).

279 John Price Hirth, J. L. *Theory of Dislocations*. (Krieger Pub Co, 1992).

280 Salje, E. K. H. *Phase Transitions in Ferroelastic and Co-Elastic Crystals*. (Cambridge University Press, 1990).

281 Maier, S. A., Brongersma, M. L., Kik, P. G. & Atwater, H. A. Observation of near-field coupling in metal nanoparticle chains using far-field polarization spectroscopy. *Physical Review B* **65**, (2002).

282 Maier, S. A., Kik, P. G. & Atwater, H. A. Optical pulse propagation in metal nanoparticle chain waveguides. *Physical Review B* **67**, (2003).

283 Maier, S. A. *et al.* Local detection of electromagnetic energy transport below the diffraction limit in metal nanoparticle plasmon waveguides. *Nat. Mater.* **2**, 229-232, (2003).

284 Maier, S. A. & Atwater, H. A. Plasmonics: Localization and guiding of electromagnetic energy in metal/dielectric structures. *Journal of Applied Physics* **98**, (2005).

285 Liu, N. *et al.* Manipulating Magnetic Plasmon Propagation in Metallic Nanocluster Networks. *ACS Nano* **6**, 5482-5488, (2012).

286 Solis, D., Jr. *et al.* Electromagnetic Energy Transport in Nanoparticle Chains via Dark Plasmon Modes. *Nano Letters* **12**, 1349-1353, (2012).

287 *Atwater Research Group*, <http://daedalus.caltech.edu/>

288 Tolbert, S. H. & Alivisatos, A. P. Size dependence of a first-order solid-solid phase-transition - the wurtzite to rock-salt transformation in CdSe nanocrystals. *Science* **265**, 373-376, (1994).

289 Mazumder, R. *et al.* Particle size dependence of magnetization and phase transition near T-N in multiferroic $BiFeO_3$. *Journal of Applied Physics* **100**, (2006).

290 Kim, T. H. *et al.* Imaging and manipulation of the competing electronic phases near the Mott metal-insulator transition. *Proc. Natl. Acad. Sci. U. S. A.* **107**, 5272-5275, (2010).

291 Narayan, J. & Bhosle, V. M. Phase transition and critical issues in structure-property correlations of vanadium oxide. *Journal of Applied Physics* **100**, (2006).

292 Ramirez, J. G., Sharoni, A., Dubi, Y., Gomez, M. E. & Schuller, I. K. First-order reversal curve measurements of the metal-insulator transition in VO2: Signatures of persistent metallic domains. *Physical Review B* **79**, (2009).

293 Klein, M. W., Enkrich, C., Wegener, M. & Linden, S. Second-harmonic generation from magnetic metamaterials. *Science* **313**, 502-504, (2006).

294 Feth, N. *et al.* Second-harmonic generation from complementary split-ring resonators. *Optics Letters* **33**, 1975-1977, (2008).

295 Linden, S. *et al.* Photonic metamaterials: Magnetism at optical frequencies. *Ieee Journal of Selected Topics in Quantum Electronics* **12**, 1097-1105, (2006).

296 Rockstuhl, C. *et al.* On the reinterpretation of resonances in split-ring-resonators at normal incidence. *Optics Express* **14**, 8827-8836, (2006).

297 Suh, J. Y. *et al.* Modulation of the gold particle-plasmon resonance by the metal-semiconductor transition of vanadium dioxide. *J. Opt. A-Pure Appl. Opt.* **10**, (2008).

298 Lopez, R., Haynes, T. E., Boatner, L. A., Feldman, L. C. & Haglund, R. F. Size effects in the structural phase transition of VO2 nanoparticles. *Physical Review B* **65**, (2002).

299 Khakhaev, I. A., Chudnovskii, F. A. & Shadrin, E. B. MARTENSITIC PHENOMENA IN THE METAL-INSULATOR PHASE-TRANSITION IN VANADIUM DIOXIDE FILMS. *Fizika Tverdogo Tela* **36**, 1643-1649, (1994).

300 Xu, G. *et al.* Electron injection assisted phase transition in a nano-Au-VO2 junction. *Applied Physics Letters* **93**, (2008).

301 Sharoni, A., Ramirez, J. G. & Schuller, I. K. Multiple avalanches across the metal-insulator transition of vanadium oxide nanoscaled junctions. *Physical Review Letters* **101**, (2008).

302 Chen, C. H., Wang, R. F., Shang, L. & Guo, C. F. Gate-field-induced phase transitions in VO2: Monoclinic metal phase separation and switchable infrared reflections. *Applied Physics Letters* **93**, (2008).

303 Fredriksson, H. *et al.* Hole-mask colloidal lithography. *Adv. Mater.* **19**, 4297-+, (2007).

304 Langhammer, C., Schwind, M., Kasemo, B. & Zoric, I. Localized surface plasmon resonances in aluminum nanodisks. *Nano Letters* **8**, 1461-1471, (2008).

305 Nasu, K. *Photoinduced Phase Transitions*. (World Scientific Publishing Co. Pte. Ltd. , 2004).

306 Wall, S. *et al.* Ultrafast changes in lattice symmetry probed by coherent phonons. *Nature Communications* **3**, 721, (2012).

307 Sciaini, G. *et al.* Electronic acceleration of atomic motions and disordering in bismuth. *Nature* **458**, 56-62, (2009).

308 Knight, M. W., Sobhani, H., Nordlander, P. & Halas, N. J. Photodetection with Active Optical Antennas. *Science* **332**, 702-704, (2011).

309 Abb, M., Albella, P., Aizpurua, J. & Muskens, O. L. All-Optical Control of a Single Plasmonic Nanoantenna-ITO Hybrid. *Nano Letters* **11**, 2457-2463, (2011).

310 Lowell, J. & Roseinnes, A. C. Contact Electrification. *Adv. Phys.* **29**, 947-1023, (1980).

311 Appavoo, K. *et al.* Role of Defects in the Phase Transition of $VO_2$ Nanoparticles Probed by Plasmon Resonance Spectroscopy. *Nano Letters* **12**, 780-786, (2012).

312 Beversluis, M. R., Bouhelier, A. & Novotny, L. Continuum generation from single gold nanostructures through near-field mediated intraband transitions. *Physical Review B* **68**, (2003).

313 Krolikow, W. F. & Spicer, W. E. Photoemission studies of noble metals. *Physical Review B-Solid State* **1**, 478-&, (1970).

314 Hohlfeld, J., Conrad, U., Muller, J. G., Wellershoff, S. S. & Matthias, E. in *Nonlinear Optics in Metals* (ed K. H. Bennemann) (Clarendon Press, 1998).

315 Hohlfeld, J. *et al.* Electron and lattice dynamics following optical excitation of metals. *Chem. Phys.* **251**, 237-258, (2000).

316 Tisdale, W. A. *et al.* Hot-Electron Transfer from Semiconductor Nanocrystals. *Science* **328**, 1543-1547, (2010).

317 Togo, A., Oba, F. & Tanaka, I. First-principles calculations of the ferroelastic transition between rutile-type and $CaCl_2$-type $SiO_2$ at high pressures. *Physical Review B* **78**, (2008).

318 Monkman, E. J. *et al.* Quantum many-body interactions in digital oxide superlattices. *Nat Mater* **11**, 855-859, (2012).

319 Pardo, V. & Pickett, W. E. Half-Metallic Semi-Dirac-Point Generated by Quantum Confinement in TiO2/VO2 Nanostructures. *Physical Review Letters* **102**, (2009).

320 Pardo, V. & Pickett, W. E. Metal-insulator transition through a semi-Dirac point in oxide nanostructures: VO2 (001) layers confined within TiO2. *Physical Review B* **81**, (2010).

321 Zhang, S., Genov, D. A., Wang, Y., Liu, M. & Zhang, X. Plasmon-induced transparency in metamaterials. *Physical Review Letters* **101**, (2008).

322 Liu, N. *et al.* Plasmonic analogue of electromagnetically induced transparency at the Drude damping limit. *Nat. Mater.* **8**, 758-762, (2009).

323 Liu, N. *et al.* Planar Metamaterial Analogue of Electromagnetically Induced Transparency for Plasmonic Sensing. *Nano Letters* **10**, 1103-1107, (2010).

324 Fan, J. A. *et al.* Self-Assembled Plasmonic Nanoparticle Clusters. *Science* **328**, 1135-1138, (2010).

325 Fan, J. A. *et al.* Plasmonic Mode Engineering with Templated Self-Assembled Nanoclusters. *Nano Letters* **12**, 5318-5324, (2012).

326 Hentschel, M. *et al.* Transition from Isolated to Collective Modes in Plasmonic Oligomers. *Nano Letters* **10**, 2721-2726, (2010).

327 Dregely, D., Hentschel, M. & Giessen, H. Excitation and Tuning of Higher-Order Fano Resonances in Plasmonic Oligomer Clusters. *ACS Nano* **5**, 8202-8211, (2011).

328 Hentschel, M., Dregely, D., Vogelgesang, R., Giessen, H. & Liu, N. Plasmonic Oligomers: The Role of Individual Particles in Collective Behavior. *ACS Nano* **5**, 2042-2050, (2011).

329 Yu, N. *et al.* Light Propagation with Phase Discontinuities: Generalized Laws of Reflection and Refraction. *Science* **334**, 333-337, (2011).

330 Genevet, P. *et al.* Ultra-thin plasmonic optical vortex plate based on phase discontinuities. *Applied Physics Letters* **100**, (2012).

331 Lysenko, S., Vikhnin, V., Rua, A., Fernandez, F. & Liu, H. Critical behavior and size effects in light-induced transition of nanostructured VO2 films. *Physical Review B* **82**, (2010).

332 Gjonaj, B. *et al.* Active spatial control of plasmonic fields. *Nat Photon* **5**, 360-363, (2011).

333 *Microchem PMMA data sheet*, <http://microchem.com/pdf/PMMA_Data_Sheet.pdf>

334 Lamprecht, B., Krenn, J. R., Leitner, A. & Aussenegg, F. R. Resonant and off-resonant light-driven plasmons in metal nanoparticles studied by femtosecond-resolution third-harmonic generation. *Physical Review Letters* **83**, 4421-4424, (1999).

335 Anderson, A., Deryckx, K. S., Xu, X. J. G., Steinmeyer, G. & Raschke, M. B. Few-Femtosecond Plasmon Dephasing of a Single Metallic Nanostructure from Optical Response Function Reconstruction by Interferometric Frequency Resolved Optical Gating. *Nano Letters* **10**, 2519-2524, (2010).

336 Diels, J. C. M., Fontaine, J. J., McMichael, I. C. & Simoni, F. Control and measurement of ultrashort pulse shapes (in amplitude and phase) with femtosecond accuracy. *Appl. Optics* **24**, 1270-1282, (1985).

337 Maznev, A. A., Crimmins, T. F. & Nelson, K. A. How to make femtosecond pulses overlap. *Opt. Lett.* **23**, 1378-1380, (1998).

338 Diels, J. D. & Rudolph, W. *Ultrashort Laser Pulse Phenomena, 2nd Ed.*, (Academic Press, 2006).

339 Lamprecht, B. *et al.* Metal nanoparticle gratings: Influence of dipolar particle interaction on the plasmon resonance. *Physical Review Letters* **84**, 4721-4724, (2000).

340 Gallmann, L. *et al.* Spatially resolved amplitude and phase characterization of femtosecond optical pulses. *Opt. Lett.* **26**, 96-98, (2001).

341 Steinmeyer, G., Sutter, D. H., Gallmann, L., Matuschek, N. & Keller, U. Frontiers in ultrashort pulse generation: Pushing the limits in linear and nonlinear optics. *Science* **286**, 1507-1512, (1999).

342 Stibenz, G. & Steinmeyer, G. Interferometric frequency-resolved optical gating. *Optics Express* **13**, 2617-2626, (2005).

343 Telle, H. R. *et al.* Carrier-envelope offset phase control: A novel concept for absolute optical frequency measurement and ultrashort pulse generation. *Appl. Phys. B-Lasers Opt.* **69**, 327-332, (1999).

344 Wyatt, A. S., Walmsley, I. A., Stibenz, G. & Steinmeyer, G. Sub-10 fs pulse characterization using spatially encoded arrangement for spectral phase interferometry for direct electric field reconstruction. *Opt. Lett.* **31**, 1914-1916, (2006).

345 Halabica, A. *et al.* Pulsed infrared laser annealing of gold nanoparticles embedded in a silica matrix. *Journal of Applied Physics* **103**, (2008).

346 Halabica, A., Pantelides, S. T., Haglund, R. F., Jr., Magruder, R. H., III & Meldrum, A. Excitation and detection of surface acoustic phonon modes in Au/Al2O3 multilayers. *Physical Review B* **80**, (2009).